Electronic Bands of Nanoporous Networks and One-Dimensional Covalent Polymers Assembled on Metal Surfaces

PhD Thesis

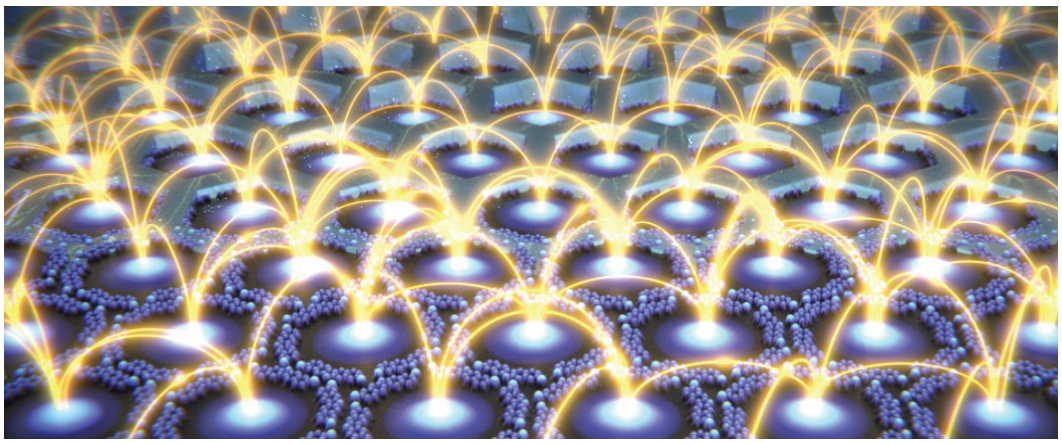

Ignacio Piquero-Zulaica

Supervisors:
Dr. Jorge Lobo-Checa
Prof. J. Enrique Ortega

eman ta zabal zazu

Universidad del País Vasco

Euskal Herriko Unibertsitatea

EUSKAL HERRIKO UNIBERTSITATEA (EHU-UPV)

Electronic Bands of Nanoporous Networks and One-Dimensional Covalent Polymers Assembled on Metal Surfaces

Author:
Ignacio Piquero-Zulaica

Supervisors:
Dr. Jorge Lobo-Checa
Prof. J. Enrique Ortega

A thesis submitted in fulfillment of the requirements for the degree of Doctor of Philosophy in Physics of Nanostructures and Advanced Materials

in the

Nanophysics Lab
Centro de Física de Materiales (CFM-CSIC)

October 19, 2018

Abstract

Complex molecular layers self-assembled on surfaces with engineered architectures and tailored properties, are expected to play an important role in the development of future devices at the nanoscale [1–3]. The reversibility of non-covalent interactions such as hydrogen bonds or metal ligand interactions, allows error correction processes in the formed structures. Such elimination of defective structures can give rise to almost defect-free, long-range ordered formations. Metal-organic networks grown on metallic surfaces fall into such self-healing structures and show novel magnetic properties [4, 5], catalytic effects [6, 7], oxidation states [8], exotic tesellation patterns [9–12] and even bear the prospect of exhibiting topological band structures [13, 14].

Nanoporous networks featuring long-range order belong to error corrected non-covalent structures. The recent finding of electron confinement of the two-dimensional electron gas (2DEG) within the nanopores of self-assembled supramolecular nanoporous networks, is an experimental demonstration of a quantum box effect. This is an effect which may play a crucial role in engineering future molecular devices [15–17]. By using scanning tunneling microscopy and spectroscopy (STM/STS), in a similar fashion to quantum corrals [18, 19], it is possible to probe such localized electronic states at the single pore or quantum dot (QD) level [15–17].

However, studies on the long-range ordered and robust 3deh-DPDI metal-organic network on Cu(111), revealed that nanopores are rather imperfect or leaky confining entities, leading to significant coupling to neighboring nanopores. The periodicity of the highly-ordered supramolecular network induces the formation of Bloch-wave states that result into new electronic bands that can be observed by spatially averaging angle-resolved photoemission spectroscopy (ARPES) [15].

The well-established control of the structures of porous networks, together with its characteristic degree of coupling between ad-molecules and the surface state, is our starting point for the fabrication and investigation of coupled electronic systems with tailored band structures. Based on the concepts of Supramolecular Chemistry on surfaces, by choosing suitable molecular constituents (functional groups and/or carbon backbone size) and guided by reversible, non-covalent bonding mechanisms, we are able to generate six different long-range ordered nanoporous networks on (111)-terminated coinage metal surfaces in ultra-high vacuum (UHV). Such nanoporous structures are analogous to QD arrays on surfaces, bearing distinct sizes, barrier separations and scattering strengths. As a result, with each particular nanoporous system grown, we not only engineer the local confinement properties at each QD, but also modulate the coherent electronic band structure steming from the overall array. We observe changes in its fundamental energy, band dispersion, effective mass, zone boundary gaps and Fermi surface contour.

Our experimental findings are supported by the electron boundary elements method in combination with the electron plane wave expansion (EBEM/EPWE)

modelling, density functional theory (DFT) calculations, and the phase accumulation model (PAM). In this way, we disentangle the repulsive scattering potential landscape of each nanoporous network and delve into subtle surface-organic overlayer interactions, such as hybridization and geometry induced effects, which are altogether responsible for the confinement effects and distinct electronic band modulations. Our findings envision the engineering of 2D electronic metamaterials, in analogy to the well-established optical metamaterials [20].

The studied electronic structure from nanoporous networks correspond to the modified substrate's surface state, which is independent of the molecular states. However, low-dimensional organic electronic states, such as the one obtained in graphene nanoribbons (GNRs) and oligophenylene chains are currently very attractive to the Scientific Community based on their industrial prospects. These one-dimensional polymeric structures have been extensively studied as simple, appealing nanostructures leading to distinct electronic features, such as gap opening and peculiar edge states. Their quantum confinement origin can be readily tuned through their width, shape, and edge terminations [21, 22]. The rapidly progressing on-surface chemistry is a highly versatile bottom-up tool for the controlled-synthesis of such atomically precise, graphene-based nanostructures [23–25]. This achievement has paved the way towards the precise mapping of their intriguing electronic structures with ARPES and STS [26–30], making them promising candidates for the realization of exotic graphene-based nanodevices [31–33].

In this thesis, we engineer the electronic band structure of the well-known poly(*para*-phenylene) (PPP), namely the $N_\alpha = 3$ armchair GNR [34], by introducing periodically spaced *meta*-junctions into its conductive path. We synthesize and macroscopically align a saturated film of cross-conjugated oligophenylene zigzag chains on a vicinal Ag(111) surface. We find that these atomically precise chains, hosting periodically spaced *meta*-junctions, remain sufficiently decoupled from each other and from the substrate. ARPES reveals weakly dispersing one-dimensional electronic bands along the chain direction, which is reproduced by DFT and EPWE. In addition, STS shows a significantly larger frontier orbital bandgap than PPP chains and that straight segments are able to confine electrons. These weakly interacting QDs confirm that periodically spaced *meta*-junctions constitute strong scattering centers for the electrons. These findings corroborate the important effects that the conductive path topology of a molecular wire has on its electronic states, which are responsible for defining its chemical, optical and electronic properties. Such arrays of semiconducting QDs hold potential for designing future oligophenylene-based quantum devices such as electrically driven, telecom-wavelength, room-temperature single-photon sources [35].

Acknowledgements

Many people have taken part in the realization and fulfillment of this thesis.

First of all, I would like to wholeheartedly thank Jorge and Kike for adopting me as their student and for guiding me during this thrilling journey. Thank you Jorge for your patience in showing me how a good scientist should work in a lab and outside. Thank you Kike for opening the doors to the world of teaching, I did not know it could be so enjoyable.

Thank you very much to the current Nanophysics laboratory family, Celia, Max, Dimas, Martina, Laura, Fred, Sara, Khadiza, Marco and Andrew. It's been a pleasure to share my time with you. I wish Fernando, Paul, Sabri and Nestor the best of luck in your own PhD journey, you are surrounded by great people.

The first steps were not easy, but when accompanied by nice people, it is always easier. I would like to thank former group members Ana, Rubén, Alejandro, Pavel, Guillaume, Jens, Mikel and Luciano for their support when the sky was dark. Mikel, eskerrik asko lankide paregabea izateagatik. Jens, thanks for sharing your knowledge and pizzas at weekends. I wish you all the best for your future.

This thesis has been possible due to many international collaborations that we have carried out. It has been a very enriching scienctific activity, but most importantly, I have had the chance of meeting incredible people from all over the world. Dziękuję Sylwia and Olha from the University of Basel for helping us understand the fascinating world of nanoporous systems. Sylwia, it was a pleasure to have you with us and show you the beauty of my land. Olha, thanks for your support during thesis, is it snowing in Basel?

Many thanks to Prof. Gottfried and Claudio from Philipps Universität Marburg for nice collaboration, it's been a pleasure to host Claudio with us and perform experiments. Also, it was a pleasure to perform a short stay in Philipps Universität Marburg at Prof. Höfers group, lovely little town and equally nice research group. Thanks for hosting us. Many thanks to Prof. Meike Stöhr from the University of Groningen for fruitful collaboration. I would like to acknowledge group members Leonid, Jun and Juan Carlos for the experiments performed together. Jun and Leonid, it was a pleasure to host you in San Sebastian, I wish you the best. Thank you very much to Prof. Nian Lin from The Hong Kong University of Science and Technology for collaborating with us. Guowen, I hope you keep nice memories of your stay in San Sebastian and hope that your thesis is successful.

I am very grateful to the people in Universidad de Zaragoza, Fernando and Leyre, for all the beamtimes that we have shared, enjoyed and suffered together. Leyre, good luck with your thesis, you will do great! Uuuum?

I am very grateful to Shigeki, Nakayama-sensei and Uchihashi-sensei for allowing me to work at your facilities in Tsukuba. Working with you and traveling to Japan has been a life changing experience. Thank you very much Atori-san, Nomura-san and Li Quiao Quiao for making my stay so enjoyable, domo arigato.

I would like to thank our theory collaborators in San Sebastian, Andrés, Iker and Aran for helping us understand our experimetal results with their wonderful DFT calculations. Thanks for your patience when answering all our questions.

Before concluding, I would like to thank Jorge, Kike, Zaka, Khadiza, Afaf, Eli and Martina for carefully reading this manuscript, suggesting wise changes and helping during writing. Thank you Eli for such a nice cover, you do have a good taste.

Zakaria, thanks a million for your support, daily scientific conversations and invaluable help with my thesis. I wish you the best in your scientific career, you will do great. Coffee?

Last but not least, I would like to thank my family for giving me the support I needed during this journey. Thank you, Marc and Ainhoa for the nice pintxopotes and dinners we shared together and *kuadrila* members for dragging me out of the office and enjoying life. Eskerrik asko Egoi for listening, afaita gaur?

Contents

List of Figures

List of Tables

List of Abbreviations

2DEG	Two-Dimensional Electron Gas
AGNR	Armchair Graphene Nanoribbon
ARPES	Angle-Resolved Photoemission Spectroscopy
BE	Binding Energy
BEM	Boundary Element Method
Br-DNF	3,9-dibromodinaphtho [2,3-b:2′,3′-d]furan
Br-DNT	3,9-dibromodinaphtho [2,3-b:2′,3′-d]thiophene
CB	Conduction Band
CCD	Charge-Coupled Device
COF	Covalent Organic Framework
DBTP	4,4"-dibromo-*p*-terphenyl
DCA	9, 10-Anthracenedicarbonitrile
DFT	Density Funcitonal Theory
DMTP	4,4"-dibromo-*meta* terphenyl
DOS	Density of States
DPDI	4,9-diaminoperylene quinone-3,10-diimine
DW	Double Wall
EBEM	Electron Boundary Element Method
EDC	Energy Distribution Curve
EPWE	Electron Plane Wave Expansion
FSM	Fermi Surface Map
GNR	Graphene Nanoribbon
Gr	Graphene
hBN	Hexagonal Boron-Nitride
IPS	Image Potential State
KPFM	Kelvin Probe Force Microscopy
LCPD	Local Contact Potential Difference
LDOS	Local Density of States
LEED	Low Energy Electron Diffraction
LT	Low Temperature
ML	Monolayer
MOCN	Metal Organic Coordination Network
MOF	Metal Organic Framework
NC-AFM	Noncontact Atomic Force Microscopy
NPG	Nanoporous Graphene

OTIs	Organic Topological Insulators
PAM	Phase Accumulation Model
PES	Photoemission Spectroscopy
Ph3	*Para*-terphenyl-dicarbonitrile
Ph4	*Para*-tetraphenyl-dicarbonitrile
Ph5	*Para*-pentaphenyl-dicarbonitrile
Ph6	*Para*-hexaphenyl-dicarbonitrile
PLS	Partially Localized State
PMP	Poly-(*meta*-phenylene)
PPP	Poly-(*para*-phenylene)
QD	Quantum Dot
QMB	Quartz Micro Balance
RT	Room Temperature
SBZ	Surface Brillouin Zone
SOC	Spin-Orbit Coupling
SS	Surface State
STM	Scanning Tunneling Microscopy
STS	Scanning Tunneling Spectroscopy
SW	Single Wall
TI	Topological Insulator
TPyB	1,3,5-tri(4-pyridyl)-benzene
TWD	Terrace Width Distribution
UHV	Ultra-High Vacuum
UPS	Ultraviolet Photoemission Spectroscopy
VB	Valence Band
VT	Variable Temperature
XPS	X-Ray Photoemission Spectroscopy
ZGNR	Zigzag Graphene Nanoribbon

To family and friends, and to you.

Chapter 1

Part I: Introduction and Motivation

The modern inspiration of nanoscience and nanotechnology, the idea that atoms and molecules could be used to construct nanoscale devices and machines, dates back to December 29^{th} 1959 when Professor Richard Feynmann delivered his famous speech *There's Plenty of Room at the Bottom* at the annual meeting of the American Physical Society at Caltech [36]. In his talk, he predicted exciting new phenomena that might revolutionize science and technology and affect our everyday lives, if only we were to gain precise control over matter, down to the atomic level.

The terms nanoscience and nanotechnology were coined, almost 15 years after Feynmann's lecture, by Norio Taniguchi in 1974 [37] to refer to the study of the intrinsic properties of nanoscale objects. These go from ~ 100 nm to ~ 1 Å in size and encompass the capabilities of observing, using, manipulating, or organizing them into assemblies in order to perform specific functions [1, 38].

Creating materials at the nanoscale is still nowadays technologically challenging. The two main basic approaches for generating surface patterns and devices in a controlled and repeatable manner are the top-down and bottom-up techniques [39]. In the former approach, materials are patterned from larger structures, while in the latter, materials are made by chemical processes starting from their atomic and molecular units. More precisely, the top-down approach [Figure 1.1 (a)] is commonly used, for instance, in manufacturing silicon integrated circuits, where tiny transistors are built up and connected in complex circuits starting from a bare silicon wafer. Relying on processes like thin film depostion, lithography and etching using masks, among others, it is possible to fabricate electronic devices with features below 100 nm. The ultimate size is limited by the physical laws governing these techniques, *i.e.* the wavelength of light and etch reaction chemistry [1].

An alternative and very promising strategy to exploit science and technology at the nanometer scale is offered by the bottom-up approach [Figure 1.1 (b)]. It starts from nano- or subnano-scale objects (namely, atoms or molecules) to build nanostructures [38]. In essence, the bottom-up approach makes use of intermolecular interactions and self-asembly to produce a desired pattern or nanostructure [38]. This approach became a reality and gained much interest with the invention of the STM in 1981. This extensively used Surface Science tool, developed at IBM Zurich Research

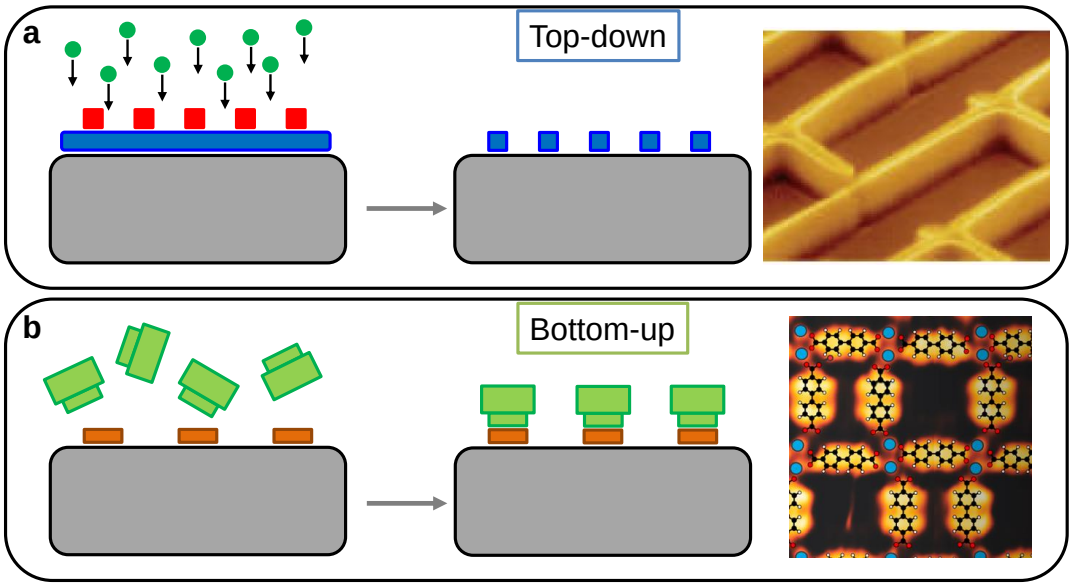

FIGURE 1.1: Building matter at the nanoscale. (a) Top-down fabrication methods such as lithography, writing or stamping are used to define the desired patterns at the nanoscale (adapted from ref. [1]). (b) The bottom-up technique makes use of self-assembly protocols in order to form ordered materials at the atomic and molecular level (adapted from ref. [6]).

Laboratory by Nobel Prize winners Binnig and Rohrer, is based on the tunneling effect [40], and enables imaging surface structures at the atomic scale [Figure 1.2 (a)]. However, STM is more than a tool for imaging surfaces, as its use was soon applied to atomic manipulation at the nanoscale. In 1990 Eigler *et al.* [41] reported the positioning of single Xe atoms on a Ni crystal surface with atomic precision [Figure 1.2 (b)]. Some years later, Crommie *et al.* [18] created a quantum corral by using Fe atoms on a Cu(111) surface, evidencing standing wave patterns of surface state electrons confined within the Fe ring [Figure 1.2 (c)]. However, such tip manipulation fails in the formation of long-range ordered nanostructures.

Supramolecular Chemistry, the chemistry of the intermolecular non-covalent bond, emerged as a powerful technique to develop nanoarchitectures with potential impact in a wide variety of fundamental and applied fields of research [44]. The concept of self-assembly has been recognized as a most elegant tool for creating ordered, functional materials at all scales [45]. The most widespread use of this autonomous assembly process is probably found in solution chemistry, where supramolecular structures are formed from tailored molecular building blocks. For the development of this strategy, Jean-Marie Lehn, Donald James Cram and Charles J. Pedersen were honored with the Nobel Prize in chemistry in 1987 [44, 46]. However, this knowledge of Supramolecular Chemistry in solution cannot be directly translated to guide the assembly of adsorbed molecules on atomically clean surfaces. The influence of the substrate's atomic lattice and electronic sturcture on non-covalent bonds strongly affects the resulting structures. Such a chellenge provides a new frontier in the field of Chemical Physics as it uniquely combines the versatility of Organic Synthesis and

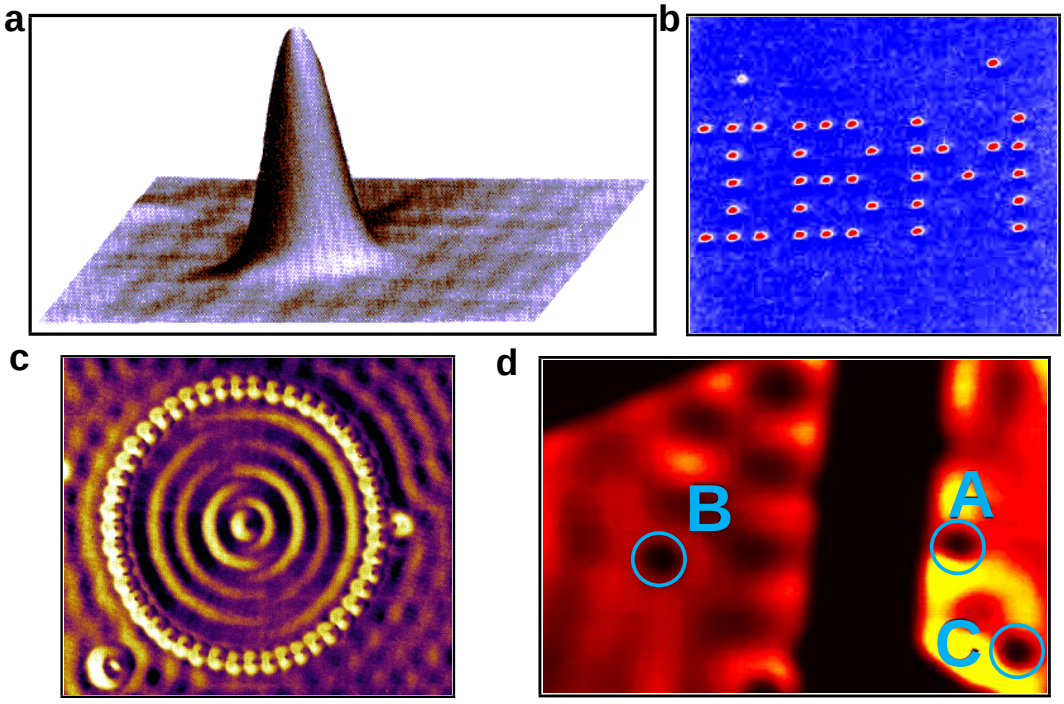

FIGURE 1.2: STM imaging and manipulation of matter at the nanoscale. (a) STM image of Xe adsorbed on Ni(110) (adapted from ref. [41]). (b) Construction of a patterned array of xenon atoms on a nickel (110) surface (adapted from ref. [42]). (c) 48-atom Fe ring constructed on a Cu(111) surface (adapted from ref. [18]). (d) Three adsorbed CO molecules (A, B and C) on a Cu(111) terrace (adapted from ref. [43]).

the Physics of Interfaces [1, 2].

This chemist's concept of molecular self-assembly was transferred to the surface science community, starting first with the adsorption of simple molecules onto single-crystal surfaces under well-controlled conditions in UHV [Figure 1.2 (d)]. The main objective of early studies was to learn about the molecules' physical and chemical interactions with the supporting/underlying substrate [43]. From this single-molecule perspective, studies moved towards investigating more complex molecular ensembles, in which intermolecular interactions began playing a role. So began the study of molecular self-assembly on surfaces [1, 47]. Guided by the advances and power of chemical synthesis, which provides access to a potentially vast range of functionally and structurally diverse building blocks (known as tectons), it was soon recognized that tuning the balance between molecule-surface and intermolecular interactions offered the potential for creating different supramolecular architectures on surfaces with tailored properties [1, 3, 46–48] [Figure 1.3 (a)].

Molecular assemblies can be classified as covalent or non-covalent, depending on the bonds formed between the molecules. The reversibility of non-covalent interactions (predominantly hydrogen bonds and metal-ligand interactions) allows error correction through elimination of defective structures. This results in the formation of almost defect-free, long-range ordered supramolecular architectures such as nanoporous networks [Figure 1.3 (b, c)]. Contrarily, molecular structures based on

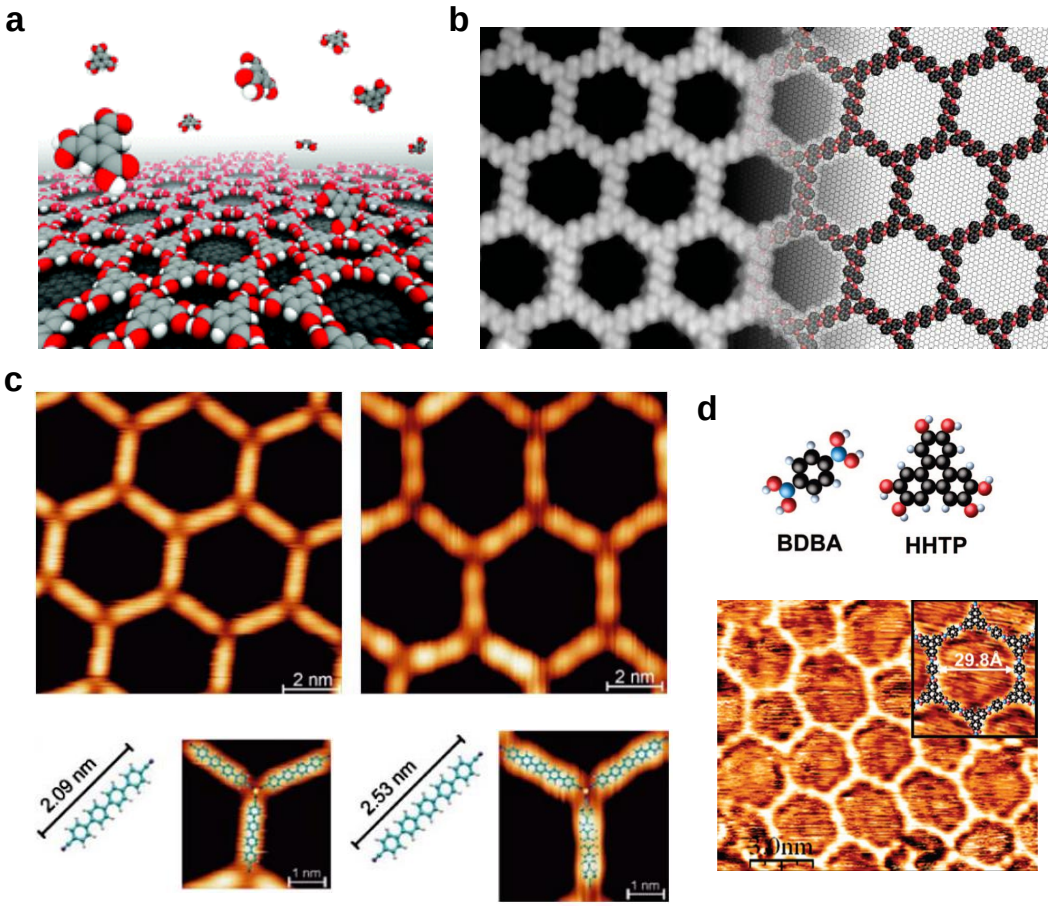

FIGURE 1.3: Self-assembled molecular nanoporous networks on noble metal surfaces varying intermolecular interactions. (a) Schematic representation of molecular self-assembly on surfaces (adapted from ref. [49]). (b) Hydrogen bond stabilized anthraquinone molecular nanoporous network on Cu(111) (adapted from ref. [50]). (c) Size varying ditopic dicarbonitrile-polyphenyl molecular linkers (NC-Ph_n-CN) coordinated with Co adatoms and forming long-range ordered metal-organic nanoporous networks on Ag(111) (adapted from ref. [51]). (d) Covalent network formed from BDBA and HHTP molecules on Ag(111) (adapted from ref. [52]).

the formation of irreversible covalent bonds do not allow for defect correction. However, their stability and distinct electronic structure is nowadays driving a strong research effort. On-surface synthesis provides the opportunity to create short-range ordered covalent organic frameworks (COFs), even if their periodicity is still not yet satisfactory [Figure 1.3 (d)].

The second part of this thesis is devoted to the growth of single domain, long-range ordered nanoporous networks on (111)-terminated coinage metal surfaces in solvent-free UHV. The nanoporous networks have been obtained from different molecular precursors and long-range ordering has been achieved through self-healing halogen bonding and metal-organic coordination of precursors. Such kind of metal-organic networks grown on metallic surfaces show novel magnetic properties [4, 5], catalytic effects [6, 7], oxidation states [8], exotic tesellation patterns [9–12]

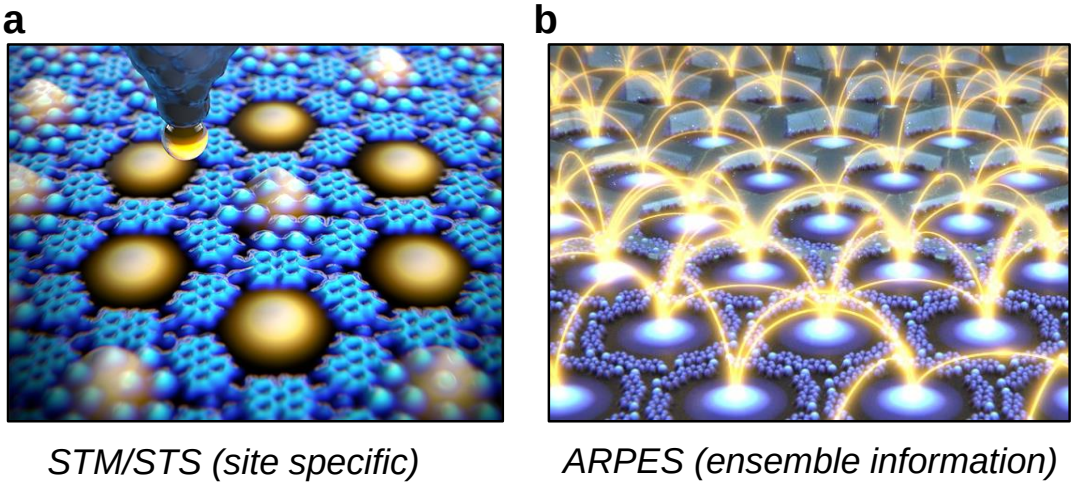

FIGURE 1.4: Electronic coupling of QD arrays on surfaces. (a) Conceptual schematic picture of a STM tip repositioning single Xe atoms on a metal-organic nanoporous network on Cu(111). This picture highlights the ability of STM not only to access the electronic structure of nanoporous networks at the single pore level but also of modifying it with adsorbate manipulation [53]. (b) Conceptual schematic picture of a halogen bond stabilized nanoporous network on Ag(111). Each pore confines the 2DEG of Ag, defining a QD. These QDs couple with the neighboring ones due to intercoupling effects and generate electronic bands which can be accessed with spatially averaging techniques such as ARPES [54].

and even bear the prospect of exhibiting topological band structures [13, 14].

Moreover, nanoporous structures with periodicities ranging from $\sim$ 2 to 6 nm are ideal 2D systems for altering the surface electronic properties of the supporting metals. The regular nanopores interact with the 2DEG present on the surface, and do so on length scales of the order of the Fermi wavelength (λ_F). This is in fact of a few nanometers on (111) surfaces of noble metals ($\lambda_F = \frac{2\pi}{k_F}$, where k_F is the momentum of the surface electron at the Fermi energy). As a consequence the 2DEG is confined inside each nanocavity and changes its energy [Figure 1.4 (a)], in a similar fashion to quantum corrals [18] [Figure 1.2 (c)]. By using scanning tunneling microscopy and spectroscopy (STM/STS), it is possible to probe such electronic features at the single pore or quantum dot level [15–17]. Interestingly, the resulting array of QDs are known to couple with each other [Figure 1.4 (b)], giving rise to the formation of new electronic bands with distinct fundamental energies, dispersion and zone boundary gaps. These features critically depend on the QD shape, size and lattice constants of the arrays formed [15]. These electronic bands become accessible when spatially averaging techniques such as angle-resolved photoemission spectroscopy (ARPES) are used.

In the second part of this thesis our aim is to study and engineer electronic bands by constructing different types of nanoporous networks. By subtle changes in the molecular constituents (functional groups and/or carbon backbone size) and guided by reversible, non-covalent bonding mechanisms, we are able to form a variety of QD arrays on noble metal surfaces with tunable QD sizes, barrier separations and

scattering strength. As a result, we engineer the surface band structure by locally controlling the confinement properties of each nanopore. Supported by semi empirical simulations, we disentangle the repulsive scattering potential landscape that organic and metal-organic nanoporous networks exert on the 2DEG and also delve into subtle surface state-organic overlayer interactions that show up as hybridization effects and geometrical variations. In this way we achieve a general understanding and predictability of the electronic properties of this family of nanoporous network overlayers grown on noble metals.

The resulting electronic structure from nanoporous networks that we study is a consequence of the modification of the substrate's 2DEG, which is independent of the existing molecular states. In the third part of this thesis, we investigate possible confinement effects on surface synthesized molecular structures. Thus, we study the electronic signal stemming from polymeric organic chains. These structures are reminiscent units of graphene, which has been studied in depth due to its exceptional electronic properties, with its singular Fermi surface with linear dispersions associated with massless Dirac electrons at the $\overline{\mathrm{K}}$ point of the surface Brillouin zone (SBZ). Many efforts have been devoted to integrating this 2D material into electronic devices. However, in electronic devices semiconducting materials play a prominent role, so using graphene as a base material in nanoelectronics would depend on the ability to engineer its semimetallic π bands in order to open energy gaps at the Fermy energy. Different attempts have been made: On the one hand, functionalization of graphene by doping with external species, such as hydrogen [55], and on the other hand, laterally reducing the dimensions of the graphene sheet limiting its size in one-dimension (1D). The latter results in a measureable band gap caused by quantum confinement of the electrons [21, 56]. A way to limit graphene to 1D with atomic precision is by on-surface chemical reactions [57, 58]. These have proven to be a highly versatile bottom-up tool for the creation of stable molecular structures such as 1D polymers [Figure 1.5 (a)] and GNRs [Figure 1.5 (b)] or 2D COFs [59–63] [Figure 1.5 (c)]. These graphitic examples bear intrinsic semiconducting properties with different bandgaps and distinct valence and conduction band dispersions. They represent interesting examples not only for studying their fundamental electronic properties [26, 28–30, 64], but also to be used in (opto)electronic and sensing devices and in catalysis [24, 33].

In 2000, Lha *et al.* [67] presented a pivotal study carried out in UHV, inducing the classical Ullmann coupling reaction with the STM tip, by creating biphenyl from iodobenzene precursor molecules on a Cu(111) surface [67, 68]. Similarly, the demonstration of the thermal initiation of an on-surface covalent linking was presented by Grill *et al.* [69] in 2007. In their study, an Ullmann-like reaction was performed using bromine substituted porphyrin molecules on Au(111). Depending on the number of halogen substituents on the precursor, dimers, linear chains or extended networks could be obtained [Figure 1.6 (a)]. A decade after Grill's seminal

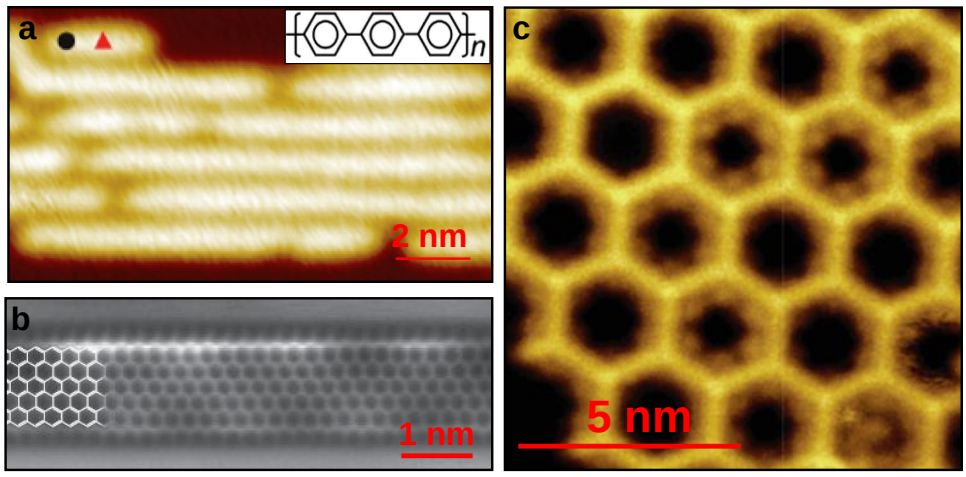

FIGURE 1.5: On-surface synthesized 1D and 2D covalent nanostructures. (a) STM image showing poly-(*para*-phenylene) oligomers (adapted from ref. [65]). (b) Constant-height nc-AFM frequency shift image taken with a CO-functionalized tip of the zigzag edge graphene nanoribbon (ZGNR) (adapted from ref. [28]). (c) STM image of a covalent network on Ag(111) (adapted from ref. [66]).

work, a multitude of different reactions have been proven possible on various conducting substrates including Ullmann-like coupling, cyclodehydrogenation, Glaser-like coupling of terminal alkynes and condensation reactions such as boronic acid based chemistry [57]. Owing to the interesting electronic properties and remarkable chemical and mechanical stability [70], there have been many attempts to achieve long-range order in COFs [52, 63, 71–74]. For instance, Figure 1.6 (b) shows a quasi-regular COF [73], but the irreversibility of covalent bonds, restricting rearrangement and self-correction processes, prevents the formation of equilibrium structures that result in an increased amount of geometrical defects [73, 75].

Guided by the asymmetry present at the surface of certain metallic crystals, it is in fact easier to synthesize and order 1D covalent nanostructures than the aforementioned 2D COFs. In this regard, 1D poly-(*para*-phenylene) chains [26, 77, 78] and GNRs with different edge topologies [27, 78, 79] have been successfully synthesized and ordered by using vicinal surfaces as nanotemplates [80–82] [Figure 1.6 (c)]. These vicinal surfaces are made up of monoatomic steps separating homogenously distributed terraces. These miscut surfaces are used as nucleation sites for the on-surface reaction, as well as for steering the alignment and packing of polymeric chains into single-domain films extending long-range on the surface. Such long-range ordering allows the access to their electronic band structure with ARPES [26, 27, 77–79, 83]. Recently, the formation of highly-regular nanoporous graphene (NPG) has been achieved by laterally fusing well-aligned GNRs with engineered edge topology [24] [Figure 1.6 (d)], proposing a promising strategy for building 2D COFs with distinct electronic properties.

The frontier orbitals of 1D oligophenyele chains and GNRs, which are responsible for their chemical, optical and electronic properties, strongly depend on the topology of the conducting pathways, *i.e.* width, edge-type and conjugation of the

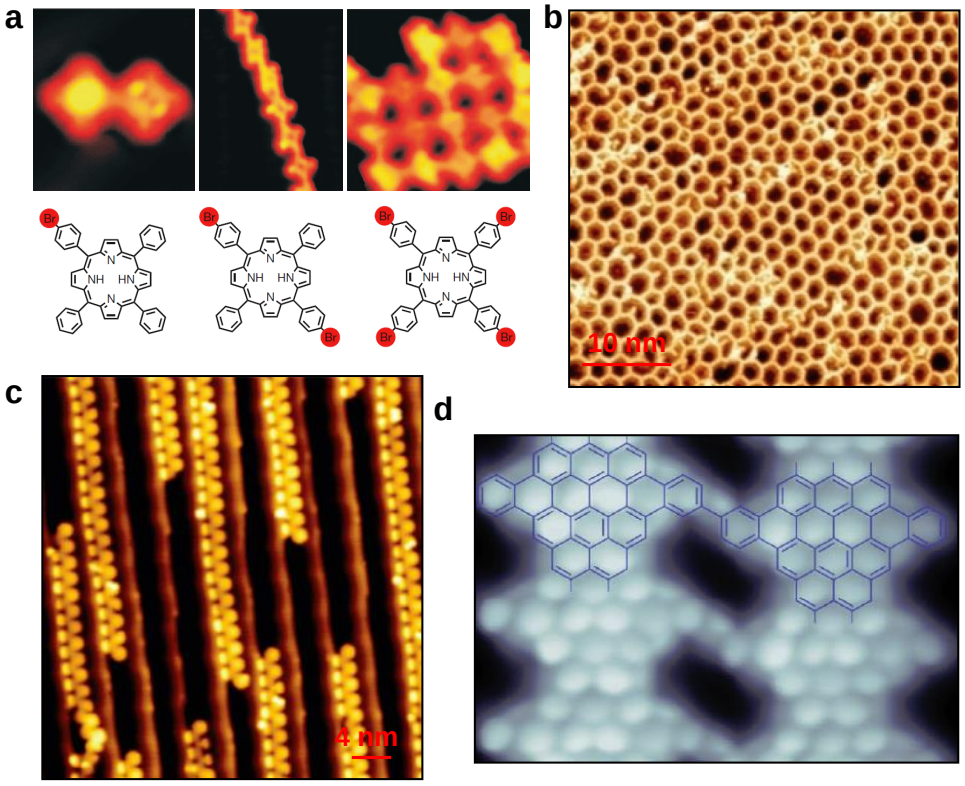

FIGURE 1.6: Ullmann coupling reaction and long-range ordering on surfaces. (a) Ullmann coupling of substituted porphyrins with control over the resulting structure dimensionality. By using different Br substituents, formation of dimers, one-dimensional lines or two-dimensional networks are generated (adapted from ref. [69]). (b) Sequential polymerization of a high quality 2D polymer with hexagonal pores accompanied by other irregular geometries (adapted from ref. [73]). (c) STM image of Chevron-type nanoribbons aligned on Au(788) (adapted from ref. [76]). (d) Nanoporous graphene (NPG) formation after laterally fusing one-dimensional GNRs (adapted from ref. [24]).

semiconducting nanostructures. In the third part of this thesis, we introduce periodically spaced topological variations in the form of *meta*-junctions into a straight and linearly conjugated poly-(*para*-phenyle) chain and proceed to synthesize and align cross-conjugated zigzag shaped oligophenylene chains into long-range ordered films on a vicinal silver crystal. ARPES and STS measurements evidence a radical change of the electronic structure as compared to its straight counterpart [26, 29], featuring shallow dispersive bands, an enhanced frontier orbtial bandgap, electron confinement effects along the interrupted small straight segments and frontier orbital bandgap tunability.

This thesis is composed by the following parts: the first part will be completed with Chapter 2 where the experimental and theoretical methods used are briefly described, highlighting the sample preparation process. This initial step, is an essential prerequisite for the formation of long-range ordered nanostructures and for probing their electronic structure with non-local techniques. In the second part of

the thesis, we start with a general introduction into nanoporous networks in Chapter 3 and unravel the electronic band structures from six different organic and metal-organic nanoporous networks grown on metal surfaces (Chapters 4 to 8). Here we also disentangle the scattering potential landscapes and their interactions with the 2DEG present on the surface. In the third part of the thesis, we move into on-surface synthesis studies and start with a general introduction in Chapter 9 and then, in Chapter 10, the electronic band structure of periodically spaced *meta*-junctioned oligophenylene chains is reported. Finally, this thesis ends presenting the main conclusions, an outook section that includes prospective new lines of research (Chapter 11), as well as a short summary in spanish (*Resumen de las principales conclusiones*), the author's publication list and the bibliography section.

Chapter 2

Experimental Techniques and Theoretical Methods

2.1 Introduction

This chapter gives a brief account of the main experimental details and techniques and theoretical methods used in this thesis. The chapter begins with an introduction into ultra-high vacuum and then, the sample preparation and coverage gradient growth method is described in detail as it is key for performing spatially averaging studies. Next, the laboratory setup in which the photoemission experiments have been carried out is shown. During the second half of this chapter the main experimental techniques (ARPES, STM and LEED) are explained, as well as, the experimental techniques provided by our collaborators (STM/STS and NC-AFM). Finally, the theoretical methods that have been used to support our experimental findings are briefly introduced: the combined electron plane wave expansion and electron boundary element method, density functional theory and the phase accumulation model. Note, that theoretical calculations have been performed through collaborations.

2.2 Ultra-High Vacuum

In surface science experiments, it is important to perform the measurements in a clean environment, where the surfaces being probed remain clean (without impurities or particles sticking on the surface) as long as possible. Such time must last at least as long as the acquisition time, that ranges from 30 min to 24 hours. To achieve this, samples must be kept in UHV conditions, which means at pressures lower than 10^{-9} mbar. UHV requires operating different types of pumps: roughing pumps, turbo pumps and ion pumps. Roughing pumps are used to put the system down to 10^{-1}mbar. Then, turbo pumps can be activated and pressures as low as 10^{-11} mbar can be obtained inside the vacuum chamber. Once such a stable pressure is reached, this conditions can be kept by using ion-pumps [84].

Another key factor for a successful study of the electronic properties of a material is its surface quality (monocrystalline and atomically flat) and cleanliness (non presence of impurities on the surface). If dirt is present on a surface it alters the measurement, for instance in ARPES, since the impurities can act as scattering centers for the 2DEG and increase dramatically the background, masking the main spectroscopic signal. Therefore, the (111)-terminated coinage metals used in this thesis require a defined cleaning protocol before any experiment is performed. This cleaning process comprises of a combination of sputtering and annealing cycles:

- For ion sputtering a noble gas (generally Ne or Ar) is injected into the vacuum chamber up to a pressure of $\sim 10^{-6}$ mbar through the sputter gun. The gas is ionized (Ne^+ or Ar^+) and a focused ion beam with an energy of 0.5 to 2 keV is directed against the sample to remove the outermost atomic layers. Such inert gases are chosen so that they do not bind to the substrate and avoid any additional source of sample contamination. The aftermath of this process is that the ion bombardment creates a large number of defects on the surface. In order to repair such defects after sputtering, a thermal annealing process is required.

- The annealing process consists in supplying thermal energy to the sample. For the noble metal single crystals studied in this thesis, the heat is generated by a filament that is placed behind the sample. In order to increase the heating efficiency and temperatures (generally up to $\sim 700 - 800$ K), a positive bias voltage (high-voltage) is applied on the sample so that the emitted electrons from the filament are accelerated against it. This process is generally done for 10 minutes reaching final pressures in the low 10^{-9} mbar.

2.3 Sample Growth: the Gradient or Wedge Method

In this thesis the *in situ* thermal evaporation is used to deposit single layer molecular films on surfaces. Molecules are sublimated in UHV conditions by supplying thermal energy from a radiative filament. For such purposes, a home-built molecular evaporator [Figure 2.1 (a, b)] is used, which is mounted inside the preparation chamber and focused into the central point of the chamber. The molecules are deposited inside a quartz crucible that is surrounded by a W filament. Upon heating the filament (direct heating evaporator), the crucible containing the organic powder raises its temperature until it sublimates with a desired rate towards the sample.

One particular advantage of our ARPES preparation setup is that instead of performing a homogeneous, single coverage deposition, we are able to perform a gradient or wedge evaporation. The gradient method gives us the possibility of altering the coverage of either molecules or metal depositions on a large sample. This gradient evaporation can be performed both on the vertical axis of the manipulator (z axis) and/or the horizontal axis of the manipulator (x axis). This is possible due to the presence of a mask and the possibility to move the manipulator in small steps (μm/s) using motors. The deposition process is as follows:

- The molecule flux is firstly monitored by using a quartz crystal microbalance (QMB) [green arrow in Figure 2.1 (c)]. During this process, the freshly clean sample is kept hidden behind the mask shielding wall (red arrow). Generally the pressure during evaporation remains below $\sim 2 \times 10^{-9}$ mbar.

- Once the rate is stable, the QMB is retracted, the mask is placed at the focal point of the evaporation beam and the sample is fully exposed to the molecules [Figure 2.1 (d)]. In the case where a clean region is required to be kept on the sample, a small fraction of the surface can be hidden behind the mask. Generally, the sample can be further approached towards the mask (y axis) so that the sample is positioned close to the focal point.

- In order to perform the gradient evaporation in the vertical (z) or horizontal (x) direction of the sample, the manipulator is moved using motors in a stepwise fashion (μm/s) during the evaporation, going from a fully-exposed situation to a completly hidden one behind the mask. A schematic picture of the final evaporation gradient is shown in Figure 2.1 (e). Note that for molecular depositions, generally a very shallow gradient is chosen, ranging from 0 to 1 ML, while the evaporation time ranges from 5 to 20 min.

- To make sure that the gradient evaporation was successful, the post-evaporation rate is again monitored using the QMB.

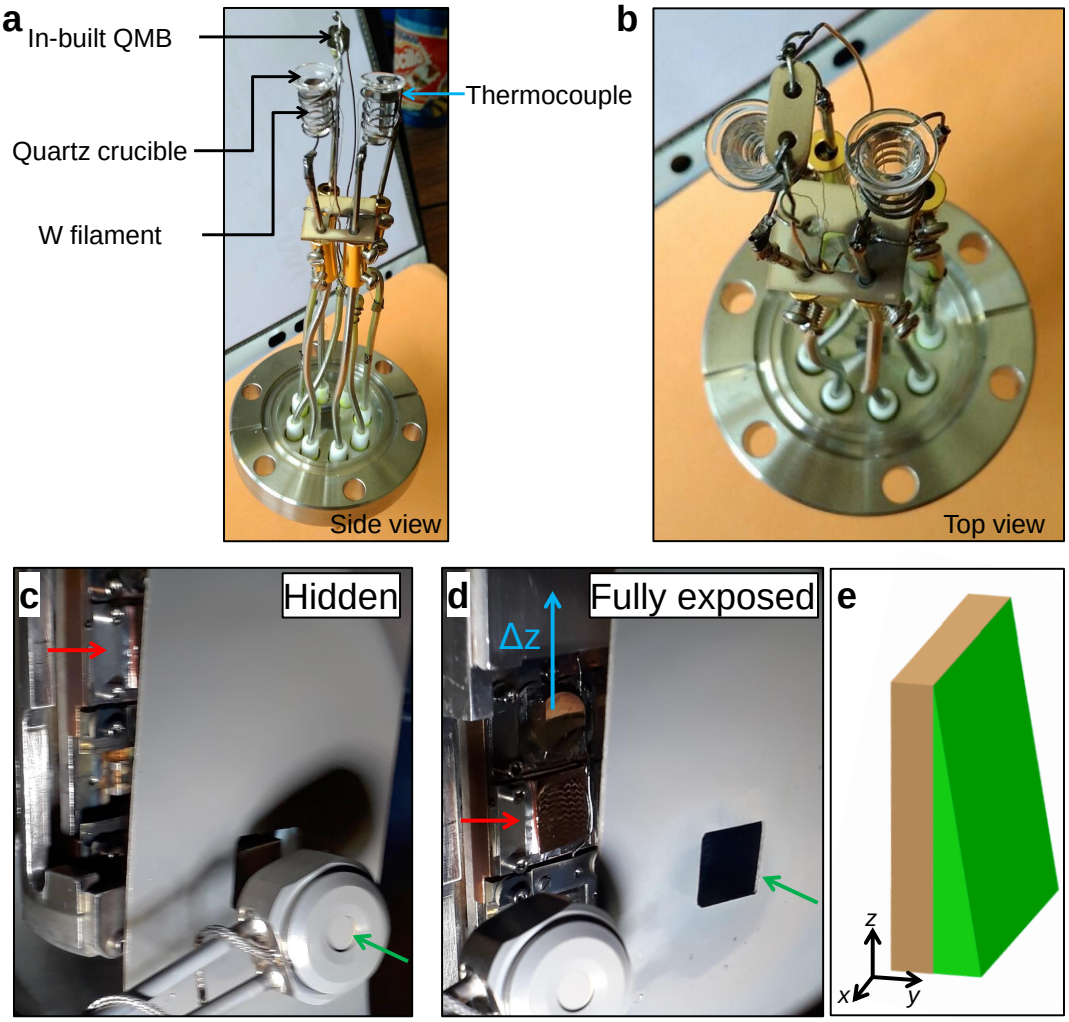

FIGURE 2.1: ARPES gradient evaporation. (a, b) Home-built direct heating evaporator. The evaporator is inserted into the exchangeable port of the preparation chamber either in ARPES or the STM side. The evaporator is composed of two quartz crucibles, which are filled with molecules. Each crucible is wound up by 0.5 mm thick W filament. Current passing through the filament (generally ranging from 1 to 5 A) will heat up the quartz crucible. The temperature can be monitored by a thermocouple (blue arrow) positioned between the filament and the crucible cap. A temperature uncertainty of ~ 50°C may exist between the inner and outer region of the crucible. (c) The molecular deposition rate is monitored by positioning a quartz micro balance (QMB) in front of the molecule evaporation beam. A mask is used in order to hide the already clean sample behind it to avoid any direct contamination. (d) When the evaporation rate is stable, the QMB is retracted and the sample is fully exposed to the molecular beam. During the evaporation, the manipulator is moved by a motor in the z or x axis in small steps until the sample is completly hidden behind the mask. (e) Schematic representation of a resulting molecular gradient evaporation (in green), which generally ranges in close proximity to 1 ML deposition.

2.4 Laboratory Setup

The laboratory setup mainly used for this thesis corresponds to the high-resolution ARPES chamber of the Nanophysics lab that is divided into two interconnected sections: the STM setup and the ARPES setup (Figures 2.2 and 2.3). In the following, both setups will be explained separately.

2.4.1 STM Setup

The STM setup (Figure 2.2) is equipped with a preparation chamber (in orange) to perform the sample cleaning process and the subsequent molecular deposition. The molecule depositions are performed using an exchangeable port with a home-built molecular evaporator (in purple). The base pressure in this chamber is 3×10^{-10} mbar. In order to characterize the samples, they are brought into the STM chamber (in blue). The STM chamber is equipped with a LEED (yellow) and a variable temperature (VT-Omicron) STM (inset). In general, the STM is operated at room temperature (RT), except for the characterization of the zigzag polymers (Chapter 10) where the sample was cooled down to $\sim$ 100 K to improve resolution and stability. The base pressure in this chamber is 1×10^{-10} mbar.

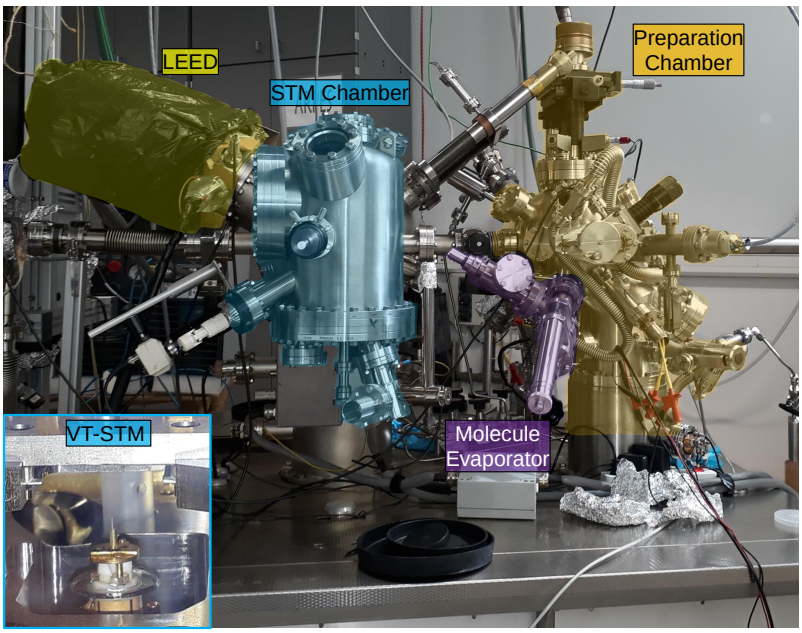

FIGURE 2.2: The STM laboratory setup used. It is divided into two main chambers, the preparation chamber (orange) and the STM analysis chamber (blue). The preparation chamber is equipped with all the necessary tools for sample cleaning and a exchangeable molecular evaporator (in purple) is used for performing the molecular depositions. The STM analysis chamber (in blue) consists of a LEED (in yellow) and a variable temperature VT-STM (see inset).

2.4.2 ARPES Setup

The ARPES setup [Figure 2.3 (a)] is divided into two sections: the preparation chamber (in blue) and the ARPES analysis chamber (in green). A vertical cryogenic manipulator (closed He cycle), which can vary its temperature from 30 to 320 K, connects both chambers. The manipulator is equipped with two large (15 x 15 mm) Au(111) and Cu(111) single crystals and an exchangeable holder to insert any other sample [Figure 2.3 (e)]. In the preparation chamber, the samples are cleaned and organic and inorganic evaporations (in orange) can be performed on a cold substrate, if desired. This chamber is equipped with a mask that enables us to perform coverage gradient evaporations into such large crystals, as described in Section 2.3 (see Figure 2.1). This is very advantageous since it facilitates obtaining the optimal coverage much quicker than performing single-shot coverage molecular depositions. Note that photoemission is a spatially averaging technique, thus, long-range ordered, single domain nanostructures have to be prepared optimally covering the surface. The base presseure of the ARPES UHV system is 8 x 10^{-11} mbar, but increases up to $\sim$ 2 x 10^{-10} mbar when operating the discharge lamp that produces the UV light.

ARPES Spectroscopy System

The ARPES spectroscopy system consists of four major components: light source or discharge lamp [Fig. 2.3 (b)], monochromator [Fig. 2.3 (c)], electron energy analyzer [Fig. 2.3 (d)] and sample manipulator [Fig. 2.3 (e)]. The photoemission data is measured with a display-type hemispherical electron analyzer (SPECS Phoibos 150) and a monochromatized He discharge lamp positioned under an incidence angle of 45° to the analyzer direction [Figure 2.3 (e)]. The lab based gas discharge lamp usually has an energy resolution of 1.2 meV (for He case), a photon flux of 10^{12}/s, a spot size of $\sim$ 1 mm^2 and the light is partially polarized (90% p and 10% s light polarization). In this thesis the He I_α line is commonly used providing a photon energy of 21.2 eV. It has a photoelectron escape depth or bulk sensitivity of $\sim 5-10$ Å, which means it is very sensitive to the low dimensional structures formed on the surface. Such low photon flux and large spot size are optimal for measuring organic systems (such as nanoporous networks) grown on surfaces since photon induced beam damage is avoided. Synchrotron radiation has a photon flux of 10^{13}/s or even larger and a very collimated spot size of less than 0.2 mm in diameter. In these conditions organic films are strongly damaged by the secondary electrons and it is specifically the beam damage the reason behind the use of the gas discharge lamp for the ARPES investigation of the selected systems in this thesis. The main drawback of the He discharge lamp is the fast aging effect of samples at very low temperatures due to the flowing helium. That is why ARPES measurements are performed at 150 K, since it provides the best compromise between measurement time and band structure quality. This temperature is controlled using a closed-cycle He

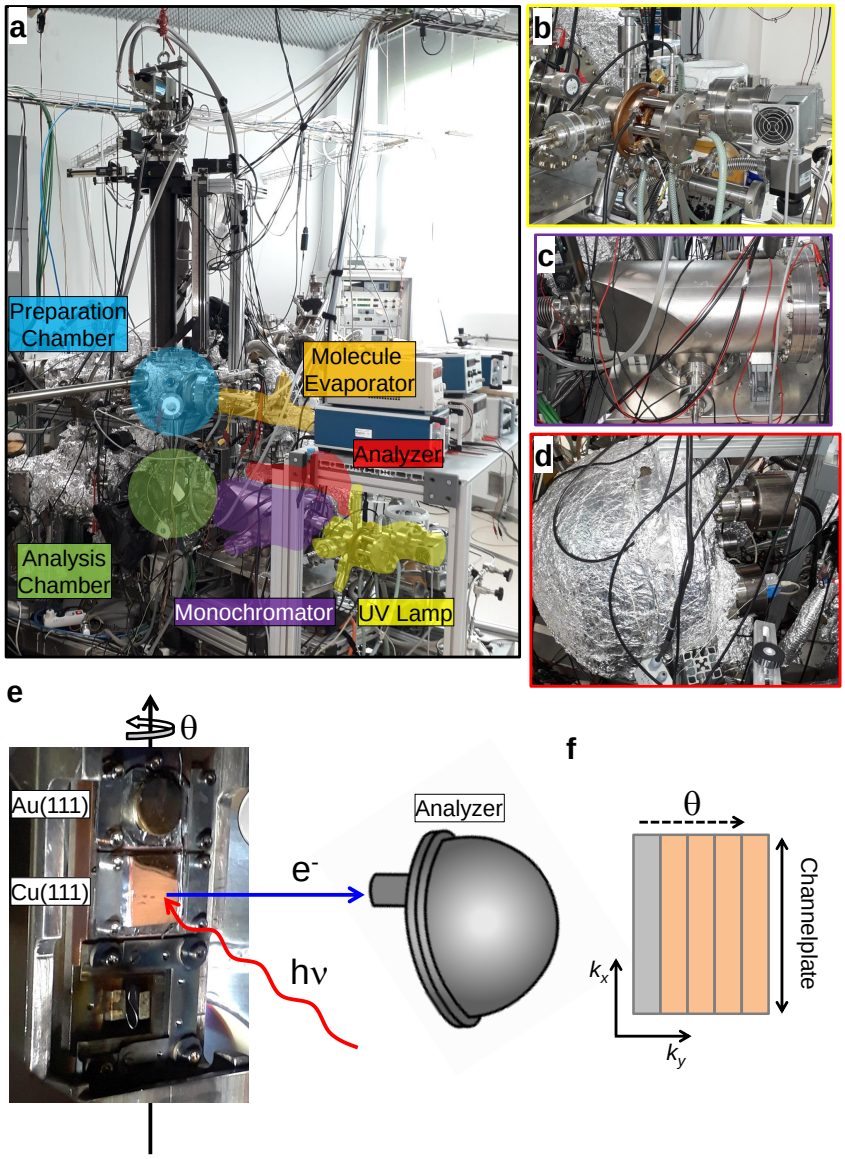

FIGURE 2.3: The ARPES laboratory setup. (a) The ARPES chamber is divided into the preparation chamber (in blue) and the analysis chamber (in green). The preparation chamber is equipped with all the necessary tools for sample cleaning. An exchangeable molecular evaporator (in orange) is used in order to perform the molecular deposition. A vertical manipulator connects the preparation chamber with the ARPES analysis chamber. The ARPES analysis chamber is equipped with an ARPES setup. A discharge lamp (in yellow) is used in order to generate the incident beam (b), then the monochromator (in purple and (c)) is used to monochromatize the light at the desired energy (for instance He I_α; 21.22 eV) getting rid of satellites. The light source impinges on the samples (e) and the emitted photoelectrons are analyzed in a hemispherical analyzer (d). (f) A channelplate detector provides a defined angular range in the vertical direction (k_x) while the manipulator polar angle (θ) around its vertical axis (z) is used to measure the dispersion in the horizontal axis (k_y).

cryogenic manipulator with a controlled temperature PID. Regarding the incoming photon energy of the light, this is properly defined by means of a monochromator. This prevents the presence of satellites and refocuses the light, which is essential

for high angular resolution. In addition, the electron energy analyzer is one of the core components on ARPES systems. Our ARPES system uses a hemispherical energy analyzer which is made by two concentric hemispheres with radius R_1 and R_2. A constant voltage V is applied between the two hemispheres, and only electrons with enegy window $E_p = e\Delta V/(R_1/R_2 - R_2/R_1)$ can go through the hemispherical analyzer and be counted by a CCD detector. The angular mode of the analyzer allows us to measure multiple energy distribution curves (EDCs) simultaneously on a channelplate window of $\pm 7^\circ$ (a 2D snapshot of energy versus momentum), which at the He I_α excitation is large enough to map the complete relevant k range in one direction without any sample rotation. The angles in the orthogonal direction required for obtaining Fermi surface mappings (FSMs) are reached by a subsequent change of the manipulator rotation around the z axis (θ polar angle) as indicated in Figure 2.3 (e, f). In our usual operation conditions, our ARPES setup features energy/angle resolution of 40 meV/0.1°.

2.5 Experimental Techniques

2.5.1 Angle-Resolved Photoemission Spectroscopy

Photoemission spectroscopy (PES) defines all techniques based on the application of the photoelectric effect as a tool for probing the collective behavior of electrons in a solid, that is, to study the electronic structure of solids [85]. PES makes it possible the understanding of fundamental physics laws which dominate the behavior of bound electrons, the chemistry of various materials and even has practical applications in several areas such as material science and surface chemistry. Ultraviolet photoemission spectroscopy (UPS), X-ray photoemission spectroscopy (XPS) and angle-resolved photoemission spectroscopy are some examples of this family.

Among the previous examples, ARPES represents a powerful and direct method to study the valence band electronic structure of solids because it directly probes the momentum-dependent electronic structure of solids, supplying detailed information on the band dispersion and Fermi surface topology. These results are achieved by measuring, at the same time, both the kinetic energy and angular distribution of the electrons photoemitted from a sample [85–89].

2.5.2 Principles of ARPES

The PES technique is based on the photoelectric effect, initially discovered by Hertz in 1887 [90], and later explained by Einstein [91]. The photoelectric effect describes the mechanism by which a metal emits electrons (thus called photoelectrons) when light shines upon it. The geometry of a PES experiment is illustrated in Figure 2.4 (a):

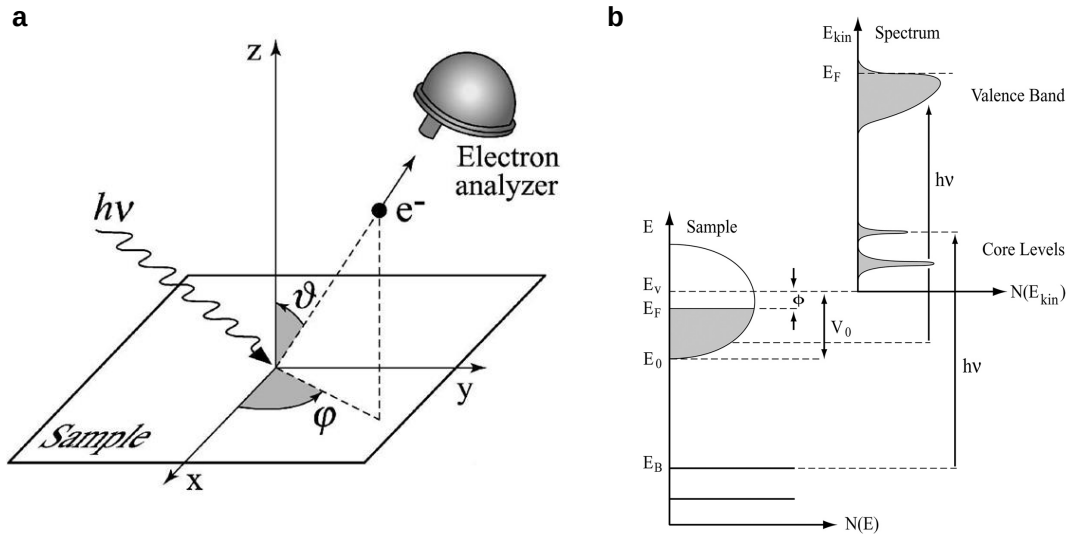

FIGURE 2.4: Geometry and energetics of ARPES. (a) In an ARPES experiment the emission direction of the photoelectron is specified by the polar (θ) and azimuthal (φ) angles. (b) The electron energy distribution produced by the incoming photons, and measured discarding the background signal as a function of the kinetic energy E_{kin} of the photoelectrons (right), can be referred to the density of states inside the solid (left) measured as a function of the binding energy E_B. Panels have been adapted from ref. [89].

a beam of monochromatic photons with energy $h\nu$ (supplied either by a gas discharge lamp or by a synchrotron beamline) is incident on the sample (typically single crystal), and those electrons which have absorbed incident photons can be excited from an initial state with energy E_i to a final state with energy E_f [85]. If the energy of the photon is high enough, an electron gains sufficient energy to escape from the solid, is ejected into the vacuum with a certain kinetic energy E_{kin} and a certain direction defined by the emission angles θ and φ. The term photoelectron is used for such ejected electrons.

By collecting the photoelectrons with an electron energy analyzer characterized by a finite acceptance angle, one measures their kinetic energy E_{kin} for a given emission direction. Knowing the work function of the material (ϕ), the kinetic energy (E_{kin}) of the photoelectron, and the energy of the incident radiation ($h\nu$), we can obtain the binding energy (E_B) of the electrons inside the solid from the conservation of energy (Equation 2.1).

$$E_{kin} = h\nu - \mid E_B \mid - \phi \tag{2.1}$$

The E_B is the minimum energy necessary for extracting a bound electron from a solid, the electron work function is a measure of the potential barrier at the surface that prevents the valence electrons from escaping into the vacuum, and is typically 4-5 eV in metals [88, 89, 92].

The energetics of the photoemission process is shown in Figure 2.4 (b). The energy level diagram of the electrons inside the solid is shown on the left side while

the PES spectrum measured by the analyzer without the background is shown on the right side [89]. Core levels give rise to sharp peaks in the photoemission spectrum. However, in this work we are more interested in the valence electrons which are close to the Fermi level since they are the ones responsible for various physical properties of solids (DC conductivity, magnetism, superconductivity, etc). Therefore, while core electrons correspond to the strongly bound electrons which are responsible for the formation of the inner orbitals of a certain material, valence electrons are responsible for the formation of the energy bands. These shared electrons are weakly bound to the nuclei and their modification can result in drastic changes in the material properties.

While in UPS experiments it is only possible to measure the kinetic energy of the electrons integrated over momentum space, in ARPES it is also possible to get information about the internal momentum **k** of the electrons, and hence to obtain the dispersion of the electronic valence bands in the reciprocal lattice inside the solid. This is done by measuring the angle at which the electrons are emitted from the sample (θ and φ). The geometry of an ARPES experiment is shown in Figure 2.4 (a): the analyzer collects the photoelectrons and measures both their kinetic energy E_{kin} and their emission direction, which finally provides the **K** in vacuum. From these values one can obtain information respectively on the binding energy and the momentum **k** of the electrons inside the solid. The magnitude of **K** is given by $K = \frac{P}{\hbar} = \frac{\sqrt{2mE_{kin}}}{\hbar}$ and the magnitudes of its components $\mathbf{K}_x$, $\mathbf{K}_y$ and $\mathbf{K}_z$ are determined in terms of the polar (θ) and azimuthal (φ) angles as follows:

$$K_x = \frac{1}{\hbar}\sqrt{2mE_{kin}}\ sin\theta\ cos\varphi \tag{2.2}$$

$$K_y = \frac{1}{\hbar}\sqrt{2mE_{kin}}\ sin\theta\ sin\varphi \tag{2.3}$$

$$K_z = \frac{1}{\hbar}\sqrt{2mE_{kin}}\ cos\theta \tag{2.4}$$

From the previous equations, the momentum **K** in vacuum is then completely determined and given by $\mathbf{K} = \mathbf{K}_x + \mathbf{K}_y + \mathbf{K}_z$.

Regarding the momentum **k** of an electron inside the solid, the in-plane component of **K**, the one lying in the plane of the surface of the sample, is $\mathbf{K}_{\parallel} = \mathbf{K}_x + \mathbf{K}_y$ while the component of **K** perpendicular to the surface is $\mathbf{K}_{\perp} = \mathbf{K}_z$. Given that the momentum component of the emitted photoelectron parallel to the sample surface is conserved (Figure 2.5), because of translational symmetry along the surface, then the component of the electron momentum parallel to the surface is also conserved at the interface, *i.e.* going from inside the solid to the vacuum,

$$\mathbf{k}_{\parallel} = \mathbf{K}_{\parallel} \tag{2.5}$$

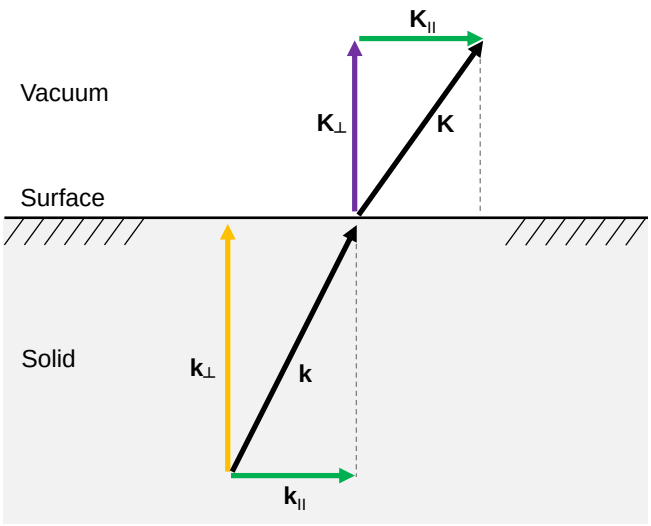

FIGURE 2.5: Schematic representation of the momentum **k** of the electron inside the solid and the momentum **K** in vacuum. The component of the momentum parallel to the surface is conserved because of the conservation of the translational symmetry going from inside to outside the solid, which means that the vectors $\mathbf{k}_{\parallel}$ and $\mathbf{K}_{\parallel}$ have the same magnitude. On the contrary, the perpendicular component of the momentum is not conserved when the electron escapes from the solid.

therefore, the parallel component of the momentum inside the solid ($\mathbf{k}_{\parallel}$) is fully determined by measuring the emission angle of the photoelectron and its kinetic energy in vacuum.

$$\mathbf{k}_{\parallel} = \sqrt{\mathbf{K}_x^2 + \mathbf{K}_y^2} = \frac{1}{\hbar}\sqrt{2mE_{kin}}\, sin\theta \tag{2.6}$$

Unfortunately, the perpendicular component of the momentum is not conserved across the sample surface because of the sudden change of potential along the z axis ($\mathbf{k}_{\perp} \neq \mathbf{K}_{\perp}$). However, if a nearly free-electron description for the final bulk states is assumed, the perpendicular component $\mathbf{k}_{\perp}$ can be determined as a function of E_{kin}, θ and the inner potential V_0, which corresponds to the energy of the bottom of the valence band referenced to the vacuum level E_V:

$$\mathbf{k}_{\perp} = \frac{1}{\hbar}\sqrt{2m(E_{kin}\, cos^2\theta + V_0)} \tag{2.7}$$

Fortunately, such uncertainty in $k_{\perp}$ is less relevant for low-dimensional systems since their band dispersion is negligible along the z axis and thus, is exclusively determined by $k_{\parallel}$. Note that in real ARPES experiments, one requires atomically-flat surfaces for an ideal conservation of surface parallel-momentum [88, 89].

2.5.3 Theoretical Description of the Photoemission Process

The most common semi-classical approach for explaining the photoemission process, particularly when PES is used as a tool to map the electronic band structure of solids, is the three-step model. This model decomposes the photoemission event into three independent steps: optical excitation between the initial and final bulk

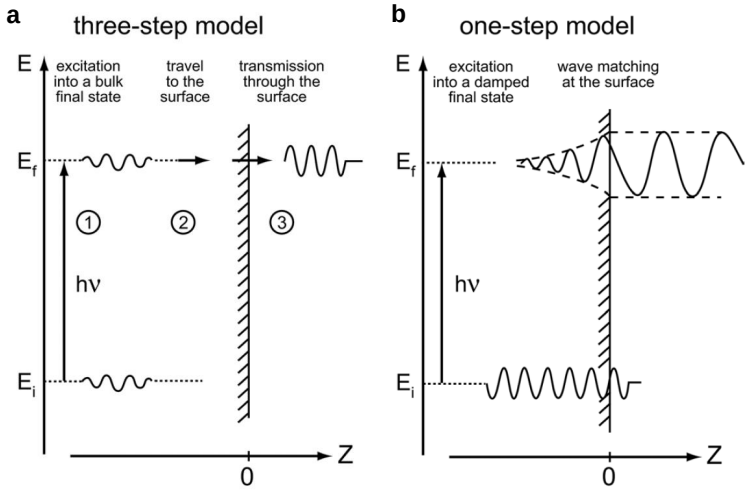

FIGURE 2.6: Pictorial representation (a) of three-step and (b) one-step model descriptions of the photoemission process. Panels have been adapted from ref. [89].

Bloch eigenstates, travel of the excited electron to the surface and escape of the photoelectron into vacuum after transmission through the surface potential barrier [Figure 2.6 (a)]. A more exact and computationally complex description is provided by the one step model, which is solely based in quantum mechanics. In the following we will discuss both models starting by the three step one.

Three-Step Model

The base hypothesis of this model is that the photoemission intensity can be decomposed as a product of three independent contributions which do not interfere with each other. The three independent steps are the following:

- Step 1: Optical excitation of the electron from the initial bulk eigenstate $\mid \psi_i >$ into the final excited bulk eigenstate $\mid \psi_f >$. It contains all the information about the intrinsic electronic structure of the material.
- Step 2: Propagation of the excited electron to the surface. Generally the propagation of the excited electron to the surface is described in terms of an electron mean free path λ, which describes the probability of the excited electron to arrive at the surface of the sample without undergoing any inelastic scattering and so without suffering any change in its kinetic energy or momentum. The curve for an electron mean free path has a universal trend, with a minimum at about 5 to 20 Å at the kinetic energies region of 20 to 100 eV, which are typical energies for ARPES experiments (Figure 2.7). This rather small electron escape depth implies that many PES experiments are sensitive only to the topmost surface layers, which is the reason why photoemission is considered a surface sensitive technique [93].

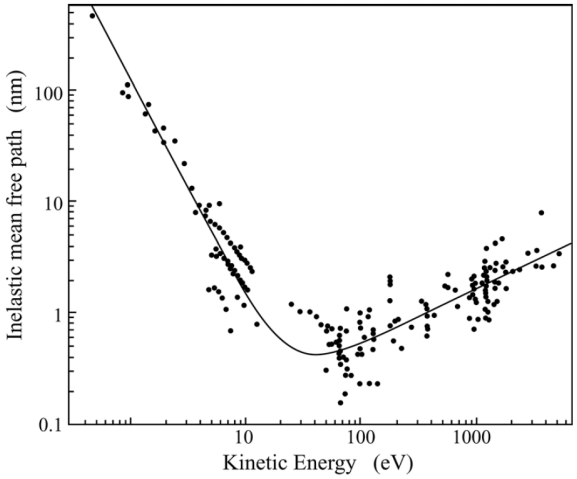

FIGURE 2.7: Universal curve. The curve for an electron mean free path for different materials show that its values closely follow the same trend, with a minimum at about 5 to 20 Å at the kinetic energies region of 20 to 100 eV, which is the typical energies for ARPES experiments [89].

- Step 3: Escape of the photoelectron into vacuum after transmission through the surface potential.

However, this model is just an approximation. From a quantum-mechanical point of view, photoemission should not be described in terms of several independent events but rather as a one-step process.

One-Step Model

The one-step model [Figure 2.6 (b)] can be explained as an optical transition between initial and final states consisting of many-body wave functions that obey appropriate boundary conditions at the surface of the solid. The photoemission process is described as a transition from an initial state ψ_i (initial electron wavefunction) to a final state ψ_f (final electron wavefunction). Such a transition occurs with a probability which is dictated by the Fermi's golden rule:

$$P_{i,f} = \frac{1}{\hbar} \mid M_{i,f} \mid^2 \delta(E_f - E_i - h\nu) \tag{2.8}$$

where $\delta(E_f - E_i - h\nu)$ is the energy conservation law and dictates that a transition between ψ_i and ψ_f can only occur when $h\nu = E_f - E_i$, *i.e.* when the photon energy matches the energy difference between the energies of initial and final states. $M_{i,f}$ corresponds to the interaction matrix element and contains all the information regarding the electronic interactions in a system and is directly connected to the Hamiltonian which describes the many-body energetic balance of the material, $M_{i,f} = < \psi_f \mid H \mid \psi_i >$.

2.5.4 Electronic Structure of Noble Metal (111) Surfaces

The electronic structure (valence band) of noble metal surfaces is composed of *d*-bands, which are occuppied and highly-dispersive *sp*-bands that cross the Fermi level. In addition to these, surface state electrons, known as Shockley states, are also present on the surface in the form of a two-dimensional electron gas. 2DEGs have played a pivotal role in fundamental condensed-matter physics for decades. While in semiconductors 2DEGs derive from the confinement of bulk states into a thin layer, electronic surface states on metals have a different origin. Understanding surface states requires understanding what happens to the Hamiltonian of the system when we approach a surface, *i.e.* when the bulk material is abruptly interrupted. The existence of a surface implies a symmetry breaking (caused by the termination of the inifinite crystal by the surface) along the direction orthogonal to the surface, and this can introduce new evanescent solutions to the Schrödinger equation in the projected bulk band gaps residing only at the surface. We can describe a bulk state [Figure 2.8 (a)] as an oscillating wave which exponentially decays into the vacuum as it reaches the surface. A surface state, on the other hand, resides at the material surface, decaying both into the vacuum and into the bulk [Figure 2.8 (b)]. Therefore, for a surface state to exist, it must lie in an energy gap between the bulk bands, otherwise it is named a surface resonance.

Prototypical examples are found at the Brillouin-zone center of the noble metal (111) surfaces [94]. These Shockley states appear in a gap of projected bulk bands along the Γ-*L* line. Electrons of the surface state behave like free electrons parallel to the surface and form a 2DEG. Thus the dispersion relation can be described approximately as

$$E(k_{\|}) = E_0 + \frac{\hbar^2}{2m^*}k_{\|}^2 \tag{2.9}$$

where E_0 is the fundamental energy of the surface-state, m^* is the effective mass of a surface-state electron, and $k_{\|}$ is the wave vector parallel to the surface [95]. As it will be observed along this thesis, such Shockley states, which originate from p_z orbitals

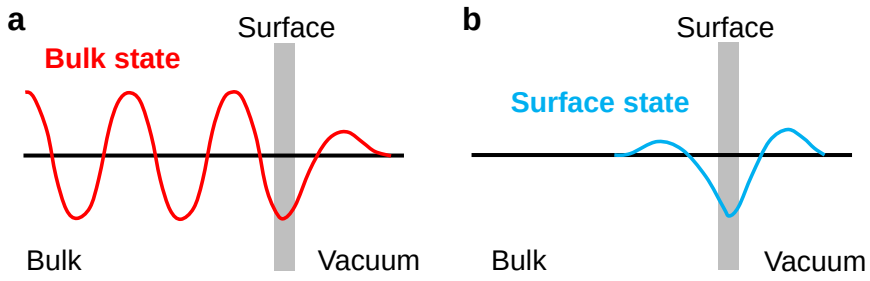

FIGURE 2.8: Surface and bulk electronic states. (a) A bulk state can be described as an oscillating wave which exponetially decays into the vacuum as it escapes the surface. (b) A surface state instead resides mainly at the material surface, so it will decay both into the vacuum and into the bulk.

within the sp inverted band gap around the L point, play an important role in the study of lateral quantum confinement effects at metal surfaces [18, 96–98].

Figure 2.9 summarizes the ARPES band dispersion of Schockley states for (111)-terminated coinage metals. Figure 2.9 (a-c) shows the E vs $k_{||}$ dispersion relation of the Cu, Au and Ag Shockley states as a grayscale plot. The surface states can clearly be detected as parabolic curves open at the Fermi energy, positioned inside the gap of the projected band structures of the bulk. Each one of them is characterized by a particular band bottom energy, effective mass and Fermi wave-vector (k_F), which are summarized in Table 2.1. The effective mass depends on the strength of the potential variations in the surface plane. Note that the particular character of each surface state is mainly affected by the lower edge of the projected bulk bands [99].

The Shockley surface state on Au(111) [Figure 2.9 (b)] served as an early model system exhibiting the characteristic spin momentum locking of a Rashba-split 2DEG. LaShell *et al.* [101] explained this splitting as due to a spin-orbit coupling, that breaks the spin degeneracy in the system. The dispersion in this case is described by two parabolic subbands of equal effective mass and energy at the band bottom, which is characteristic for a Rashba momentum splitting of a free-electron-like band near the Brillouin-zone center. However, it was not until the impoved resolution of electron spectroscopic techniques incorporating lasers that the spin-orbit splitting of the

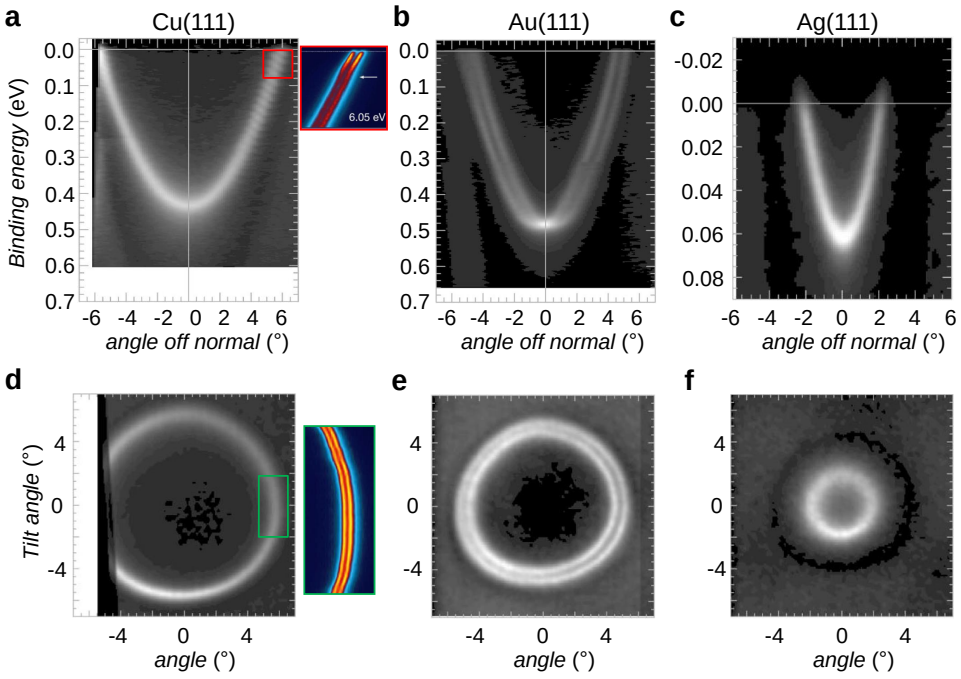

FIGURE 2.9: Dispersion and Fermi surface maps (FSM) of Noble metal (111) Shockley states. (a, b, c) Dispersion of the Cu(111), Au(111) and Ag(111) surface states. The spin-orbit splitting of Au(111) is clearly visible in (b), while the one of Cu(111) could recently be achieved by using a focused laser excitation of 6 eV [inset in (a)]. (d, e, f) FSMs of the investigated Cu, Au and Ag noble metal surface states centered at $\overline{\Gamma}$. The two individual Fermi surfaces in (e) form two closed concentric circles connected to the inner and outer branches of the spin-orbit split parabolas. Panels have been adapted from refs. [94, 100].

Shockley surface state on Cu(111) could be observed as well [94]. For doing so, a focused (~ 3 μm) 6 eV continuous-wave laser was used as the excitation source [insets in Figure 2.9 (a, d)]. Figure 2.9 (d, e, f) shows the Fermi Surface Maps (FSM) of the investigated Cu, Au and Ag noble metal surface states centered at $\overline{\Gamma}$. The circular shape of the FSM is an indication of the isotropic dispersion of these surfaces. The radius of the ring depends on both the band bottom and the effective mass of the surface state and gives information on the number of electrons the 2DEG contains (electron density $n = \frac{k_F^2}{2\pi}$). In all cases the ring is centered at $\overline{\Gamma}$, where the center of the gap is. Note that photoemission with the discharge lamp generally integrates over a large sample area of about 1 mm^2, with all its steps and defects and other imperfections. Hence, preparing a homogeneous atomically-flat sample in the illuminated area and avoiding the aging effect due to contamination are key for obtaining well-resolved datasets.

TABLE 2.1: Noble metal (111) parabolic Shockley state dispersion fit results with T_S = 30 K (values have been taken from ref. [100]).

	E_0 [meV]	m^*/m_e	k_F [Å^{-1}]
Ag	63 ± 1	0.397	0.080
Au	487 ± 1	0.255	0.167/0.192
Cu	435 ± 1	0.412	0.215

2.5.5 Low Energy Electron Diffraction

LEED is the principal technique for determining surface structures in reciprocal space by means of the diffraction of an electron plane wave at the sample surface. When the diffraction pattern is recorded, the analysis of the spot positions yields information on the size, symmetry and rotational alignment of the adsorbate unit cell with respect to the substrate unit cell. In a LEED experiment, monochromatic electrons are accelerated from a filament and focused with a lens system [Figure 2.10 (a)]. After reflection from the sample surface, only the elastically-scattered electrons contribute to the diffraction pattern: the lower energy (secondary) electrons are removed by energy-filtering grids placed in front of the fluorescent screen that is employed to display the pattern. The fluorescent screen then detects only the elastically backscattered electrons. The LEED experiment uses a beam of electrons in the range 10-200 eV and beam size of around 0.5 mm^2. These electrons can be diffracted by lattices of atomic dimensions. This is so because the de Broglie wavelength of the low energy electrons ($\lambda = \frac{h}{p}$) is comparable to the interatomic distances in the crystal (a few Å). Since low energy electrons are strongly back-scattered by the target electronic cloud, their elastic penetration is low $\sim 10 - 50$ Å, making LEED a surface sensitive technique. The sample itself must be a single crystal with a well-ordered surface structure in order to generate a back-scattered electron diffraction

pattern. To explain the diffraction pattern it is usual to work in reciprocal space ($\vec{g}_i$) instead of in the real space ($\vec{a}_i$). The reciprocal surface lattice is defined as follows,

$$\vec{g}_i = \frac{2\pi(\vec{a}_j \times \vec{n})}{\mid \vec{a}_i \times \vec{a}_j \mid}, i, j = 1, 2 \tag{2.10}$$

The Laue conditions, which express the conditions required for diffraction to occur, in a two dimensional system are given by,

$$(\vec{k}_i - \vec{k}_f) \cdot \vec{a}_i = 2\pi k, i = 1, 2 \tag{2.11}$$

On the other hand, energy conservation requires that,

$$\mid \vec{k}_f \mid = \mid \vec{k}_i \mid \tag{2.12}$$

Both conditions can be represented in the Ewald construction [Figure 2.10 (b)]. Here, rods represent the reciprocal lattice of the two-dimensional surface. The initial momentum vector ($\vec{k}_i$) is drawn ending at the origin of the reciprocal lattice. Therefore, a circle of radius ($\mid \vec{k}_i \mid$) will contain all the possible final momentum vectors ($\vec{k}_f$), according to energy conservation (Equation 2.12). The radius of the circle depends on the energy of electrons as $\sqrt{\frac{2m^* E_{kin}}{\hbar^2}}$. The intersenction between the circle and the rods gives the $\vec{k}_f$ vectors fulfilling the Laue conditions and showing diffraction maxima. Hence, the diffraction pattern observed on the screen is nothing but a projection of the reciprocal lattice, which reflects the symmetry, the size, and the shape of the unit cell in real space.

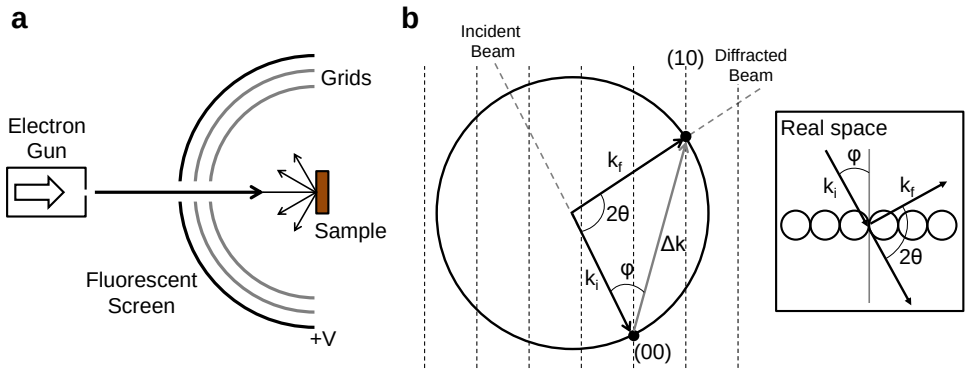

FIGURE 2.10: LEED schematics. (a) The LEED experiment uses a beam of electrons of a well-defined low energy incident normally onto the sample. The sample itself must be a single crystal with a well-ordered surface structure in order to generate a back-scattered electron diffraction pattern. Only the elastically-scattered electrons contribute do the diffraction pattern: the lower energy (secondary) electrons are removed by energy-filtering grids placed in front of the fluorescent screen that is employed to display the pattern. (b) The diffraction pattern is an image of the reciprocal space. The Ewald sphere is showing the Laue condition for the existence of a diffracted beam, $\vec{k}_i - \vec{k}_f = \Delta\vec{k} = \vec{g}$

In this thesis the LEED is used to gain information about the symmetry and superlattice constants of the on-surface self-assembled nanoporous networks and polymeric arrays with respect to the crystal surface. The LEED is also used for checking the cleanliness of the (111) noble metal surfaces after sputtering and annealing, as well as the quality and homogeneity of the terraces on vicinal surfaces [102].

In the following we will discuss different examples yielding particular LEED patterns. For a crystalline surface, for instance Cu(111), six sharp spots are observed at low energies when the surface is atomically-flat hosting ~ 100 nm size or larger terraces. The six-fold symmetry of the LEED pattern is directly related to the (111) termination symmetry of the crystal [Figure 2.11 (a)].

Regular step arrays on a vicinal surface cause the spots to split in two or more satellite spots. The split spots are due to the superperiodicity from the step array. This happens because the vertical rods in the Ewald sphere are repeated due to the extra periodicity introduced by the step array. The splitting is oriented perpendicular to the steps (it gives the step flow direction), thus the step direction can be determined by LEED [102]. A typical LEED pattern of a vicinal Cu(111) surface is displayed in Figure 2.11 (b). In addition, the size of the spot splitting is $\frac{2\pi}{d}$, so that the terrace width (d) can also be determined by LEED analysis. Clearly separated spots indicate a well-defined terrace width distribution (TWD). In addition a low background and sharp spots indicate good crystal quality free of defects.

For two-dimensional molecular nanoporous networks, superlattice spots provide information of the commensurability, periodicity, chirality and single or multi-domain scenarios present. For instance, Figure 2.11 (c) shows a *flower-shape* metal-organic nanoporous network on Cu(111) [104]. This particular nanoporous network forms a single-domain and commensurate 8×8 superstructure on the surface. This means that its periodicity (~ 2 nm) is eight times the interatomic distance of Cu(111). The high quality of the LEED pattern confirms that these molecules form a long-range ordered metal-organic coordination network (MOCN) extending up to the mm range.

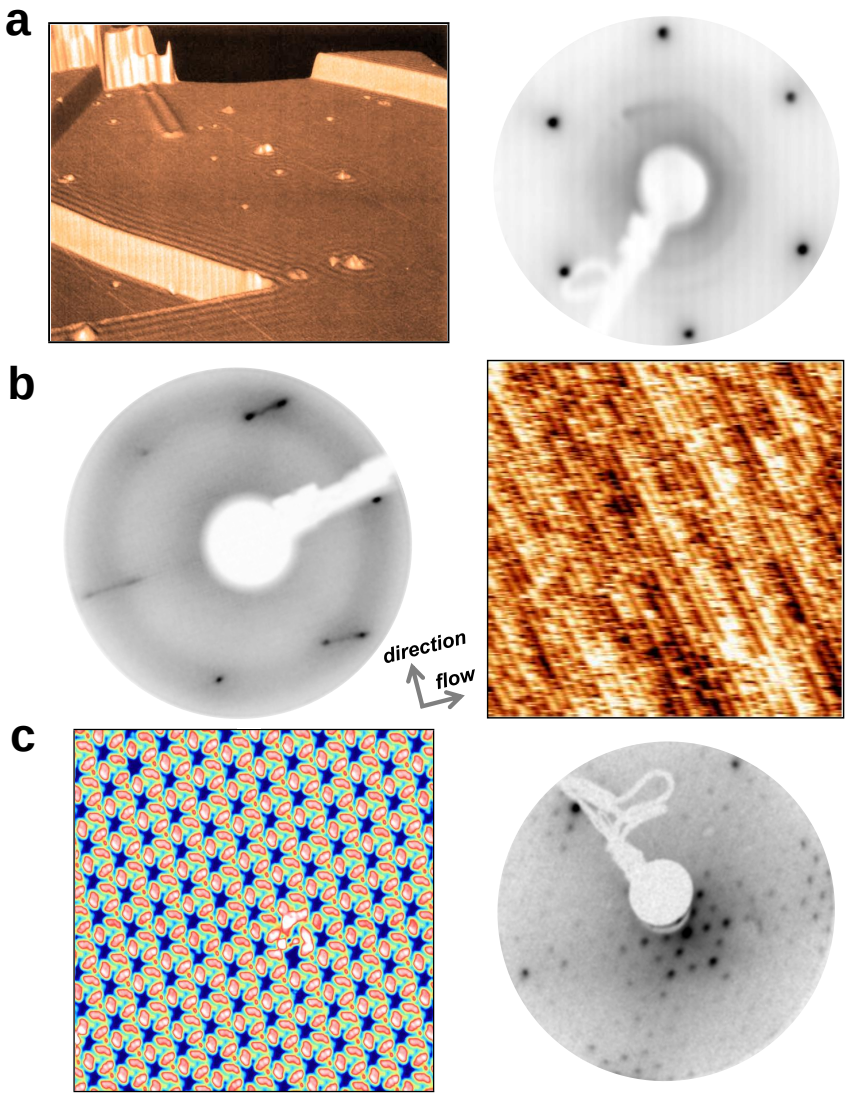

FIGURE 2.11: LEED patterns compared to STM images. (a) LEED pattern of the six-fold Cu(111) surface and corresponding STM image highlighting the existance of large terraces separated by monoatomic high steps. Ripples observed in the STM image correspond to the standing waves of the 2DEG after scattering at step edges with oscillations of 15 Å. LEED parameters: 80 eV; STM image adapted from ref. [19]. (b) LEED pattern obtained at a highly stepped region of a curved Cu(111) crystal. The splitting of the spots is directly related with the average terrace size. 30 x 30 nm^2 STM image of Cu(335) vicinal surface with a terrace size of 8.1 Å. LEED parameters: 152 eV; STM image adapted from ref. [103]. (c) LEED pattern corresponding to a 8 x 8 molecular DCA nanoporous superlattice on Cu(111), demonstrating its commensurate and single domain character of the overlayer extending in the long-range. The STM image (20×20 nm^2) corroborates the high degree ordering of such metal-organic assembly (Courtesy of Leyre Hernández). LEED parameters: 50 eV and STM parameters: I=300 pA/V=-1 V

2.5.6 Scanning Tunneling Microscopy and Spectroscopy

In STM a sharp metallic tip (normally W or PtIr that is ideally terminated by one single atom) is scanned over the surface and the tunneling current between the tip and the slighlty biased sample is measured [Figure 2.12 (a)]. The most important prerequisite of the scanned surface or material is that it has to be conductive. Theoretical analysis of electron tunneling through the vacuum barrier showed that the tunneling current I_T depends on the local density of states (LDOS) of the sample [105]. For low bias voltages V_s the tunneling current I_t can be written in terms of LDOS of the sample (D_s), the tip-sample distance d, and the work functions of the sample (Φ_s) and the tip (Φ_t):

$$I_t \propto D_s(E_F) \exp\left(-2d\sqrt{\frac{2m}{\hbar^2}\frac{\Phi_s + \Phi_t}{2}}\right) \tag{2.13}$$

The sign of the bias voltage V_s determines whether the STM probes filled ($V_s < 0$ V, electrons tunnel into the tip) or empty ($V_s > 0$ V, electrons tunnel into the sample) states. Hence, due to the exponential dependence of the tunneling current on the distance d, it is possible to measure topographic contrast of the surface. There are two main operating modes that depend on the feedback control (height) between the tip and the sample: constant current or constant height mode. In constant current mode [Figure 2.12 (b)], the z position of the tip is adjusted in a feedback loop during the scan so that the tunneling current is kept at a desired value. The change of tip height is then recorded as a function of the lateral coordinate. In constant height mode the feedback loop is disabled, so the z is fixed while the tunneling current I_t is recorded.

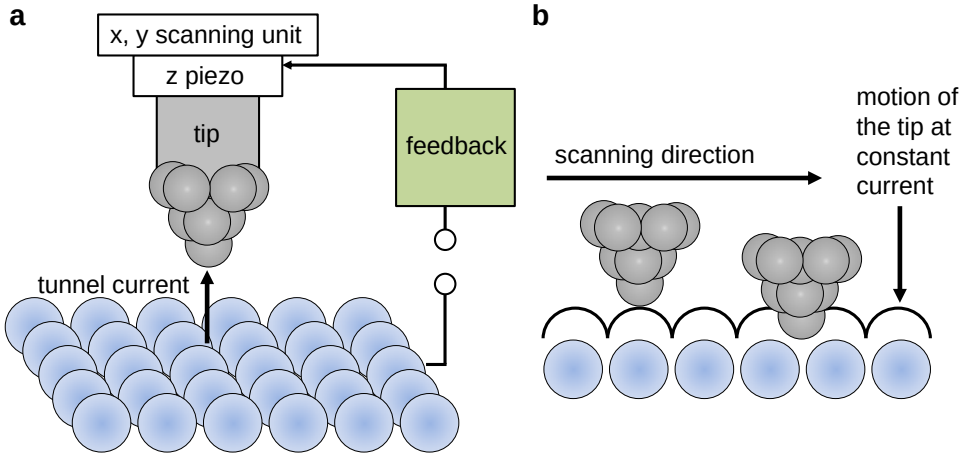

FIGURE 2.12: Schematic drawing of scanning tunneling microscopy (STM). (a) Piezoelectric elements position a metallic tip with fine resolution in three dimensions over the sample surface. (b) A feedback loop adjusts the tip-sample separation z to keep the tunneling current constant (adapted from ref. [106]).

2.5.7 Scanning Tunneling Spectroscopy

The signal detected by STM is the convolution of surface electronic and topographic landscapes. In order to measure the surface electronic states, it is necessary to deconvolute the electronic information from the topographic structure. This is accomplished through scanning tunneling spectroscopy. STS enables the local, energy-resolved investigation of a sample surface density of states (DOS) by measuring the differential conductance (dI/dV), which is approximately proportional to the DOS. STS enables the local characterization of physical and chemical properties of conducting samples. Typically, a small AC modulation (V_{rms}< 100 mV at 1 kHz) is superimposed on the DC bias voltage while a lock-in amplifier records the first harmonic of the signal that is in phase with the modulation. Unlike ARPES, STM/STS can probe both occupied and unoccupied states depending on the selected bias voltage polarity [99]. In addition, it has the capability to investigate the electronic structure at the atomic scale, while simultaneously providing topographic information. Therefore, STS is perfectly suited to study adsorbates positioned on substrates and confinement effects of surface state electrons, providing a complementary approach to k-vector resolving photoemission spectroscopy techniques.

A comparison between STS and ARPES was done on Cu(111) by Crommie *et al.* [108]. They found a sharp increase of the differenctial conductande *dI/dV* signal at -0.45 V and explained this increase as electrons tunneling from the occupied surface state of Cu(111) into empty states of the tip. Therefore, such a sharp increase of the *dI/dV* signal is recognized as the onset of the two-dimensional surface-state band of the noble metal (111) surfaces [Figure 2.13 (a)]. Note that, apart from temperature induced variations on the onset energy of the surface state E_0 [109], this is usually

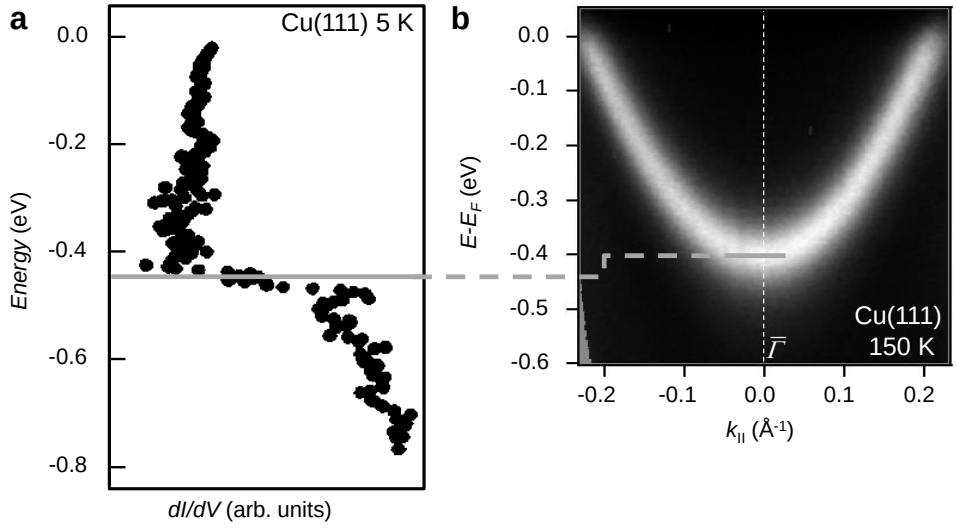

FIGURE 2.13: STS vs ARPES Cu(111) surface state measurements. (a) Experimental *dI/dV* spectrum taken from the bare Cu(111) sample highlights the step-like character of the surface state [107]. (b) ARPES band structure of Cu(111) Shockley state shows its parabolic dispersion with a well-defined band bottom energy, effective mass and Fermi wave-vector (k_F).

lower in STS measurements than ARPES [Figure 2.13 (b)] by 5-10 meV because the electric field induced by the presence of an STM tip affects the surface electronic structure, *via* the so-called Stark effect [95].

2.5.8 Noncontact Atomic Force Microscopy

Since the first systematic achievement of atomic resolution in 1995 [110], noncontact atomic force microscopy (NC-AFM) became an important tool for real-space high-resolution imaging. The tip-sample interaction force gradient is detected *via* the resonance frequency shift Δf of an oscillating cantilever. The atomic resolution mainly arises from the short-range interactions [111]. In NC-AFM, atomic resolution on molecules can be achieved by employing functionalized tips, which enhances the chemical sensitivity of the tip. For instance, CO molecule funtionalization can be used in order to increase the lateral resolution down to the submolecular regime [112] [Figure 2.14 (a)]. The requirements of the functionalization agent are the following: inert tip to prevent the molecule to be imaged from being picked up or displaced by the tip, small-size of the tip apex for improved lateral resolution, atomic relaxations of the tip apex due to the forces acting on it and its charge distribution (tip dipole) at its apex [112, 113].

The CO tip funtionalization [Figure 2.14 (b)] can be schematically summarized as follows: CO molecules are deposited on the surface once the prepared sample is in cryogenic conditions (normally at 4 K). A CO molecule is identified and picked up by approaching the tip vertically towards the molecule by applying a certain voltage (C atom is attached to the tip while the O atom points towards the molecule being imaged). Finally, the tip functionalization is confirmed by detecting an image contrast change or by checking the non-presence of the CO molecule on the surface.

For instance, the constant-height AFM image of pentacene with a CO functionalized tip is shown in Figure 2.14 (a). At this particular height, the mixture of attractive and repulsive forces felt by the CO tip is responsible for the submolecular resolution. Indeed, the maximal attractive forces are observed above the hollow sites of the carbon rings while the repulsive force originating from Pauli repulsion above the molecules is responsible for the bright features at the positions of atoms and bonds. In atomically resolved AFM images of molecules, the overall interaction forces are attractive due to the electrostatic and vdW forces, but the atomic constrast stems from repulsive contributions of the shorter-ranged Pauli repulsion. Such atomic resolution due to Pauli repulsion above the atoms and bonds becomes only apparent for the smallest accessible tip heights [Figure 2.14 (c)]. The CO tip also tends to tilt under the influence of the interaction forces. This tilting gives rise to an apparent sharpening of the bonds and to distortions of the imaged molecular structures. In addition, the increased brightness at the pentancene molecular ends and differences between lower and upper edges stem from the non-planar adsorption geometry of pentance. Hence, NC-AFM also provides information on the molecule adsorption

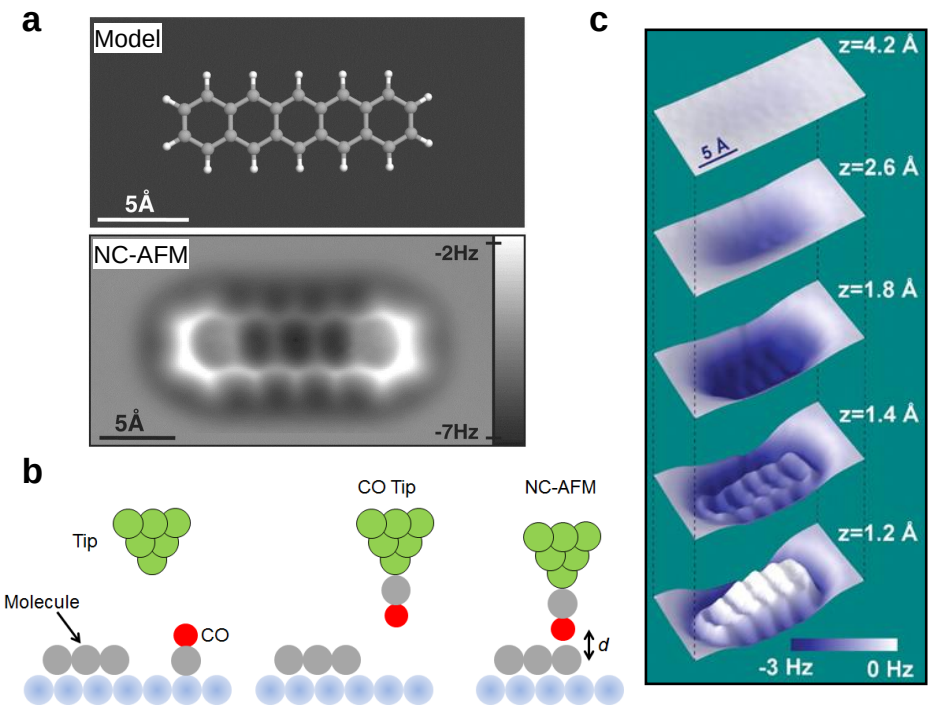

FIGURE 2.14: NC-AFM measurements on pentacene. (a) Model of pentacene and constant-height AFM measurement of pentacene on Cu(111) acquired with a CO functionalized tip. (b) Schematic representation of the functionalization process of the tip with a CO molecule. (c) Submolecular resolution of the pentacene molecule depending on the molecule-tip separation. (a) and (c) have been adapted from ref. [114].

geometry on the surface [113, 114].

2.6 Theoretical Methods

In this section we introduce the main modelling and theoretical methods that have been used throughout this thesis, *i.e.* the combined electron plane wave expansion (EPWE) and electron boundary elements method (EBEM), density functional theory (DFT) and the phase accumulation model (PAM). Note that these calculations have been performed by our collaborators.

2.6.1 Electron Boundary Elements Method and the Electron Plane Wave Expansion Method for Periodic Systems

The combined EPWE [115] and EBEM [17, 116] have been developed by Prof. Dr. García de Abajo and represents a scalar variant of the electromagnetic PWE/BEM extensively used for solving Maxwell's equations and optical response for arbitrary shapes. It is based on Green's functions for finite geometries and electron plane wave expansion for periodic systems. For the band structure calculations, the particle-in-a-box model is extended to infinite 2D systems by defining an elementary cell and using periodic boundary conditions. Within the EPWE code, solutions of the Schrödinger equation are represented as a linear combination of plane waves and a satisfactory convergence is achieved with a basis set consisting of ~ 100 waves [34, 115, 117].

In this thesis the local electronic properties of nanoporous networks such as LDOS at a single nanopore as well as band structure calculations and photoemission intensity simulations of periodic arrays and one-dimensional polymeric chains are performed by using this method. The Schrödinger equation for electrons experiencing an effective potential V (for instance when surface electrons encounter a molecular barrier in a hexagonal molecular nanoporous network) is written as:

$$\frac{-\hbar^2}{2m_{eff}}(\nabla^2 + k^2 - \frac{2m_{eff}}{\hbar^2}V(x,y))\psi = 0 \tag{2.14}$$

where $k = \sqrt{\frac{2m_{eff}E}{\hbar^2}}$ is the electron momentum, E being its energy, and m^* is the effective mass. In the EPWE method, both the wavefunctions and the periodic potential are Fourier expanded to obtain the following Equation 2.15, which is then solved numerically by terminating the expansion at some finite reciprocal lattice vectors (g_{max}, where $g_{max} = 10$ is a good compromise for capturing all the details such as band dispersion and energy gaps).

$$(\frac{\hbar^2 k^2}{2m_{eff}} - E)C(k) + \sum_{G=g_{max}} U_G C(k-G) = 0 \tag{2.15}$$

Here C and U are the Fourier coefficients of the wavefunctions and potential, respectively, and G is the reciprocal lattice vector. Further details on the simulation procedure of each particular nanoporous network system and one-dimensional polymers studied in this thesis are provided in each chapter.

2.6.2 Density Funcitonal Theory

In 1998 Walter Kohn was awarded with the Nobel Prize in Chemistry for his development of DFT, which was introduced in two seminal papers in the 60's [118, 119]. DFT is presently the most successfull approach to compute the electronic structure of matter. Its applicability ranges from atoms, molecules and solids to nuclei and quantum and classical fluids. In its original formulation, DFT provides the ground state properties of a system and the electron density plays a key role. For instance, in the chemistry field, DFT predicts a great variety of molecular properties: molecular structures, vibrational frequencies, atomization energies, ionization energies, electric and magnetic properties, reaction paths, *etc.*

Since the field of molecular electronics came to birth, propelled by the possibility of manipulating single molecules on surfaces, it became desirable to understand the relation between conduction channels and molecular orbitals. For such purposes *ab initio* quantum chemistry DFT became of great use [120]. In this thesis DFT has been used for two purposes: on the one hand, to elucidate how single metal atoms such as Co can influence the electronic properties of a 2DEG on a Au(111) sample, and, on the other hand, for characterizing the electronic band structure and morphology of zigzag-shaped organic semiconducting chains. More details on these two particular examples are provided in Chapter 6 and Chapter 10.

In the following the basic principles of DFT will be introduced.

The Many-Body Problem

Calculating the properties of materials requires solving the Schrödinger equation for a system of interacting N_e electrons and N_n nuclei, *i.e.* diagonalizing the many body Hamiltonian,

$$\hat{H} = \hat{T}_n + \hat{T}_e + \hat{V}_{ne} + \hat{V}_{ee} + \hat{V}_{nn} \tag{2.16}$$

which can be written as,

$$\hat{H} = -\frac{\hbar^2}{2m_e}\sum_i \nabla_i^2 - \sum_{i,I}\frac{Z_I e^2}{\mid \vec{r}_i - \vec{R}_i \mid} + \frac{1}{2}\sum_{i\neq j}\frac{e^2}{\mid \vec{r}_i - \vec{r}_i \mid} - \sum_I \frac{\hbar^2}{2M_I}\nabla_I^2 + \frac{1}{2}\sum_{I\neq J}\frac{Z_I Z_J e^2}{\mid \vec{R}_I - \vec{R}_J \mid} \tag{2.17}$$

where, indices i, j are for electron degrees of freedom and I, J for nuclei, M_n denotes the mass of nucleus at position $\vec{R}_I$ and m_e denotes the mass of the electron at $\vec{r}_i$. The

first two terms denote the kinetic energies of nucleus ($\hat{T}_n$) and electron ($\hat{T}_e$) respectively. The other three terms describe the Coulomb interaction energy between the electron - nucleus ($\hat{V}_{ne}$), electron - electron ($\hat{V}_{ee}$) and nucleus - nucleus ($\hat{V}_{nn}$).

In practice, solving the Schrödinger equation using the full many-body Hamiltonian, as shown in Equation 2.17, is not easy and thus, approximations are usually made. In general the Born-Oppenheimer approximation or adiabatic approximation is used. By fixing the positions of the nuclei the ionic kinetic energy term vanishes. Further, the ion-ion interaction term can be replaced by a constant energy term and electron-ion interactions by an external potential. This reduces the Hamiltonian in the following form,

$$\hat{H} = -\frac{\hbar^2}{2m_e}\sum_i \nabla_i^2 + \frac{1}{2}\sum_{i\neq j}\frac{e^2}{\mid \vec{r}_i - \vec{r}_j \mid} + V_{ext} + E_{II} \tag{2.18}$$

with V_{ext} and E_{II} being the external potential and the ion-ion interaction energy, respectively. These simplifications are possible due to the large ratio between the masses of nuclei and electrons. Also, the motion of nuclei is very slow, and their position quasi fixed, while electrons react almost instantaneously to changes in the external potential. Within this scenario, it is valid to neglect the kinetic energy terms for the nuclei.

Density Functional Theory: Hohenberg-Kohn Theorems and Kohn-Sham Equations

Hohenberg and Kohn used the simplified Hamiltonian from Equation 2.18 as the starting point for the development of DFT. This theory, which is based on two theorems, states that the properties of a system of interacting particles can be described as a functional of the ground state density. DFT reduces the complex many body problem of 3N variables (N electrons each having 3 spatial coordinates) to simply 3 variables, where they appear in the electron density functional. According to Hohenberg-Kohn first theorem, the ground state density $n_o(\vec{r})$ of any system of interacting particles is sufficient to uniquely, except for a constant, determine the external potential $V_{ext}(\vec{r})$ acting on the particles. The second theorem describes the possibility to define a universal functional $E[n]$, valid for any external potential $V_{ext}(\vec{r})$, for determining the energy in terms of the density $n_o(\vec{r})$. Then, the exact ground state density $n_o(\vec{r})$ is the one which minimizes this energy functional. Therefore, knowing the functional $E[n]$ is sufficient to determine the ground state energy and density. The ground state total energy functional can be written as,

$$E_{HK}[n] = T[n] + E_{int}[n] + \int d^3r V_{ext}(\vec{r})n(\vec{r}) + E_{II} \tag{2.19}$$

$T[n]$ being a functional of the kinetic energies of the interacting particles, $E_{int}[n]$ describing the interaction energy of the electrons and E_{II} the interaction energy of the nuclei. Using a functional of the form of Equation 2.19 to obtain the ground state density leaves one with the following problem: in principle, the ground state density is sufficient to determine the properties of a material, but the DOS cannot be directly extracted from the density. For physically solving this problem, in 1965 Kohn and Sham proposed a new approach, where they assumed that the ground state properties of a system of interacting particles can be described by the ground state of a non-interacting system. Based on this assumption, they introduced an auxiliary system of independent electrons with its density given by,

$$n(\vec{r}) = \sum_{i=1}^{N} \mid \phi_i^{KS}(\vec{r}) \mid^2 \tag{2.20}$$

In Equation 2.20, $\phi_i^{KS}(\vec{r})$ denote the single particle wave-functions of the non interacting auxiliary system, the so-called Kohn-Sham orbitals [121].

2.6.3 Phase Accumulation Model

In PAM, the surface state energies are calculated assuming constructive interference of free-electron waves reflected back and forth at the crystal-vacuum interface [122, 123]. This is represented in the following equation:

$$\Phi_B + \Phi_C = 2\pi n \tag{2.21}$$

Here Φ_C and Φ_B are the crystal and barrier phase changes, respectively, and n is an integer number with $n \geq 1$ for image and $n = 0$ for surface states. The energy dependences of both Φ_C and Φ_B are given by the following expressions:

$$\Phi_C = 2arcsin\sqrt{\frac{E - E_L}{E_U - E_L}} \tag{2.22}$$

and

$$\Phi_B = \pi \left(\sqrt{\frac{3.4\ eV}{E_V - E}} - 1 \right) \tag{2.23}$$

Where E_L, E_U, and E_V are the lower and upper edges of the crystal bulk gap along ΓL and the vacuum energy, respectively.

The PAM nicely predicts the band bottom energy of Au(111), Cu(111) and Ag(111) Shockley states when using the initial values summarized in Table 2.2. The surface state enegy is found when the $\Phi_C + \Phi_B$ cuts the $n = 0$ phase (see Figure 2.15). The PAM is used in this thesis to study the effect that a metallic overlayer causes on the surface state fundamental energy, *i.e.* acting on the crystal phase Φ_C [123]. Further details on this procedure are included in Chapter 6.

TABLE 2.2: Noble metal (111) vacuum level and bulk band gap edges. Values have been taken from ref. [124]

	Au(111)	Cu(111)	Ag(111)
E_V (eV)	5.3	4.94	4.74
E_U (eV)	3.5	4.25	4
E_L (eV)	-1.05	-0.91	-0.3

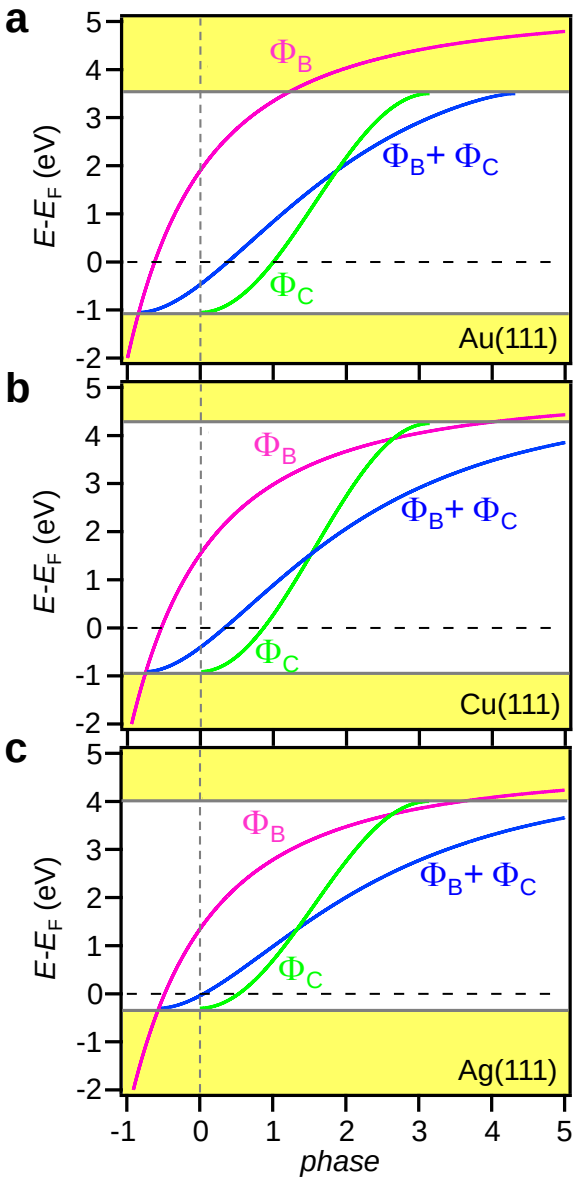

FIGURE 2.15: PAM solutions for the energy position of the Shockley state for Au(111) (a), Cu(111) (b) and Ag(111) (c) respectively. The upper and lower edges of the crystal bulk gap along ΓL are indicated in yellow, the crystal phase (Φ_C) is indicated in green, the vacuum phase in pink (Φ_B) and their addition (Φ_C+Φ_B) in blue. The solution for the energetic position of the surface state comes at $n = 0$.

Chapter 3

Part II: An Introduction to Assembly and Electronic Bands of Nanoporous Networks

The discretization of the electronic bands into distinct energy levels in nanometer-size solid systems when quantum confinement takes place is a fundamental result of Quantum Mechanics. In nanostructures, confinement is usually related to the reflection of the electronic wave function at their surfaces or interfaces by combining different materials, giving rise to diverse optical and transport properties of semiconductor Quantum Dots, Wires and Wells [125].

As indicated in the previous chapter, noble metal (111) surfaces host 2DEGs, which are ideal systems to study low-dimensional electronic properties dealing with electron scattering at the existing nanostructures [126–131]. It is known that if electrons are confined to structures with size comparable to the de Broglie wavelength, that is, if the lateral dimensions are in the nanometer range, quantum-size effects emerge. In this regard, STM studies have demonstrated that Shockley electrons can be confined parallel to the surface by artificially built nanoscale assemblies [95], for example man-made quantum corrals [18, 19], metal atom and molecular resonators [132], vacancy and ad-atom islands [133, 134], vicinal surfaces [80] and molecular nanoporous networks [15, 16]. In the following paragraphs a brief account for these systems is provided since they represent the foundations for the second part of this thesis

Taking advantage of the cryogenic temperatures in combination with the ability to position single atoms with the tip of an STM, in the 90's quantum corrals were assembled by repositioning Fe atoms on a Cu(111) surface [18]. The quantum mechanical interference patterns of 2DEG as standing waves could be imaged [Figure 3.1 (a) (left)]. Indeed, such nanostructures confine electrons into discrete eigenstates, shown in the LDOS taken at the center of the quantum corral [Figure 3.1 (a) (right)]. These features could be qualitatively understood by considering the textbook particle in a box system and modelling the Fe atoms as an impenetrable boundary, a hard-wall barrier [135]. Even though such a perfect quantum box should show

eigenstates or resonances as delta functions (practically widthless), the experimental peak widths lead instead towards considering corrals as leaky barriers [19]. This means that in quantum corrals only a small fraction of the incident amplitude is reflected by their walls [135]. This inelastic absorptive channel was proposed to be related to coupling surface electrons with bulk states [19, 136]. However, it turned out that it could also be explained by using elastic scattering theory (finite-height potential barriers) [137, 138].

In a similar fashion, quantum resonators built atom by atom on a metal surface can also trap surface state electrons [139, 140]. Figure 3.1 (c) shows such atomic arrangements (Ag adatoms forming walls on Ag(111)), where surface electrons are confined so the movement of the electrons is only constrained perpendicular to the barriers [140]. Interestingly, the formation of strongly anisotropic diffusion channels were observed. Thus, additionally deposited single atom adsorbates appeared guided by the surface state confinement features along such channels [139].

A greater mass-production of highly regular low-dimensional nanostructures on surfaces was achieved with hexagonal islands [144] or hexagonal and triangular vacancy islands formed on Ag(111) [Figure 3.1 (b) (left)]. The higher yield demanded little effort compared to the atomic manipulation examples, since it was obtained by self-assembly after a very soft sputtering of the surface [98, 133, 141, 145]. These nanostructures were phenomenologically similar to quantum corrals, but the discrete energy levels could be easily tuned with the cavity size (ranging from 30 to 100 Å wide). It was found that the standing wave patterns do not correspond to individual eigenstates, but reflect superpositions of several of them that are very close in energy due to intrinsic and thermal broadening [98, 133]. The term lossy scattering (reflection coefficient < 1 at the barrier) [141] was proposed as the most plausible cause, which reflects the fact that electrons might be scattered out of surface states into bulk states, greatly contributing to the energy width of the confined states [146] [Figure 3.1 (b) (right)].

The existence of highly ordered 1D nanostructures at the macroscopic level made possible to study such confined electronic structures with averaging techniques such as ARPES. Vicinal surfaces are among the simplest periodic surface formations generated by introducing a small angle miscut with respect to a high symmetry plane of the crystal. This results in terraces periodically separated by monoatomic steps [103, 130, 142, 147]. 1D electron confinement effects are observed in single terraces [97, 148] [Figure 3.1 (d) (left)], although coherent coupling of the two-dimensional surface state between terraces and the formation of Bloch wave states is detected when probing vicinal surfaces [95] [Figure 3.1 (d) (right)]. These propagating superlattice electronic bands can be understood and their physical nature well-captured by applying the 1D-Kronig Penny (KP) model [103], where steps are considered as repulsive square-shaped finite potential barriers $U_0 \times b$ (where U_0 corresponds to the height of the barrier and b to its width) [149].

Not only steps or adatoms scatter the surface electrons, but also molecules. They

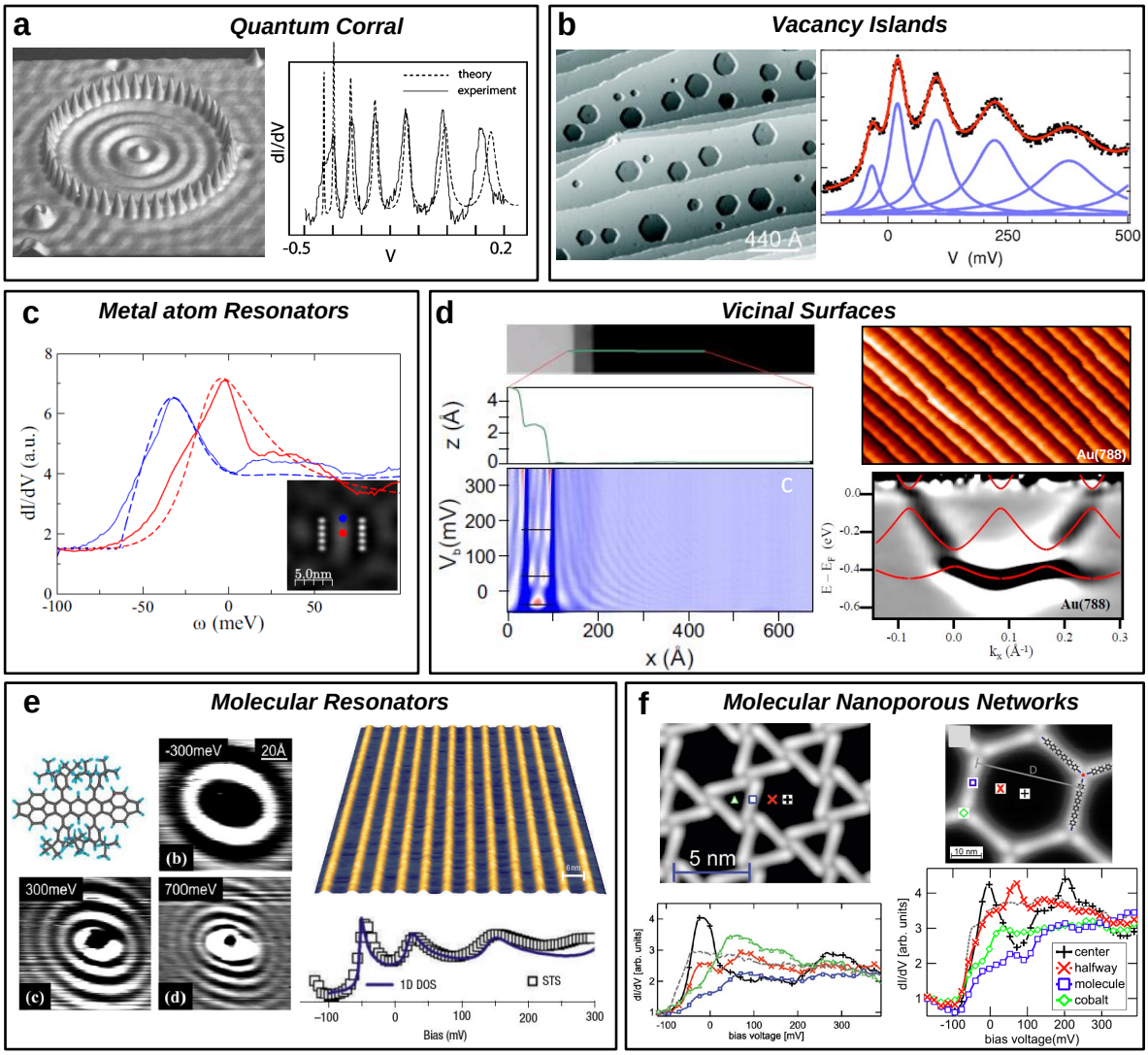

FIGURE 3.1: A journey into confining nanostructures. (a) Circular quantum corral, 142.6 Å in diameter, built from 48 Fe atoms on the Cu(111) surface (adapted from ref. [18]). Experimental and theoretical voltage dependence of *dI/dV*, with the STM tip located at the center of the circular corral (adapted from ref. [136]). (b) STM image of hexagonal vacancy islands on a Ag(111) surface and *dI/dV* spectrum at the center of a hexagonal vacancy island fitted with a superposition of Lorentzians (adapted from ref. [141]). (c) Differential conductance for the Ag resonator at two different positions of the STM tip: near the center (red) and slightly outside the resonator (blue) (adapted from ref. [140]). (d) (Left) Topographic image of a step resonator, profile along the green line and color scale *dI/dV* spectra acquired along the same line (adapted from ref. [142]); (Right) The Shockley state in Au(788), showing step superlattice bands and gaps (adapted from ref. [103]). (e) (Left) Reactive Lander (RL) molecule model and *dI/dV* maps highlighting standing wave patterns (adapted from ref. [143]); (Right) Self-assembled regular methionine grating on Ag(111). Tunneling spectrum taken at Ag patches in between the molecular chains demonstrating the 1D confinement of surface state electrons (adapted from ref. [132]). (f) (Left) Purely organic kagome network and experimental *dI/dV* spectra demonstrating a strong position-dependent modulation of the LDOS (adapted from ref. [16]); (Right) Topograph of a Ph6Co nanopore on Ag(111) and the experimental *dI/dV* spectra demonstrating a strong position dependent modulation of the nearly constant DOS of the pristine surface (adapted from ref. [17]).

create standing wave patterns of surface state electrons by scattering them with the aromatic π system of the molecular backbone [143] [Figure 3.1 (e) (left)]. Notably, the concepts proposed by Supramolecular Chemistry [150] could be successfully transferred to metal surfaces producing a myriad of self-assembled molecular arrangements with different symmetries and periodicities capable of interacting with the 2DEG [1]. For instance, one-dimensional arrays of molecular resonators were among the first examples [Figure 3.1 (e) (right)] [132]. Here, surface state resonances could be tuned by playing with the separation between the scattering molecular barriers while the 2DEG would remain practically unaffected in the direction parallel to the barriers. Adding up more complexity into the molecular design, by the proper selection of ligands, molecular linker dimensions, metal coordination agents and the templating effect of the surface, nanoporous networks were built. Such robust structures were mainly stabilized by hydrogen-bonds [50] or metal-organic coordination [9, 16, 47, 151, 152], showing long-range order and a low amount of defects. Interestingly, by the use of the local STM/STS technique, evidence of electron localization [Figure 3.1 (f) (left)] was shown inside the two-dimensional nanocavities defined by the molecular barriers [15–17, 129, 153, 154]. Such confined states were shown to be sensitive to the nanocavity size and shape [Figure 3.1 (f) (right)].

However, confinement of surface electrons within the pores of such molecular nanoporous networks turned out to be quite leaky. Owing to the finite scattering barrier represented by the molecular backbones (far from hard-wall potentials), some degree of coupling was allowed between neighboring pores. According to the concepts of band theory [155], this situation gives rise to the formation of distinct electronic bands, as confirmed by Lobo-Checa *et al.* [15] for the 3deh-DPDI metal-organic nanoporous network on Cu(111) [Figure 3.2]. STS measurements inside the ~ 2 nm wide nanocavities [yellow cross in Figure 3.2 (a)] showed electronic confinement into different localized states [Figure 3.2 (c)], in a similar fashion to previous examples in Figure 3.1 (f). In addition, dI/dV maps at the resonance peak energy [Figure 3.2 (b)] confirmed the localization of the 2DEG inside each nanocavity, resembling a quantum dot. However, the large broadening of this confined state already suggested certain interpore coupling [156]. ARPES measurements detected the presence of a shallow dispersive, cosine-shape electronic band matching the STS energy [black dashed line in Figure 3.2 (d) (top)]. In comparison to the pristine Shockley state, the fundamental energy of the band is shifted towards the Fermi level due to confinement effects and the bandwidth gives an indication of the degree of QD intercoupling. A faint onset attributed to the second confined state was then detected close to the Fermi level separated by 120 ± 30 meV from the first confined state (appearing as a plateau region in STS). The magnitude of the gap between states has been attributed to the lateral scattering strength of the potential barriers (in this case the DPDI molecular backbone) [157].

All the aforementioned examples summarized in this introduction build the ground for the second part of this thesis. Here, we study the electronic properties

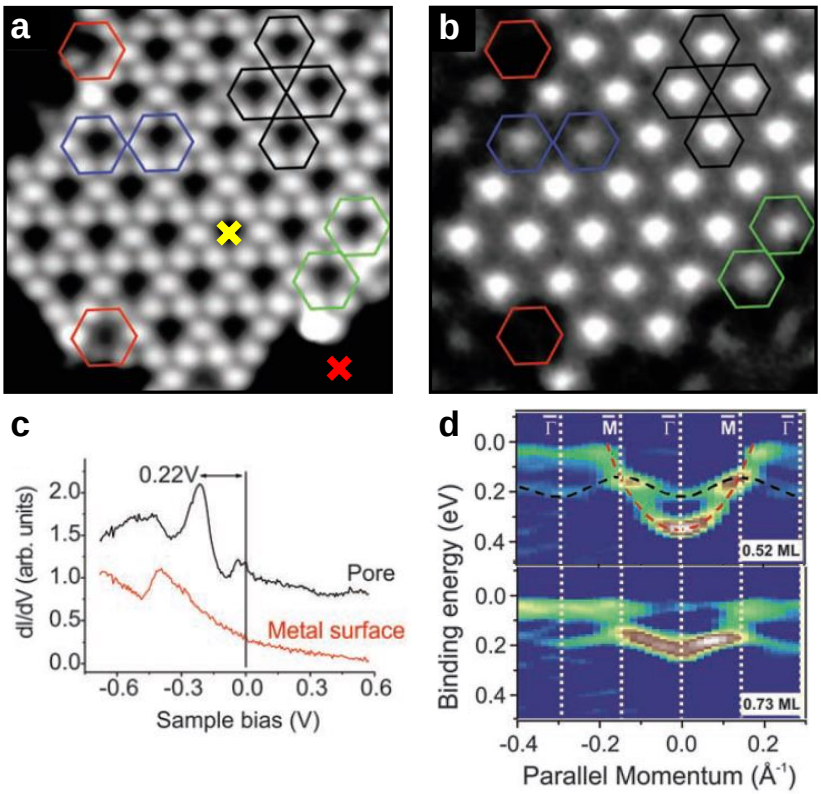

FIGURE 3.2: Electronic band structure of 3deh-DPDI nanoporous network generated on Cu(111). (a) STM image of the 3deh-DPDI nanoporous network. (b) Simultaneously recorded *dI/dV* map at the confined state resonance maximum (-0.22 V). (c) STS spectra obtained at 5 K on the clean surface state (red) and inside a pore of the 3deh-DPDI metal-organic nanoporous network (black). (d) Energy dispersion curves of the pristine state (red dashed line) and the confined state (black dashed line) measured along the $\overline{\Gamma M}$ high symmetry direction and visualized as the second derivative of the photoemission intensity for two different molecular coverages. Both EDCs at 0.52 ML and 0.73 ML were acquired at RT. All panels have been adapted from ref. [15].

of different kinds of nanoporous networks grown on (111)-terminated noble metal surfaces. For this family of nanostructures in particular, we try to find answers to the following fundamental questions:

- *Does the new electronic band formed in a nanoporous network [Figure 3.2] stem from the Shockley state, as it is generally assumed?*

Traditionally, confinement STS spectra inside single pores and the new electronic bands steming from nanoporous networks have been assigned to the pristine surface state [15, 129]. However, direct experimental evidence to this assignment is desirable. In Chapter 4 we take advantage of the fact that the fundamental energy of Shockley states is related to the position of the projected bulk band gaps, which are highly sensitive to temperature-induced variations of the lattice constant, causing the supported Shockley state to shift in energy. Therefore in a similar fashion to Paniago *et al.* [109], we study the temperature dependence of the shallow dispersive band formed by the 3deh-DPDI metal-organic network on Cu(111) [15] and observe

that it follows the trend of the pristine Cu surface state. This evidences that both bands have the same origin. This work has been published in ref. [158].

- *Is it possible to tune or engineer the degree of QD intercoupling in a nanoporous network by altering the separation among identical QDs?*

In Chapter 5 we show that it is possible to tune the confinement and intercoupling properties of QDs by precisely engineering the barrier width on surface self-assembled organic nanoporous networks. The selective barrier width is obtained by substitution of a single atom (O vs S) in the haloaromatic compounds used. As a result two similar arrays of QDs are obtained that share the same QD dimensions but different barrier width: in one case they are separated by just one molecule while two molecules space the other. We observe that such barrier separation tunability strongly affects the QD intercoupling degree as evidenced by the width variations of the confined states in STS and bandwidth in ARPES. Both complementary techniques are further supported by EBEM/EPWE and DFT calculations, which give conclusive evidence of such interpore-coupling tunability. This work has been published in ref. [54].

- *How is the band structure modified when the pore size is linearly reduced in scalable (homothetic) nanoporous networks?*

Tunability of confined state energies has already been achieved in nanoporous networks by varying the pore dimensions, *i.e.* QD size, through its organic units and observed in STS measurements on a single nanopore level [16, 17, 159]. However, such effects on the electronic band structure have not yet been studied with ARPES. In Chapter 6 we form two homothetic (scalable) Co-coordinated nanoporous networks on Au(111) where the QD size is tuned while keeping the interpore coupling unaffected. Apart from confirming the pore size effects on the electronic band structures by opening zone boundary gaps at different energies, we find an unexpected downward energy shift of the fundamental energy and a lightening of the effective mass. These counterintuitive shifts are gradual and dependent on the QD size. As the effect of the metal-organic overlayer upon the 2DEG onset has been traditionally overlooked, we infer that metal-organic layer-substrate interactions in the form of adatom hybridization effects and geometrical variations are at the origin of such unexpected effects. DFT and PAM simulations provide insight into the nature of this phenomenom which we infer to be quite general since such effects are also observed on a similar Cu-coordinated nanoporous network.

- *Can we parametrize and model in a rational way the scattering effect of the nanoporous network upon the surface 2DEG?*

Even though many theoretical models have been able to accurately explain confinement effects in quantum corrals [135, 136], vicinal surfaces [103], vacancy islands [133, 141] and resonators [140], we find that the understanding of the confinement properties and interaction effects between a nanoporous network and a 2DEG is still elusive. To explain the scattering effects of these novel organic nanoporous overlayers, Electron Boundary Element Method in combination with the Electron Plane Wave Expansion has been used, which is key to understand the observed confinements and interpore couplings. It serves not only for modelling local confinement effects inside each QD [16, 17, 129], but also to simulate the electronic band structures arising from interdot coupling [54, 129, 160]. In Chapter 7 we perform EBEM/EPWE simulations on the widely studied 3deh-DPDI nanoporous network. We conclude that, if the appropriate scattering geometry is designed and ARPES band structure and *dI/dV* curves at different positions of the metal-organic network are used as experimental input, a repulsive scattering barrier geometry (even for the metal linkers) is required, together with a 2DEG renormalization to account for the overlayer-surface vertical interactions.

- *Since nanoporous networks can serve as ideal templates for hosting additional adsorbates, is it possible to tune the electronic states of the QDs by the direct repositioning of weakly interacting atomic adsorbates (such as Xe) in the nanocavities?*

Based on the sensitivity of surface states to adsorbates and knowing that regular nanoporous structures stand out as ideal host templates [153, 161–166], in Chapter 8 the 3deh-DPDI metal-organic network on Cu(111) is used to adsorb weakly physisorbed Xe inside the nanocavities. STS measurements show that confined states shift in energy towards the Fermi level upon filling all the pores simultaneously with Xe. This tendency, is qualitatively corroborated by ARPES measurements. In addition, by STM tip repositioning of individual Xe atoms inside the nanocavities, it is also possible to study with STS the local modification of the confined state energy and QD intercoupling for different Xe occupancy configurations. These Xe-filling configurations are accurately simulated with EBEM/EPWE, delving into the intricacies of confinement and interpore coupling effects. This work has been published in ref. [53].

In the following, Chapters 4 to 8 will have a paper-like format. In particular, each chapter will start with a brief introduction indicating the main motivation. After this, the main results will be described and discussed supported by a number of figures. The chapter will end with its particular conclusions and additional supplementary information whenever not previously described in Chapter 2.

Chapter 4

Temperature Dependence of the Partially Localized State in a 2D Molecular Nanoporous Network

4.1 Introduction

Quantum states have always been related to a modification of the intrinsic surface states of the substrate material. In this chapter we study the thermally induced energy shifts of the electronic bands formed in a metal-organic nanoporous array to confirm it. By probing regions of the surface where molecular network patches of 3deh-DPDI coexist with pristine Cu regions, we observe by ARPES, that both, the pristine Shockley state of Cu(111) and the partially localized states from the molecular network, shift by the same amount upon sample temperature variation. These findings provide clear evidence that partially localized states on the pores of a network originate from the pristine Shockley state. This work has been published in ref. [158].

4.2 Results and Discussion

We study by ARPES the temperature dependence of the electronic structure that arises from the interaction of the Cu-coordinated triply dehydrogenated perylene derivative DPDI (4,9-diaminoperylene quinone-3,10-diimine) porous network generated on Cu(111). For doing so, we use a large (15 $\times$ 15 mm) Cu(111) single crystal. DPDI [Figure 4.1 (a)] [164, 167, 168] is sublimated from a Knudsen cell ($\sim$ 515 K) onto the clean Cu(111) surface held at room temperature (RT) in a gradient coverage geometry from 0 to 1 monolayer (ML), following the procedure described in Section 2.3 [see Figure 4.1 (c)]. 1 ML is defined as the amount of molecules that saturates the surface in the closed-packed assembly [168]. After the deposition of the well-defined coverage gradient of DPDI, the sample is annealed to 550 K [159]. This step is critical since DPDI undergoes a triple dehydrogenation process [3deh-DPDI

in Figure 4.1 (a)] and the necessary Cu surface adatoms become available for coordination to generate a p(10 $\times$ 10) commensurate and homogeneous metal-organic network. A model of this array is shown in Figure 4.1 (b), which is formed in the lower coverage regions (up to 0.73 ML) [168, 169]. This nanoporous arrangement leads not only to a characteristic LEED pattern [Figure 4.1 (d)] but also to a transformation of the Cu Shockley state into a shallow dispersive band visible in the ARPES channel plate detector close to the Fermi energy [cf. Figure 4.2 (a)] [15].

The coverage gradient allows us to study different network density regions within the same sample preparation [see Figure 4.1 (c)]. In essence, well-formed molecular network islands progressively colonize the surface as the molecular coverage is increased, as shown by the STM images of Figure 4.1 (e, f) (0.45 ML and 0.65 ML, respectively) [167]. Above the critical coverage of $\sim$ 0.73 ML, the porous network gradually collapses into a close-packed assembly [168].

Unlike other nanoporous networks, which remain mobile at the ARPES measurement temperatures (150 K) and can only be stabilized by saturating its coverage (network fully covering the surface), 3deh-DPDI metal-organic network islands remain stable (even as small island formations) up to 720 K [168]. As a result, ARPES probes the signal stemming from clean Cu regions and network patches simultaneously. This is illustrated in Figure 4.2 (a), where the formation of a n=1 partially localized state band (n=1 PLS) is monitored with increasing coverage, while the parabolic Cu Shockley state (Cu SS) becomes fainter and eventually vanishes. For the pristine case, the fundamental energy of the 2DEG at 150 K is at -0.4 eV and is characterized by an effective mass (m^*/m_0) of $\sim$ 0.4 [100]. As the 3deh-DPDI nanoporous network islands start to populate the surface (from 0.25 ML to 0.5 ML) the Cu SS is still visible but becomes broader and shifts slightly towards the Fermi level ($\sim$ 40 meV). This happens because the 2DEG scatters with island edges that progressively become closer to each other. At the same time, a second contribution starts to build up close to -0.25 eV. This intensity corresponds to the n=1 PLS band which originates from the coupling of the n=1 confined state of each nanopore with the neighboring ones. When the islands are small (0.25 ML), the number of nanopores or QDs is not sufficient to develop a coherent and well-defined electronic band. This shallow dispersive band with its band bottom energy at -0.25 eV, bandwidth of $\sim$ 90 meV and $m^*/m_0 \sim 0.56$ is ultimately best observed when the network practically covers the surface (0.7 ML) [15, 53]. Note that at this coverage there is no sign of the pristine Cu SS. This transition can also be nicely followed by looking at the Energy Distribution Curves at the $\overline{\Gamma}$ point [Figure 4.2 (b)]. In the same way, the intensity of the pristine Cu SS (in grey) decreases with increasing molecular coverage and the n=1 PLS band evolves until it is fully formed (in red). The relative intensities do not exhibit a one to one ratio. In particular, the peak area of the n=1 PLS has been reported to be $\sim$ 30 % with respect to the Cu SS for the optimal coverage of 0.73 ML [15]. One possible reason is the appreciable defect concentration and the relative small average domain

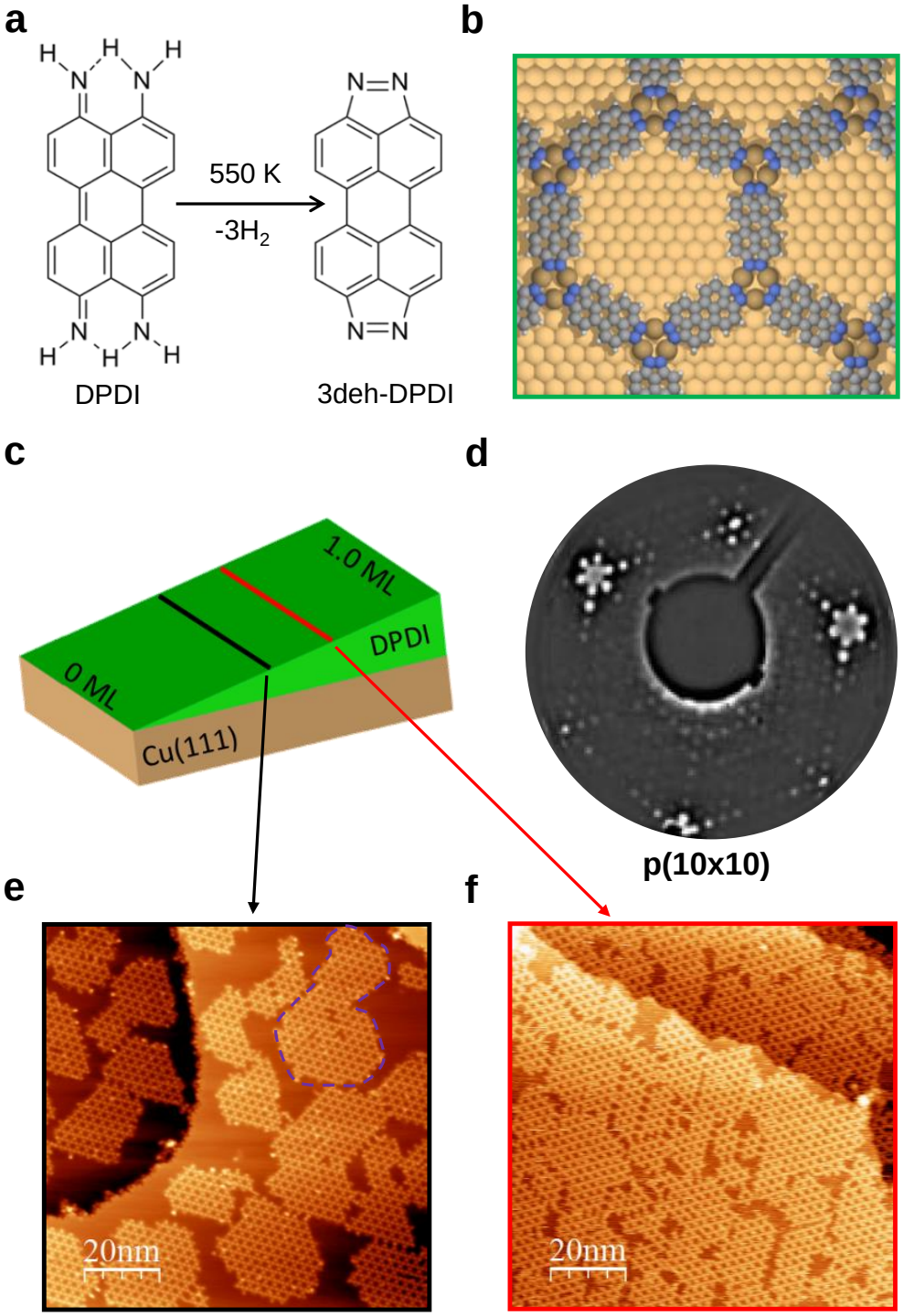

FIGURE 4.1: A variable density of nanoporous network realized through a coverage gradient geometry. (a) Thermally induced triple-dehydrogenation of DPDI acts as an exoligand in the formation of the metal-organic network on Cu(111) [169]. (b) Structural model for the Cu-coordinated 3deh-DPDI nanoporous network forming a p(10 x 10) superstructure (adapted from ref. [167]). (c) Schematic view of the DPDI deposition gradient performed on Cu(111). (d) LEED pattern obtained at 52 eV showing the Cu(111)-p(10x10) DPDI network lattice (adapted from ref. [168]. (e) and (f) STM images for 0.45 ML (left) (4 K, -0.8 V, 5 pA) and 0.65 ML (right) (297 K, 2 V, 6 pA) network coverage. The network structure is maintained throughout the coverage gradient up to ~ 0.73 ML.

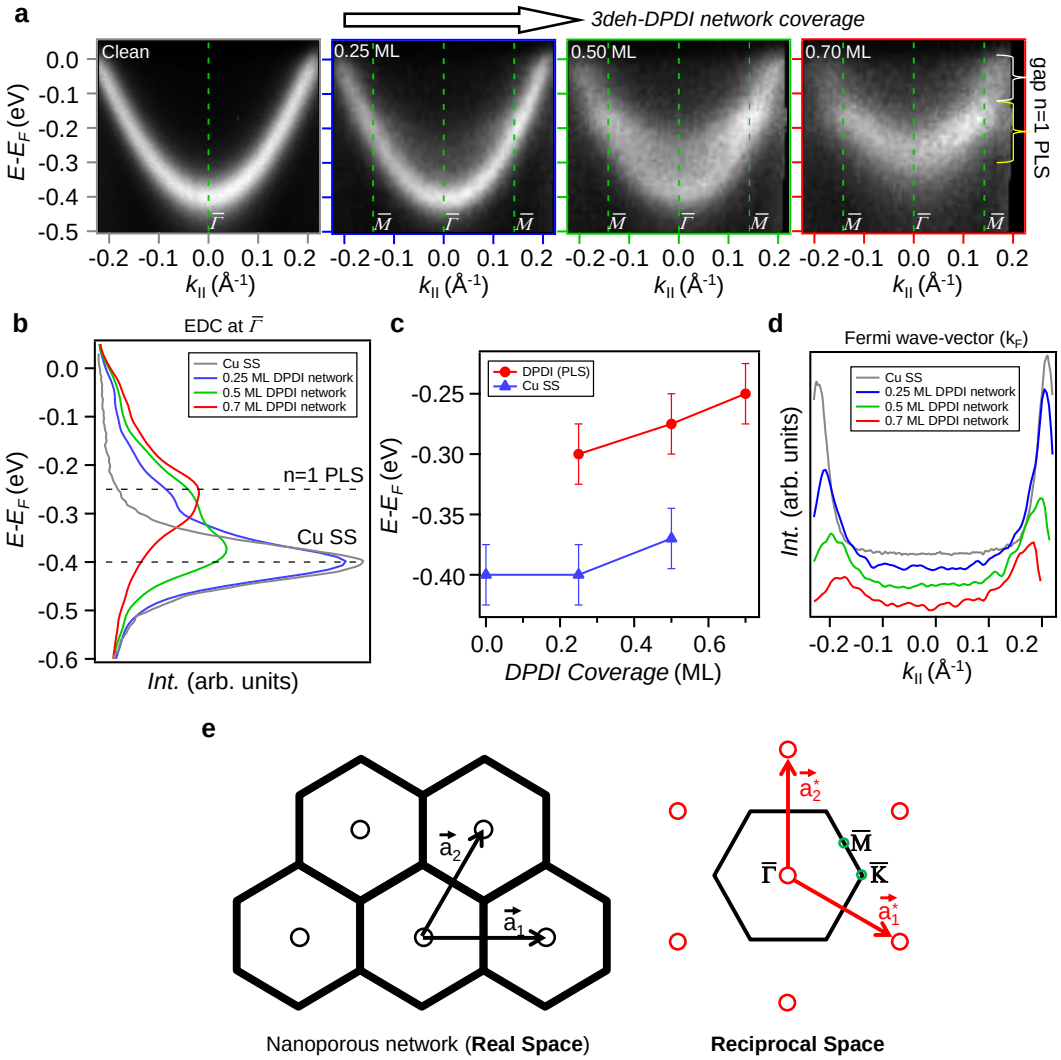

FIGURE 4.2: Coverage dependent network island induced electronic band formation measured with ARPES. (a) Coverage gradient formation of the partially localized state band. Between 0.25 ML and 0.6 ML, both Cu SS and PLS bands coexist. (b) Energy distribution cuts at $\bar{\Gamma}$ highlight the intensity variations for both Cu SS and PLS bands as the coverage of the network islands is increased until fully covering the surface. (c) Fundamental energy variations of Cu SS and PLS bands with coverage. Scattering effects produce a slight shift of the Cu SS when the network islands become predominant (0.5 ML). The fundamental energy of the PLS is also better defined when the network practically covers the surface (0.7 ML). (d) Fermi wave-vector (k_F) spectra with coverage. Slight shrinking of the wave-vector is observed due to the formation of a hexagonal Surface Brillouin Zone produced by the network. (e) Representation of the surface unit cell (real space) and the Brillouin zone (reciprocal space) of the 3deh-DPDI network.

size that the networks exhibit compared to an atomically perfect Cu surface. In addition, lossy scattering effects with the network barrier may also be responsible for such intensity decrease and increased background [141, 146]. Moreover, the energy position of both Cu SS and the n=1 PLS is slightly sensitive to the coverage of the network islands on the surface [Figure 4.2 (c)]. As the density of islands becomes more predominant (0.5 ML), the Cu SS scatters with the network edges and presents

a minor ~ 40 meV shift towards the Fermi level. Similarly, the fundamental energy of the n=1 PLS is better defined when the network fully covers the surface. Figure 4.2 (d) captures the evolution of the Fermi wave-vector (k_F) with coverage. A tendency towards smaller values can be observed. Such k_F shrinking evidences a distortion of the Fermi surface into a new hexagonal Surface Brillouin Zone. This happens because the highly ordered hexagonal nanoporous network sets a new and periodic scattering landscape for the surface 2DEG and new zone boundaries and symmetry points ($\overline{\mathrm{M}}$ and $\overline{\mathrm{K}}$ points) appear in reciprocal space. Figure 4.2 (e) shows the conversion from real space unit cell of 3deh-DPDI network to the first Brillouin zone in reciprocal space. The p(10×10) unit cell of 3deh-DPDI network is defined with unit-cell vectors $\vec{a_1}$ and $\vec{a_2}$ ($|\vec{a_1}| = |\vec{a_2}| \equiv a \approx 2.55$ nm). The unit cell in reciprocal space with the first Brillouin zone (black hexagon) and the symmetry $\overline{\Gamma}$, $\overline{\mathrm{M}}$ and $\overline{\mathrm{K}}$ points are defined by $\vec{a_1^*}$ and $\vec{a_2^*}$. The length of the unit-cell vectors amount to $|\vec{a_1^*}|$ = $|\vec{a_2^*}| = 4\pi/\sqrt{3}a \approx 0.283$ Å^{-1}. The distances between the critical points are $2\pi/\sqrt{3}a$ ≈ 0.142 Å^{-1} ($\overline{\Gamma\mathrm{M}}$) and $4\pi/3a \approx 0.164$ Å^{-1} ($\overline{\Gamma\mathrm{K}}$). This matches Figure 4.2 (a) where the ARPES spectral functions along $\overline{\Gamma\mathrm{M}}$ show the shallow dispersive band that follows a cosine shape with an opening of a gap at each $\overline{\mathrm{M}}$ point. This energy gap corresponds to the separation between the n=1 and n=2 PLS bands.

Once the formation of the network islands and its coverage dependent n=1 PLS band have been well characterized and introduced, we proceed to study its energy dependence with temperature. ARPES spectral functions close to the Fermi level were systematically acquired as a function of sample temperature (from 315 K to 136 K) for two coverage regions: the first, where the molecular network completely covered the surface (~ 0.75 ML) and the second, where it coexisted with molecule-free areas (~ 0.50 ML) [close to the coverage of Figure 4.1 (e, f)]. For each temperature, a normal emission ARPES spectral function is captured in the channelplate detector for each coverage region. This is done by sequentially moving the z-axis of the manipulator. Then the sample temperature is fractionally increased (ΔT ≈ 15 K) and the measurement is repeated.

Figure 4.3 (a) shows the ARPES spectral function corresponding to the temperature extremes (315 K and 136 K) for ~ 0.50 ML DPDI. The intensity distributions I($E - E_F$, k) reflect a coexistence of the Cu SS band originating from the molecule-free areas and the n=1 PLS band arising from the coupling between pores [15]. While the former has an upward parabolic dispersion [85], the latter exhibits a lower binding energy at $\overline{\Gamma}$ and a limited bandwidth together with an apparent increase of the effective mass [53].

As the temperature of the sample decreases from 315 K to 136 K, both electronic bands of Figure 4.3 (a) become better defined and gain amplitude [85, 170]. As reported by Paniago *et al.* [109], the bottom of the Cu SS band shifts towards higher binding energy [171], but is difficult to discern the behavior of the n=1 PLS band from the raw data. To follow its evolution, the energy distribution curves of the ARPES spectral funcitons at $\overline{\Gamma}$ (k = 0) are represented in Figure 4.3 (b) for both end

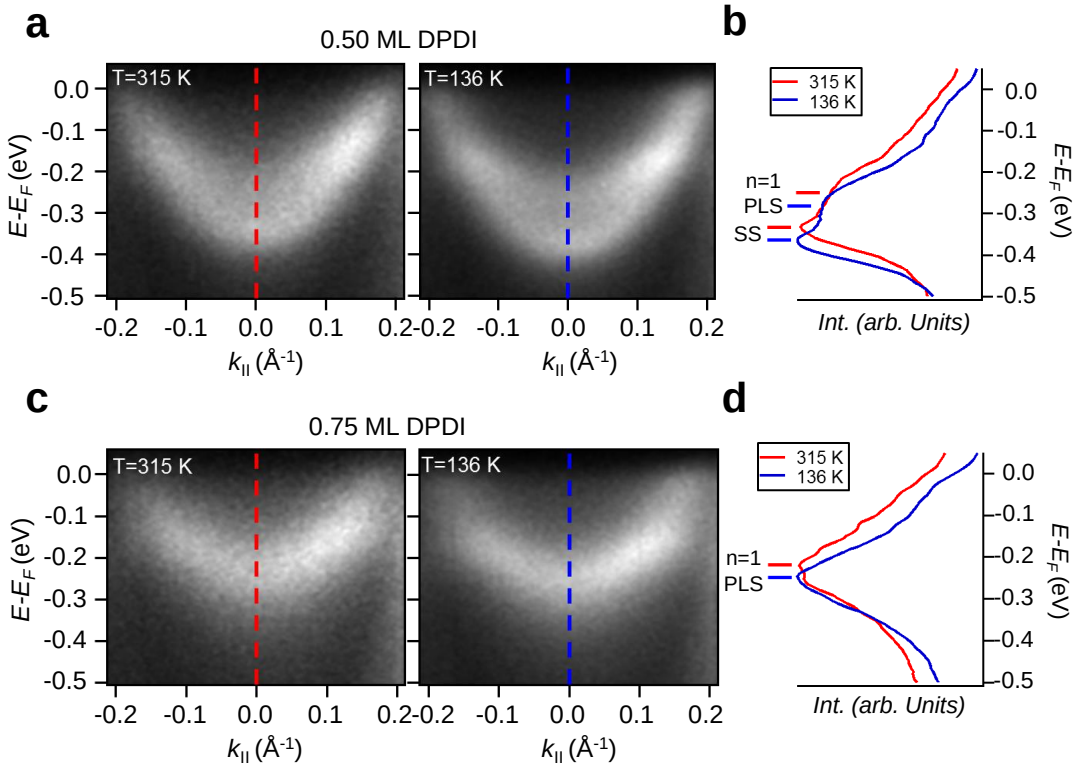

FIGURE 4.3: Temperature dependence of the PLS band and Cu SS band at the two extreme temperatures studied. In contrast to ref. [15], raw ARPES data is presented here to directly compare the resulting EDCs. (a) ARPES experimental spectral function acquired at 315 K and 136 K for the coverage of 0.50 ML, in which regions of the network and molecule-free areas coexist. (b) Smoothened, normal emission ($k_{||}$= 0) EDCs for both temperatures in (a). The horizontal lines mark the energy positions of the Cu Shockley state (SS) and the partially localized state (PLS) band minima obtained from a two component Lorentzian fit. (c) ARPES experimental spectral function acquired at 315 K and 136 K for the coverage of 0.75 ML featuring the surface completely covered by the network. (d) Smoothened, normal emission ($k_{||}$= 0) EDCs for both temperatures in (c) with horizontal lines indicating the energy positions of the PLS band minimum.

temperatures, red being the higher temperature spectrum and blue the lower one. We observe that the well-known Shockley state band minimum (peak closest to $E_i \approx -0.4$ eV) is shifted away from the Fermi energy by $\sim$ 30 meV as the sample is cooled down. The same trend is observed on the shoulder feature located in the proximity of $E_i \approx -0.25$ eV. This peak corresponds to the n=1 PLS and is in part masked by its proximity to the Cu SS. For a better visualization of the thermal energy shift of this state, it is best to study the higher coverage regions that lack the molecule-free areas, such that the Shockley state is quenched. This case is shown in Figure 4.3 (c), corresponding to 0.75 ML and exhibiting only bands attributable to the porous network. Once more, a clear energy shift for the band minimum and a sharpening of the features are observed as the temperature is lowered. The comparison between the temperature dependent EDCs, represented in Figure 4.3 (d), shows that the n=1 PLS also shifts around 30 meV to higher binding energies as the sample is cooled down.

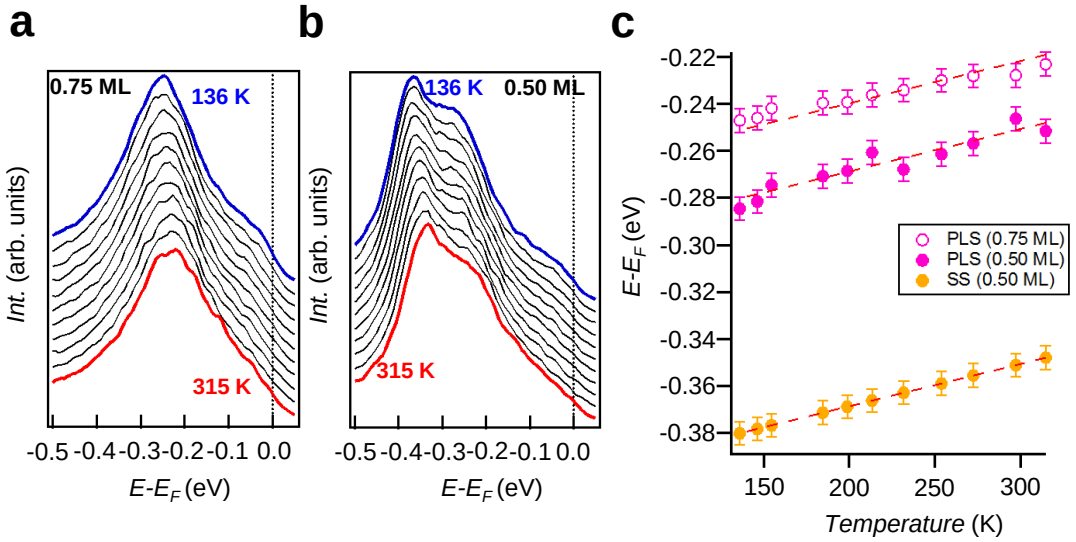

FIGURE 4.4: Full range temperature dependence of the PLS and Cu SS. Normal emission EDC temperature waterfalls for 0.75 ML (a) and 0.50 ML (b) coverages. A clear trend towards higher binding energy and a sharpening of the features is observed as the temperature is lowered. (c) Temperature variation of the energy position of the PLS and SS band minima as extracted from the fit for each spectral line represented in the waterfall. The fit was carried out using one (0.75 ML) or two (0.50 ML) Lorentzian components with a linear background convoluted with a Fermi function. The dashed lines correspond to variation rates with a common slope for the three components, all of which agree with the Shockley state variation reported in ref. [109].

The nature of the energy shift observed for the n=1 PLS is still undefined at this stage and so we must follow the temperature transition at intermediate points. In this regard, the Shockley state of Cu(111) has been shown to linearly shift with temperature, with a slope of $(1.8 \pm 0.1) \times 10^{-4}$ eV/K [109]. This linear behavior is also present for Ag(111) and Au(111) Shockley states, each one possessing a particular rate. For the nanoporous network, EDC waterfall plots at normal emission ($\overline{\Gamma}$) for the studied temperature range are shown in Figure 4.4 (a, b) corresponding to full network coverage (0.75 ML) and to coexisting regions of molecular network and molecule-free areas (0.50 ML). We observe that the energy position of the band minimum of the n=1 PLS as well as the Cu SS shift in a progressive way as the temperature is varied. There are no abrupt energy changes of the features, which sharpen up as the temperature is lowered.

A quantitative analysis of the temperature dependence of these states is achieved by Lorentzian fitting with a linear background convoluted with a Fermi function from the spectra in Figure 4.4 (a, b) (see Section 4.4.3). Figure 4.4 (c) summarizes the results from such analysis and shows the variation of the initial state energy with sample temperature. As expected, the Cu SS band (yellow dots) follows the red dashed line which accounts for a rate of $(1.8 \pm 0.1) \times 10^{-4}$ eV/K, in agreement with Paniago *et al.* [109], resulting in an increase of 32 ± 2 meV in binding energy

for the investigated temperature range. The other two sets of magenta points in Figure 4.4 (c) correspond to the n=1 PLS for the 0.50 ML (full circles) and 0.75 ML (open circles) and they differ in energy by $\sim$ 30 meV. We attribute this offset to the coverage effect in its fundamental energy already discussed in Figure 4.2. For 0.5 ML the n=1 PLS is shifted by 33 $\pm$ 5 meV within the probed temperature range, which agrees with the variation of the Cu SS, while a slightly smaller overall shift of 26 $\pm$ 5 meV is measured for 0.75 ML. This is still consistent with the Cu SS behavior within the experimental error. As the temperature dependence is unique for each of the electronic states in Cu(111) [171, 172], the demonstration that the n=1 PLS band associated with the nanoporous network exhibits an identical temperature variation of its energy to the Cu SS, supports that both have the same electronic nature. The energy shift is due to temperature induced variations of the lattice constant and this affects bulk and surface differently. According to Knapp *et al.* [171], the magnitude of the energy shift for the surface band, which is 50%- 75% larger than typical shifts for bulk bands, may reflect a thermal distortion of the lattice at the surface. Furthermore, each bulk band exhibits its own temperature dependence, *i.e.* the Λ_3 and Λ_1 *d*-bands as well as the *sp*-band all have different temperature coefficients, most likely due to their different orbital character. At the same time, all these temperature trends are different from the Cu SS. Moreover, according to Knoesel *et al.* [172], the image states of Cu(111) show an opposite rate with respect to the Shockley state, since they are related to the bulk band projection at the top of the gap (L_1). All this demonstrates that the Cu SS has a unique temperature dependence, different from the rest of electronic states. The fact that the n=1 PLS follows precisely the same trend of the SS evidences their common origin. For some closed packed molecular assemblies, such as CoPc on Au(111), similar trends for the Shockley derived interface state have been observed. However, in this case, it is also argued that on organic/metal interfaces the Shockley state energy shift with temperature not only originates from the sum of the changes in the Au substrate lattice constant but also slight temperature dependent interfacial bonding distance variations have to be considered [173].

4.3 Conclusions

Upon the 3deh-DPDI nanoporous network formation, the surface state electrons are subjected to a 2D finite periodic potential imposed by the network structure. The network thus alters the Shockley state giving rise to the scattering phenomena capable of generating partially localized states and new band structures with different dispersion relations [15, 129]. In this experimental study we validate the origin and nature of such PLS observed in a 2D metal-organic nanoporous network self-assembled on the Cu(111) surface. By studying the temperature dependence of two different coverage regimes of the network, we corroborate that the n=1 PLS existing

in the pores of the network originates from the Cu(111) Shockley state. The energies of both states display the same temperature dependence, directly relating the n=1 PLS to the Cu SS observed on the pristine metal surface. This experimental demonstration supports that the surface state electrons are affected by the periodic molecular potential of the network. Therefore, as it will be shown in the next chapters, semiempirical models such as the Electron Boundary Elements Method [116] in combination with the Electron Plane Wave Expansion [115] can be confidently used to derive the observed electronic states and to model the surface potential landscape created by molecular nanoporous networks [129].

4.4 Supplementary Information for This Chapter

4.4.1 ARPES Measurements

ARPES measurements were performed in UHV conditions (base pressure of 1×10^{-10} mbar) with a lab-based experimental setup equipped with a display-type hemispherical electron analyzer (SPECS Phoibos 150), an energy/angle resolution of 40 meV/0.1°and a monochromatized Helium I ($h\nu = 21.2$ eV) source. Variable temperature measurements were performed using a closed-cycle He cryogenic manipulator with a controlled temperature range between 320 K and 30 K.

4.4.2 STM Measurements

STM measurements performed by the group of Prof. T. A. Jung from the University of Basel (Switzerland). They were carried out at both low temperature (Omicron Nanotechnology GmbH with Nanonis SPM control system) and room temperature (home built STM). The bias voltages given here refer to a grounded tip. The measurements were performed with Pt-Ir tips (90% Pt, 10% Ir) prepared by mechanical cutting and followed by *in-situ* sputtering with Ar^+ ions and controlled indentation in the bare Cu(111) substrate. STM data were acquired in constant current mode and were processed with the WSxM software [174].

4.4.3 Method Used for the ARPES Spectral Deconvolution

- For the quantitative analysis performed in Figure 4.4, we performed a Lorentzian fitting with a linear background convoluted with a Fermi function. Figure 4.5 shows the fittings performed for Cu(111) surface state (one Lorentzian component), 0.5 ML DPDI network (two Lorentzian components) and 0.75 ML DPDI network (one Lorentzian component) coverages respectively. These spectra were taken at 150 K. For 0.5 ML DPDI case, the Cu SS appears slightly shifted to lower BEs, while the opposite trend is observed for the n=1 PLS.

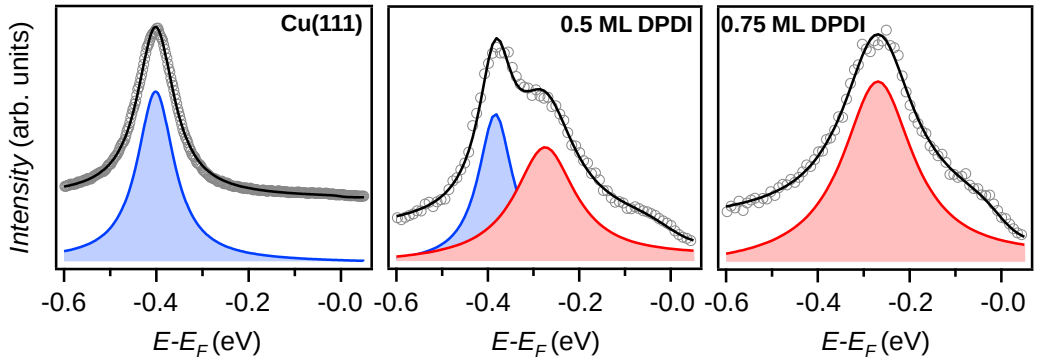

FIGURE 4.5: Cu SS and DPDI n=1 PLS spectra fittings. From left to right: Cu SS, 0.5 ML DPDI and 0.75 ML DPDI spectra fittings using a Lorentzian component for each peak and a linear background convoluted with a Fermi function (not shown).

Chapter 5

Precise Engineering of Quantum Dot Array Coupling Through Their Barrier Widths

5.1 Introduction

Quantum dots are known for confining electrons within their structure. Whenever they periodically aggregate into arrays and cooperative interactions arise, novel quantum properties suitable for technological applications show up. Control over the potential barrier existing between neighboring QDs is essential to alter their mutual crosstalk or coupling. In this chapter we show that precise engineering of the barrier width can be experimentally achieved by a single atom substitution (sulphur vs oxygen) in a haloaromatic compound, which in turn tunes the degree of QD intercoupling. We achieved this by generating self-assembled, halogen bond stablilized, long-range ordered nanoporous networks that confine the surface 2DEG. Indeed, these extended QD arrays form up on bulk silver (Ag(111)) and thin silver films on gold (3 ML Ag/Au(111)) alike, maintaining their overall structure, confinement and interdot coupling properties. This work has been published in ref. [54]

5.2 Results and Discussion

Our concept to control the interpore barrier width while maintaining the pore size [Figure 5.1 (a, b)] is based on the halogen bond versatility to generate artificial nanostructures [12, 175, 176]. The two hexagonal nanoporous networks show single-molecular and double-molecular separation between practically identical pores, which extend into long-range ordered network films. This has been achieved by just a single atom substitution (sulphur vs oxygen) in the haloaromatic precursors used, reminiscent of a butterfly effect. We employed two molecules [Figure 5.1 (c, d)]: 3,9-dibromodinaphtho [2,3-b:2′,3′-d]thiophene (Br-DNT) [177] and 3,9-dibromodinaphtho

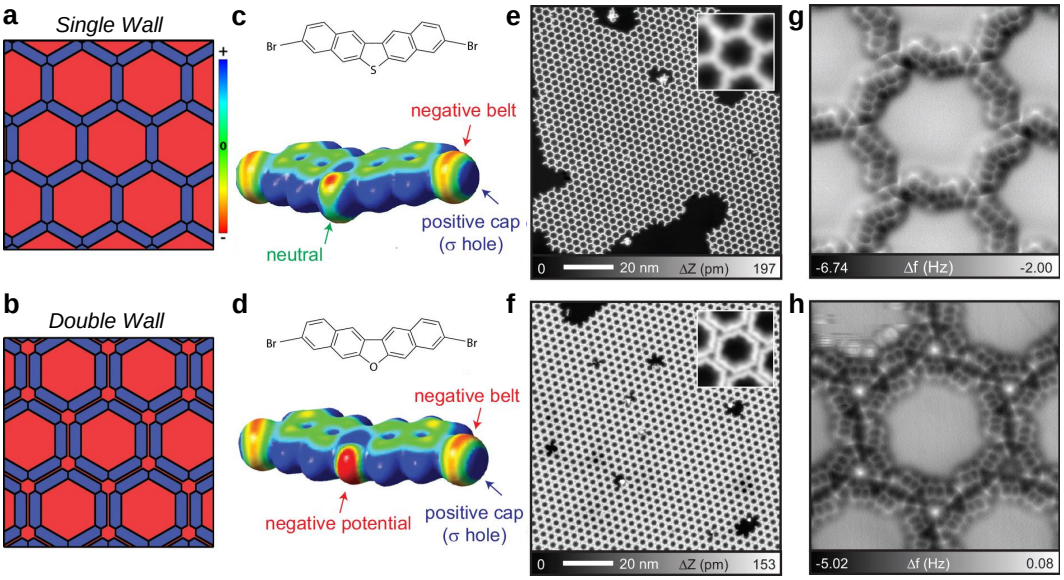

FIGURE 5.1: QD arrays generated by single-wall (SW) and double-wall (DW) nanoporous networks that confine the surface 2DEG. (a, b) Schematic representations of the concept behind SW and DW networks. (c, d) Chemical structures and electrostatic potential maps of Br-DNT and Br-DNF. (e, f) Large scale STM topographies for the SW network generated with Br-DNT and the DW network with Br-DNF. Insets show close-views of each network. (g, h) High-resolution atomic force microscopy (AFM) images of the SW network and DW network. Measurement parameters: tunneling current I= 5 pA, bias voltage V= 200 mV (e, f); V= 0 mV, oscillation amplitude A= 60 pm (g, h).

[2,3-b:2′,3′-d]furan (Br-DNF). Intermolecular electrostatic attraction between the positive cap (σ hole) and the electron-rich regions (negative belt of bromine atoms in Figure 5.1 (c) or oxygen atom of the furan core in Figure 5.1 (d)) are responsible for the condensation into two distinct molecular networks [178, 179] (see Figure 5.2). Our STM images (acquired by our collaborator Dr. Shigeki Kawai from MANA/NIMS, Japan) [Figure 5.1 (e, f)] show extended (over 100 nm) nanoporous network formations on Ag(111) with small amount of defects. Such hexagonal nanoporous assemblies, are the most energetically favorable and stable below RT. Above this temperature, thermal fluctuations overcome the halogen bond strength ($\sim$ 33 kJmol^{-1}) [178] and the nanoporous structure is destabilized while the surface catalyzed Ullmann coupling reaction starts to dominate. This leads to the formation of covalent one-dimensional polymers [180] (see Section 5.4.2).

Detailed structures are derived from atomic force microscopy (AFM) with a CO functionalized tip [112, 114]. The pores of the Br-DNT network are separated by single molecules [Figure 5.1 (g)], whereas two molecules are required in the Br-DNF network [Figure 5.1 (h)]. Note that bright spots at the nodal sites of the latter are CO molecules adsorbed for tip functionalization (see Section 5.4.2). While the condensation of Br-DNT happens solely through trigonal halogen bonding [176, 181] [Figure 5.2 (a)], the furan group presence in Br-DNF introduces higher interaction complexity due to the electronegativity of oxygen and it also tends to participate in the assembly [Figure 5.2 (b)]. The O$\cdots$Br-C bonding (oxygen is faintly observed

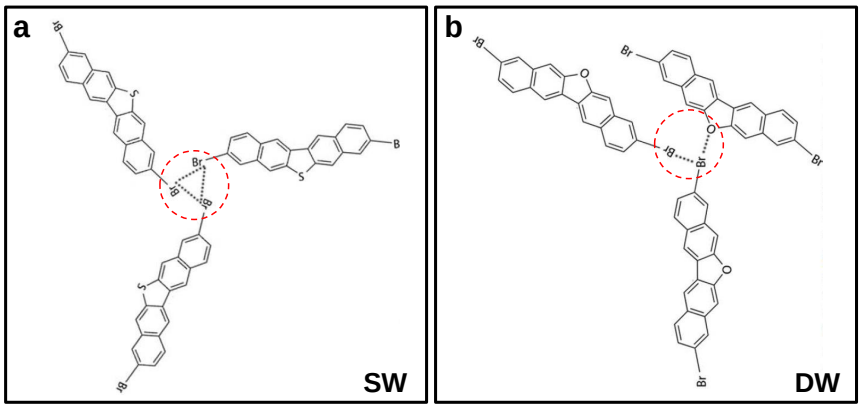

FIGURE 5.2: Bonding motifs that stabilize the SW and DW formations. (a) The formation of SW network occurs *via* a triple halogen bond. Br atoms form a triangle that stabilizes the whole structure. (b) The formation of DW network is induced by the furan group presence in Br-DNF that introduces higher interaction complexity due to the electronegativity of oxygen.

in AFM) is apparently stronger (based on the electric potentials of Figure 5.1 (c, d)) than the Br···Br-C homo-halogen bond, leading to a shorter bond. Both hexagonal arrays are commensurate with the pristine Ag(111) surface, according to density functional theory (DFT) calculations performed by Dr. Ali Sadeghi from Shahid Beheshti University (Iran) (see Section 5.4.4). Indeed, the Br-DNF network interpore distance is larger (by 14%) than that of Br-DNT, as a consequence of the molecular pairing. Note, however, that the enclosed pore areas remain identical to both assemblies since the perimeter of each pore is constructed by 6 molecules with the same dimensions in a hexagonal conformation. Essentially, we confirm structurally that these arrays are extended model systems to investigate the 2DEG confinement and interpore coupling, as they feature identical QDs separated by different wall widths. For clarity, we will hereafter refer to the Br-DNT and Br-DNF networks as Single-Wall (SW) and Double-Wall (DW) networks, respectively.

Next we consider the QD local electronic structure using STS, as this technique measures the LDOS of the surface at a particular bias voltage [19]. Figure 5.3 (a) shows conductance (dI/dV) spectra acquired at the center of the pores of SW and DW networks and referenced to the clean Ag(111) substrate. The pristine Ag(111) surface state reveals its presence by a strong variation in the conductance at -65 meV, corresponding to the surface state band edge (black curve). Indeed, clear energy shifts of the pristine surface state onset (-65 meV) are induced by the QD confinement, peaking at 72 meV for the SW network and 45 meV for the DW network. These values are unexpectedly inverted since a stronger confinement (higher peak energy) is anticipated for the wider barrier (DW) [19]. It could be argued that it originates from a difference in the molecule-substrate interaction affecting the potential amplitude, where Br-DNT would have a larger value than Br-DNF [182]. However, not only a larger interaction is expected for Br-DNF due to the extra oxygen electronegativity but also the measured full width at half maximum of the confined state for the DW

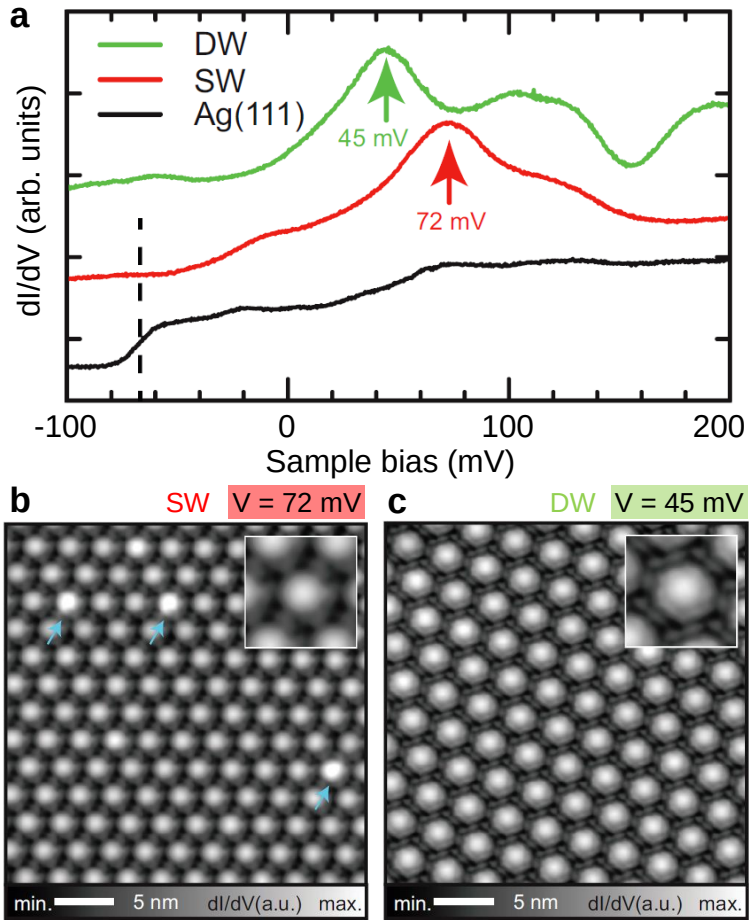

FIGURE 5.3: Local electronic structure of the SW and DW networks. (a) Conductance (*dI/dV*) spectra on the pristine Ag(111) (*black*), on the pore centers of the SW network (*red*) and DW network (*green*). (b, c) *dI/dV* maps on the SW and DW networks acquired on the peak maxima in (a), enlarged in the corresponding insets. Measurement parameters: I= 10 pA, V= 72mV, modulation voltage V_{ac}= 10 mV, oscillation frequency f_{ac}= 513 Hz (b); I= 10 pA, V= 45 mV, V_{ac}= 10 mV, f_{ac}= 515 Hz (c).

network (32 meV) is narrower that that for the SW network (45 meV), suggesting a stronger confinement [19]. The conductance maps at those particular peak energies show high conductance within the pores, exhibiting the dome shape of the n=1 confined state [Figure 5.3 (b, c)] [17, 133, 141]. Note that some pores rarely present brighter contrast (indicated by blue arrows), which we assign to defects (see Section 5.4.2). Moreover, the AFM images show both molecules lying flat on the surface [Figure 5.1 (g, h)], suggesting a similar and weakly interacting regime [128].

Since these networks are analogous to coupled QDs [15], due to the leaky molecular potential barriers, in principle, one should expect the formation of shallow dispersive bands in photoemission. Therefore, we should perform ARPES measurements in both these networks. However, this technique endures the intrinsic restriction of being sensitive only to the occupied electronic structure, so the confined states from the SW and DW networks on Ag(111) become undetectable [100, 183, 184]. In order to push both confined state peaks into the occupied region, we grew SW and

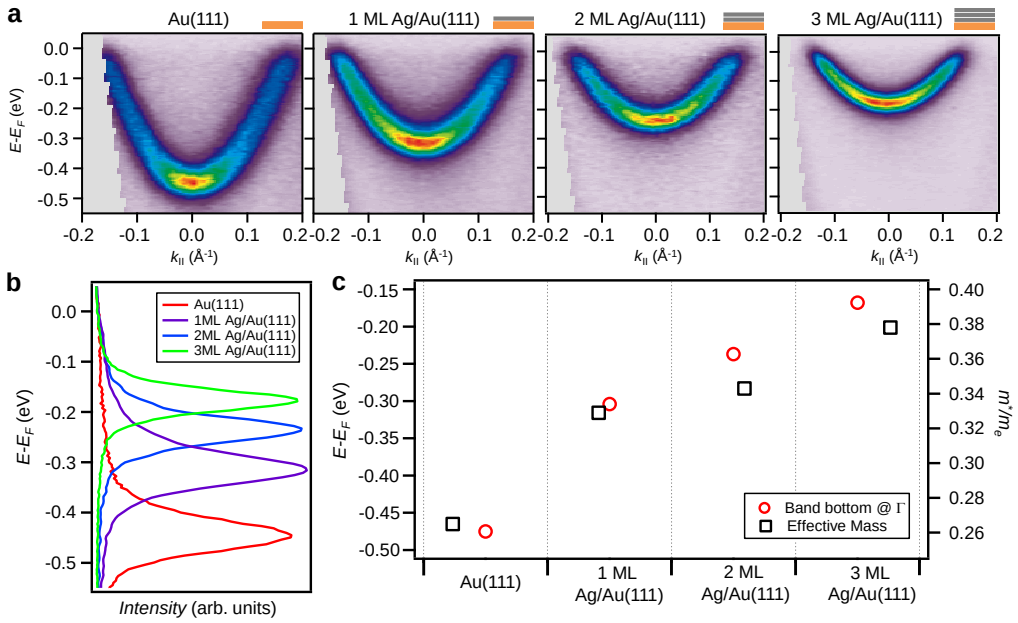

FIGURE 5.4: Modification of the Au(111) 2DEG with Ag film thickness. (a) ARPES maps along $\overline{\Gamma M}$ measured directly on Au(111), after 1 ML, 2 ML and 3 ML of Ag deposition (T_{sample} = 130 K) and subsequent annealing to 450 K. According to the EDCs at $\overline{\Gamma}$, the surface state shifts its energy towards the Fermi energy in defined steps (b) and increases its effective mass (c). Values shown in (c) have been adapted from ref. [157].

DW onto a 3 monolayer (ML) Ag thin film on Au(111), which shifts the Ag(111) surface state by -100 meV while preserving its 2DEG character (Figure 5.4). The formation of Ag thin films on Au(111) can be monitored by following the evolution of the Shockley state (its fundamental energy and sharpness) with Ag coverage. This transition from the Au(111) Shockley state up to the Shockley state corresponding to 3 ML Ag/Au(111) is shown in Figure 5.4 (a) [157]. Note that the spin-orbit splitting of Au(111) is not observable in this channelplate image because of the low resolution conditions used in exchange of a faster acquisition. From 1 ML Ag/Au(111) to 3 ML Ag/Au(111) the surface state shifts towards the Fermi level and its effective mass is increased. The energy shift can be observed in the EDCs at the $\overline{\Gamma}$ point [Figure 5.4 (b)]. Here, the peak width can also serve as a direct indication of the quality of the film formed. In Figure 5.4 (c), the values of the fundamental binding energy and the effective mass are summarized for each complete monolayer (adapted from ref. [157]). Note that the surface state will become pure Ag like, when 10 ML Ag/Au(111) is reached (E= -65 meV, m^*= 0.4 m_0). This means that for the 3 ML Ag/Au(111) case, even though the 2DEG is quite similar, there is still 100 meV difference between both fundamental energies.

These networks cannot be formed for 1 ML and 2 ML Ag/Au(111) films (see Section 5.4.1). However, when using the 3 ML Ag film the ARPES data in Figure 5.5 exhibit distinct network bands that are characteristic of coupled QD arrays [15, 53]. If we compare them with the pristine parabolic surface state, they shift their minima (band bottom at $\overline{\Gamma}$) to higher energy due to confinement in the pores and deviate

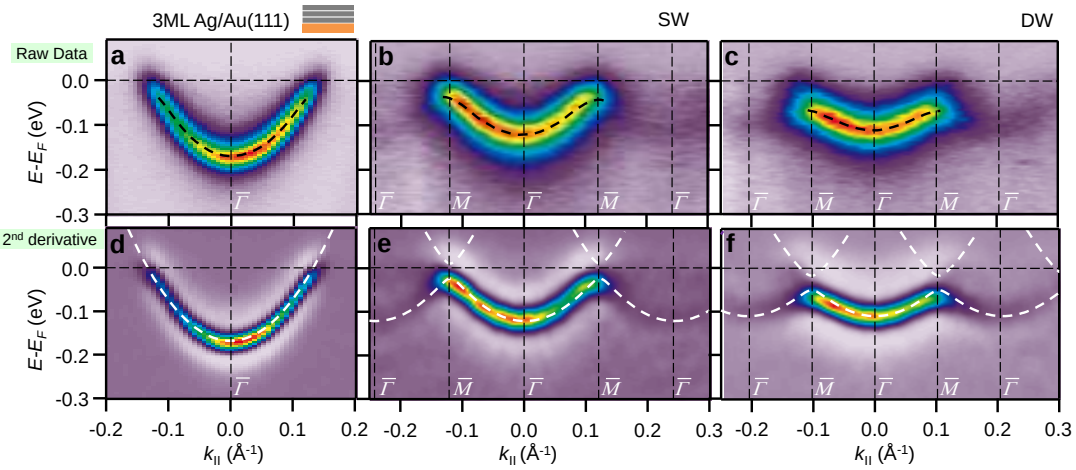

FIGURE 5.5: 2DEG modification induced by the SW and DW network potential barriers along $\overline{\Gamma M}$. (a-c) ARPES map along $\overline{\Gamma M}$, obtained on the 3ML Ag/Au(111) as well as on the SW and DW networks. The EDCs close to $\overline{\Gamma}$ were fitted using a Lorentzian component and a linear background convoluted with a Fermi function (black dahsed lines). (d-f) Second derivative maps of the above raw data for an improved visualization of the second SBZ. The white dashed lines correspond to the EBEM/EPWE calculated electronic bands generated by altering the 2DEG with the molecular surface potentials.

rapidly from the initial quasi free-electron like parabolic dispersion (as evidenced by the weak side replicas away from $k_{||} \simeq \pm 0.1$ Å^{-1}). Such replicas are generated by the scattering potential at the molecular barriers and always appear with weaker intensity than the main band from the first Surface Brillouin Zone [157]. Note that, these subtle effects can only be observed whenever a single domain, long-range ordered system exists on the surface reaching the micron-size regime. The network band periodicities (evidenced by its cosine-like shape in the $\overline{\Gamma M}$ high symmetry direction) relate to the real space network periodicity and match our DFT calculations and STM data (cf. Table 5.1). Contrary to STS, we find that the band minimum shift (taking as reference the onset of the 3 ML Ag/Au(111) surface state) is larger for the DW than the SW network (by 10 meV) and exhibits a narrower bandwidth (almost half). This confirms a lower coupling between adjacent QDs for the DW case due to the doubling of the barrier.

Moreover, the characteristic cosine-shape band observed when following $\overline{\Gamma M}$

TABLE 5.1: Extracted ARPES experimental parameters from the electronic bands

	3 ML Ag film	SW/Ag film	DW/Ag film
Band bottom	-160 meV	-120 meV	-110 meV
Band width	—	92 meV	51 meV
$\overline{M}$ point	—	0.120 Å^{-1}	0.104 Å^{-1}
Interpore distance	—	3.02 nm	3.49 nm
(DFT)	—	(3.03 nm)	(3.45 nm)
m^*/m_0	0.38	0.47	0.59

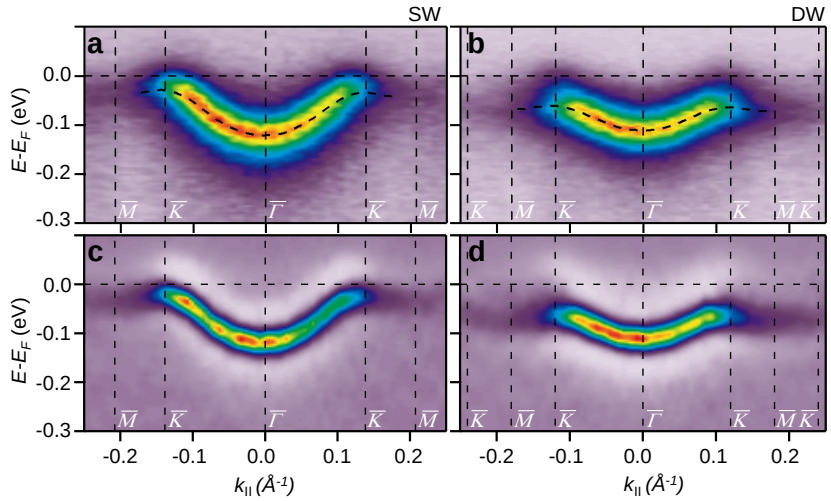

FIGURE 5.6: 2DEG modification induced by the SW and DW network potential barriers along $\overline{\Gamma K}$. (a, b) ARPES map along $\overline{\Gamma K}$, obtained in the SW and DW networks. The EDCs close to $\overline{\Gamma}$ were fitted using a Lorentzian component and a linear background convoluted with a Fermi function (black dashed lines). (c, d) Second derivative maps of the above raw data for an improved visualization of the second Surface Brillouin Zone. Contrary to the cosine-shape band structure of the $\overline{\Gamma M \Gamma}$ high symmetry direction, the bands look even flatter in the $\overline{\Gamma K M}$ direction.

symmetry direction of these QD systems, appreciably changes its dispersion when following the $\overline{\Gamma K}$ high symmetry direction (30° rotated from $\overline{\Gamma M}$). This is highlighted in Figure 5.6 where SW and DW bands become flatter beyond the $\overline{K}$ points. This is a clear indication that the isotropic paraboloid of the pristine 2DEG becomes distorted due to the newly formed hexagonal shape SBZ, which is induced by the honeycomb lattice of the SW and DW nanoporous networks (see Figure 5.7).

To emphasize the SBZ induced distortions on the 2DEG, isoenergetic cuts in second derivative (k_x vs k_y) are compared for the three cases: 3 ML Ag/Au(111), SW and DW respectively [Figure 5.7]. The selected energies correspond to the band bottom region of the first confined states (-110 meV), the lower edge of the $\overline{\mathrm{M}}$ point gap for DW (-65 meV) and the lower edge of the $\overline{\mathrm{M}}$ point gap for SW (-30 meV). For the last case, no cut for DW is shown, since this energy falls at the gap between the first and second confined states. In all cases, the pristine 2DEG shows a circular shape with different radius typical of an isotropic electronic state. However, at -110 meV [Figure 5.7 (a, d, g)], the band bottoms of SW and DW are nicely observed replicating even at the second SBZ (as dim purple circles). At -65 meV [Figure 5.7 (b, e, h)], while SW exhibits some circular shape (with a smaller wave-vector than the pristine), DW shows a clear hexagonal distortion because it has reached the zone boundary ($\overline{\mathrm{M}}$ point). We observe the same isoenergetic morphology for the SW at higher energies (-30 meV). Such observations provide evidence of the modulation of the 2DEG upon the formation of a honeycomb nanoporous network.

At this point STS and ARPES results seem to be in contradiction. To shed light into these discrepancies, we performed model calculations with the Electron Boundary Elements Method in combination with the Electron Plane Wave Explansion [115,

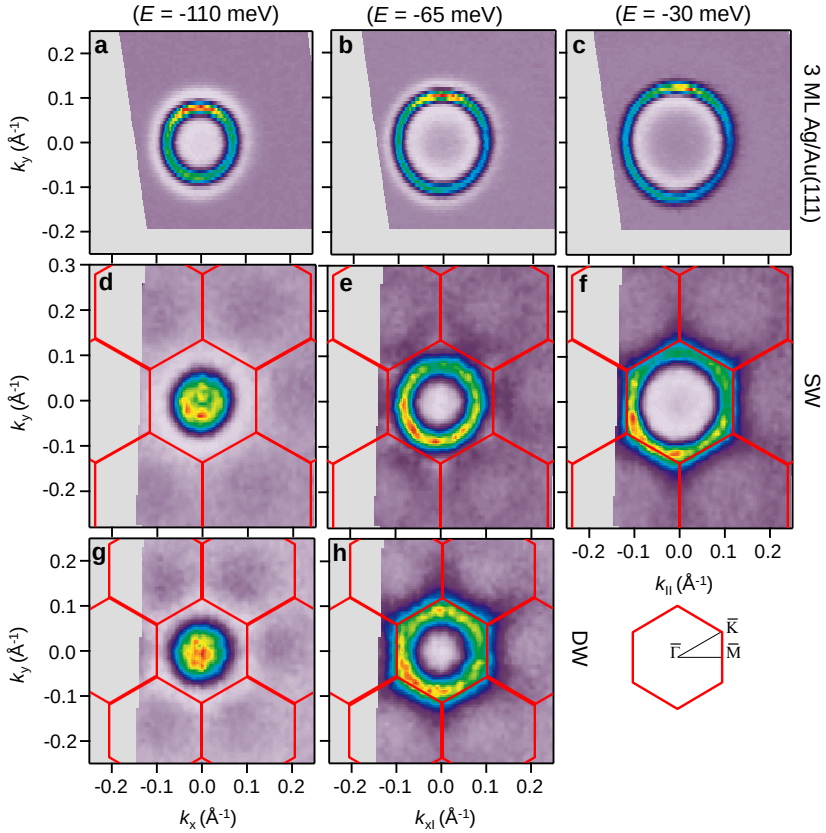

FIGURE 5.7: SW and DW induced SBZ distortions of the 2DEG observed in k_x vs k_y isoenergetic cuts. (a-c) Cuts corresponding to the isotropic Shockley state of 3 ML Ag/Au(111) at different energies. (d-f) Identical isoenergetic cuts corresponding to the SW induced electronic band. A clear hexagonal distortion is observed as one moves from its fundamental energy (-110 meV) up to the top of the band or $\overline{\text{M}}$ point at -30 meV. (g, h) Isoenergetic cuts corresponding to the bottom and top of the DW induced confined state band. The hexagonal distortion becomes apparent when the zone boundary is reached at the top of the band. All isoenergetic cuts are shown in second derivative to emphasize the weak replicating bands away from the first SBZ.

116, 129]. The simulations were done in collaboration with Dr. Zakaria M. Abd El-Fattah (Al-Azhar University, Egypt). We used simplified structures (straight beads) for the molecules (inset in Figure 5.8), which agree well with our DFT calculated iso-potential surfaces (see Figure 5.16). Note that this geometry became valid after corroborating that a more complicated shape of the barrier yields practically the same results. In EBEM/EPWE the Schrödinger equation is solved for independent electrons (2DEG) of effective mass m^* within periodic domains containing two different potential areas: zero for Ag sites (pores and substrate) and constant non-zero potential (V_{eff}) for the molecular positions (walls) that scatter the electrons. The m^* and V_{eff} parameters are determined by an iterative fitting using both STS and ARPES data (more details on the simulation process are included in Section 5.4.3). The agreement of these calculations to the experimental data (both STS and ARPES) turns out to be excellent, confirming that both substrates (bulk and thin film) are equivalent for our study. The only requirement is a 100 meV shift to account for the

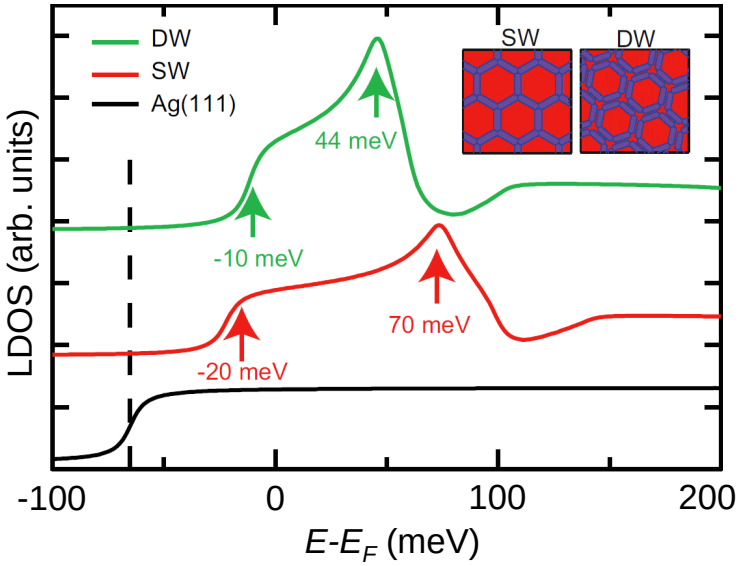

FIGURE 5.8: EBEM/EPWE simulations of the local electronic structure. Calculated *dI/dV* spectra, obtained after fitting the experimental data with EBEM/EPWE. The ARPES fit was shifted by 100 meV for direct comparison with the *dI/dV* spectra in Figure 5.3 (a). Insets show both molecular geometries used in EBEM/EPWE calculations that closely match the STM topographies [Figure 5.1 (e, f)] and DFT calculated electric field profiles (Section 5.4.4).

different 2DEG onset between Ag(111) and 3 ML Ag/Au(111). We obtain a common repulsive scattering amplitude of V_{eff} = 140 meV at the molecular sites for both SW and DW, but different effective masses: m^*_{Ag}= 0.38 m_0, m^*_{SW}= 0.49 m_0 and m^*_{DW}= 0.54 m_0. Such effective mass increase suggests a change in the electron wavefunction overlap with the crystal substrate concomitant to an enhancement of the pore confinement that leads to a reduction of the QD coupling when going from SW to DW (the effect of the effective mass increase is discussed in Section 5.4.3). The reproduced band structures [white dashed lines in Figure 5.5 (d-f)] match exceptionally well with our ARPES data, validating the expected pore coupling difference and periodic long-range order of these arrays. EBEM/EPWE simulated bands also mimic very nicely the spectral intensity and band replicas beyond the first BZ (see Figure 5.15 in Section 5.4.3). Moreover, the calculated local electronic structure (Figure 5.8) also agrees with the STS data of Figure 5.3 (a), not only in the peak values but also in shape. Therefore, the EBEM/EPWE simulations bring conclusive consistency when comparing the experimental STS on Ag(111) and ARPES on 3 ML Ag/Au(111), corroborating that these techniques are complementary to each other.

The inverted order of the STS energy peaks observed in Figure 5.3 (a) can now be explained. Coupled QDs give rise to bonding and anti-bonding continuum states when set in arrays [160]. The fundamental energy is established by the bonding state and the overall bandwidth (proportional to the QD intercoupling) is limited by the anti-bonding ones [conceptually explained in Figure 5.9 (b) for two coupled QDs]. The reduced bandwidth of the DW network compared to the SW (by$\sim$ 45%,

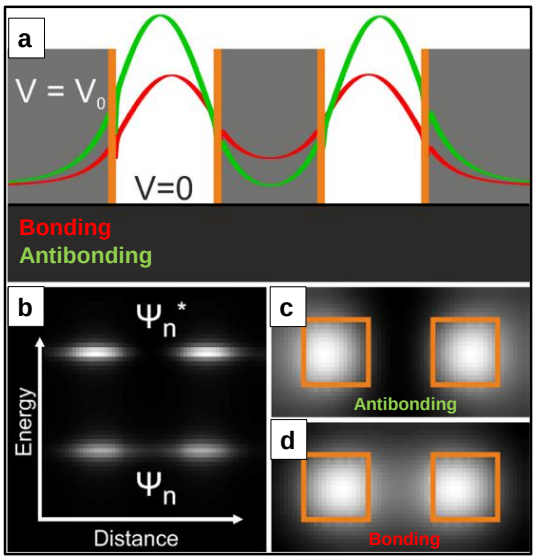

FIGURE 5.9: Localization of bonding and antibonding states for two coupled QDs. (a) Simplified model supporting a bonding (red) and antibonding (green) state. (b) EBEM calculated LDOS as a function of electron energy and position along the axis through the centers of the QDs. Ψ_n and Ψ_n^* label the bonding and antibonding states, respectively. (c, d) Two-dimensional LDOS maps at the energies of the antibonding (c) and bonding (d) states. The QDs have a square shape. Note that the bonding state shows considerable intensity between QDs (at the molecular sites) in comparison to the antibonding. Figure has been adapted from ref. [160]

cf. Table 5.1) confirms the lower interpore coupling imposed by the wider barriers. However, this does not explain yet the larger STS peak shifts at the pore center with respect to the ARPES fundamental energies. The underlying reason is that the STS technique reveals an enhanced sensitivity to probe the anti-bonding state [53, 160]. According to Seufert *et al.* [160] the wavefunction shape for the bonding state is more spread out than the anti-bonding one [Figure 5.9 (c, d)]. Thus, as shown in Figure 5.9 (a) the antibonding state (in green) peaks more abruptly at the pore center than the bonding state (in red), yielding a higher conductance (for a particular tip height). Consequently, the peak lineshapes are generally asymmetric with maxima displaced towards the top of the band (Figures 5.3 and 5.8), which in ARPES matches the $\overline{\mathrm{M}}$ point energy (after shifting 100 meV).

Another way of explaining this particular STS lineshape can be done from the band structure perspective: at the bottom of the band, close to the $\overline{\Gamma}$ point, electrons have the largest possible wavelenght of the state (λ=$\frac{2\pi}{k}$), which means that they are sensitive to a large fraction of the overall potential of the nanoporous network. Thus, they spread out over the network and limit their nanopore contribution at the center when probed by the STS tip. Contrarily, electrons close to the $\overline{\mathrm{M}}$ point, exhibit the shortest wavelength of the state, which is of the order of the network interpore periodicity. This means that they are more prone to be trapped within the QD walls as they are highly sensitive to the periodic potential landscape (molecular network) [as already observed in Figure 5.3 (b, c)]. As a consequence, the overall shape of the

LDOS at the pore center reflects a wide and asymmetric shape, gathering more intensity for the higher energy states (cf. Figure 5.8). In fact, the width of the STS peak is a fingerprint for the degree of coupling between neighbouring QDs. Nevertheless, the STS is still sensitive enough to the fundamental energy (bonding state) as onsets are sometimes observed in the spectra. In particular, these can be deduced from Figure 5.8 (at -20 meV for the SW and -10 meV for the DW), matching the ARPES energy minima ($\overline{\Gamma}$ point) after shifting 100 meV. Therefore, the bandwidth and corresponding QD interaction could be estimated from STS peak width whenever sharp cutoffs show up in the spectra.

The value of V_{eff}= 140 meV from our model calculations yields an overall barrier of $V_{eff}{\cdot}d$ = 0.7 eV·Å per molecule, which is small compared to other networks already reported [16, 129]. Such weak potential barrier can originate from the weak interaction between the haloaromatic compound and the substrate or by the absence of metallic coordination in our arrays. Moreover, the use of solely the substrate's 2DEG m^* does not provide a good agreement with the SW and DW electronic bands and we recurrently use an increased value (m^*_{SW}= 0.49 m_0 and m^*_{DW}= 0.54 m_0) close to the experimental one in order to match the shallow dispersions (cf. Table 5.1). This suggests that, besides the lateral scattering at the molecule network, there is a subtle change in the electron wavefunction overlap with the crystal substrate. Note, however, that we expect this vertical overlap to be practically identical for both networks, given that V_{eff} is the same. Therefore, the additional increase of m^* when going from SW to DW barriers, with the associated flattening of the bands, suggests a correlation with QD intercoupling. In essence, the m^* increase and band flattening (reduction in band width) could be considered like fingerprints for increased electron localization and reduced interdot coupling. Finally, we point out that charge transfer effects (from sulphur and oxygen) are ruled out from being detrimental in the observed confinement and coupling effects. This is because the EBEM/EPWE model considers only homogeneous periodic repulsive scattering potentials and can precisely simulate the experimental observations.

5.3 Conclusions

In this chapter we have shown that precise engineering of QD array coupling is possible by modifying just the barrier width (without affecting the QD's size). These halogen-bond stabilized organic nanoporous networks are generated on bulk (Ag(111)) and Ag films (3 ML Ag/Au(111)) alike by substitution of a single atom (sulphur vs oxygen) in the precursor molecule, reminiscent of a butterfly effect. The extended and periodic nature of these arrays provides access to their distinct band structures, which are directly compared with their local density of states and merged through calculations. Such complementary experimental and theoretical synergy provides complete fundamental insight into the nature of QD intercoupling processes. Even

though substrate contributions cannot be discarded, our findings clearly suggest that the reduction of the QD coupling (from SW to DW) is associated with a flattening of the band dispersion and increase of the effective mass.

5.4 Supplementary Information for This Chapter

5.4.1 ARPES Sample Preparation

A clean Au(111) surface was *in-situ* prepared by repeated cycles of standard sputtering and annealing (Ar^+ sputtering at energies of 1.2 keV, followed by annealing to 800 K). To form Ag films of controlled monolayer on Au(111) a gradient evaporation of Ag with the substrate at 150 K was performed. Afterwards, to improve the Ag thin film quality, the sample was annealed to ~ 450 K [185].

Br-DNT and Br-DNF molecules were deposited from a Knudsen cell heated at 440 K on the substrate at ~ 130 K in order to make sure that the networks were formed. Note that these halogen-bonded assemblies are only stable below RT.

The presented Ag thin film engineering turns out of utmost importance in bringing the SW and DW confined state peaks from the unoccupied region down to the occupied region [compare Figures 5.3 (a) and 5.5 (a)]. Both SW and DW only formed on 3 ML Ag/Au(111), even though the film quality for 1 ML and 2 ML was excellent. It is not discarded that the herringbone reconstruction induced surface corrugation, atomic scale defects, modified diffusion rates as compared to the flat bulk Ag(111) are affecting the formation of such long-range ordered assemblies. Hence, we speculate that beyond 3 ML, both networks should form indistinctly of the number of Ag layers.

Even though Au(111) and Ag(111) have an almost identical lattice constant (~ 2.89 Å), SW and DW networks do not form on Au(111). This is probably due to the change of diffusion and surface adsorption energies induced by the presence of the herringbone reconstruction. The herringbone induced corrugation dominates over the formation of the SW network as nicely illustrated in Figure 5.10 (a-h). As the deposition coverage is increased, with the sample temperature kept at 150 K [Figure 5.10 (a-d)], chain-like structures, distorted hexagonal pores and closed-packed assemblies can be identified, always guided by the herringbone pattern. Each one of these structures can be better observed in the close-up images [Figure 5.10 (e-h)]. Such differences between Ag(111) and Au(111) illustrates the intricate balance between molecule-molecule and molecule-substrate interactions required for the stabilization of long-range ordered systems.

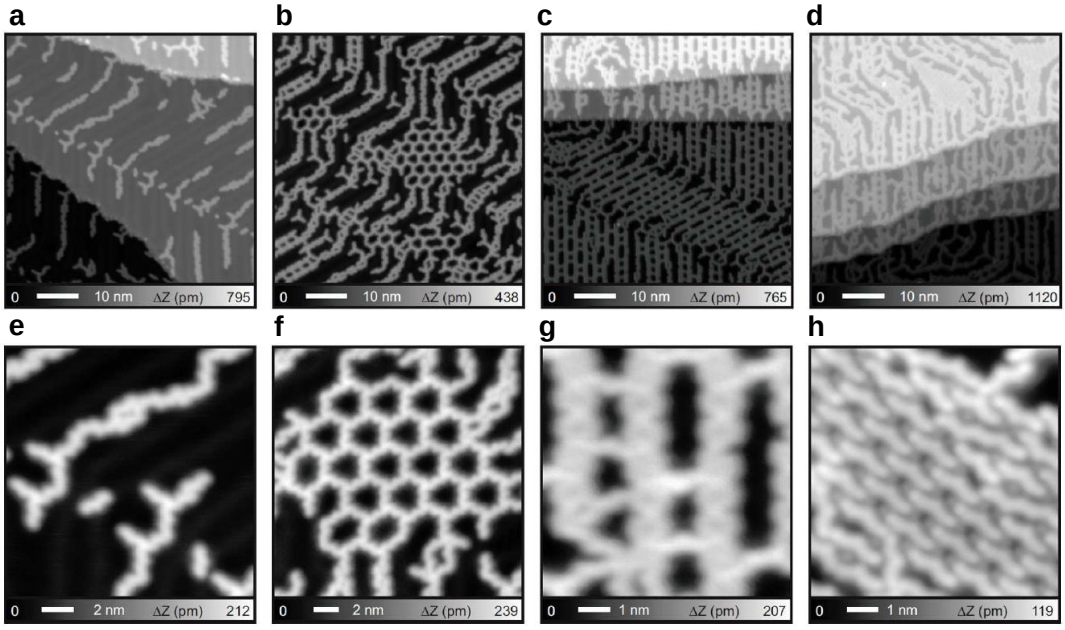

FIGURE 5.10: Molecular arrangements of Br-DNT deposited on Au(111) at 130 K. (a-d) A series of STM topographic images, with increasing molecular coverage and (e-h) corresponding close views. The surface corrugation prevents the long-range formation of 2D hexagonal molecular networks, facilitating chain structures following the herringbone reconstruction. We stress that if an ideally regular 2D porous network as the one observed in (f) would fully extend over the whole surface, the obtained band structure would be different from the SW and DW cases shown for Ag(111) because the pores have different symmetries (three-fold vs six-fold) and exhibits different interpore dimensions. Measurement parameters: V_{tip}=-200 mV for all images, I= 10 pA in (a) and (b); I = 2 pA in (c) and (d); I = 5 pA in (e); I = 20 pA in (f); I = 2 pA in (g); I = 20 pA in (h).

5.4.2 STM/AFM Measurements

All experiments were performed by Dr. Shigeki Kawai from MANA/NIMS (Japan) with an Omicron STM/AFM with a qPlus configuration [186], operating at 4.8 K in UHV. A clean Ag(111) surface was *in-situ* prepared by repeated cycles of standard sputtering and annealing. The W tip of a tuning fork sensor was *ex-situ* sharpened by focused ion beam milling technique and was then *in-situ* covered with Ag atoms by contacting to the sample surface.

3,9-dibromodinaphtho [2,3-b:2′,3′-d]thiophene (Br-DNT) [177] and 3,9-dibromodinaphtho [2,3-b:2′,3′-d]furan (Br-DNF) were deposited on Ag(111) surfaces at 150 K from a crucible of Knudsen cell. The resonance frequency of the self-oscillating qPlus sensor was detected by a digital lock-in amplifier (Nanonis: OC4 and Zurich Instruments: HF2LI and PLL). In STM mode, the tip was biased while the sample was electronically grounded. The topographic images were taken in a constant current mode. In AFM mode, the tip apex was terminated by a CO molecule [114] and all images were taken at a constant height mode.

Detection of CO Molecules and Furan Group in DW Network

The appearance of bright spots at the coordination sites in DW network [Figure 5.1 (h)] may initially induce to consider the formation of a metal-organic coordination with surface Ag adatoms. However, upon a closer look at Figure 5.1 (h), one can inmeadiately notice that not all coordination sites appear bright (5 out of 6 corners). Hence, this leads towards considering the presence of an adsorbate. This is indeed the current scneario since CO molecules were intentionally dosed for tip funtionalization purposes. In order to further corroborate this, a series of AFM images are obtained at the same position while altering the tip-sample separation [Figure 5.11 (a-c)]. Due to accidental CO manipulation the initially vacant region [highlighted with a red arrow in Figure 5.11 (a)] becomes occupied by a CO molecule in the subsequent scan repetitions [Figure 5.11 (b, c)].

Further understanding of the intricate bonding mechanism for the formation of the DW network is given by AFM. However, certain elements become more complicated to be detected than others, and this depends on their height with respect to the surface or their electronic configuration [187–189]. Hence, as illustrated in

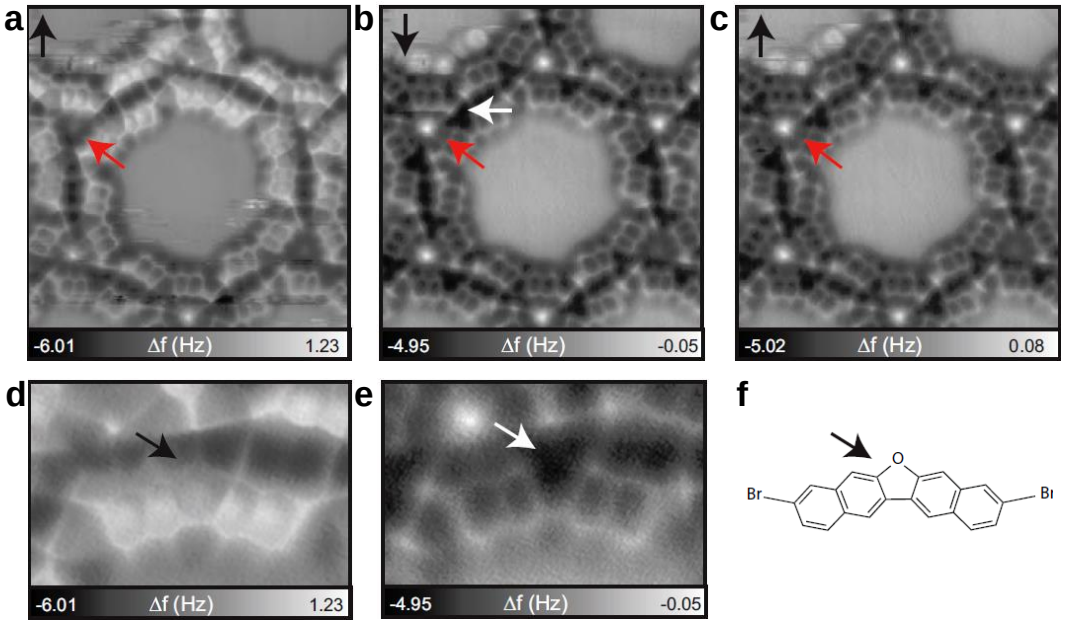

FIGURE 5.11: Adsorption of CO molecule on the nodal site and AFM imaging of the oxygen atom of the furan group. (a-c) AFM image series of the DW network when CO is intentionally dosed into the system for the preparation of the CO functionalized tip. Vertical black arrows indicate the slow scan directions. The tip and sample separation in (a) is smaller than those in (b) and (c) by 80 pm. In (a), four CO molecules are found at the nodal sites. By accidental manipulation, the node indicated by the red arrow becomes filled in (b). The horizontal white arrow marks the discontinuous frequency shift detected. Measurement parameters: V= 0 mV, oscillation amplitude A= 60 pm. (d-f) Close view AFM image of the furan moiety in Br-DNF, taken in constant height mode at different tip-sample distances. (d) is taken closer than (e) by 80 pm. The O-C bond (f) appears in (d) while it vanishes in (e). The naphthalene moieties are flat on the surface and no steric stress is induced by the adsorption at the furan moiety.

Figure 5.11 (d-f), when the tip comes closer to the sample (by 80 pm), the initially unobservable oxygen atom [Figure 5.11 (e)] becomes visible in Figure 5.11 (d), exhibiting an excellent matching with the expected chemical structure of the Br-DNF molecule sketched in Figure 5.11 (f).

Defect Concentration in SW and DW Networks

STM measurements can provide a good idea about the quality of the formed nanoporous network. As evidenced in Figure 5.1 (e, f), such QD arrays are very stable at low temperatures (below RT) and due to the self-healing character of the halogen bond, such structures self-correct until an almost perfect nanoporous organic layer is formed. However, some electronic irregularities were detected when looking at the confined state features at certain pores in Figure 5.3 (b) (blue arrows) apparently missing in Figure 5.3 (c). Looking at their corresponding STM images [Figure 5.12 (a, b)], we can identify such imperfections as Br-DNT single molecules or possible Br adatoms trapped inside some nanocavities (yellow arrows). However, the amount of such trapped entities is so scarce that they are irrelevant to the ARPES signal.

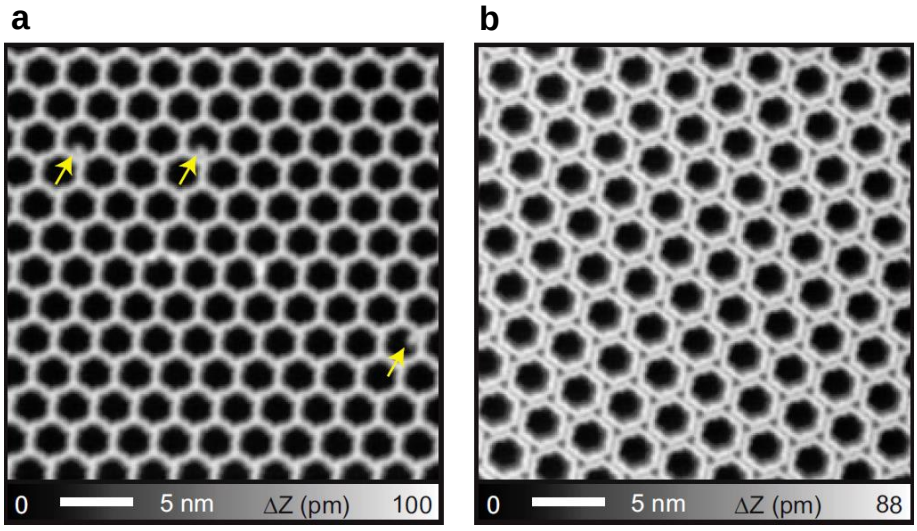

FIGURE 5.12: Network imperfections after array formation. STM topographic images of SW (a) and DW (b) networks simultaneously recorded with the *dI/dV* maps shown in Figure 5.3 (b, c). The yellow arrows mark defects that we assign to possible Br adatoms or excessive Br-DNT at the pore and which modulates its local electronic structure. In (a), only three defective pores out of a total of 132 (2.3%) can be observed. Such amount of imperfections is irrelevant to the ARPES signal.

From 2D Halogen-Bonded Networks to 1D Covalent Polymers

As it has been already mentioned, such halogen-bonded networks are only stable below RT. Above this temperature, the surface catalyzed Ullmann coupling reaction

takes place. Molecules are dehalogenated and a C-C covalent bond is formed, triggering the formation of one-dimensional covalent conjugated polymers on the surface. This effect is illustrated in Figure 5.13 where the SW halogen-bonded network (a) evolves into one-dimensional polymer chains (b) after annealing the sample at 600 K [180, 190].

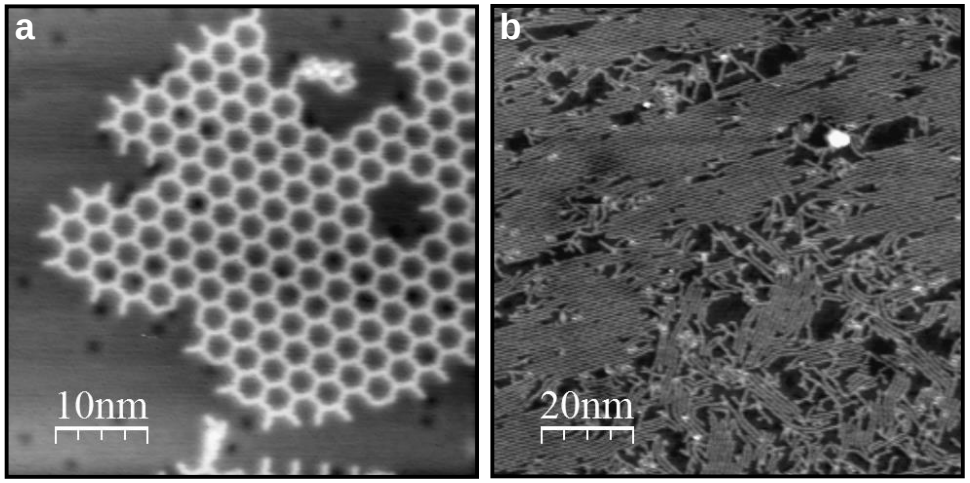

FIGURE 5.13: Halogen bond stabilized 2D nanoporous network transformation to 1D covalent polymers upon annealing to $\sim$ 600 K. (a) 50 x 50 nm^2 STM image showing the SW network configuration. Black spots on the Ag surface correspond to CO molecules. STM parameters: V = 200 mV; I = 50 pA, T= 6.5 K. (b) 100 x 100 nm^2 STM image highlighting the one-dimensional covalent polymer formation. STM parameters: V = 200 mV; I = 50 pA, T= 77 K.

5.4.3 EBEM/EPWE Simulations

The simulations for this chapter have been performed in collaboration with Dr. Zakaria M. Abd El-Fattah (Al-Azhar University, Egypt).

Simulation Procedure

In the following, the EBEM/EPWE simulation procedure is explained step by step: the first step is to parametrize the geometrical structure of the networks that will represent the potential barriers that scatter the 2DEG. The complexity of the geometries can be simplified since the molecular electrostatic clouds, that are responsible for the potential barriers, are generally smooth and relatively featureless. We choose the width and length of the straight beads to match the molecular width (d $\sim$ 5 Å) and the network dimensions. Note that this step of considering the scattering barrier geometry (length and width) as accurate as possible to the STM observations of the backbone dimensions is of key importance for a successful matching and understanding of confinement and coupling effects in such nanoporous systems. After this parametrization, the V_{eff} (scattering potential at the molecules) and m^* parameters

are iterated to fit the experimental data. With V_{eff} the scattering of the surface state with the molecular barriers is defined and both the band bottom ($\overline{\Gamma}$ point in ARPES and onset of bonding state in STS) and opening of the gaps are quantitatively simulated. The effective mass parameter is inversely proportional to the curvature of the band so by varying its value, the top of the band or antibonding state is accurately placed in energy. Note that changes in m^* do not alter significantly the energetic position of the band bottom of the first confined state, but it affects the lower edge of the $\overline{\mathrm{M}}$ point gap or anti-bonding state. This is the reason why we are forced to recurrently use a larger effective mass than for the pristine case in order to fit the ARPES experimental bands [Figure 5.14 (a, b)]. From Figure 5.14 it is evident that when the pristine surface state m^* is used (black curves), the band dispersion strongly deviates from the experimental bands (in yellow). We achieve the best ARPES and STS agreement for the red curve case. Finally, once the iterative fitting is satisfactory for both STS and ARPES matching, the electronic band intensity can also be obtained from EBEM/EPWE (Figure 5.15). The simulations show a very nice agreement with the experimental raw data and the second derivative with replicating bands appearing as weak intensity bands at the second SBZ, similar to Figure 5.5 (e, f).

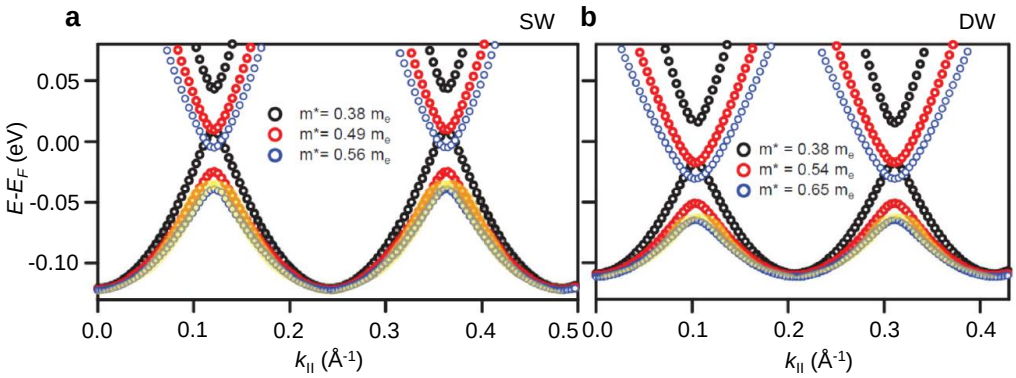

FIGURE 5.14: Influence of the effective mass m^* upon the calculated band structure for the same geometry and molecular potential V_{eff} using EBEM/EPWE. (a) Calculated electronic bands along $\overline{\Gamma\mathrm{M}}$ for the SW geometry using the effective masses of 0.38 m_e (clean substrate case, black), 0.49 m_e (optimal agreement for both ARPES and STS, red), and 0.56 m_e (best fit for only the ARPES data but deviating slightly from the STS, blue). (b) Calculated electronic bands along $\overline{\Gamma\mathrm{M}}$ for the DW geometry using the effective masses of 0.38 m_e (clean substrate case, black), 0.54 m_e (optimal agreement for both ARPES and STS, red), and 0.65 m_e (best fit only for the ARPES data but deviating slightly from the STS, blue). The results of these calculations can be compared with the experimental band structure represented as yellow transparent traces. It is observed that the pristine m^*= 0.38 m_e deviates substantially from the experimental bands and larger effective masses are required to fit all the experimental data. The differences found between the red and blue calculations in (a) and (b) falls practically within the experimental error.

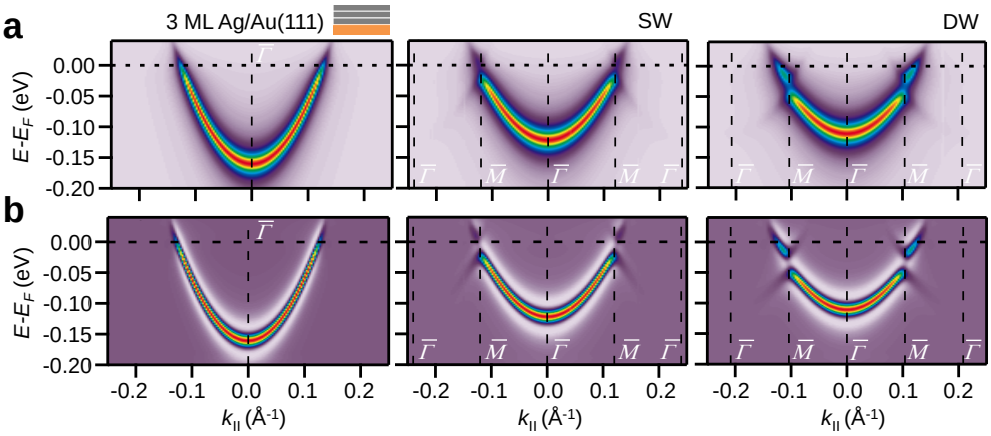

FIGURE 5.15: Electronic band structure simulated by EBEM/EPWE. (a) Simulated ARPES EDCs along $\overline{\Gamma M}$ high symmetry direction for the pristine 3 ML Ag/Au(111), SW and DW cases. Such bands exquisitely agree with the experimental ARPES data shown in Figure 5.5 (a-c). The replicating bands away from the prominent spectral function close to $k_{||} = 0$ can also be nicely seen when the second derivative is taken in (b). However, in the simulations the gap between n=1 and n=2 localized states is better defined than in the experiments (Figure 5.5). The possible reason is the ubiquitous inhomogeneities present when these networks are formed that broadens our experimental spectra, increases the background and washes out the gaps along with the inherent broadening of the bands due to lossy scattering effects and the proximity to the Fermi energy.

5.4.4 *Ab-Initio* Calculations

DFT calculations have been performed by Dr. Ali Sadeghi from Shahid Beheshti University (Iran). The calculations are carried out within the local density approximation of DFT as implemented in the BigDFT code [191]. A wavelet basis set is used to expand the wavefunction of the valence electrons while the core electrons are removed using norm-conserving HGH pseudopotentials [192]. Calculating the electrostatic potential (and the electric field) for a surface system is uniquely precise by the Poisson solver of this DFT code that allows to apply periodic boundary conditions along two in-plane directions while keeping free boundary conditions in the out of plane direction [193].

In the SW molecular network, the structure is stabilized through purely halogen bonding in a trimer configuration [Figure 5.16 (a)] [194]. The halogen atom, when covalently bonded to a molecule, induces an area of positive electrostatic potential on the outermost portion of the atom along the bond axis (σ-hole) [176, 178, 194] [Figure 5.1 (c)], thus stabilizing the network by the attraction between positive and negative electrostatic poles on the Br atoms [Figure 5.16 (a)]. The structure transforms in the DW network as halogen bonding is combined with Br $\cdots$ O bonds generating the double molecular barrier between nanocavities [Figure 5.16 (b)].

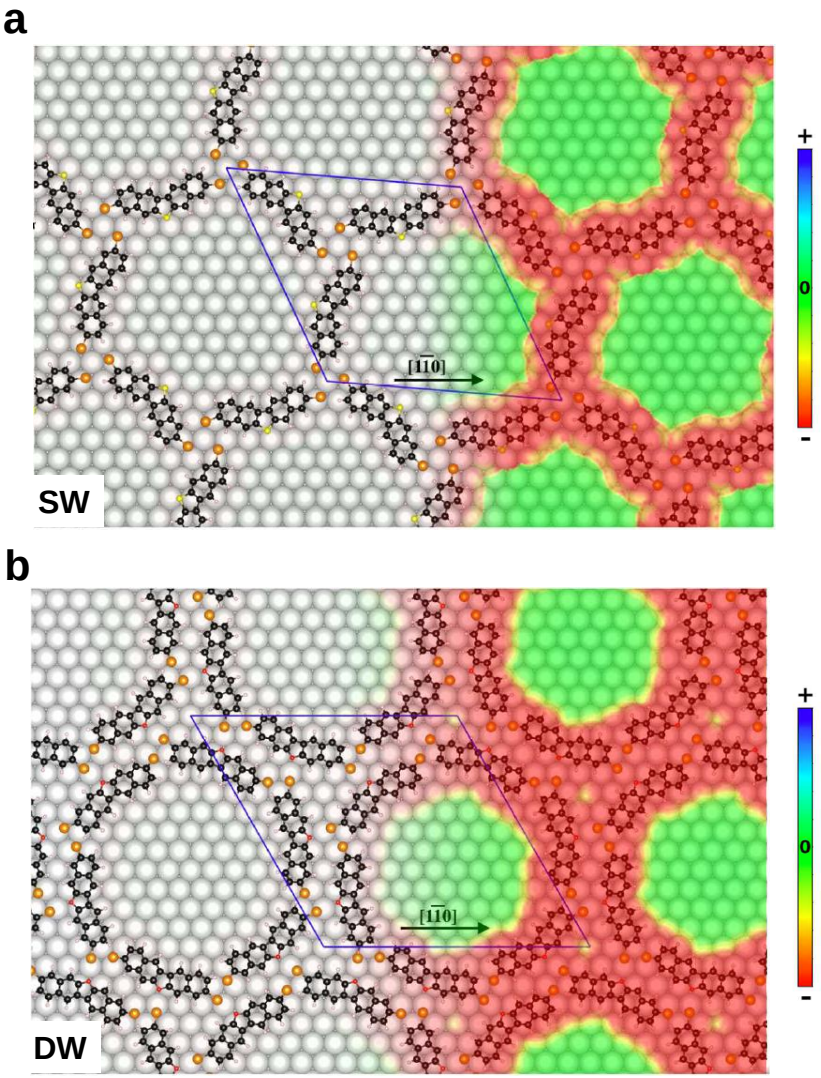

FIGURE 5.16: Models for SW and DW networks on Ag(111). Corresponding models predicted by DFT calculations for the arrangement of the SW (a) and DW (b) halogen based networks on Ag(111). Br atoms are shown in brown, O in red, S in yellow and Ag by large gray spheres. The hexagonal lattice of the DW network matches a (12 x 12) surface unit cell. This results in an inter-pore distance of $12a = 3.45$ nm (a is the Ag-Ag distance) and the molecular layer lattice vector aligns along the [1$\bar{1}$0] direction. Conversely, the hexagonal lattice of the SW network exhibits a $\begin{pmatrix} 10 & -1 \\ 1 & 11 \end{pmatrix}$ surface unit cell concomitant with atomic positions of the Ag substrate and presenting a small angle of 4.7° with the [1$\bar{1}$0] direction. The inter-pore distance in this case is $\sqrt{111}a = 3.03$ nm. The 4 Å difference between the inter-pore distances in the two cases is very close to the width of a molecular unit. Therefore, the size of the nanocavities by SW and DW networks are practically identical. The color maps in (a) and (b) illustrate the distribution of the normal component of electric field E, on a plane 3 Å from the molecular layers (*i.e.* at the position of the metal surface). The plots share the same color scale, where red corresponds to $E < -0.015$ V/Å, blue to $E > -0.015$ V/Å, and green to zero. The local electric field, acting as a scatterer for the surface electrons, becomes significant only underneath the molecular units. The effective geometry and width of the barriers is estimated from these plots. The width per molecular unit turns out to be $d \approx 5$ Å, coinciding with the one used in the EBEM/EPWE models.

Chapter 6

Tunable Energy and Mass Renormalization from Homothetic Quantum Dot Arrays

6.1 Introduction

In this chapter we show that the fundamental energy of confined states within nanoporous networks can exhibit downward shifts from E_F accompanied by a lowering of the effective masses in the presence of small gap openings at zone boundaries. We observe these effects by ARPES in two homothetic (scalable), cobalt coordinated metal-organic arrays obtained by self-assembly on Au(111). Specifically, we find that the effective mass lowering and downward energy shift are gradual, *i.e.* dependent on the network dimensions. Local scanning tunneling microscopy and spectroscopy measurements agree with these findings as evidenced by the gradual downward shift of the density of states onset and the presence of confined states at the nanocavities. EBEM/EPWE simulations, DFT calculations and PAM provide insight into the nature of this phenomenon, which we infer is related to overlayer-substrate interactions in the form of adatom hybridization effects and geometrical variations of the metal-organic assembly.

6.2 Results and Discussion

The studied cobalt coordinated networks are practically homothetic (scalable) and generated from two cyano-polyphenyl precursors deposited on Au(111). Specifically, we used *para*-hexaphenyl-dicarbonitrile (Ph6) and *para*-terphenyl-dicarbonitrile (Ph3) molecules that coordinate with Co atoms in a 3:2 stoichiometry. These tectons are thermally and sequentially evaporated (molecules first, then Co) followed by a mild annealing at 400 K and result in two scalable, periodic, long-range, single domain and practically defect-free QD arrays, as shown in Figure 6.1 (a, e) and named hereafter Ph6Co (top row) and Ph3Co (bottom row). In agreement with previous work [17], these networks present sixfold symmetry with unit cell vectors of 5.78 nm

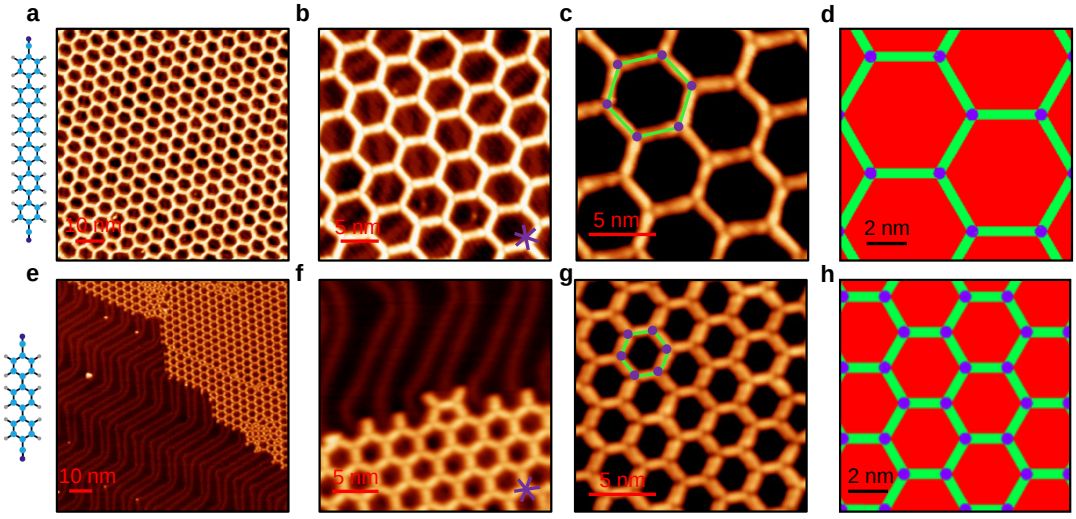

FIGURE 6.1: STM characterization and EBEM/EPWE scattering regions of Ph6Co and Ph3Co QD arrays. (a-c) STM images of Ph6Co network on Au(111). STM parameters: V = -1 V; I = 10 pA, T_{sample} = 77 K. (d) 2D potential geometry used for Ph6Co EBEM/EPWE modelization. (e-g) STM images of Ph3Co network on Au(111). STM parameters: V = -2V; I = 20 pA and T_{sample} = 77 K for (e); V = -1 V; I = 10 pA and T_{sample} = 4.5 K (f, g). (h) 2D potential geometry used for Ph3Co modelization. According to (b, f) both networks grow 30° rotated from the $[1\bar{1}0]$ direction of the surface. The herringbone periodicity is unchanged for both networks (b, f), demonstrating the weak chemical interaction with the Au surface [10, 195].

(for Ph6Co) and 3.53 nm (for Ph3Co) along the $[11\bar{2}]$ direction and, respectively enclose pore areas of 24 nm^2 and 8 nm^2 [Figure 6.1 (c, g)]. Note that the chemical interaction of both networks with the substrate must be rather weak based on the fact that the herringbone reconstruction is not lifted or visually modified [Figure 6.1 (b, f)] [10, 195]. We experimentally probe these networks at two labs, first mesoscopically by means of ARPES (see Section 6.5.1) and then at the nanoscale by means of a STM / STS setup at 5 K (see Section 6.5.2). We shed light on these experimental data by means of EBEM/EPWE simulations, DFT calculations and PAM, all of which are detailed in the Supplementary Information of this chapter (Section 6.5). This work has been done in collaboration with the group of Prof. M. Stöhr (University of Groningen, Netherlands) that performed the LT-STM/STS, Zakaria M. Abd El-Fattah (Al-Azhar University, Egypt) that contributed with the PAM and EBEM/EPWE simulations and the group of Prof. A. Arnau (University of the Basque Country UPV-EHU, Spain) that performed the DFT calculations.

Ph6Co and Ph3Co networks are formed on Au(111), where the surface state onset can be comfortably accessed by ARPES and STS [Figures 6.2 (a), 6.4 (j)]. Nevertheless, obtaining the corresponding QD array band structure by means of ARPES is exceedingly challenging as the networks must be periodic, extended, almost defect-free and fully spread over the probed surface [15, 54]. To achieve such demanding conditions we evaporate the molecules and Co adatoms by creating two orthogonal shallow gradient depositions on a large (15 mm in diameter) circular Au(111)

substrate, ensuring the existence of an area hosting optimal coverage and the exact 3:2 stoichiometry [158]. The sample is then mildly annealed to 400 K in order to improve the quality of the networks formed (see Section 6.5.1 for more details on the preparation process). Figure 6.2 (b, c, e, f) shows the second derivative of the ARPES spectral density from Ph6Co and Ph3Co along the $\overline{\Gamma M}$ and $\overline{\Gamma K}$ high symmetry directions. The dispersion intensities and zone boundary gaps vary depending on the SBZ direction followed and the size of the QDs [Figure 6.2 (d)]. We unambiguously observe a gradual downshift of the fundamental energy ($\overline{\Gamma}$ point) towards higher binding energies as the pore size is reduced, which can be quantified in the normal emission EDCs (Fig. 6.2 (g) and Table 6.1). Note that this goes in the opposite direction to the energy shift expected from conventional lateral confinement scenarios [18, 97, 98]. Simultaneously to this downshift, we observe a reduction in the effective mass (Figure 6.2 (i) and Table 6.1), leading to an effective 2DEG Fermi wave-vector (k_F) pinning [Figure 6.2 (h)]. The partial confinement of the substrate's 2DEG is inferred from the presence of small gaps (observed as slight intensity variations) at the symmetry points, which denotes weak scattering from the network molecular barriers [157]. Note that the absence of spin-orbit splitting in our data when the networks are present on the surface, in no way outrules this effect, as it could be masked by intrinsic broadening of the ARPES lineshape [157, 173, 196].

To find out the surface potential landscape that the networks generate to the 2DEG, we perform EBEM/EPWE simulations. Firstly, the geometry of both systems [Ph6Co and Ph3Co in Figure 6.1 (d, h)] is generated following STM images [see Figure 6.1 (c, g)], assigning two repulsive scattering potential sites: $V_{mol} = 250$ meV for molecules (in green) and $V_{Co} = 50$ meV for the Co regions (in purple). For more details on the scattering potential landscape assignment see Section 6.5.4 and Chapter 7. Such potentials perfectly reproduce the experimental band dispersion and energy gaps (~ 25 meV for Ph6Co and ~ 30 meV for Ph3Co at $\overline{M}$), reflecting the weak scattering strength (second Fourier component) of the networks [cf. superimposed red bands in Figure 6.2 (b, c, e, f)]. However, repulsive scattering is known to shift upwards the 2DEG fundamental energy (at $\overline{\Gamma}$), opposite to what is observed here. Thus, the ARPES dispersions can only be matched by EBEM/EPWE

TABLE 6.1: ARPES experimental binding energies at $\overline{\Gamma}$ and effective masses (columns $E_B^{\overline{\Gamma}}$ and m^*/m_0) for the substrate and the two networks. Matching the network band structures by EBEM/EPWE simulations demands downshifting the SS references accompanied by a reduction of the effective masses with respect to the Au(111) Shockley state (columns $E_{EBEM}^{Ref,\overline{\Gamma}}$ and $m_{EBEM}^{*,Ref}/m_0$).

	$E_B^{\overline{\Gamma}}$ (eV)	m^*/m_0	$E_{EBEM}^{Ref,\overline{\Gamma}}$ (eV)	$m_{EBEM}^{*,Ref}/m_0$
Au(111)	0.45	0.255	0.45	0.26
Ph6Co	0.49	0.24	0.52	0.24
Ph3Co	0.55	0.22	0.59	0.21

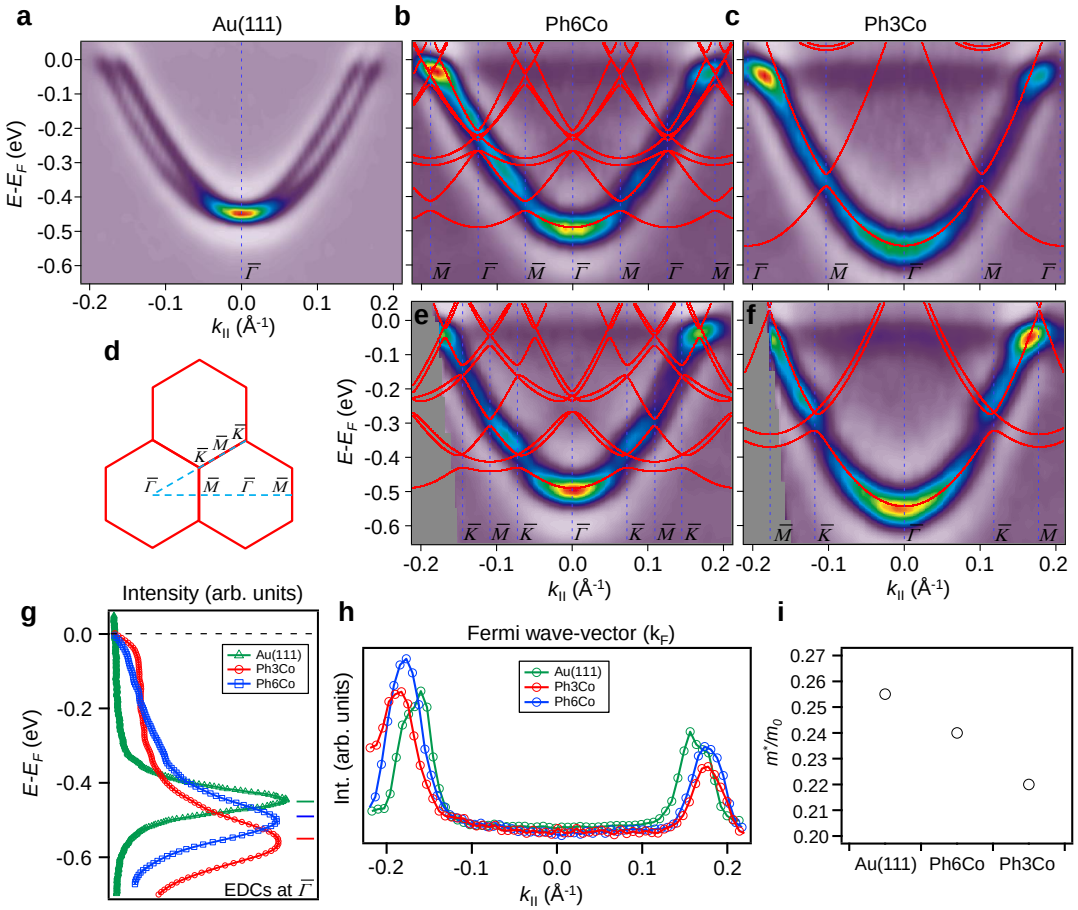

FIGURE 6.2: Ph3Co and Ph6Co electronic band structure studied with ARPES. (a) Electronic structure of the Au(111) Shockley state, highlighting its well-known spin orbit splitting. ARPES spectral density obtained along $\overline{\Gamma M}$ (b, c) and $\overline{\Gamma K}$ (e, f) high-symmetry directions for both Ph6Co and Ph3Co nanoporous networks. The EBEM/EPWE simulated band structure appears superimposed in red, showing nice agreement with the intensity modulations, gaps and replicating bands. (d) Reciprocal space directions followed along the new SBZ originated by the nanoporous networks. (g) EDCs at normal emission ($\overline{\Gamma}$ point) for pristine Au(111) (green), Ph6Co (blue) and Ph3Co (red). A gradual downshift of the fundamental energy as the pore size is reduced (ΔE_{Ph6Co} = 40 meV and ΔE_{Ph3Co} = 100 meV with respect to the Au SS) is observed. (h) Fermi wave-vector (k_F) features are plotted for both Ph3Co (red) and Ph6Co (blue) networks and compared to the pristine Au surface state (green). (i) The effective mass reduction tendency as the pore size decreases (from Ph6Co to Ph3Co). ARPES measurements are shown in second derivative (T_{Sample}= 150 K).

when adopting higher binding energy references and smaller effective masses than the pristine Au(111) SS (Table 6.1). In other words, the original 2DEG of the Au(111) surface fails when used as scattering reference for both these networks. Figure 6.3 (a, b, d, e) summarizes the EBEM/EPWE simulated band structures, which match the experimental findings of the gradual downward energy shift from Ph6Co to Ph3Co in Figure 6.3 (c) and the effective Fermi wave-vector (k_F) pinning with respect to the pristine Au(111) in Figure 6.3 (f).

Before exploring these 2DEG reference shifts in more detail by using local spectroscopic techniques (STM/STS), we should verify that these networks confine the

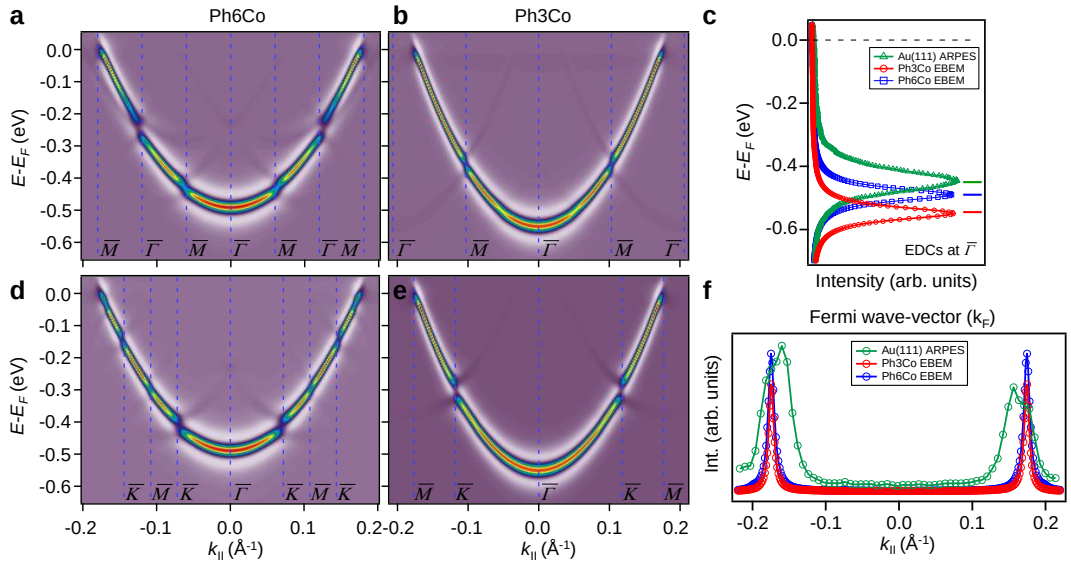

FIGURE 6.3: Ph6Co and Ph3Co EBEM/EPWE simulated bands in second derivative. The $\overline{\Gamma M}$ high-symmetry direction is shown in (a, b) while $\overline{\Gamma K}$ in (d, e). The gradual downward shift is corroborated by the EDCs at $\overline{\Gamma}$ (c) and k_F pinning in (f). For the latter two cases (c, f) the pristine Au(111) ARPES data is shown as a reference.

Au SS. We do this for Ph6Co network expecting the same behavior for Ph3Co [17, 166]. Figure 6.4 (a) (middle) shows two position dependent experimental conductance (dI/dV) spectra for Ph6Co, one located at the pore center (C) and the other halfway (H) (see inset). The lineshapes together with the differential conductance maps in Figure 6.4 (b - e) exhibit clear confinement eigenstates [15–17, 53, 54, 166]. Note that for ascending energies a transition from the n=1 confined state to the higher order confined states (n = 2, 3 and 4) is observed. This electron localization mirrors the one observed for the same network on Ag(111) [17, 166]. To compare them directly we must adapt the reported dI/dV spectra of ref. [17] by normalizing the energy axis by the ratio of their corresponding effective masses ($m^{*,Ph6Co}_{Ag}/m^{*,Ph6Co}_{Au} = 0.41/0.24$) and shifting the onset to the Au reference (-485 meV at 5 K). The agreement (lineshape and peak energies) between the two datasets is satisfactory [cf. middle and top of Figure 6.4 (a)], proving that these 2DEGs are similarly confined by Ph6Co on both Ag(111) and Au(111). The expected confined state energy variation with the reduction in pore size (from Ph6Co to Ph3Co) is summarized in Section 6.5.3, also agreeing with previous observations of Ph6Co and Ph4Co on Ag(111) [17].

Once confinement is demonstrated, we can address the 2DEG reference shift upon network formation using local techniques. Prior to this, we recall from the previous chapter that fundamental energies of QD arrays (LDOS onset) are inherently ill-defined by STS. The reason is that the dI/dV lineshapes of partially localized states are broad (by the interdot coupling) and quite asymmetric (the maxima are displaced towards higher energy). Figure 6.4 (j), shows *dI/dV* blow-ups at the pore center of the two, Ph3Co and Ph6Co networks and of the Au SS as reference.

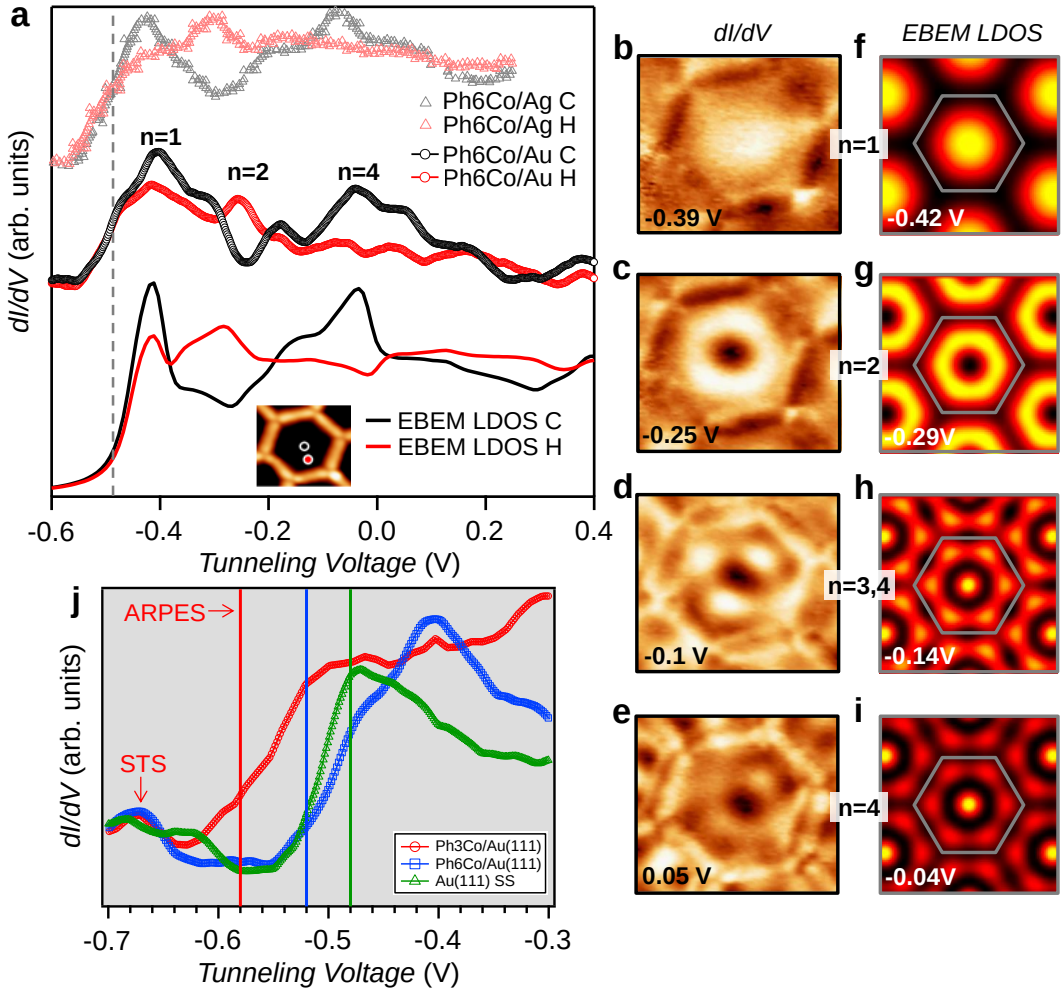

FIGURE 6.4: Ph6Co confinement effects and downward shift observed by STM/STS. (a) *dI/dV* spectra at the pore center (C, black) and halfway (H, red) for three Ph6Co datasets (see inset): Experimental conductance of this network on Au(111) (middle), corresponding EBEM/EPWE conductance simulations using the ARPES parameters (bottom), and experimental spectra of Ph6Co on Ag(111) adapted from ref. [17] and normalized to Au(111) (top). Each spectrum is made up of the characteristic confined states that alternate depending on the wavefunction spatial distribution, *i.e.* $n = 1$ and $n = 4$ peaks at the pore center spectrum and $n = 2$ and $n = 3$ in the halfway one. (b - e) Experimental *dI/dV* maps reproducing standing wave patterns of the different energy levels n showing reasonable agreement with the EBEM/EPWE simulated ones at similar energies (f - i). (j) Zoom-in onto the experimental *dI/dV* onset for the pristine Au(111) SS (green), Ph6Co network (blue) and Ph3Co (red) probed at the center of the pores. A gradual downshift of the fundamental energy is observed as the pore is reduced, agreeing with the ARPES data of Figure 6.2 (g). The ARPES energetic position is indicated by the vertical lines (temperature corrected by 30 meV).

For Ph3Co (in red) the LDOS onset is clearly away from the Au SS, whereas for Ph6Co (in blue) is much closer to it. In the latter case, we could simulate and match the experimental conductance spectra and maps [Figure 6.4 (a, f-i)] using the same scattering parameters and effective mass reduction as for fitting the Ph6Co ARPES bands [Figure 6.2 (b, e)]. In these LDOS maps we observe slight discrepancies for the higher energy maps [Figure 6.4 (h, i) vs Figure 6.4 (d, e)], which we ascribe to

weak potential variations introduced by the herringbone reconstruction. Indeed the Ph6Co unit cell (5.78 nm) is large enough to host both fcc and hcp regions within a single pore, which was not accounted for in the EBEM/EPWE simulations. Such slight variations become evident as higher energies are probed.

In essence, the STS shifts qualitatively agree with the ARPES results, as observed in Figure 6.4 (j) (vertical lines), supporting a change of the 2DEG reference upon the metal-organic nanoporous network presence on the surface. We believe that subtle downward energy shifts, such as the ones present in Ph3Co and Ph6Co, may also exist in other published metal-organic networks [17, 166, 182], but become practically undetectable unless STS measurements are complemented with photoemission experiments that can unambiguously define the reference substrate energy for the QD array (see Section 6.3).

Many factors might be responsible for these counterintuitive, downward energy shifts set by the 2DEG reference modification. Likely, it can be attributed to general overlayer-substrate interactions in the form of charge transfer (doping effects), hybridization effects with metal adsorbates or geometrical variations (overlayer-substrate distance) that may renormalize the surface state band. As the shift is gradual, being larger for Ph3Co than Ph6Co, and the networks are homothetic, it could be induced by charge transfer from the Co adatoms (in numbers ranging from 0.015 monolayers (ML) to 0.005 ML) to the Au SS, similar to the downshift induced by alkali metals [197]. However, the fact that m^* decreases such as to keep the Fermi wave-vector (k_F) practically pinned suggests unaltered occupancy of the 2DEG (the electron density n is directly related with k_F by $n = \frac{k_F^2}{2\pi}$) [126, 198].

To examine the possible Co/Au hybridization, we have performed DFT calculations of Co atom arrays onto a non-reconstructed Au(111) surface. Figure 6.5 (a) shows the calculated band structure from two selected supercells: the 2×2 (0.25 ML of Co) on the left and the 3×3 (0.11 ML of Co) on the right. These superstructures introduce an evident difference in the folding of the Au bands (in black), but more importantly, a clear downshift of the pristine Au SS (in red). We find that the magnitude of such downshift is directly related to the amount of isolated Co adatoms on the surface (Table 6.2). The actual experimental Co coverage is much lower by about an order of magnitude, the main consequence being that the corresponding shift is of the order of 50 meV, comparable to the experimental observations. We assign this effect to a coupling (hybridization) between the Co 3*d*-bands [indicated in blue in Figure 6.5 (a)] with the Au(111) SS [140, 198]. The effect of a Co network (without molecules) on the Au SS cannot be tested with ARPES, since at low coverages Co atoms aggregate forming clusters at herringbone elbows [199, 200], inducing, in fact, the opposite energy shift of the Au SS [Figure 6.6 (a)]. Figure 6.6 (b, c) show a similar effect with increasing Ph3 and Ph6 coverages, respectively.

In addition to the aforementioned effects, that is, pure charge transfer and

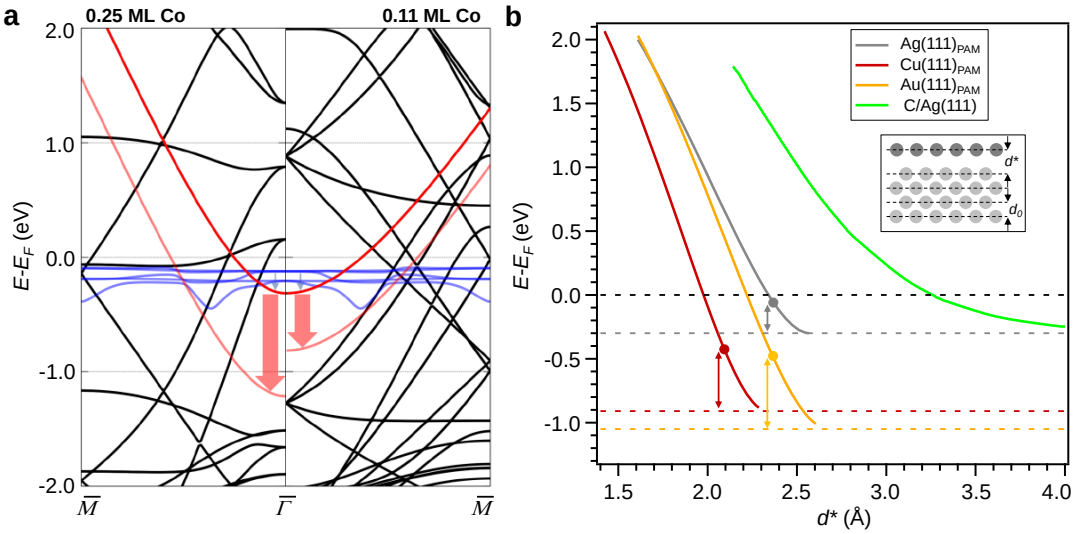

FIGURE 6.5: DFT and PAM simulations on hybridization and overlayer height effects on the 2DEG reference. (a) Visualization of the Au(111) surface state (red curve with parabolic dispersion centered at $\overline{\Gamma}$) downward energy shift at two different Co coverages. The left panel corresponds to 0.25 ML and the right panel to 0.11 ML, as obtained using a 2x2 and a 3x3 surface unit cell, respectively. The different supercells introduce an evident difference in the folding of the Au bands. The blue curves near the Fermi level correspond to Co 3*d*-bands. (b) Effect of the overlayer distance on the 2DEG reference for the three (111) noble metal surfaces studied using PAM. The full colored dots (red, orange and gray) indicate the pristine SS bottom energy and the arrows indicate the maximum downshifts that depend on the projected bulk gap position. On the other hand, the rightmost green curve is obtained from the model developed for studying the influence of an organic overlayer on the Ag(111) SS, starting from a neutral overlayer distance of ~ 3.2 Å (adapted from ref. [201]).

hybridization effects, other mechanisms could also be considered. In particular, geometrical variations of the overlayers (vertical displacements) are also known to affect the SS reference [122, 123]. Specifically, molecular assemblies generally tend to increase their separation to the surface when they form metal-organic assemblies (adatoms embedded into the structures) [167, 202, 203]. Accordingly, two different models (one based on the PAM for metallic overlayers [122, 123] and the other

TABLE 6.2: Energy shift of the Au(111) SS with Co adatom concentration and array size obtained from our DFT calculations. The Co adatoms relax ~ 2.5 Å above the unreconstructed Au(111) surface. The calculations show an increasing downward shift of the SS with Co content. Note that the experimental amounts of Co used are significantly lower, corresponding to 0.015 ML for Ph3Co and 0.005 ML for Ph6Co (very diluted).

Co concentration	Array size	ΔE_{SS} (eV)
0.25 ML	2×2	-0.94
0.17 ML	3×2	-0.7
0.11 ML	3×3	-0.49
0.08 ML	3×4	-0.54

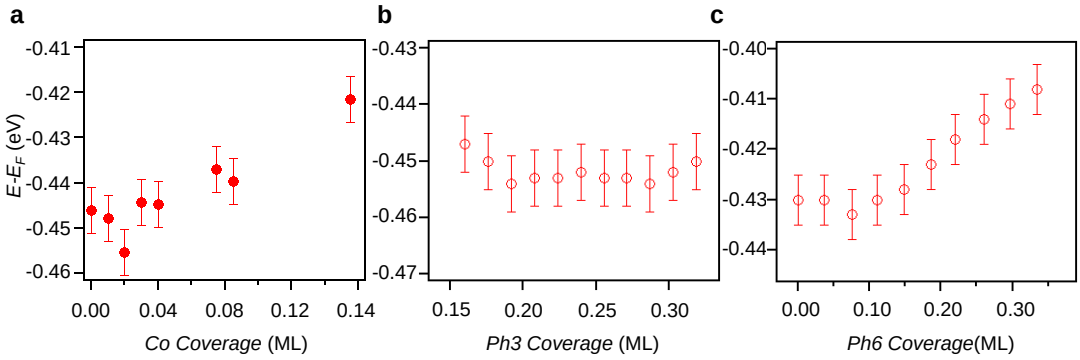

FIGURE 6.6: Gradual band bottom energy shift of Au(111) SS upon Co, Ph3 and Ph6 gradient depositions. (a) (E vs $Coverage$) plot shows a tendency of the Au SS to shift towards the Fermi level as the Co deposition is increased. For the diluted amount of Co required for both Ph3Co and Ph6Co network formations, the surface state remains unaltered within the experimental error. (b, c) (E vs $Coverage$) plots for Ph3 and Ph6 gradient depositions respectively. For both cases, at low coverages the surface state remains energetically unchanged and gradually shifts towards the Fermi level, which is more clearly observed for Ph6.

for molecular overlayers [201]), show that significant energy downshifts are also possible whenever the metal/molecule overlayer-surface distance increases [Figure 6.5 (b)]. For instance, for the Ag(111) case (in grey), when an Ag overlayer is positioned at a distance ($d^* \sim 2.3$ Å, inset), the Ag SS remains at its original energy (grey dot). As the overlayer is lifted up from the surface ($d^* > 2.3$ Å), the Ag SS shifts its reference to lower energies until it meets with the projected bulk band position (horizontal dashed grey line). The same mechanism holds for Au(111) and Cu(111) (see Section 6.5.5 for more details). Besides, if an organic overlayer, such as graphene on Ag(111) is considered, a similar behavior is predicted (green curve) [201]. As the organic layer is lifted up from the surface (beyond ~ 3.2 Å), the Ag SS shifts downwards in energy. Similarly, we speculate that subtle vertical increments in both of our networks could be another plausible reason behind the observed counterintuitive Au surface state renormalization.

6.3 Corroboration of 2DEG Renormalization in Other MOCNs

In an attempt to extend the previously observed 2DEG renormalization effects, we grow a similar metal-organic nanoporous network to Ph3Co and Ph6Co using single Cu atoms as coordination. For such purposes, in collaboration with the group of Prof. N. Lin (The Hong Kong University of Science and Technology, China), we chose TPyB (1,3,5-tri(4-pyridyl)-benzene) since we judged it could form a long-range ordered metal-organic film on Cu(111) [154, 182] [Figure 6.7 (a)]. After molecules are deposited on the surface following a wedge evaporation, the sample is post-annealed to 420 K to improve the formation of the nanoporous network. When the film is saturating the surface, a single domain and long-range ordered phase is observed in STM and LEED, which corresponds to a nanoporous network with 2.65 nm periodicity and a $6\sqrt{3} \times 6\sqrt{3}$ R30° superstructure [Figure 6.7 (b, c)].

This long-range ordered nanoporous film provides exceptional QD bands when probed by ARPES: i) the Cu(111) Shockley state [Figure 6.7 (d)] shifts significantly to higher binding energies, ii) clear replicas appear away from the main intensity when following $\overline{\Gamma M}$ and $\overline{\Gamma K}$ high symmetry directions of the hexagonal SBZ that originate from the nanoporous overlayer [Figure 6.7 (e, f)]. Indeed, EDCs at $\overline{\Gamma}$ show a $\sim$ 70 meV shift of the band bottom (fundamental energy) to higher binding energies [Figure 6.7 (g)]. In addition, the Fermi wave-vector (k_F) seems practically unaffected, evidencing that such a downward shift is not caused by charge transfer effects [Figure 6.7 (h)]. Finally, photoemission observations are complemented by LT-STS (5 K) measurements performed at the pore center of the network [Figure 6.7 (i)]. The onset of the Cu SS shifts $\sim$ 70 mV to higher binding energies, in total agreement with ARPES results (dashed vertical lines). Note that this observation contrasts with the electronic properties reported for this nanoporous network in ref. [154], where an opposite shift of the fundamental energy was claimed. The reason for such discrepancy is that the fundamental energy of partially localized states in STS was positioned at the top of the asymmetric peaks instead of choosing its lowest energy onset (see Chapter 5).

With this observations we unambiguously find that the surface state renormalizes by shifting its energy to higher BEs upon the formation of certain metal-organic coordination networks on surfaces. We have identified such effect in single metal atom coordination networks, in particular: Ph3Co and Ph6Co on Au(111), Ph4Co and Ph6Co on Ag(111) [17], Ph5Cu on Cu(111) [166], Cu-TPyB and Cu-ExtTPyB [154]. Note that the most evident energy shifts are detected for the smallest pores, *i.e.* the larger amount of single coordination metal atoms.

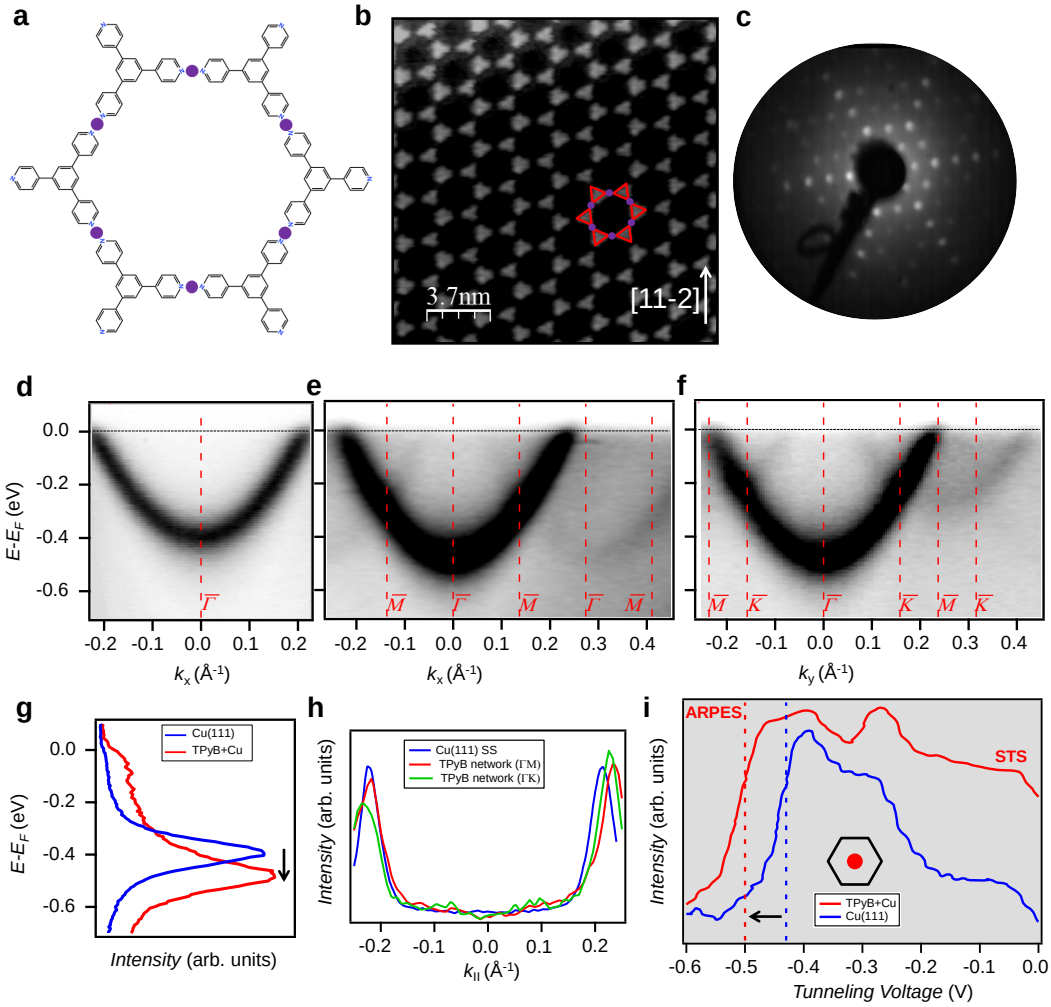

FIGURE 6.7: Cu-TPyB network on Cu(111): growth and electronic properties. (a) Schematic drawing of the Cu-TPyB network where Cu coordination atoms are shown in purple. (b) STM image shows the long-range ordered formation, in agreement with ref. [154]. STM parameters: $V = 1$ V; $I = 100$ pA. (c) LEED pattern showing the $6\sqrt{3} \times 6\sqrt{3}$ R30° superstructure of the network (LEED energy = 19 eV). (d) Electronic ARPES band structure of the pristine Cu(111) and the network modulated 2DEG along $\overline{\Gamma M}$ (e) and $\overline{\Gamma K}$ (f) high-symmetry directions . (g) EDCs at the $\overline{\Gamma}$ point showing a shift of the fundamental energy of 70 meV to lower energies for the network. (h) Fermi wave-vector (k_F) measurements for the pristine Cu SS and network. (i) Experimental *dI/dV* onset for the pristine Cu SS (blue) and partially localized state at the pore center of the network (red). The vertical dotted lines mark the position of the ARPES band bottom.

6.4 Conclusions

In summary, ARPES and STS results evidence a gradual energy and mass renormalization of the Au(111) SS upon formation of two homothetic Co-coordinated metal-organic networks (Ph3Co and Ph6Co). EBEM/EPWE simulations could match the experimental data only after the 2DEG reference is shifted to higher binding energies. Notably this downshift is gradual with decreasing pore size and occurs in spite of the demonstrated confining attributes of the nanocavities. Our EBEM/EPWE simulations can satisfactorily match our experimental data by means of weakly repulsive potentials for molecules and Co atoms. Overlayer-substrate vertical interactions must be responsible for these effects on the Au SS reference. Our DFT calculations and PAM simulations help us to disentangle possible mechanisms responsible for these downshifts, where Au SS-Co adatom hybridization and Co/molecule vertical displacements appear as the most plausible causes. Whatever the reason may be, we hereby demonstrate that the effect of the 2DEG renormalization is a rather general effect for certain single metal atom coordinated nanoporoous networks.

6.5 Supplementary Information for This Chapter

6.5.1 Sample Preparation for ARPES

A circular 15 mm Au(111) sample was *in situ* prepared using standard sputtering and annealing cycles in the preparation chamber (base pressue $\sim 2 \times 10^{-10}$ mbar). Ph3 and Ph6 molecules were evaporated from a Knudsen cell-type home-built crucible evaporator at 510 K and 670 K respectively. The pressure in the preparation chamber was kept below 10^{-9} mbar with the sample at 150 K. The molecular deposition was calibrated then by measuring the onset of the Au SS in ARPES. The Au SS tends to broaden and shift towards the Fermi level as the molecular coverage is increased and it can even quench for close to 1 ML coverages. This trend is illustrated in Figure 6.6. Since the formation of Ph3Co and Ph6Co requires a particular 3:2 stoichiometry (molecule/Co), the Co deposition was performed after the molecular vertical gradient deposition using a commercial metal evaporator with a Co rod. For the latter case, the gradient was performed in the horizontal axis (orthogonal to the molecular one). Then the sample was slightly annealed to 400 K in order to enhance the surface mobility of Co and molecules and promote the coordination. Once the right coverage was calibrated, we measured the ARPES bands looking for the key features of a partially confined 2DEG, *e.g.* shift of the band bottom (generally with molecular overlayers towards the Fermi level), opening of gaps at zone boundaries (depends on the lateral scattering strength), changes in the dispersion and replicating bands due to the superperiodicity of the newly formed SBZ.

6.5.2 STM/STS Measurements

The experiments were carried out within the group of Prof. Meike Stöhr (University of Groningen, Netherlands) in a two-chamber UHV system (base pressure of 4×10^{-11} mbar) housing a commercial LT-STM instrument (Scienta Omicron GmbH). The Au(111) substrate was cleaned by repeated cycles of Argon ion sputtering followed by annealing at 800 K. The Ph3 (Ph6) molecules were heated to 445 K (550 K) inside a commercial molecule evaporator (OmniVac) and deposited onto the Au(111) substrate held at room temperature. The Co atoms were deposited with an electron beam evaporator (Oxford Applied Research Ltd). STM measurements were performed at both 77 K and 4.5 K with a mechanically cut Pt/Ir wire in constant current mode. All bias voltages are given with respect to a grounded tip. The STM images were processed with the WSxM software [174]. STS measurements were performed at 4.5 K by using a lock-in amplifier (typical modulation parameters used: amplitude of 10 mV (rms) and frequency of 677 Hz).

6.5.3 Confined State Tunability with Pore Size

In addition to the gradual renormalization process observed for Ph6Co and Ph3Co networks on Au(111), confined state tunability with pore size should also be expected, as already reported in [17]. Figure 6.8 summarizes such confined state tunability, which is best illustrated in the EBEM/EPWE simulated LDOS curves and maps. While in Ph6Co the experimental and EBEM/EPWE LDOS curves clearly show the appeareance of confined state peaks, Ph3Co shows flatter spectra, making the experimental observation of such localized states more difficult. This happens because gaps between states are more separated in energy for the smaller pore (Ph3Co) than for Ph6Co, thus, DOS features become more planar. As the pore size in enlarged (Ph6Co), confined states pile up in a smaller energy range and become more visible [17, 133, 166].

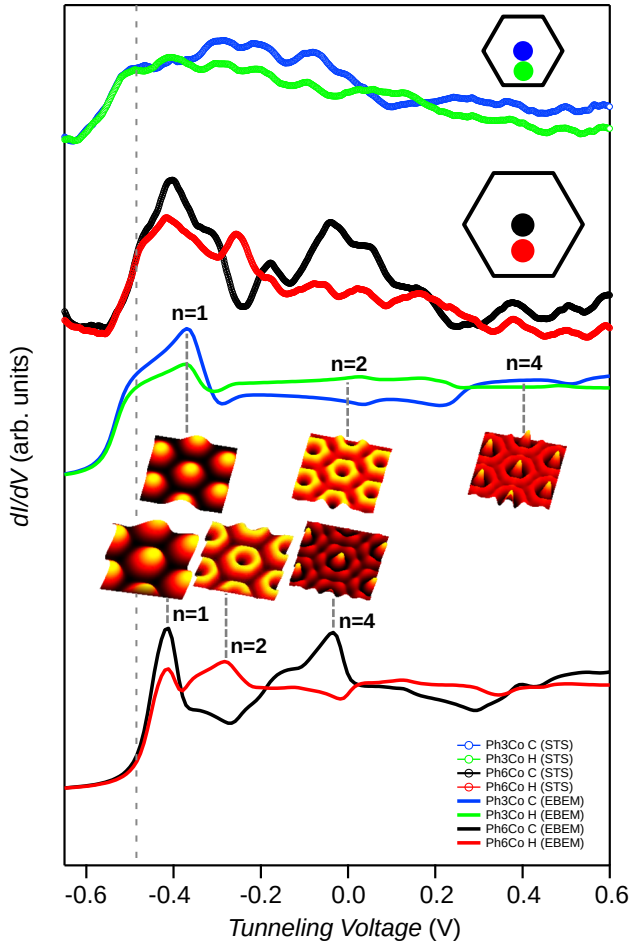

FIGURE 6.8: Ph6Co and Ph3Co confined state energy tunability is illustrated by comparing STS spectra and EBEM/EPWE simulated LDOS. Confined states are better defined and observed for the largest pore size, Ph6Co. For the Ph3Co case, the DOS adopts a much flatter configuration due to the wider energy separation between energy gaps. However, EBEM/EPWE simulated spatial LDOS maps clearly show that confined states are sensitive to the pore size, spreading more in energy for the Ph3Co case than the Ph6Co case.

6.5.4 EBEM/EPWE Simulations

For the band structure and LDOS simulations it is very important to follow the geometry of the scattering barriers. The periodicity of the networks (3.53 nm for Ph3Co and 5.78 nm for Ph6Co) and size of molecules (5 Å width) are used in order to build the geometry in EBEM/EPWE (Figure 6.1). Then a repulsive scattering potential is assigned to the molecular region ($V_{molecule}$ = 250 meV). Note that in ref. [17], a higher repulsive potential was used (V = 500 meV) with a narrower molecular width (2.5 Å) but still yielding the same $V \cdot d$ effective potential. In addition, we keep the scattering potential at the Co sites as slightly repulsive (V_{Co} = 50 meV), contrarily to previous published works [16, 17, 129]. The reason for this is that the assigment of an attractive character to the Co region has never been clarified in previous works, hence, we challenge such an assumption. Indeed, we systematically change the scattering potential landscape of Ph6Co (Figure 6.9) in four different scenarios: Ph6 molecules and Co region with the same repulsive scattering character and amplitude [Figure 6.9 (a, e)], Co regions with a less repulsive character than the Ph6 molecules [Figure 6.9 (b, f)], repulsive scattering character for Ph6 and slightly attractive for Co as in ref. [17] [Figure 6.9 (c, g)] and the same attractive scattering potential amplitudes for both Ph6 molecules and Co regions [Figure 6.9 (d, h)].

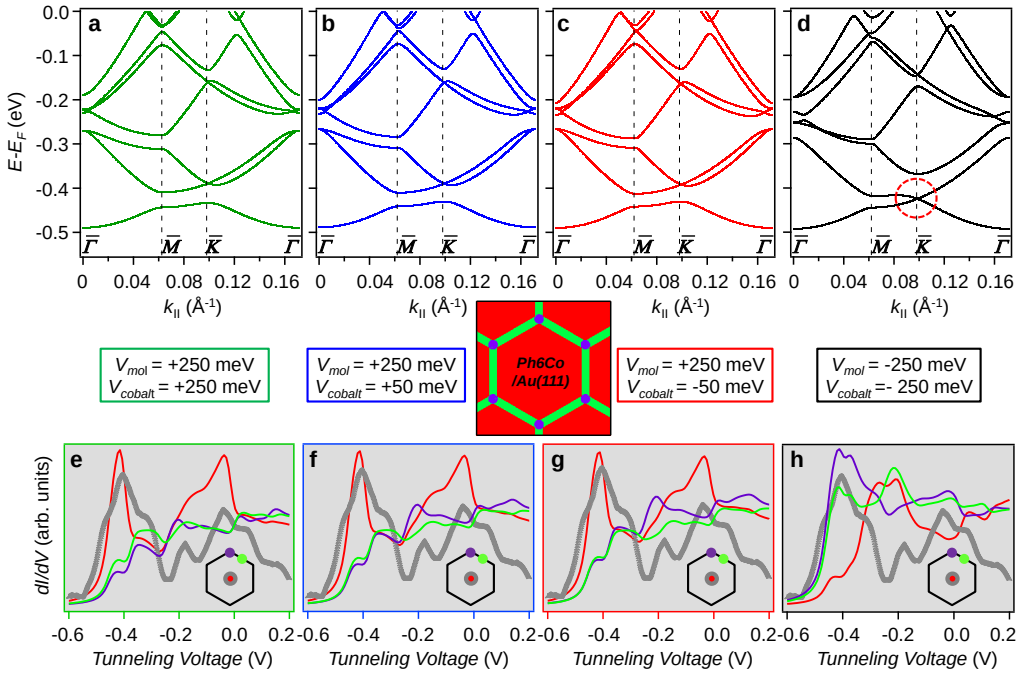

FIGURE 6.9: EBEM/EPWE band structure and LDOS simulations on Ph6Co using four repulsive/attractive potential combinations. (a-d) Band structure simulations for different scattering potentials (V_{mol} and V_{cobalt}). (e-h) LDOS simulations at different positions [pore center (red), molecule (purple) and cobalt (green)] using the same scattering potentials as in (a-d). The experimental spectrum at the pore center (in grey) is to be compared with the red LDOS.

The electronic band structure for the first three cases are identical [Figure 6.9 (a, b, c)] and no effect is observed by changing the scattering character of the Co region from the expected repulsive character to the attractive one. LDOS simulations in Figure 6.9 (e, f, g) also nicely match the experimental findings at the pore center (compare red spectrum with experimental gray one). In addition, spectral features at the Ph6 molecular backbone (in green) and in the Co region (in purple) are practically identical, coinciding with the experimental observation reported in ref. [17]. Finally, we consider a totally attractive scattering barrier situation [Figure 6.9 (d, h)]. For this particular case, we immediately observe that the $\overline{\mathrm{K}}$ point gap in the electronic band structure is closed (dashed red circle), resembling a graphene-like behavior. This can be explained with an inversion of the scattering barrier in the molecular honeycomb lattice. While for the previous three examples, surface electrons are scattered by molecules and Co atoms, which act as barriers, now the situation is reversed, electrons are delocalized trough the molecule and Co regions (in green and purple) and are scattered by the Au surface (red region). This situation resembles an artificial graphene structure, a situation that has been already experimentally studied [204] and recently used in order to model graphene-like structures by EPWE [34]. Such a scattering barrier inversion also produces clear effects on the LDOS at the pore center, where the red spectrum no longer matches the experimental observations [Figure 6.9 (h)].

All the aforementioned observations guide us towards considering both molecular and metal coordination regions as repulsive scattering potentials, finding no evidence for assigning an attractive character to the cobalt region. These observations are further discussed and supported in Chapter 7, concluding that both molecules and coordination metal atoms represent repulsive scattering potentials (barriers) for surface electrons.

6.5.5 The Phase Accumulation Model

The phase accumulation model provides a good estimate of the surface state energies by setting the constrain on the total phase accumulated by electrons reflected at the crystal (Φ_C)-vacuum (Φ_B) interface to produce constructive interference. That is:

$$\Phi_C + \Phi_B = 2\pi n \tag{6.1}$$

where n is an integer and $n = 0$ is a solution for surface states [205]. The empirical energy-dependence forms of Φ_C and Φ_B are [205, 206]:

$$\Phi_C = 2\arcsin\sqrt{\frac{E - E_L}{E_U - E_L}} \tag{6.2}$$

and

$$\Phi_B = \pi\left(\sqrt{\frac{3.4\ eV}{E_V - E}} - 1\right) \tag{6.3}$$

where E_L, E_U and E_V, are the lower and upper edges of the crystal bulk gap along ΓL direction and the vacuum energy, respectively, and their reported values for the three noble metals are given in Table 6.3.

TABLE 6.3: The parameters used in PAM calculations. Values have been taken from ref. [124].

	E_L (eV)	E_U (eV)	E_V (eV)	d_0 (Å)
Ag(111)	-0.30	4.00	4.70	2.361
Cu(111)	-0.91	4.25	4.94	2.087
Au(111)	-1.05	3.50	5.30	2.361

The vertical displacement of the outermost surface layer ($d^* = d_0 \pm \Delta d$), when considered [see inset in Figure 6.5 (b)], contributes a new phase (Φ^*) which is acquired by electrons traveling the corresponding optical path [207, 208]. In this case, the form of the accumulated phase can be written as:

$$\Phi_C + \Phi_B + \Phi^* = 2\pi n \tag{6.4}$$

where $\Phi^* = 2k_\perp d^*$ considering the outermost layer as a quantum well, and $k_\perp$ stands for the electron momentum perpendicular to the surface [207, 209]. Assuming $k_\perp$ equals to the fundamental π/d_0 wave-vector, for the neutral interplanar distance (d_0), $\Phi^* = 2\pi$, implying that the solution for the surface state is found at $n = 1$. The value of d_0 for the three noble metals is given in Table 6.3. Solving Equation 6.4 for different d^* we obtain the surface state energy as a function of the vertical displacement of the metallic overlayer, as shown in Figure 6.5 (b) for the three noble metals. Indeed, for $d^* > d_0$ the surface state shifts downwards until it meets the lower edge

of the projected bulk bands. For $d^* < d_0$, on the other hand, the surface state shifts to higher energies.

6.5.6 DFT Calculations

Density functional theory calculations have been performed by Prof. A. Arnau and I. Gallardo (CFM, Spain) using the VASP code [210–212]. The interaction of the valence electrons with the ion cores was described with the projector augmented wave method (PAW) and the Perdew-Burke-Ernzerhof [213] exchange-correlation functional was used. An energy cutoff of 300 eV in the plane wave expansions and different K-point samplings, depending on the size of the surface unit cells, were employed and checked in order to achieve good convergence. A four layer Au(111) slab with hydrogen atoms passivating one of the two vacuum-metal interfaces was used to model the Au(111) surface state [214], while a Co atom was placed on the other interface at 2.5 Å vertical distance at a fcc hollow site. At this distance the Co-Au(111) interaction is weaker than for the optimal adsorption distance but it is the way we mimic a less reactive Co atom in the metal-organic network. Table 6.2 summarizes the effects that an array of isolated Co adatoms deposited on Au(111) at different concentrations have on the reference energy of the Au SS. A more pronounced downward shift of the Au SS is observed with increasing Co content.

Chapter 7

Effective Determination of Surface Potential Landscapes from Metal-Organic Nanoporous Overlayers

7.1 Introduction

Determining the scattering potential landscape for two-dimensional metallic superlattices is key to understand fundamental quantum electron phenomena. Theoretical and semiempirical methods have been extensively used to simulate confinement effects on superlattices with a single scatterer in the form of vicinal surfaces [103] and dislocation networks [215] or single structures such as quantum corrals and vacancy islands [135, 136, 141]. However, the complexity of the problem increases when the building blocks (or scatterers) are heterogeneous, as in metal-organic networks, since additional potentials may come into play.

The modelization of electron scattering by 2D arrays (organic and metal-organic nanoporous networks) is often performed using EBEM/EPWE, which accounts for the local confinement response (local density of states) [16, 17, 129] and the electronic band structures arising from Boch-wave states generated from interdot coupling [15, 54, 129, 160]. However, it is a semiempirical method, so some assumptions need to be made regarding the potential barrier strength, sign (repulsive/attractive) and geometries, which often lead to arbitrary or unphysical conditions. In particular, published works use thinner molecular geometries than the actual molecular backbones [16, 17], altered effective pore sizes [17, 160], attractive scattering potential regions at the metal sites in metal-organic systems [16, 17, 129] or enlarged effective masses (m^*) than the 2DEG reference [54, 129]. The evident question is whether such ambiguous assumptions are necessary when simulating the electron confinement by 2D nanoporous networks.

Here, we answer this question by studying in depth the interaction between the 3deh-DPDI metal-organic nanoporous network [15, 53, 129, 158, 164, 167, 168, 216] and the two-dimensional electron gas of Cu(111). Based on a combination of

STM/STS, ARPES and Kelvin probe force microscopy (KPFM) measurements, together with EBEM/EPWE simulations, we demonstrate that both local confinement effects and interpore coupling induced electronic bands can be satisfactorily reproduced. This is achieved by starting from a realistic scattering geometry and then assigning physically sound repulsive scattering potentials to its barriers (both for molecules and adatoms). However, we require a 2DEG renormalization that afffects the effective mass (m^*) and energy reference (E_{Ref}), that agrees with our observations of previous chapters. Our explaination for these changes is assigned to the alteration of the vacuum region upon network presence, which is known to partly define the Shockley state [122, 201]. This experimental-theory synergy enables us to capture the intricacies of the scattering potential landscape, and to reveal systematic modeling procedures. Note that KPFM measurements have been performed by Dr. Shigeki Kawai from MANA/NIMS (Japan), STM/STS by Dr. Sylwia Nowakowska from Basel University (Switzerland) and EBEM/EPWE simulations in close collaboration with Dr. Zakaria M. Abd El-Fattah from Al-Azhar University (Egypt).

7.2 Results and Discussion

The organometallic network that we study is the same as the one presented in Chapter 4. It is formed by DPDI (4,9-diaminoperylene quinone-3,10-diimine), which undergoes a triple dehydrogenation process when deposited on Cu(111) and heated to 250°C. These organic tectons coordinate with Cu adatoms, and form a long-range ordered, commensurate metal-organic nanoporous network [15, 53, 158, 164, 167, 168, 216] [see Figure 7.1 (a)]. As indicated previously, the unit cell is composed of 3 molecules and 6 Cu adatoms and bears a periodicity of 25.5 Å. The model shown in Figure 7.1 (b) highlights the three-fold symmetry of 3deh-DPDI network. The three-fold symmetry of this network arises from the different registry of the Cu coordination atoms with the surface: One type of Cu trimer (*i*) surrounds an on top site, while the other Cu trimer (*ii*) surrounds a hollow site [167, 216].

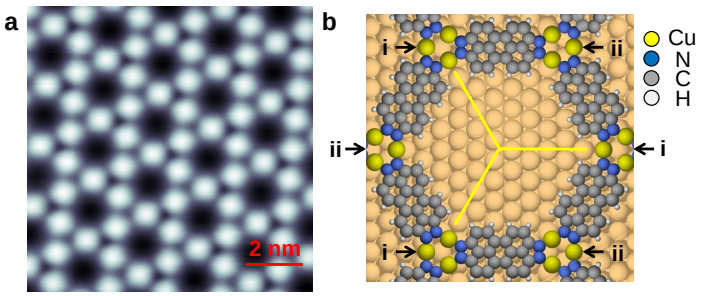

FIGURE 7.1: 3deh-DPDI metal-organic network on Cu(111). (a) STM image of the long-range ordered metal-organic network. STM parameters: I= 10 pA ; V= -1V. (b) 3deh-DPDI network model exhibiting the three-fold symmetry due to variations in the registry of the metal linkers.

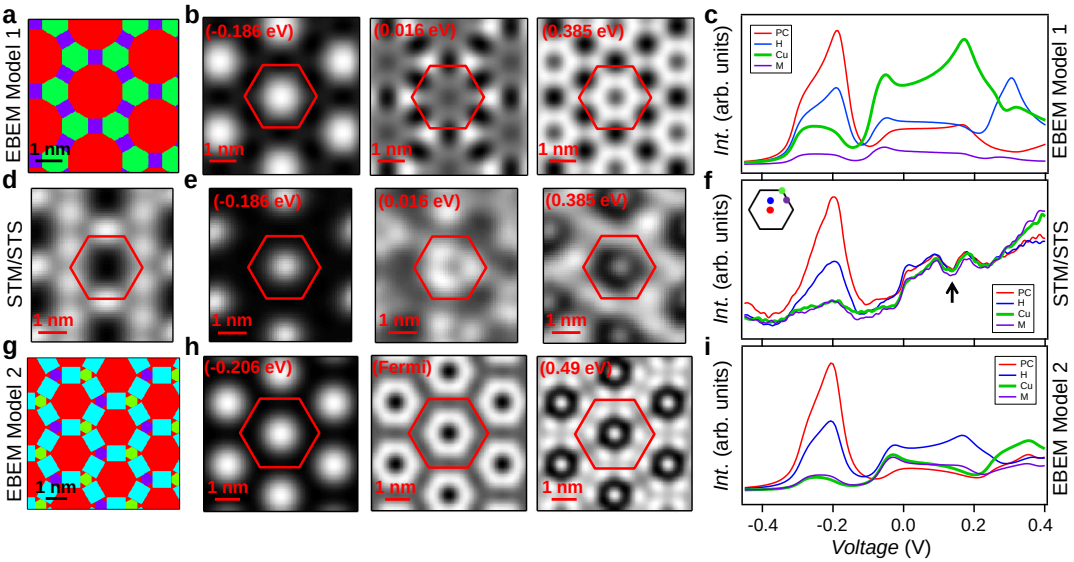

FIGURE 7.2: EBEM/EPWE simulated and experimental LDOS for the 3deh-DPDI metal-organic network. The top (a-c) and bottom (g-i) rows correspond to two different EBEM/EPWE simulations that we compare to the experimental case shown at the center row (d-f). This STM/STS row consists of a topographic image (d), three *dI/dV* maps at constant height at different energies [-0.186 eV (n=1 PLS), 0.016 eV (n=2 PLS) and 0.385 eV (n=4 PLS)] (e) and four *dI/dV* spectra acquired at relevant positions of the unit cell (see inset) (f). All experimental data can be vertically compared to two EBEM/EPWE models: the top reproduces the one in ref. [129] and the bottom is a new one proposed in this work. The scattering geometries shown in (a) and (g) consist of three parts: Cu substrate area (shown in red), molecules (shown as rectangles in purple or light blue) and metal coordination regions (as hexagons in green or violet/yellow). The corresponding potential values are indicated in Table 7.1. Experimental parameters: *dI/dV* maps and *dI/dV* spectra obtained from a grid spectroscopy measurement (35 $\times$ 30 points) with initial tip conditions 400 mV/70 pA and lock-in frequency 513 Hz; zero-to-peak amplitude: 8 mV. A binning of 30 meV is applied to each *dI/dV* map.

Figure 7.2 shows this network and compares the experimental STM/STS data (center row) with two EBEM/EPWE simulations obtained using the scattering geometry shown in panels (a) and (g) and barrier potentials specified in Table 7.1. The top row in Figure 7.2 assumes a scattering geometry proposed in ref. [129], which is formed by hexagons at the Cu adatom coordination sites (in green) connected by molecular potentials of 5.5 Å wide (in purple). In this model the metal adatom regions dominate spatially over the molecules and weakly resembles the STM topography of Figure 7.2 (d) and network model in Figure 7.1 (b). Furthermore, the potential at the Cu coordination region presents a negative sign, denoting attractive scattering character to this region, similar to other simulated coordinated metal-organic networks [16, 17]. Using the 2DEG reference of E_{Ref} = -440 meV (at 5 K) and m^* = 0.44 m_0 (slightly larger than the pristine substrate), we find in the simulations a very good match for the n=1 partially localized state (n=1 PLS) *dI/dV* map, but this agreement is lost for the higher orders [vertically compare Figure 7.2 (b) and (e)]. Note, for instance, that the LDOS central intensity is reversed for the highest *dI/dV* map shown. Similarly, when comparing the *dI/dV* spectra at selected unit cell

TABLE 7.1: EBEM/EPWE potential parameters used in the models discussed throughout this chapter. V_{mol} refers to space occupied by the molecule and V_{met} to the metal coordination centers, which are respectively shown as purple or light blue rectangles, and as green or violet/yellow hexagons in Fig. 7.2 (a) and (g). The large red areas corresponding to the Cu substrate are fixed to $V_{subs} = 0$ eV. The 2DEG scattering reference (E_{Ref} at 5 K and m^*) used for the EBEM/EPWE simulations is indicated in the last two columns. The first model is taken from ref. [129], the second one is generated from a realistic geometry of the network, whereas the third one is identical to the second model, but differentiates the two types of metal coordination centers discussed in Fig. 7.3.

	V_{mol} (meV)	V_{met} (meV)	E_{Ref} (meV)	m^*/m_0
Model 1 ref. [129]	1500	-100	-440	0.44
Model 2	390	390	-440	0.49
Model 3	390	440 (Type i) 340 (Type ii)	-440	0.49

positions [Figure 7.2 (c, f)], we find that only the pore center spectrum (PC, in red) acceptably matches the experimental curves, but the rest deviate strongly when the bias exceeds -0.12 V. Firstly, at the halfway (H, in blue) spectrum, the dominant peak at 0.32 V is experimentally absent. Secondly, for the metal center (Cu, in green), two prominent peaks are observed at -0.09 V and 0.18 V and show a drop of the intensity at the right side of the simulation, which are absent in the experimental data. In particular, the strong localization at the Cu atoms for the 0.18 V state, with LDOS as large as the fundamental n=1 PLS, is farthest from experiment, indicating unplysical potential assignment for this region.

The pronounced discrepancies between the experimental data and the EBEM/EPWE model generated with the parameters of ref. [129] demands the reconsideration of the scattering potential and geometries in these simulations. Based on previous high resolution AFM and STM work [167, 216] and the network model of Figure 7.1 (b), we start from a realistic geometry where the repulsive nature of molecules dominate, instead of the metal coordination regions [cf. Figure 7.2 (g)]. This leads to a molecular geometry of 9 Å in length and 8 Å in width and much smaller metal coordination regions that realistically fill the space left between molecules. Instead of allowing this geometry to change, we provide flexibility to the 2DEG reference [54]. We find that using E_{Ref} = -440 meV (for 5 K) and m^* = 0.49 m_0, which notably deviate from the pristine Cu(111) surface state [100, 108], together with homogeneous repulsive barriers (V_{mol} = V_{met} = 390 meV), we can finely capture most details of the experimental LDOS and *dI/dV* spectra. Note that these are not just arbitrary values (scattering parameters indicated as Model 2 in Table 7.1), but the result of simultaneously simulating the ARPES and STS experimental data [54]. These parameters turn out to be crucial for pushing to lower energies the higher order confined states (for instance lowering n=4 PLS to ~ 0.49 V) [Figure 7.2 (h)]. Interestingly, the *dI/dV* spectrum on top of the metal adatom region (green curve) shows a relevant attenuation

of the spectral features above -0.1 V that agrees very well now with the experimental curves and corroborates the repulsive character of this region of the network [cf. Figure 7.2 (f, i)].

We further backup the choice of repulsive scattering parameters for both molecules and metal centers by performing Local Contact Potential Difference (LCPD) measurements using the Kelvin probe force microscopy method [217, 218]. The KPFM constrast is known to correspond qualitatively to the z-component of the electrostatic field E_z at a constant-height plane above the molecule. The simple interpretation is that a more positive LCPD corresponds to more negative charge below the tip. Even though the tip radius is expected to be much larger than the local variations of the surface potential, in Figure 7.3 (a), we observe that the molecular scattering backbone (in red) is similar in size to the molecular dimensions [216]. In addition,

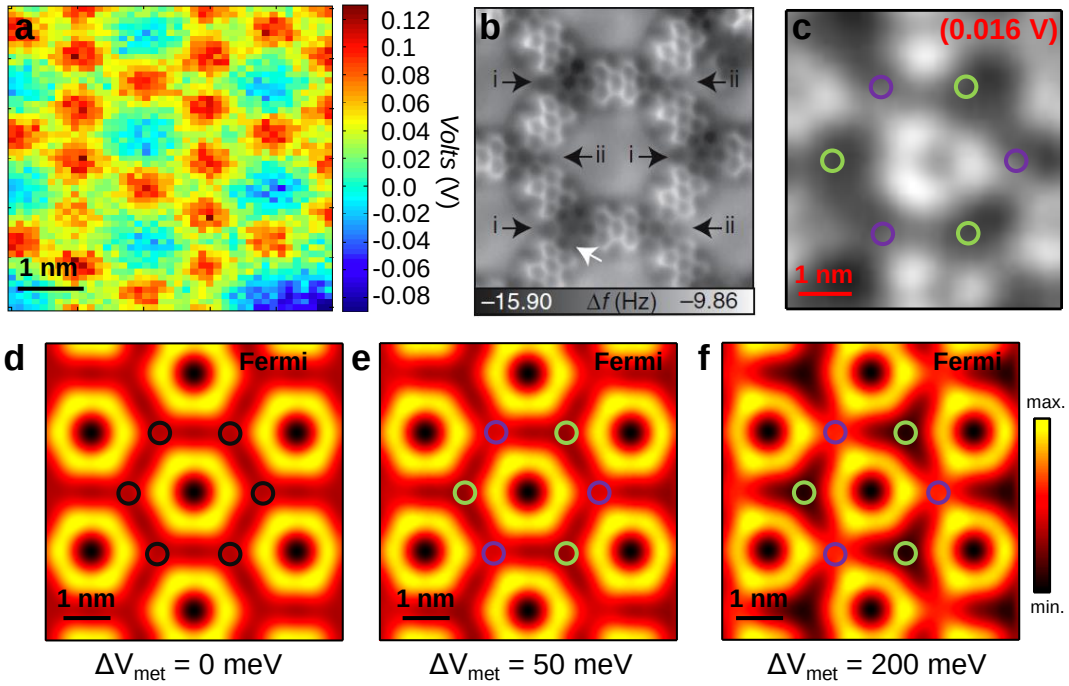

FIGURE 7.3: Corroboration of three-fold symmetry at metal coordination positions, influence upon the confined states and EBEM/EPWE implementation. (a) Kelvin probe force microscopy image of several pores showing local contact potential difference variations at the sub-nanometer scale confirming the existence of surface potential variations upon the formation of the molecular network. (b) Noncontact AFM measurements (adapted from ref. [216]) with sub-molecular resolution differentiating the two types of metal coordination centers (denoted *i* and *ii*). (c) *dI/dV* constant height map for the n=2 PLS (slightly above E_F) indicating the different metal adatom regions as two colored circles (purple and green). The sensitivity to the three-fold symmetry potential is demonstrated by the triangular shape (instead of hexagonal) observed inside the pore. The LDOS asymmetry can be simulated in EBEM/EPWE as a perturbation of the scattering potential. In particular, (d) shows the unperturbed case (hexagonal case) when ΔV_{met}= 0 eV (V_{met} = 0.39 eV), whereas (e) and (f) introduces potential variations of ΔV_{met}= 50 meV and ΔV_{met}= 200 meV, respectively. The green metal coordination position has a higher potential value than the violet one and, correspondingly, the distortion becomes stronger the larger the difference between the two sites is.

the smaller Cu coordination regions, which appear less intense than the molecules most probably due to their different height [167], do not drastically change its color when compared to the pore regions, ruling out any tendency towards a sign reversal of the scattering potential and therefore maintaining a repulsive character to the surface electrons. Note however, that the LDOS simulation shown in Figure 7.2 (h) displays a six-fold symmetry that contradicts previous experimental findings reporting the existence of two structurally different adatom coordination sites within the network [167, 216]. This difference is explained as a variation of the registry with the substrate, where the three metal adatoms binding the molecules of the network arrange either surrounding a three-fold hollow site or a Cu atom of the substrate [see Figure 7.1 (b)]. This subtle variation shows up in the AFM images acquired with a CO functionalized tip [see Figure 7.3 (b)] and in the *dI/dV* maps whenever the intensity shifts away from the pore center, as is the case of n=2 PLS [cf. Figure 7.3 (c)]. It is worthy to note that, this is the first experimental observation of the triangular shape of n=2 PLS, although they were predicted for hexagonal lattices with three-fold symmetry [163]. EBEM/EPWE can simulate this behavior by inducing a slight potential variation (ΔV_{met}) between Cu regions while keeping the molecular potential at V_{mol} = 0.39 eV (Model 3 in Table 7.1). In this way, we observe a clear transition of the n=2 PLS from hexagonal to triangular, as shown in the bottom row of Figure 7.3 (d-f). We find that the green regions correspond to a stronger potential than the purple regions. Likely, the two types relate to a subtle energy imbalance stemming from its vertical packing. Following the herringbone reconstruction potential difference between fcc and hcp sites of 25meV [219], we tentatively assign the green sites to larger potentials (fcc) and the purple to lower ones (hcp).

The synergy between our local spectroscopies and EBEM/EPWE simulation has produced two relevant results: first, the metal coordination sites exhibit repulsive scattering potential character compatible with the presence of three-fold symmetry in the higher energy states and, second, a mass renormalization of the 2DEG occurs upon the presence of the network on the Cu(111) surface. These findings should be compatible with the ARPES data shown in Figure 7.4. This situation corresponds to the one in which 3deh-DPDI network completly saturates the surface and no trace of the Cu SS is observed (see Figure 7.7). It is straightforward to confirm that the 2DEG renormalization is correct since both the simulated band structure and the isoenergetic cuts fit exceptionally well to the experimental data when using the scattering parameters indicated in Model 2 of Table 7.1. In Figure 7.4 (a), the second derivative of the experimental data (raw data in Figure 7.8) exhibits the expected shallow dispersive bands of organic QD arrays [15, 54, 129]. The lower energy band corresponding to n=1 PLS has a $\sim$ 80 meV bandwidth and shifts $\sim$ 150 meV towards E_F with respect to the pristine Cu surface state and increases m^* to $\sim 0.58\ m_0$ [15, 53, 54]. This effective mass is higher than the 2DEG reference as a result of the confinement induced by the nanoporous network [54], which is certainly substantial

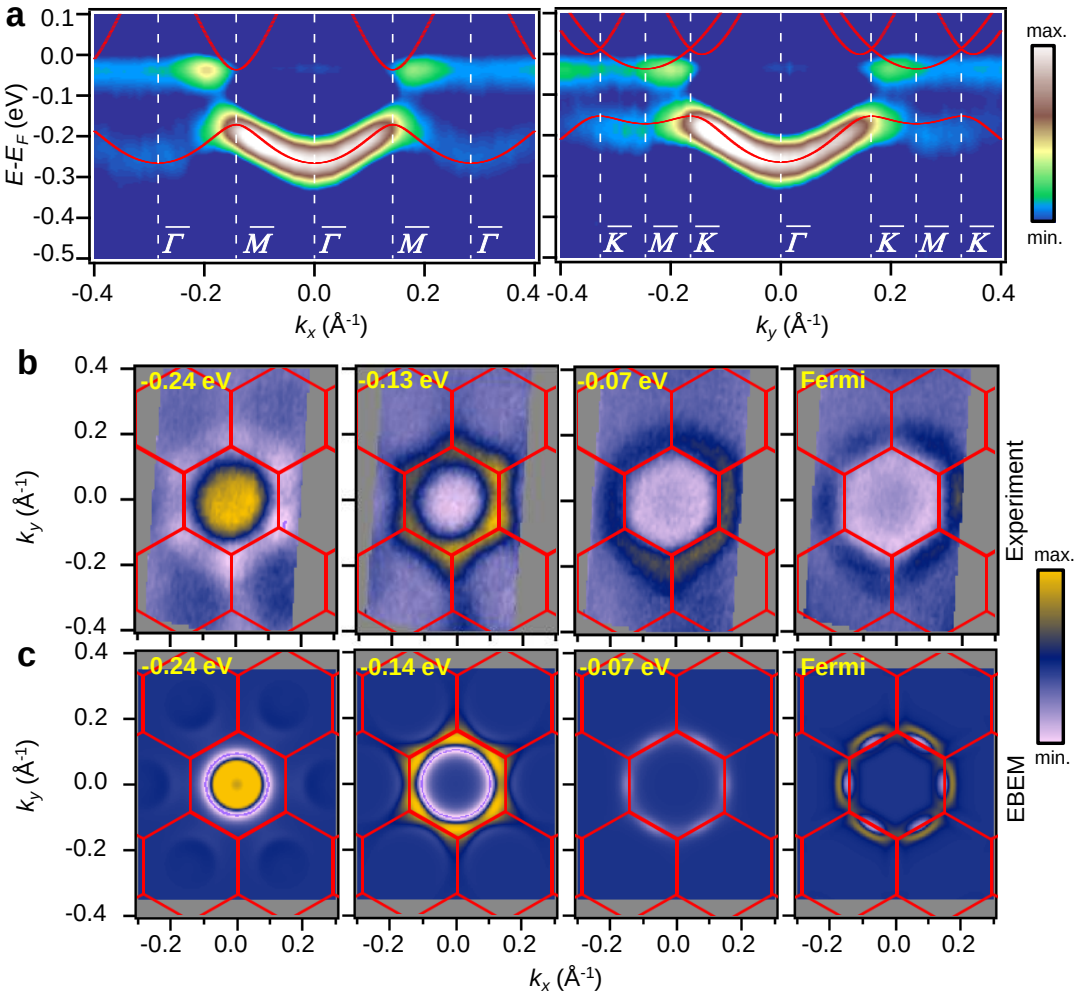

FIGURE 7.4: Experimental and simulated electronic band structures and isoenergetic maps of the 3deh-DPDI network saturating the Cu(111) surface. (a) Energy dispersion maps for the two high symmetry directions $\overline{\Gamma M}$ and $\overline{\Gamma K}$. The color-plot represents the second derivative of the intensity to enhance the weak details with respect to energy and parallel momentum. The high quality of the network allows to observe faint replica bands in adjoining Brillouin zones. Simulated EBEM/EPWE bands using the scattering potentials of Model 2 (see Table 7.1) are superimposed as red lines onto the experimental data and match perfectly both high symmetry directions. Experimental (b) and simulated (c) isoenergetic cuts (k_x vs k_y) obtained at the band-bottom (-0.24 eV), lower edge of the $\overline{\mathrm{M}}$ point (-0.13 eV), inside the gap (-0.07 eV) and at the Fermi level. As a reference, the metal-organic network induced hexagonal SBZ is superimposed onto the second derivative data. Experimental ARPES parameters: hν = 21.22 eV, T_s = 10 K for (a) and 150 K for (b).

judging from the prominent energy gap (120 ± 30 meV) detected at the zone boundaries ($\overline{\mathrm{M}}$ point) separating the n=1 and n=2 PLS bands [157] (see Figure 7.9).

However, the three-fold symmetry observed in the LDOS for the n=2 PLS is absent in the fermi surface map of Figure 7.4 (b). Instead, all isoenergetic cuts (k_x vs k_y) exhibit six-fold symmetry (hexagonal shape) that diverges from the circular and isotropic pristine Cu surface state. It could be argued that due to the averaging character of ARPES, the illuminated (probed) area contains, with equal probability, network patches with (*i*) and (*ii*) metal coordination regions at equivalent pore sites

(60° relative rotations). Nonetheless, the primary reason behind is the conservation of time reversal symmetry, which requires $E(k) = E(-k)$. Hence, isoenergetic cuts should appear as six-fold even if a single three-fold symmetric 3deh-DPDI network domain was present on the surface. This is in agreement with other three-fold symmetric surface structures such as Ag/Cu(111) superlattices, where the band structure also appears as six-fold symmetric [215]. Indeed using the scattering parameters of both Model 2 and Model 3 in Table 7.1, the electronic band structure agrees with the band structure dispersion, gap size and isoenergetic shapes experimentally observed. Thus, the nice agreement between theory and experiment supports and validates the repulsive scattering character assigned for molecules and metals, as well as the imposed renormalization of the 2DEG reference.

Our results prove that an appropriate EBEM/EPWE simulation of the electron confinement by QD arrays should be achieved by having at hand STM/STS and ARPES experimental data and using realistic geometries of the overlayer before

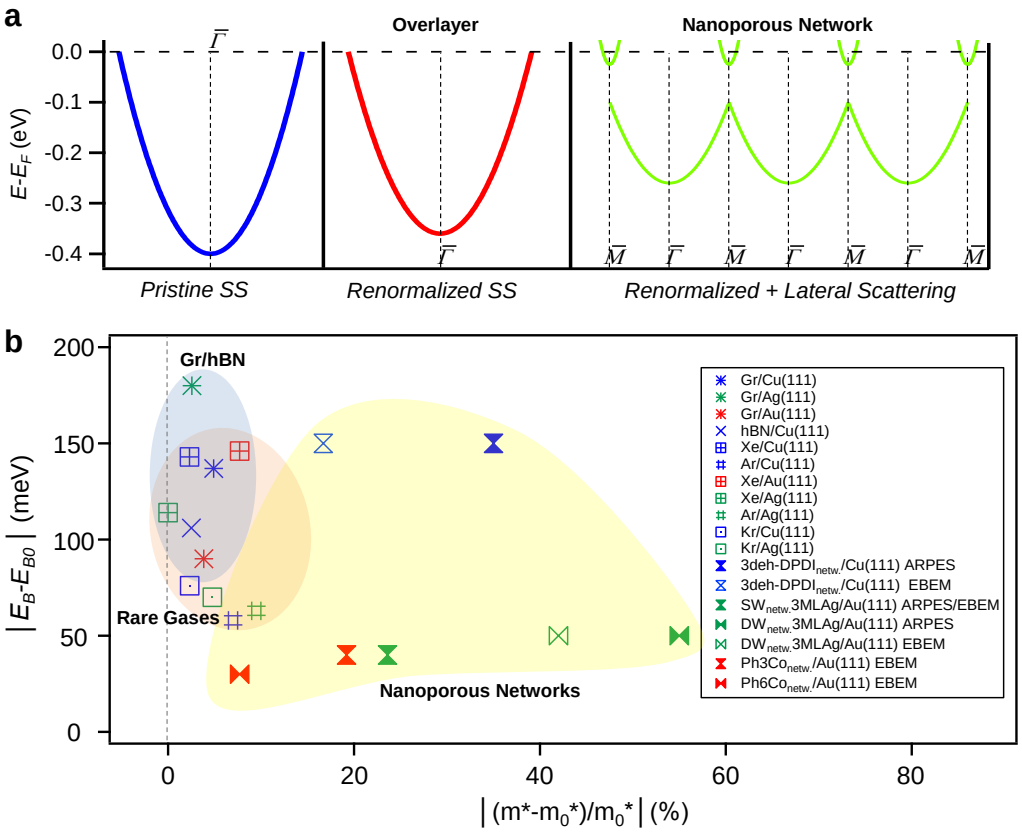

FIGURE 7.5: Reported renormalization of 2DEGs by physisorbed overlayers. (a) Schematic band renormalization of the Cu Shockley state resulting in an increase of its reference energy and effective mass upon the presence of the studied nanoporous network. (b) Renormalization chart (ΔE_B vs Δm^*) reported for families of physisorbed systems onto substrates exhibiting 2DEGs. Nanoporous networks (yellow area) [53, 54] are compared with rare gas overlayers (orange area) [220, 221] and with graphene [222, 223] and h-BN [224] (blue area). Note that m^* renormalization becomes relevant only for nanoporous networks.

defining the strength of the scattering potential barriers. Moreover, the 2DEG reference requires certain flexibility, especially in m^*, in agreement to previous work [54, 129]. The 2DEG reference changes upon the growth of the organic overlayer, as schematically shown in Figure 7.5 (a). The resulting (leaky) confinement depends on the detailed potential landscape exerted by the nanoporous network on the 2DEG, defining the interpore coupling and producing new electronic bands separated by gaps at zone boundaries [54, 160].

The 2DEG renormalization here proposed is not uncommon and has been observed in numerous physisorbed overlayers, such as graphene (Gr), boron-nitride (hBN) and rare gases physisorbed on noble metals. Figure 7.5 (b) compiles selected results from these related systems where the surface state shifts towards the Fermi level while varying its m^*. It is interesting that even if the energy shifts can be of similar magnitude, the effective masses do considerably increase in the case of nanoporous systems. This is likely caused by the QD intercoupling extending through the surface. Note that absolute values have been used to also include Ph3Co and Ph6Co network results (Chapter 6).

Once the 2DEG reference modification has been justified, the scattering potential values call for attention. When comparing the molecular potential V_{mol} obtained in this work (see Table 7.2) we find that its value (390 meV) is larger than other reported cases with ARPES experimental data access [54]. The 3deh-DPDI generates potential barriers capable of strongly confining the surface electrons and opening significant energy gaps in the band structure. Nevertheless, the magnitude of the value is reasonable when compared to other networks, suggesting that limitations to the potential magnitude should exist when used to simulate the molecular scattering potentials. As an educated guess, this limit could be of the order of $V_{mol}^{max} \sim 0.5$ eV. Note however that ultimately the effective potential that 2DEG electrons encounter depends on the separation between the nanopores, *i.e.* the molecular widths. The value here proposed would also be restricted to planar and single layer molecular systems.

Furthermore, we demonstrate that the scattering character of the adatom metal centers is repulsive for the 3deh-DPDI network. This follows a similar pattern to

TABLE 7.2: Scattering potential values for molecules (V_{mol}) and metal centers (V_{met}) for three different types of networks. The selected networks correspond to the one from this study (top row), the homothetic Ph6Co and Ph3Co metal-organic networks on Au(111) (middle, Chapter 6) and the two halogen bonded SW and DW networks on Ag(111) (bottom row, Chapter 5). The values are taken from EBEM/EPWE simulations based on STS and ARPES datasets.

	V_{mol} (meV)	V_{met} (meV)
3deh-DPDI network	390	340 / 440
Ph3Co / Ph6Co	250	50
SW / DW (ref. [54])	140	–

molecular backbones and to other atomic-like surface 2DEG confining entities in the form of step-edge adatoms, quantum-corral barriers or dislocation networks [18, 103, 108, 135, 225]. We infer that this effect is quite general and has in the past been incorrectly considered for the case of organometallic nanoporous networks [16, 17, 129]. Indeed, the repulsive potential values proposed for Ph3Co and Ph6Co in Table 7.2 and discussed previously in Chapter 6 are more physicaly sound and in agreement with the present observations.

It is interesting to discuss further the implications of the observed LDOS deviation from the hexagonal shape induced by scattering potential imbalance at the metal sites. The local three-fold appearance of the higher order n=2 PLS comes not solely as variations of the metal center registry with the substrate (as shown here in Figure 7.3), but can also be generated from small relative displacements of the building blocks defining the pores. An example of the latter has been already reported for chiral networks stabilized by non-metallic intermolecular bonds [153, 163]. Accordingly, it is the ultimate geometry of the tectons that dictates the LDOS shape if the scattering potential barriers have similar magnitudes.

Finally, it is plausible that the confined states at the pores could play a role in guest filling of QD arrays through minimization of the electronic contributions [139, 163, 166]. A way of confirming this hypothesis would require the observation of certain symmetries imposed on the external species adsorbed into the QDs. In particular, the 3deh-DPDI nanopores can host up to 12 Xe atoms per pore that are clustered into four atom bunches [164] [Figure 7.6 (left)]. Since these rare gas atoms maintain exactly the same relative bunch orientation to all neighboring pores in an overall three-fold symmetry [164], we infer that the n=2 PLS (closest to the E_F) could participate in guiding the observed Xe pore condensation [Figure 7.6 (right)]. Alternatively, these Xe atoms could be just marking three equivalent metal sites exhibiting the lowest surface potential of the whole network [226].

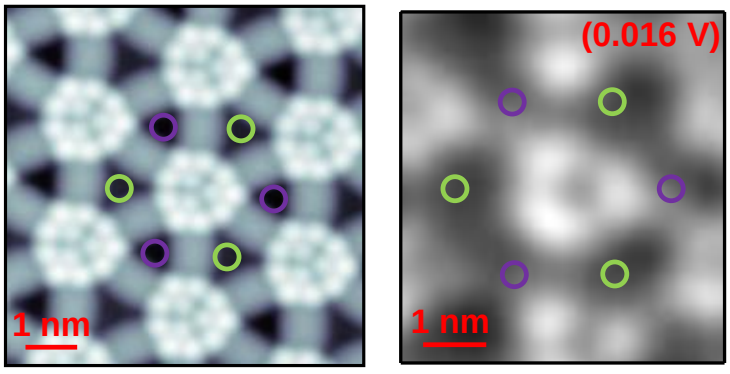

FIGURE 7.6: Confined state influence upon the Xe adsorption. Up to 12 Xe atoms adsorbs into the nanopores of 3deh-DPDI, as observed from the STM image acquired with a Xe functionalized tip (left) ($6 \times 6\,\mathrm{nm}^2$, $I = 50\,\mathrm{pA}$, $V = 10\,\mathrm{mV}$). Since the packing occurs as three tetramers that follow a three-fold symmetry, it is most likely guided by the triangular shape of the n=2 PLS, which is closest to the Fermi level (right). The left image has been adapted from ref. [164].

7.3 Conclusions

In conclusion, we have shown that it is possible to obtain the scattering potential landscape exerted by a nanoporous metal-organic overlayer onto a 2DEG and determine the relevant confinement details and interaction effects. This is achieved by combining semi-empirical EBEM/EPWE simulations with local and averaging electronic experimental techniques (STM/STS, AFM, KPFM and ARPES). We showed that the scattering potential must be parametrized as realistically as possible to the network geometry while providing flexibility to the 2DEG, which requires a slight energy and/or mass renormalization due to the interactions between overlayer and substrate. Our simulations unambiguously define that both the molecules and the metal adatoms forming the network exhibit repulsive character to the surface electrons. Following other works, we provide a tentative upper limit to the repulsive scattering magnitude of the molecules for related systems. We also find that slight perturbations in the scattering potential at the metal sites are responsible for the deformation of the confined states, which show up as three-fold. Our work confirms that the confined 2DEG is sensitive to existing subtle interactions of the overlayer with the substrate and corroborates the surface state renormalization, which provides consistency to the results obtained by these semi-empirical simulations.

7.4 Supplementary Information for This Chapter

7.4.1 ARPES Measurements

ARPES measurements for Figures 7.4 (b), 7.7 and 7.8 (b) were performed with our lab-based experimental setup at 150 K as described in Chapter 2. ARPES measurements of Figures 7.4 (a) and 7.8 (a) were performed at 10 K with $h\nu$ = 21 eV at Cassiopee beamline of the Soleil Synchrotron in Paris.

Sample Preparation

To avoid contributions from the Shockley surface state of bare Cu(111) to the ARPES signal, it was crucial to achieve a homogeneous Cu-coordinated 3deh-DPDI network completly covering the surface. Therefore, DPDI was sublimated onto Cu(111) held at RT in a wedge geometry (producing a coverage gradient) in the proximity of the optimal coverage ($\sim$ 0.75 ML) and then annealed (250°C) until a sharp and intense signal emerging from the n=1 PLS was visible in the ARPES channelplate detector [15] (Figure 7.7). The annealing step is crucial for conversion of the DPDI molecules into 3deh-DPDI molecules that will create the Cu-coordinated network [158, 168, 169].

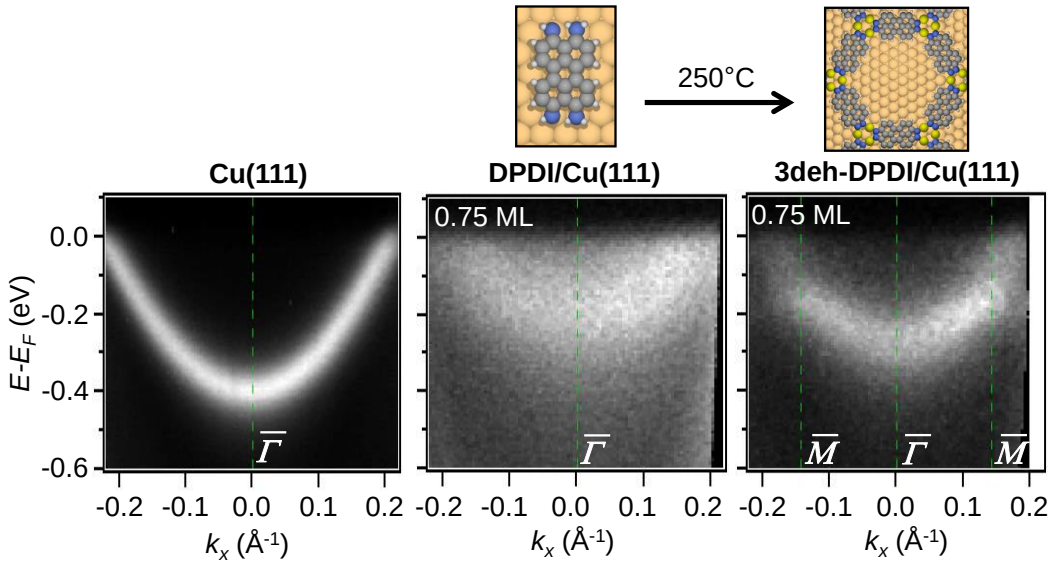

FIGURE 7.7: Electronic structure evolution from the pristine state, to the confined case from the 3deh-DPDI network. From left to right, ARPES (E vs k_x) band structure corresponding to the pristine Cu(111) surface state, 0.75 ML DPDI on Cu(111) and 0.75 ML 3deh-DPDI molecular network on Cu(111). The band structure clearly evolves into a shallow dispersive band for the n=1 partially localized state (n=1 PLS) and an energy gap is created between n=1 and n=2 PLS.

7.4.2 STM/STS Measurements

STM/STS measurements have been performed by Dr. Sylwia Nowakowska from Basel University (Switzerland) and close to liquid He temperatures (5 K). The bias voltages provided refer to a grounded tip. All *dI/dV* spectra were recorded with open-feedback loop. The *dI/dV* data presented in Figures 7.2 and 7.3 were extracted from the grid spectroscopy measurements, in which an area of 5.45 $\times$ 4.3 nm^2 was mapped by acquisition of *dI/dV* spectra above each point with the resolution of 35 points $\times$ 30 points. The initial tip conditions amounted to 400 mV/70 pA (lock-in frequency: 513 Hz; zero-to-peak amplitude: 8 mV). The value of the initial voltage was chosen such that no contribution from quantum dot states or network backbone is present [227]. Under this conditions, normalization could be performed by setting the same *dI/dV* value at the setpoint energy for all other spectra. In this way artifacts originating from local surface potential variations are minimized [17, 53, 227].

7.4.3 LCPD/AFM Measurements

KPFM measurements have been performed by Dr. Shigeki Kawai from MANA/NIMS (Japan). All experiments were performed with Omicron STM/AFM with a qPlus configuration, operating at 4.8 K in UHV. The W tip of a tuning fork sensor was *ex-situ* sharpened by focused ion beam milling technique and was then *in-situ* covered with Cu atoms by contacting to the sample surface.

7.4.4 Side Considerations to This Chapter

- In Figure 7.4 the second derivative of the raw data has been used in order to enhance details such as the replicating bands away from the first SBZ and the opening of gaps at zone boundaries [15]. In the following Figure 7.8, the raw data is included for completeness.

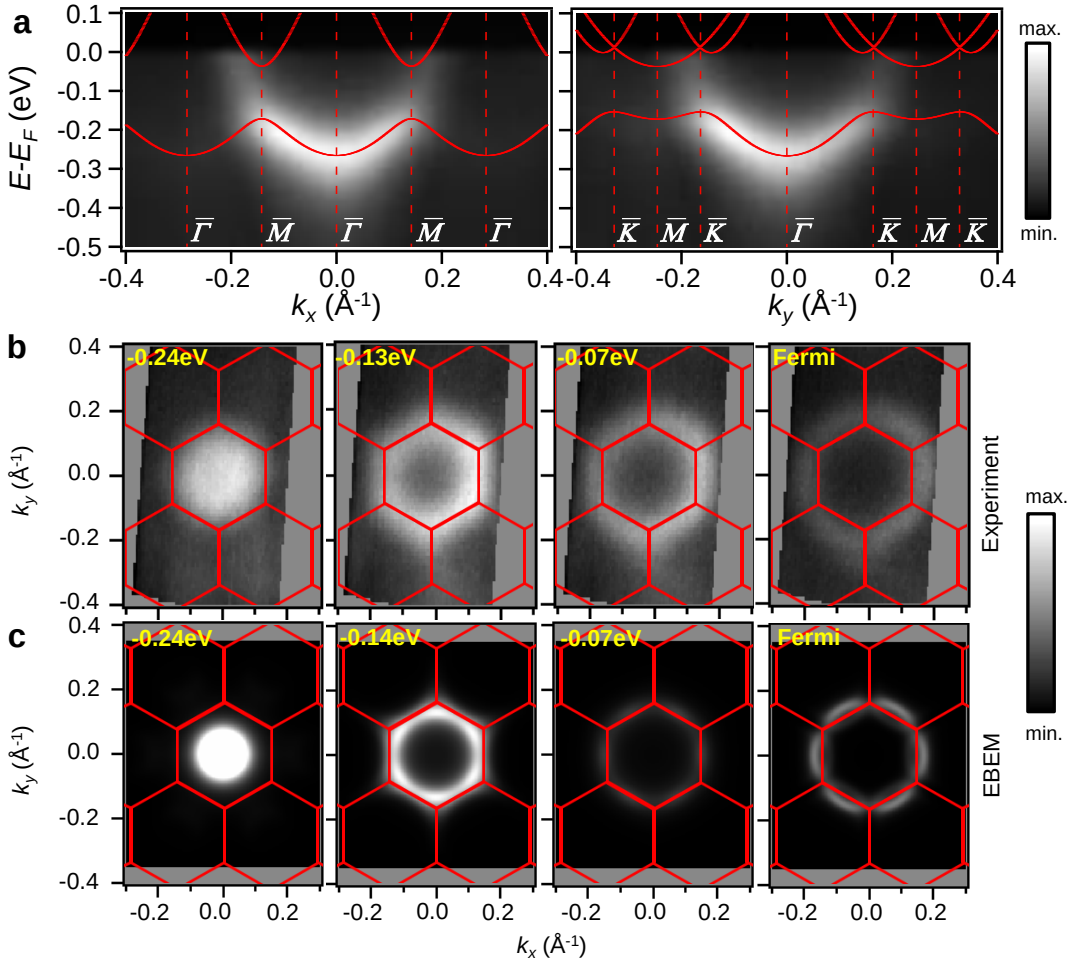

FIGURE 7.8: Experimental and simulated electronic band structures and isoenergetic maps in raw data when the 3deh-DPDI metal-organic network saturates the Cu(111) surface. (a) Energy dispersion maps for the two high symmetry directions $\overline{\Gamma M}$ and $\overline{\Gamma K}$. The high quality of the network allows to observe faint replica bands in adjoining Brillouin zones. Simulated EBEM/EPWE bands using the scattering potentials of model 2 (see Table 7.1) are superimposed as red lines onto the experimental data and match perfectly both high symmetry directions. Experimental (b) and simulated (c) isoenergetic cuts (k_x vs k_y) obtained at the band-bottom (-0.24 eV), lower edge of the $\overline{\text{M}}$ point (-0.13 eV), inside the gap (-0.07 eV) and at the Fermi level. As a reference, the metal-organic network induced hexagonal SBZ is superimposed. Experimental ARPES parameters: hν = 21.22 eV, T_s = 10 K for (a) and 150 K for (b).

- The energy dispersion maps shown in Figures 7.4 (a) and 7.8 (a) correspond to measurements performed at 10 K and hν = 21 eV at the Soleil Synchrotron in Paris, while the isoenergetic cuts shown in Figures 7.4 (b) and 7.8 (b) have

been performed at our laboratory setup in San Sebastian at 150 K and Helium I (hν = 21.22 eV). This is done because the quality of the former Energy dispersion maps (E vs k) at 10 K is higher while the statistical points gathered for the isoenergetic cuts (k_x vs k_y) in the latter case is larger. The only difference between both measurments is the temperature variation induced energy shifts of the n=1 PLS band bottom which amounts to $\sim$ 30 meV as shown in Figure 7.9 (a).

- The effective mass of the n=1 shallow dispersive PLS band generated by the 3deh-DPDI nanoporous network has been calculated using the same procedure as in refs. [53, 54]. We consider a small momentum region of ± 0.05 Å^{-1} around the $\overline{\Gamma}$ point since this region is not distorted by the gap openings at zone boundaries [Figure 7.9 (b)].

- Figure 7.9 (c) shows that the gap opening at the zone boundary ($\overline{\mathrm{M}}$ point) between n=1 and n=2 PLS bands amounts to 120 ± 30 meV, agreeing with previous observations [15] and evidencing a strong scattering potential at the molecular backbone.

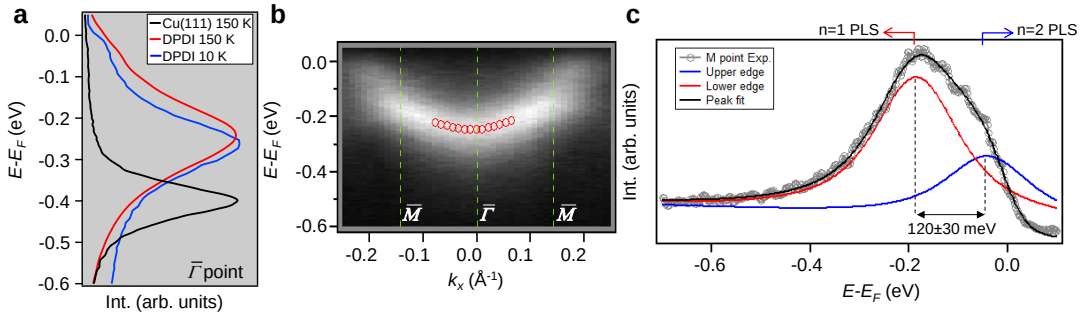

FIGURE 7.9: Characterization of the 3deh-DPDI band structure. (a) EDCs taken at the $\overline{\Gamma}$ point for the pristine Cu surface state (black) and 3deh-DPDI network (red) at 150 K. The EDC for 3deh-DPDI network (blue) is taken at 10 K. Both features are identical except for the well-known energy shift ($\sim$ 30 meV) to higher binding energies as the temperature is decreased [158]. (b) Effective mass extraction from the n=1 shallow dispersive PLS band. Following the procedure explained in ref. [53] an effective mass of m^*= 0.57 m_0 is obtained. (c) $\overline{\mathrm{M}}$ point fitting of the peaks using a Lorentzian-Gaussian distribution convoluted with a Fermi edge yields a band gap of 120 ± 30 meV, a value that agrees well with EBEM/EPWE simulations and previous observations [15].

- For the correct EBEM/EPWE simulation of the 3deh-DPDI induced band structure and LDOS features, an increase of the effective mass was required (m^*=0.49 m_0). This requirement is not only essential for matching the dispersion of the n=1 shallow disperive PLS band of Figure 7.4 (a), but also for bringing higher confined states such as n=4 PLS to lower energies. This energetic shift with increasing m^* can be conceptually understood by simulating a hard-wall potential hexagonal single pore as in Figure 7.10. First of all, a large potential amplitude is chosen [V_{mol} = 20 eV, Figure 7.10 (c)], which mimics an infinite

potential wall. Then the confined states are simulated for two different effective masses: 0.44 m_0 and 0.58 m_0. The first value resembles the one for pristine Cu(111) [108], while the second one corresponds to the experimental effective mass observed for 3deh-DPDI network. It immediately becomes clear that higher confined states are more sensitive to effective mass changes as their energy shifts are larger [Figure 7.10 (a, b)]. Note that by changing m^* in EBEM/EPWE, confined states can be shifted in energy but the spatial features (LDOS) appear unchanged [Figure 7.10 (c)]. This mass renormalization becomes necessary for matching the experimental findings in 3deh-DPDI network as well as in other networks [54].

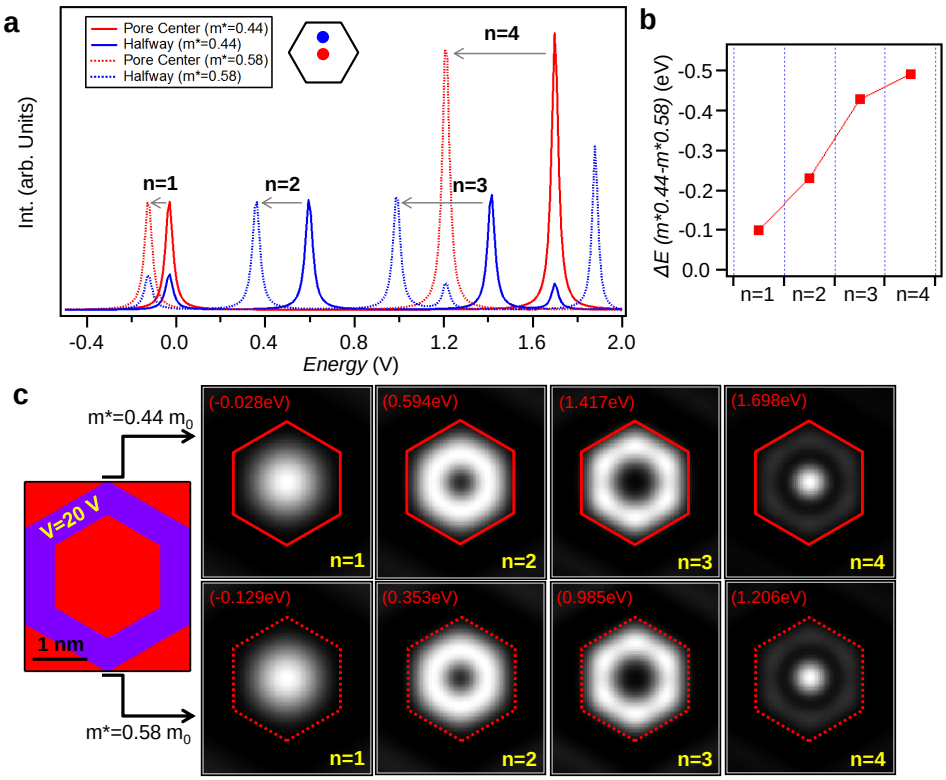

FIGURE 7.10: EBEM/EPWE simulations of the confined state energy variations with m^* inside a practically infinite potential hexagonal pore. (a) Discrete confined state levels from n=1 to n=4 are shown for two relevant effective masses: 0.44 m_0 and 0.58 m_0. While n=1 and n=4 confined states can be traced at the center of the pore (red), n=2 and n=3 confined states shift away from it and peak at halfway position (blue). (b) Upon increasing the effective mass, the confined states shift towards lower energies, the higher ones being more sensitive (larger energy shifts) to this changes. (c) EBEM/EPWE simulated LDOS are identical for both effective masses, but peak at lower energies for the larger m^* value.

- Starting from a realistic scattering geometry and allowing the 2DEG to renormalize in energy and/or mass has a critical effect in higher order confined states. For instance by looking at Figure 7.11, we clearly observe that the highly localized confined state predicted by Model 1 (blue spectrum) at 1 V is not present in the experimental STS curve (grey). In order to simultaneously push the energy of this confined state down and quench its intensity, the geometry of the scattering landscape has to be changed [Figure 7.2 (g)], adopting a realistic geometry, and an increased effective mass of m^*= 0.49 m_0 must be used (Model 2, red spectrum).

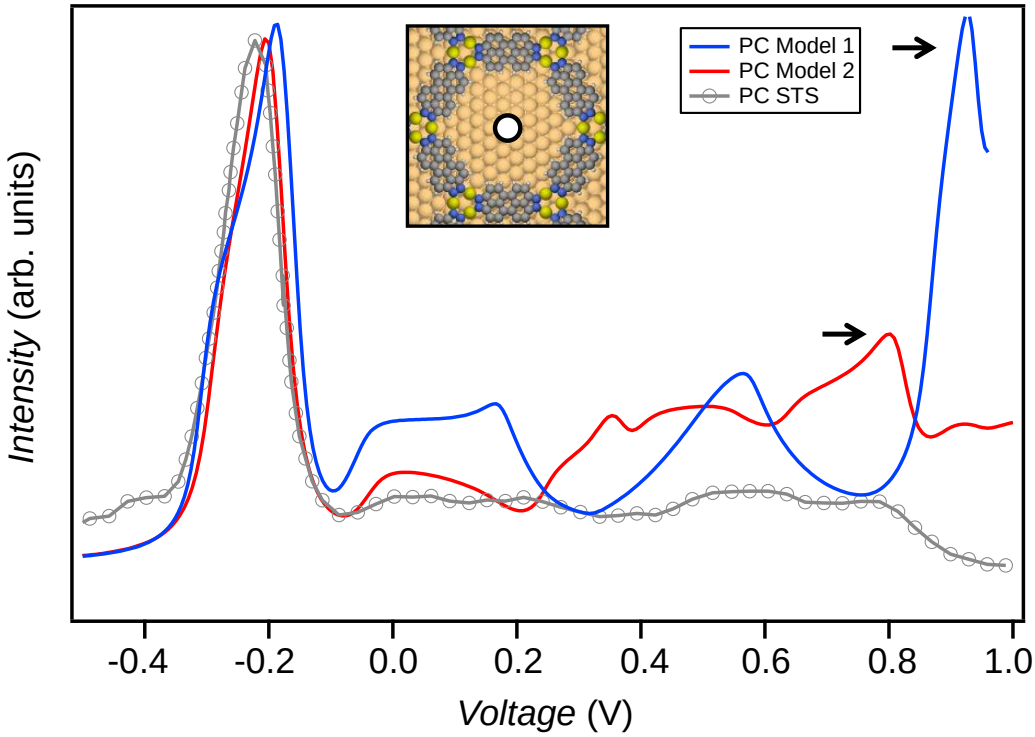

FIGURE 7.11: EBEM/EPWE simulated LDOS curve at the pore center (PC), using scattering parameters from Model 1 (blue) and Model 2 (red). The experimental STS curve at the pore center is shown as grey color. While the matching for both Models is reasonable below 0.4 V, Model 1 clearly deviates at 1 V since a very localized state appears which is absent in the experiment. This state has been attenuated and shifted to lower energies in Model 2 by using a reasonable scattering geometry and by increasing m^*, yielding a match with the experiment.

Chapter 8

Configuring Electronic States in an Atomically Precise Array of Quantum Dots

8.1 Introduction

2D arrays of electronically coupled QDs fabricated on metallic surfaces by means of molecular self-assembly, assure ultimate precision of each confining unit and long-range order. These molecular nanoporous templates serve as ideal candidates for hosting adsorbates in an ordered fashion inside each nanocavity. For instance, single Fe atoms, Bi clusters, Xe, C_{60} and ZnOEP molecules have been orderly trapped [161, 164–166, 228]. The periodically extended and robust 3deh-DPDI nanoporous network grown on Cu(111) represents an ideal template for such purposes. An interesting effect of using weakly physisorbed adsorbates such as Xe is that the energy of the quantum states embedded in the dots can be delicately altered with Xe occupancy. This is a process that can be controlled with atomic precision and engineered at will by using atomic manipulation. We followed this procedure to study the desired occupancy configurations, getting access to single pore and interpore coupling effects by LT-STM/STS (experiments performed by Dr. Sylwia Nowakowska from Basel University) and simulated with EBEM/EPWE (by Dr. Zakaria M. Abd El-Fattah from Al-Azhar University). In addition, by means of ARPES, we observed a fundamental energy shift of the n=1 PLS band to lower binding energy upon adsorption of Xe in the nanocavities, in agreement with STS. We followed such ensemble electronic band changes by simultaneously detecting the appearance of the Xe core levels in the spectra, from which the adsorption position could be monitored. This work has been published in ref. [53].

8.2 Results and Discussion

The array of coupled QDs employed in this work is the 3deh-DPDI network generated on Cu(111) [Figure 8.1 (a)], extensively described in Chapters 4 and 7 [15, 167–169]. The low intensity of the n=2 PLS close to E_F and the absence of higher order bound states [166] simplify the analysis of the targeted perturbation of the PLS by adsorbates and its interaction with surrounding QDs. To modify the n=1 PLS in these pores we chose Xe atoms, first for their well-characterized effects upon the surface state electrons of Cu(111), which is dominated by Pauli repulsion [107, 196], and second, for its preferential adsorption in the pores of the Cu-coordinated 3deh-DPDI network with maximal occupancy of 12 atoms [inset in Figure 8.1 (b)] [164]. In this way we can discretely modify the electronic state of QDs by STM repositioning. As already reported by Nowakowska et al. [164], the 12 Xe occupancy inside each pore consists of three tetramers, with Xe atoms adsorbed in on-top sites of the Cu(111) atomic lattice in a ($\sqrt{3}$ x $\sqrt{3}$)R30° overlayer structure, in agreement with previous studies on Cu(111) [229, 230].

In our studies we characterize the 2D array of QDs by STM/STS providing site specific, *local* information on the effect of Xe adsorption on the n=1 PLS and by complementary ARPES giving access to the coherent part of the interaction between the QDs.

In the following we characterize two extreme QD occupancy cases: the vacant network and the fully filled network with 12 Xe atoms adsorbed in each QD. The *local* STM/STS results are presented in Figure 8.1. The spatially resolved *dI/dV* line scan (white solid line) in Figure 8.1 (a) illustrates the spectral and spatial distribution of the n = 1 PLS within the vacant network, whose maximum is observed at -201 $\pm$ 6 mV [15]. Note that the $\sim$ 90 mV FWHM and its asymmetric peak shape are characteristic signatures of coupled QDs [54, 160]. Upon adsorption of 12 Xe atoms in each pore of the network (see Section 8.4.2 for experimental details) [164, 226], the n=1 PLS appears modified, shifting to lower BE, whose maximum peaks at -136 $\pm$ 7 mV, amounting to a $\sim$ 60 mV shift [Figure 8.1 (b)]. A FWHM of $\sim$ 110 mV is measured which is comparable to the $\sim$ 90 mV for the empty case observed in Figure 8.1(a).

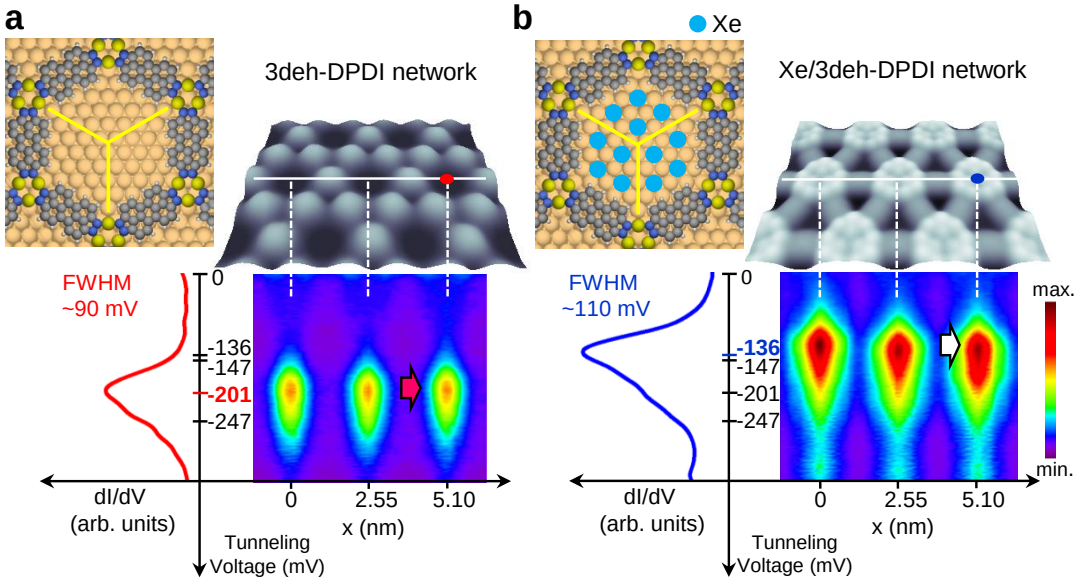

FIGURE 8.1: QD electronic structure alteration through Xe occupation. Two different network configurations have been measured by STS for investigating cooperative interactions between the QD states: Empty 3deh-DPDI network (a) and filled network (b) with 12 Xe atoms adsorbed in each QD are shown in their corresponding upper insets. In each case, a series of *dI/dV* spectra was acquired along the white solid line (indicated in the STM images) crossing three QDs. The *dI/dV* spectra taken at the red and blue dots on the insets are plotted on the left-hand side of the *dI/dV* traces (size of STM images 7.8 x 4.3 nm^2. STM parameters: V = -200 mV; I = 700 pA (a) and V = -10 mV; I = 50 pA (b).

In the same way, such electronic effects on the n= 1 PLS when the network pores are fully filled with Xe atoms can be studied with ARPES (Figure 8.2). The quasi free-electron like Cu(111) Shockley state [purple line in Figure 8.2 (a)] is modulated into a shallow dispersive band consistent with the coupling between the QDs [15], when the network saturates the surface. Upon Xe filling of the pores (see Section 8.4.1 for preparation details), no pronounced changes are observed, apart from a certain broadening and loss of intensity in the n=1 PLS band [Figure 8.2 (b)]. However, the second derivative treatment of the data [Figure 8.2 (c, d)] exhibits a slight upward shift of the fundamental energy of the band ($\overline{\Gamma}$ point) and a smearing of the features due to the Xe adsorbates [196].

Some quantitative values can be extracted from the ARPES spectra (Figure 8.3 and Table 8.1): First, the dispersion of the n=1 PLS in close proximity to the $\overline{\Gamma}$ point (k_x= $\pm$ 0.06 $Å^{-1}$) for the empty and Xe filled cases. We consider only this region around the $\overline{\Gamma}$ point because it is far from the dispersion reversal of the zone boundary gaps ($\overline{M}$ point) [Figure 8.3 (a, b)]. A slight shift of the fundamental energy ($\sim$ 30 meV) is found when extracting and comparing EDCs at the $\overline{\Gamma}$ point [Figure 8.3 (c)]. We interpret this energy shift as the result of Pauli repulsion between the electronic states of Xe and the n=1 PLS, similar to the previously reported shift of the Cu(111) Shockley state caused by the adsorption of Xe (Table 8.1) [196]. Second, the effective

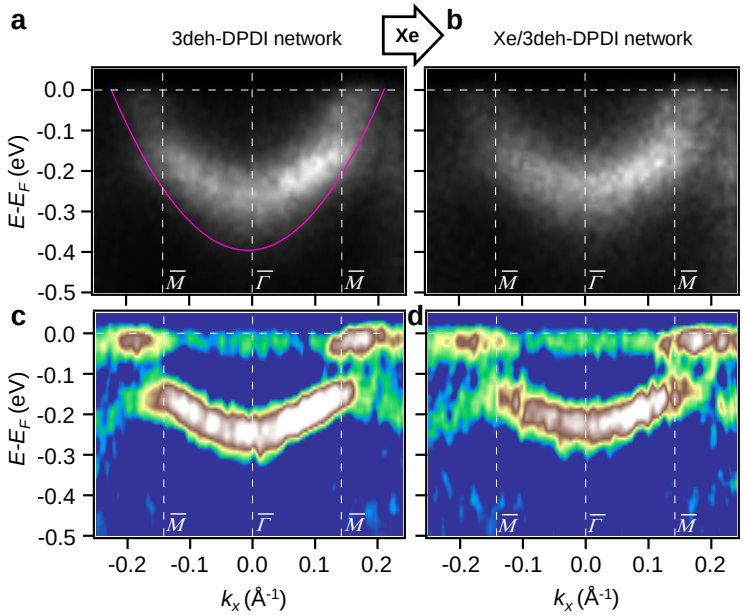

FIGURE 8.2: Influence of Xe adsorption on the partially localized states hosted at the pores of the network. (a) ARPES experimental spectral function acquired for the empty network. Compared to the pristine Cu(111) Shockely state (in purple), the characteristic cosine shape band develops when the n = 1 PLS couples among neighboring pores of the network (measured along $\overline{\Gamma M}$ high symmetry direction). (b) ARPES experimental spectral function after Xe adsorption in the pores. A slight shift towards higher energies is observed. (c, d) Second derivative treatment of the bands in (a, b) to better visualize the replicating bands and gaps at the zone boundaries ($\overline{M}$ point).

mass can also be extracted from fitting the EDCs [Figure 8.3 (d)]. A slight flattening of the band is dectected, evidenced by a notable increase in the effective mass ($m^*/m_0 = 0.57$ for the empty and $m^*/m_0 = 0.66$ for the filled case). This effect may suggest a slight loss of interpore-coupling and consequently, an increased localization of the n=1 PLS [54]. Note that such strong vertical interaction effects between Xe and n=1 PLS are not present for the free-electron-like Cu(111) Shockley state, where no significant change of the effective mass is observed with an adsorbed Xe layer (cf.

TABLE 8.1: Band structure parameters extracted from ARPES measurements for the pristine substrate and the network with and without Xe. [a)] The values refer to $E - E_F$ at normal emission (band bottom); [b)] The effective mass and the bandwidth of the n=1 PLS along $\overline{\Gamma M}$ (details of how m^* is extracted from the ARPES spectral functions can be found in Section 8.4); [c)] DPDI$_{net}$ denotes the Cu-coordinated 3deh-DPDI network formed on Cu(111); [d)] Values from ref. [196].

Sample	$E - E_F$ at $\overline{\Gamma}$[a)] (meV)	m^*/m_0[b)]	Bandwidth (meV)
Cu(111)	-434 $\pm$ 2[d)]	0.43 $\pm$ 0.01[d)]	—
Xe/Cu(111)	-291 $\pm$ 2[d)]	0.44 $\pm$ 0.02[d)]	—
DPDI$_{net}$[c)]/Cu(111)	-270 $\pm$ 10	0.57 $\pm$ 0.02	90 $\pm$ 10
Xe/DPDI$_{net}$[c)]/Cu(111)	-240 $\pm$ 10	0.66 $\pm$ 0.02	70 $\pm$ 10

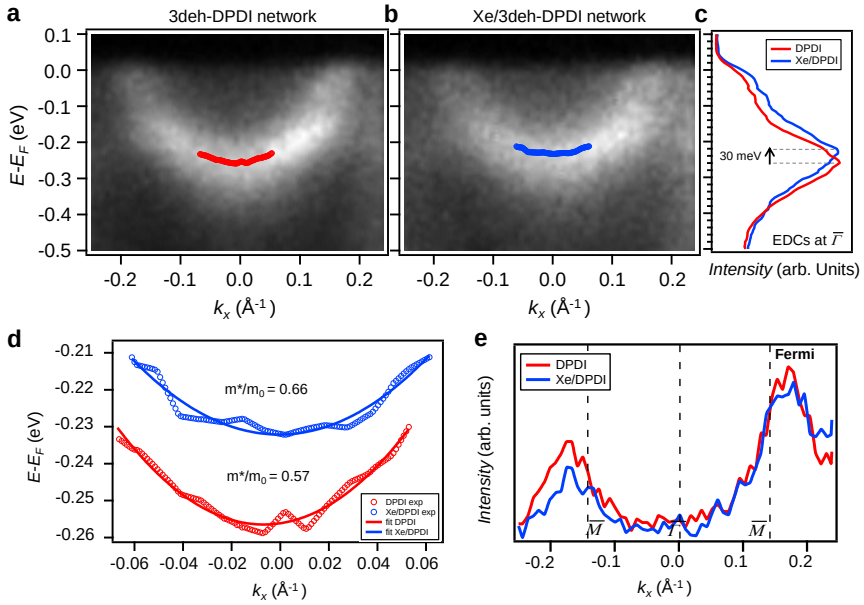

FIGURE 8.3: Effective mass renormalization after Xe adsorption. ARPES spectral function of the surface state region (a) without Xe and (b) after Xe adsorption fully covering the pores (12 Xe atoms per pore) of the Cu-coordinated 3deh-DPDI network on Cu(111). The data were fit using a single convoluted Lorentzian-Gaussian component on a linear background and multiplied by a Fermi-Dirac distribution. (c) Normal emission EDCs (k_x = 0) from (a, b) where a $\sim$ 30 meV shift to higher energies is found. (d) From the band bottom dispersion fitting close to the $\overline{\Gamma}$ point, an upward energy shift of the minimum energy and a reduction of the band dispersion are observed when Xe is adsorbed in the pores. Using a parbolic fit to each we extract an apparent increase of the effective mass from (a) m^*_{empty}/m_0 = 0.55 $\pm$ 0.02 to (b) m^*_{Xe}/m_0 = 0.66 $\pm$ 0.02. (e) Fermi wave-vector (k$_F$) measurements don't reveal apparent differences in the number of electrons present in between both 2DEGs cases.

Table 8.1) [196]. Finally, in Figure 8.3 (e) we monitor the Fermi wave-vector (k_F) and no change is detected, corroborating that the number of electrons in the 2DEG is not affected by the Xe presence [220].

To investigate the influence of the surrounding QDs upon the electronic state of an isolated unit, we generated different configurations by repositioning single Xe atoms with the STM tip [231–233]. Two model arrangements were studied in detail: a filled QD surrounded by empty ones [Figure 8.4 (a)] and an empty QD surrounded by filled ones [Figure 8.4 (b)].

In the first model case [Figure 8.4 (a)], the spatially resolved *dI/dV* line scan of the QDs for the filled pore is significantly different from the one observed for the individual pore in the Xe filled network [cf. Figure 8.1 (b)]: the Xe induced component at lower BE dominates in intensity [Figure 8.4 (a), white arrow] exhibiting a sharp QD state peak with a FWHM of $\sim$ 50 mV [Figure 8.4 (a), blue *dI/dV* spectrum]. We attribute this sharpening to the additional out-of-plane confinement of the state via the Pauli repulsion imposed by Xe and the loss of coupling with the empty neighboring pores. The surrounding empty QDs still feature the same spatially resolved *dI/dV* trace as the vacant array [cf. Figure 8.1 (a)]. Closer inspection reveals that the

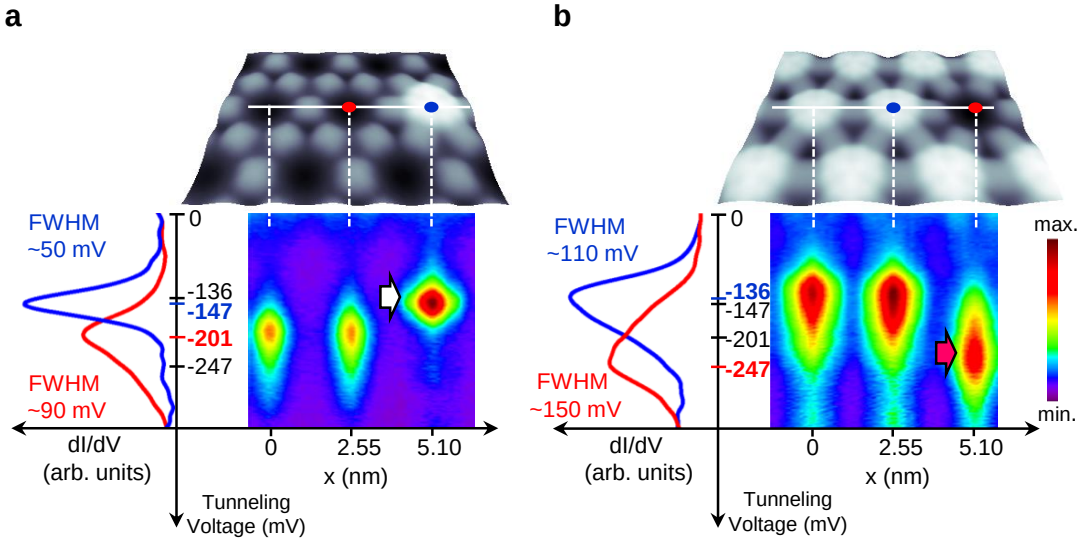

FIGURE 8.4: QD electronic structure alteration through Xe single occupation or depletion. Using STM atom manipulation two different network configurations are engineered for investigating local interactions at each particular QD: Filled QD with 12 Xe atoms surrounded by empty QDs (a) and empty QD surrounded by filled QDs with 12 Xe atoms adsorbed in each QD (b). In each case, a series of *dI/dV* spectra were acquired along the white line (indicated in the top STM images) crossing three QD units. The *dI/dV* spectra taken at the red and blue colored dots superimposed on the STM images are plotted on the left-hand side of the *dI/dV* traces. Size of STM images 7.8 x 4.3 nm^2. STM parameters: V = -145 mV; I = 100 pA (a) and V = -145 mV; I = 100 pA (b).

single filled pore exhibits a QD state peak at slightly higher BE ($\sim$ 10 meV) than the filled network [Figure 8.1 (b)]. We tentatively attribute this to the fact that when electronic states couple, the n=1 PLS peak broadens and the peak shape becomes asymmetric.

In the second model case, we consider a central empty QD surrounded by filled ones [Figure 8.4 (b)]. The spatially resolved *dI/dV* trace of the QD state of the empty pore does not exhibit the Xe induced localization of the previous case. On the contrary, a bound state-like feature is observed, whose peak shifts to higher BEs (-247 $\pm$ 7 mV) than the reference case of the vacant network [cf. Figure 8.1 (a)] [234, 235]. The *dI/dV* signal of the surrounding QDs is the same as for the filled network reference [Figure 8.1 (b)]. In addition, the single empty pore peak looks broadened, showing a FWHM of $\sim$ 150 mV. At this point, the origin and shape of this confined state cannot be explained.

To explain all the different cases, we turn to simulating the electronic properties for all the aforementioned Xe-filling configurations using EBEM/EPWE. These simulations have been performed in close collaboration with Dr. Zakaria M. Abd El-Fattah (Al-Azhar University, Egypt). We first simulate the electronic structure of the 3deh-DPDI metal-organic network on Cu(111). As we are mainly interested on the n=1 PLS and in the pore center spectra, following Model 2 in Chapter 7 we parametrize the scattering potential landscape of 3deh-DPDI and assign both

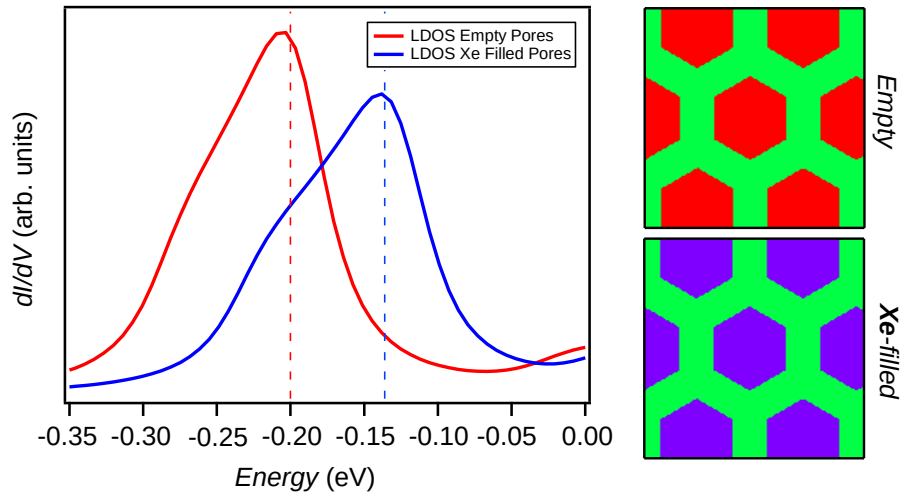

FIGURE 8.5: LDOS at the pore center for all empty and all Xe-filled pore configurations simulated with EBEM/EPWE. The scattering potential landscape for the all empty case in shown in red while the Xe-filled case is shown in blue. The scattering potential amplitudes used and Cu SS renormalization values are indicated in Table 8.2. Both simulated LDOS at the pore center match the experimental observations of Figure 8.1.

molecules and Cu adatoms in coordination a common repulsive scattering amplitude ($V_{network}$). The Cu SS renormalization is also taken into consideration (see Table 8.2). The LDOS at the center of an empty pore (red spectrum in Figure 8.5) matches the peak shape and energy of the n=1 PLS. The vertical red dashed line corresponds to the peak energy measured with STS in Figure 8.1 (a). To simulate the Pauli repulsion effect produced by Xe adsorbates on the n=1 PLS, we slightly increase the potential inside the pore by 80 meV (Table 8.2) so that the resulting n=1 PLS (blue spectrum) matches the experimental shift ($\sim$ 60 mV) measured in Figure 8.1 (b) (dashed blue line). A small increase in coupling is detected since the molecular barrier now represents a smaller effective scattering potential ($V_{network}$ = 310 meV) than the empty network. This is in agreement with the slight increase in the peak width detected in Figure 8.1 (b).

Once we have verified that EBEM/EPWE can accurately simulate the Xe induced electronic effects, we proceed to simulate the two Xe filling configurations studied in Figure 8.4. First, we simulate the scenario where all the pores are empty (V_{pore}

TABLE 8.2: EBEM/EPWE reference and scattering parameters used for different Xe-filling configurations

Configuration	$E_{EBEM}^{Ref,\overline{\Gamma}}$ (eV)	m^*/m_0	V_{pore} (meV)	$V_{network}$ (meV)
All Pores Empty	-0.45	0.49	0	390
All Pores Xe-Filled	-0.45	0.49	80	390
All Empty/ One Xe-Filled	-0.45	0.49	0/80	390
All Xe-Filled/ One Empty	-0.45	0.49	80/0	390

= 0 eV) and only one single pore is filled with Xe (V_{pore} = 80 meV) [Figure 8.6 (a) and Table 8.2]. The LDOS for the empty pore is taken at a pore that is completly surrounded by empty pores (black dot in the scattering landscape inset). The LDOS peak (red spectrum) matches the expected shape and energy for the characteristic n=1 PLS. This means that a coherent electronic band exists from the coupling between empty pores, irrespective of the presence of a single pore filled with Xe. Such condition supports the experimental observation that ARPES will still detect the n= 1 PLS band structure upon preseence of a small amount of defects. The LDOS at the Xe-filled pore shows a localized state found at higher energies, nicely matching the experimental peak position (dashed blue line). In addition, a broad weak shoulder is detected at ~ -0.25 eV. This feature corresponds to the lower energy part of the states (bonding side) of the n=1 PLS band. As mentioned already in Chapter 5, bonding states are more spread out due to their large electron wavelength than the antibonding ones and therefore can slightly leak into the isolated Xe-filled pore. However, there is no sign of the antibonding states, since they are much more localized inside each pore [54, 160].

Next, we invert the scenario, and in Figure 8.6 (b) simulate the case where all the pores are filled with Xe and only one single pore is left empty. This configuration corresponds to the one experimentally studied in Figure 8.4 (b). For the Xe-filled pore, a position is chosen so that it is only surrounded by identical pores (yellow dot in the scattering landscape inset). The blue LDOS matches the expected n=1 PLS both in shape and energy position (cf. dashed blue line for STS). Notably, the empty pore (in red) also agrees with the experimental findings and represents an interesting case. The overall peak shape agrees with the inverted asymmetry and width detected experimentally in Figure 8.4 (b). The lineshape can be rationalized as a combination of the lack of coupling of the empty pore with the neighboring Xe-filled ones and a localized state that appears at high BEs, whose fundamental energy is located around -0.23 eV. This localized state cannot couple with neighboring ones since their fundamental energy is at lower energies (blue spectrum). Contrarily, the bonding states of the Xe n=1 PLS band can leak into the isolated empty pore, inducing a prominent shoulder at -0.17 eV and increasing considerably the overall peak width of the red spectrum. Note that we practically do not observe any sign of the antibonding states in the red spectrum due to their more localized nature.

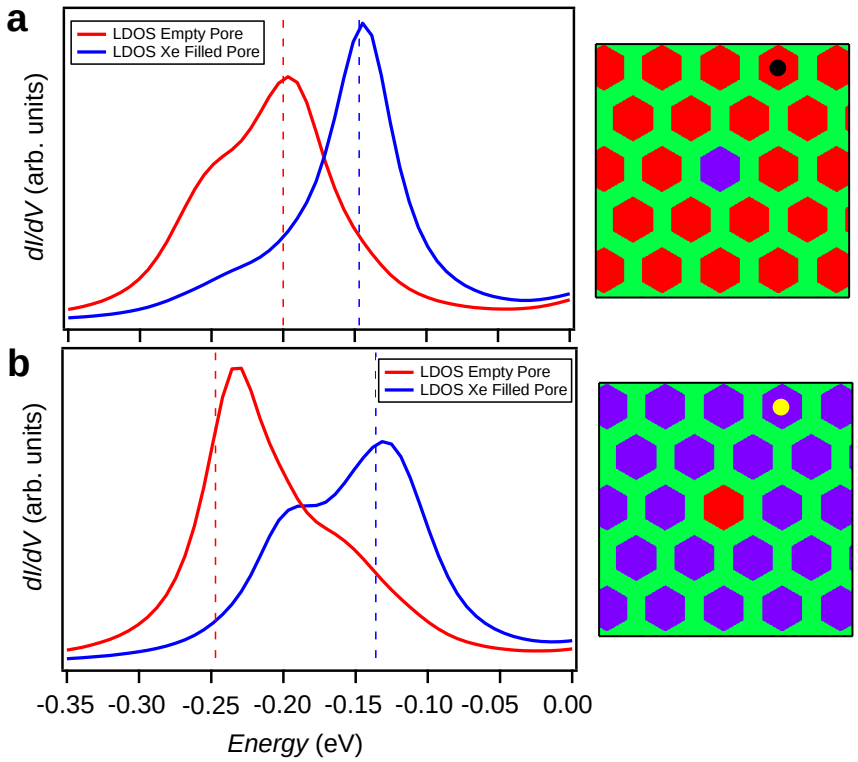

FIGURE 8.6: EBEM/EPWE simulated LDOS for isolated Xe-Filling Configurations. (a) Situation where a single Xe-filled pore is surrounded by empty pores. The LDOS at the Xe-filled pore matches the localized state detected experimentally and the features at the empty pore correspond to the expected n=1 PLS. The weak shoulder at lower energies in the blue spectrum evidences the widely spread bonding states leaking inside the pore. (b) Inverted scenario where a single empty pore is surrounded by Xe-filled pores. Xe-filled pores bear the characteristic n=1 PLS shifted in energy due to Pauli repulsion effect. The empty pore shows and inverted asymmetric peak with two contributions: a localized state at high BEs (-0.23 eV) and a prominent shoulder at -0.17 eV corresponding to the leaky bonding states of neighboring (Xe-filled) pores.

8.3 Conclusions

In summary, we demonstrate that it is possible to engineer the electronic structure of the n=1 partially localized state (n=1 PLS) in an array of QDs by globally adsorbing Xe guests inside the nanocavities or locally repositioning Xe atoms. Due to Pauli repulsion effects, the n=1 PLS shifts to lower binding energies (~ 60 meV) when the pores are fully filled with Xe atoms. This tendency is corroborated by ARPES measurements, where the fundamental energy of the n=1 PLS band also shifts towards the Fermi energy. By atomic manipulation with STM, we can design and engineer different Xe filling configurations at the *local* or first neighbor scale: an empty pore surrounded by filled ones and *vice versa*. Such configurations yielded highly localized states accompanied by features stemming from the surrounding states of the n=1 PLS electronic band. In contrast, the QDs surrounding the isolated one remain practically unaffected in their LDOS lineshape. These results, have been corroborated by EBEM/EPWE modelling by using the same scattering potential landscape

as in model 2 of Chapter 7 (repulsive scattering potentials) along with the required Cu SS renormalization. The additional Xe induced effect has been simulated by introducing a shallow 80 meV potential inside the pores. Such delicate electronic effects observed with Xe adsorbates demonstrates the consistency obtained in previous chapters of the manuscript that delves into the intricacies of confinement and interpore coupling effects.

8.4 Supplementary Information for This Chapter

8.4.1 Sample Preparation and ARPES Acquisition Details

To avoid contributions from the Shockley state of bare Cu(111) to the ARPES signal, DPDI was sublimated onto Cu(111) held at room temperature (RT) in wedge geometry (coverage gradient) in proximity of the optimal coverage. Afterwards the sample was annealed to $\sim$ 520 K until a sharp and intense signal emerging from partial localization of the QD state, as in refs. [15, 158], was visible in the ARPES channel plate detector [Figure 8.2 (a)]. The Xe dosing experiment was started immediately after the sample temperature dropped below 60 K, but was higher than 25 K to keep the adsorbate mobility [226, 236]. Xe core level (9-5 eV BE) and surface state (close to Fermi energy) regions at normal emission were acquired alternatively as a function of time while keeping Xe pressure in the chamber constant (5×10^{-10} mbar). The evolution of the $5p_{3/2}$ and $5p_{1/2}$ core levels and the n=1 PLS band (at $\overline{\Gamma}$) as function of the Xe exposure time is shown in Figure 8.7 (total exposure time amounted to $\approx$ 30 min). At 0 Langmuir (L), without any Xe exposure, the n=1 PLS looks as in Figure 8.2 (a) while no Xe core level features are visible [black spectrum in Figure 8.7 (b) and dashed black line in Figure 8.7 (a)]. At 0.4 L the single Xe core level features start to be predominant, where a doublet at 7.46/6.23 eV is observable in Figure 8.7 (b) (blue line). This corresponds to the situation where the pores are filled with 12 Xe atoms each. At this point, the n=1 PLS already responds by shifting its fundamental energy $\sim$ 30 meV while the intensity begins to drop as seen for the blue spectrum in Figure 8.7 (d) and dashed blue line in Figure 8.7 (c). Beyond this dose (> 0.4 L up to 1.0 L) a less bound Xe component evolves (doublet at 7.29/6.08 eV). We attribute this new peak to the deposition of Xe atoms on top of the molecular backbone and coordination sites. For 1.0 L and beyond, the n=1 PLS appears already quenched [green spectrum in Figure 8.7 (d) and green dashed line in Figure 8.7 (c)] coinciding with the Xe multilayer formation.

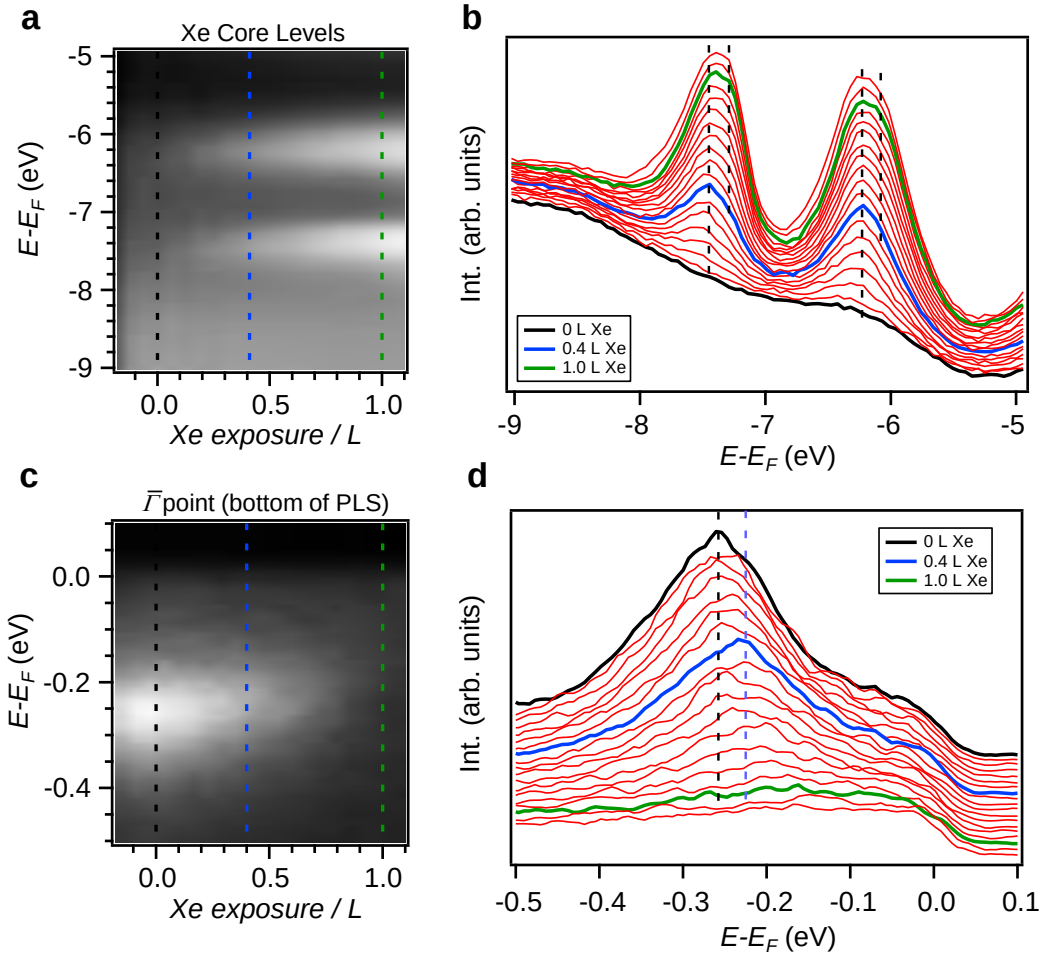

FIGURE 8.7: Changes in the electronic structure of the Cu-coordinated 3deh-DPDI network on Cu(111) upon Xe exposure monitored by ARPES. (a, b) The $5p_{3/2}$ and $5p_{1/2}$ Xe core levels and (c, d) the surface state region alternatively recorded during Xe exposure expressed in Langmuirs. In (a) the photoemission intensity is represented as a grayscale plot, whereas in (b) selected EDCs are shown as a waterfall. Initially, a single component (doublet at 7.46/6.23 eV), which we attribute to the adsorption within the network pores, increases in intensity up to ~ 0.4 L (blue line in (a); blue spectrum in (b)). From that moment, a less bound component (doublet at 7.29/6.08 eV) develops, which we attribute to adsorption at the network backbone, until completion of the full layer (green line in (a); green spectrum in (b)). Both doublet energies are indicated as vertical dotted lines. The evolution of the n=1 PLS at $\overline{\Gamma}$ is shown as a grayscale plot in (c) and as selected EDCs in (d). We observe a strong attenuation of the state and a decrease of its BE upon increase of Xe exposure. The ~ 30 meV shift of the n=1 PLS is determined from the black and blue spectra which were acquired at the same Xe exposure as the black and blue spectra in (a, b).

8.4.2 STM/STS Measurements

Sample Preparation for STM/STS Measurements

All STM/STS measurements have been performed by Dr. Sylwia Nowakowska from Basel University (Switzerland). The Cu-coordinated 3deh-DPDI network on Cu(111) was prepared according to the preocedure described in ref. [169]. Xe of purity 99.99% was dosed onto the sample placed in the STM (Omicron Nanotechnology GmbH with Nanonis SPM control system) operated at 4.2 K, with the cryoshields open and the leak valve being in line-of-sight with the sample. The sample was exposed to 120 L (Langmuir) of Xe (1.3×10^{-7} mbar for 1200 s) resulting in the increase of the sample temperature to 9 K. The STM measurements performed after cooling the sample back to 4.2 K revealed different numbers of Xe atoms adsorbed in the pores as well as the domain boundaries and step edges. Filling of all pores with 12 Xe atoms was performed by subsequent annealing to 45 K followed by cooling to 4.2 K for the STM measurements.

Repositioning of Single Xe Atoms

All the condensates discussed here were obtained by controllably removing of Xe atoms from the pores of the network by means of STM repositioning. Noticeably, new configurations that are not occurring spontaneously upon Xe exposure can be created in this way [Figure 8.4 (a, b)] [53, 164].

STM/STS Measurement Details and Data Analysis

In the STM the bias voltage is applied to the tip. The bias voltages given in this chapter refer to a grounded tip. STM measurements were performed in constant current mode with Pt-Ir tips (90% Pt, 10% Ir), prepared by mechanical cutting followed by sputtering and controlled indentation in the bare Cu(111) substrate. All STM images were acquired with a Xe functionalized tip, which allows for obtaining atomic resolution of Xe condensates [53, 164].

To avoid modification of the condensates via interaction with the tip, the sample bias was selected within a range of -10 mV to -80 mV, whereas the tunneling current was set within the range of 5-50 pA. The STM data were processed with the WSxM software [174]. For better comparability of the data the color histograms of the STM images were adjusted. Low-pass filtering was used for noise reduction.

All *dI/dV* spectra were recorded with open-feedback loop and with Xe functionalized tip. Control spectra were acquired with a metallic tip and no difference was observed in accordance with [237].

The *dI/dV* data presented in Figures 8.1 and 8.4 were extracted from the grid spectroscopy measurements, in which an area of 7.8 x 4.3 nm^2 was mapped by acquisition of *dI/dV* spectra above each point with the resolution of 50 points x 30 points for the empty network and 60 points x 30 points for the other three cases [16, 17]. The initial tip conditions amounted to 400 mV/70 pA (lock-in frequency: 513 Hz; zero-to-peak amplitude: 8 mV). As described in detail in ref. [227] the value of the initial voltage was chosen such that no PLS or network backbone related contribution was present. Owing to that, normalization could be performed by setting the same *dI/dV* value at the setpoint energy of all *dI/dV* spectra. In this way artifacts originating from local work function (surface potential) variations are minimized [227].

Chapter 9

Part III: Introduction to On-Surface Synthesized One-Dimensional Zigzag Covalent Polymers

The discovery of graphene's exceptional electronic properties [238, 239] triggered the research of graphene-based electronic devices. However, the absence of a bandgap has precluded the use of this two-dimensional material in electronic applications. A band gap can be introduced into graphene through quantum confinement in one of its lateral dimensions, forming graphene nanoribbons [240]. Since the electronic properties of GNRs are sensitively dependent on their width and edge structure, it is an essential requirement to control their morphology down to the atomic level, a degree of precision that currently cannot be obtained through top-down methods [241]. Recently established bottom-up techniques based on on-surface synthesis in UHV [57, 242], have facilitated the manufacture of atomically well-defined GNRs of various widths and edge structures [28, 29, 243]. Notably, numerous types of armchair edge nanoribbons [Figure 9.1 (a)], as well as ribbons with chiral and zigzag edges have been produced, the latter ones hosting low energy edge-localized states [28]. The high degree of control obtained so far has not only facilitated fabrication of atomically precise GNRs of a single type, but also heterojunctions, such as metal-semiconductor junctions [244], type-I (straddling gap), type-II (staggered gap) junctions [23, 188] and topological GNR superlattices [25, 30] [Figure 9.1 (b)]. Recently, even multifunctional nanoporous graphene has been synthesized from GNR fusing, representing a highly versatile semiconductor for simultaneous sieving and electrical sensing of molecular species [24] [Figure 9.1 (c)]. They all constitute primary building block examples for nanoelectronic applications such as high-performance field-effect transistors and ultra-low power devices such as tunneling field-effect transistors [32, 245, 246].

GNRs are conjugated polymers highly related to other types of organic chains that are extensively used in industry as light emitting materials, photocatalysts, solar cells and biosensors due to their large and tunable bandgaps [247–250]. Control over their electronic properties is accomplished through topological functionalization of

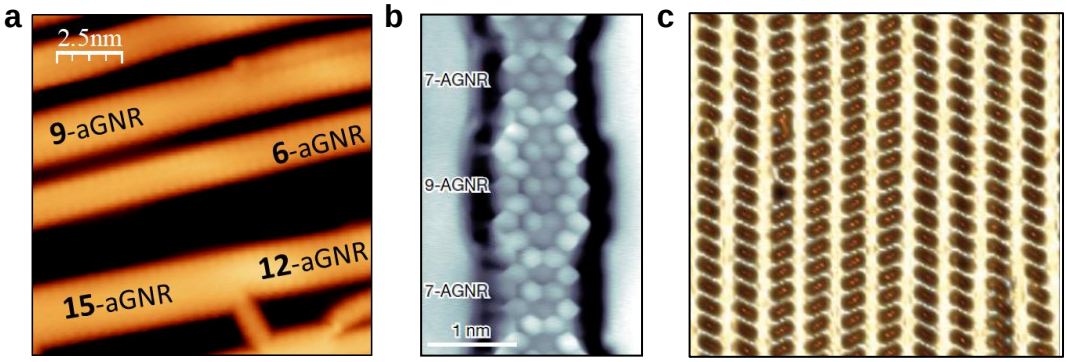

FIGURE 9.1: On-surface synthesis of GNRs and nanoporous graphene. (a) STM image of armchair type GNRs with varying widths obtained after laterally fusing poly-(*para*-phenylene) chains (adapted from ref. [29]). (b) A bond-resolved STM image of 7/9-AGNR superlattice shows the bond-resolved structure of the heterojunction interface (adapted from ref. [25]). (c) STM image (18×18 nm^2) of the nanoporous graphene overlayer synthesized on Au(111) (adapted from ref. [24]).

these π-conjugated oligophenylene chains, *i.e.* modification of their conductive pathways. In particular, changes of conjugation (from linear to cross-conjugation) by precise transitions from *para*- to *meta*-ligand substitutions [251, 252] weaken the electronic communication between the repeating units of the polymer [253, 254]. Such modifications have also been described as quantum interference electron pathways [255–257], and bear predicted effects such as scarcely dispersive bands [251], wider electronic bandgap [258], distinct optical properties [250], electronic switching capabilities [259] and low conductance properties [65, 255–257, 260]. However, periodic *meta*-junctioned zigzag chains may also show enhanced charge mobility as compared to their poly-(*para*-phenylene) counterparts, reaching values comparable to those of amorphous silicon [261].

Despite this wealth of industry attractive properties of cross-conjugated polymers, key fundamental information, such as the predicted electronic structure awaits experimental validation. Such deficiency of fundamental knowledge limits the confidence in the existing predictions, according to which topology is expected to affect the electronic properties of the polymer. Several obstacles are responsible for the lack of the aforementioned experimental confirmation: i) the need of generating atomically identical chains exhibiting repeated *para*- to *meta*-ligand substituted units, ii) the synthesis of well-aligned chains, to be probed by non-local, averaging spectroscopies, iii) the minimization of lateral interactions, prone to affect their intrinsic band structure, and iv) the right choice of a support that sufficiently decouples the electronic signal from the investigated oligophenylene chains.

To overcome such obstacles, solutions can be found within the context of Surface Science. Particularly, the first prerequisite for obtaining perfectly reproducible cross-conjugated zigzag polymers can be accomplished by bottom-up on-surface synthesis. Surface-assisted C-C coupling processes such as the Ullmann coupling

reaction, have recently been applied to generate GNRs with different edge terminations and widths [25, 27, 30, 62, 243, 262], and other types of oligophenylene chains [26, 77, 263–265]. Secondly, the chain alignment for non-local characterization can be achieved by the use of nanotemplated substrates, such as vicinal surfaces [81, 82, 103, 147]. These special surfaces have been successfully used for the macroscopic alignment of carbon-based chains, a fundamental requirement for ARPES experiments [26, 27, 77–79]. With respect to the minimization of lateral interchain coupling, this is an inherent feature of the Ullmann-type surface reactions [263] since the halogens are cleaved during the synthesis positioning themselves between neighboring chains [26, 77, 78, 265]. These adatoms are reported to laterally decouple adjoining chains, without affecting the polymer's band structure, except for a minimal rigid energy shift similar to doping effects [26, 78]. Finally, the substrate plays a fundamental role as a catalyst of the Ullmann reaction, making its choice crucial for a successful oligomer coupling. Good candidates that present excellent yields, control and reproducibility are the closed packed surfaces of coinage metals, which are extensively used for Ullmann-type surface reactions.

In the following Chapter 10, we show how we have overcome all the aforementioned obstacles and have generated an extended film of atomically precise oligophenylene zigzag chains on a vicinal Ag(111) surface, as evidenced by STM and LEED. The electronic band structure of such films has been unravelled by means of ARPES and complemented by STS measurements on Ag(111). In this way, we determine the experimental energy gap and visualize the spatial distribution of the frontier orbitals. Such wealth of experimental information is clarified and expanded by a comprehensive set of DFT calculations and EPWE simulations. This work has been recently accepted for publication [266].

As previous chapters, the next one will have a paper-like format, starting with a brief introduction indicating the main motivation. After this, the main results will be described and discussed supported by several figures and it will end with the conclusions and some additional supplementary information.

Chapter 10

Electronic Structure Tunability by Periodic *meta*-Ligand Spacing in One-Dimensional Organic Semiconductors

10.1 Introduction

In the previous part of this thesis, the electronic structure studied from nanoporous networks came as a consequence of the modification of the substrate's 2DEG, which was independent of the existing molecular states. In this chapter, the molecular structures are dominant and we investigate possible confinement effects on 1D organic nanostructures generated with atomic precision by on-surface synthesis processes. We use this 'dry' chemistry to introduce topological variations in a conjugated poly-(*para*-phenylene) chain in the form of *meta*-junctions. As evidenced by STM and LEED, we produce a long-range ordered, monolayer thin zigzag chain film on a vicinal silver crystal. These cross-conjugated nanostructures are expected to display altered electronic properties, which are now unravelled by two highly complementary experimental techniques (ARPES and STS) and theoretical calculations (DFT and EPWE). We find that *meta*-junctions dominate the weakly dispersive band structure, while the bandgap is tunable by altering the linear segment's length. These periodic topology effects induce significant loss of electronic coupling between neighboring linear segments leading to partial electron confinement in the form of weakly coupled quantum dots. Such periodic quantum interference effects determine the overall semiconducting character and functionality of the chains. Designing such molecular organic semiconductors with distinct frontier orbitals is key for the development of devices with desirable properties.

10.2 Results and Discussion

In collaboration with Prof. Gottfried from Philipps-Universität Marburg (Germany), we have produced a monolayer film of cross-conjugated zigzag chains from the surface polymerization of the 4,4"-dibromo-*meta* terphenyl (DMTP) molecular aromatic precursors *via* C-C coupling [see Figure 10.1 (a) and Section 10.4.4]. The template of choice is a vicinal Ag(111) crystal surface with linear, monoatomic steps running parallel to the [11$\bar{2}$] direction [82] that corresponds to the so-called fully-kinked (100% kinked) configuration of the step-edge [Figure 10.1 (c, d)]. We used this particular substrate since it provides a higher flexibility to reconstruct and therefore accommodate the produced zigzag structures more efficiently (cf. Section 10.4.4). Indeed, we can already disclose that we achieved an excellent film featuring a high yield of well-ordered and aligned zigzag chains. This alignment is critical for the ARPES measurements performed afterwards.

The formed zigzag chains appear practically planar on the surface [Figure 10.1 (b)] and are covalently bonded displaying the characteristic phenyl-phenyl distance of $a \sim 4.3$ Å along the straight segments and a superperiodicity of $L \sim 2.24$ nm between equivalent elbows [263, 267]. The unit cell of the chain features two straight subunits made up of two phenyl rings (in *para*-positions) linked to two edge rings acting as *meta*-junctions [green dots in Figure 10.1 (a)]. Note that in the STM image these chains are separated by spherical features that are attributed to Br atoms split off from the precursor molecules at the initial step of the on-surface reaction [29, 74, 175, 268–273]. The LEED pattern reveals that the organic chains are aligned parallel to the steps and show long-range order as they are commensurate with the underlying substrate [Figures 10.1 (b) and 10.9 in Section 10.4.4]. Particularly, the main silver diffraction spots (red and green circles) are sided by a set of spots aligned along the average step direction yielding a (9, 5; 0, 4) superstructure. Note that the best alignment is observed on a vicinal plane $\sim 3.6°$ off from the (111) crystal position [see Figure 10.1 (c) and Section 10.4.4].

Our STM and LEED structural results contain the required ingredients (atomic precision of the structure, defined alignment, long-range order and minimization of lateral interactions by Br adatom presence) to expect the existence of a defined and coherent electronic band structure from these chains. Figure 10.2 (a-c) shows the second derivative (to enhance the details) of the ARPES spectral weight obtained from such a film saturating the surface (raw data is shown in Section 10.4.5). The resulting electronic structure in the direction parallel to the average step direction and the main axis of the zigzag chains (E vs k_y with k_x = 0.1 Å^{-1}), exhibits weakly dispersive bands between -1.8 eV and -3.5 eV, separated by a ~ 0.6 eV gap [Figure 10.2 (a)]. None of these ARPES features are observable on the pristine substrate (cf. Figure 10.8). A closer inspection reveals that each one of them consists of a pair of anti-phase oscillatory bands [Figure 10.11]. The spectral intensity peaks around $\frac{2\pi}{a^*}$, where a^* represents the projected phenyl-phenyl distance along the average chain

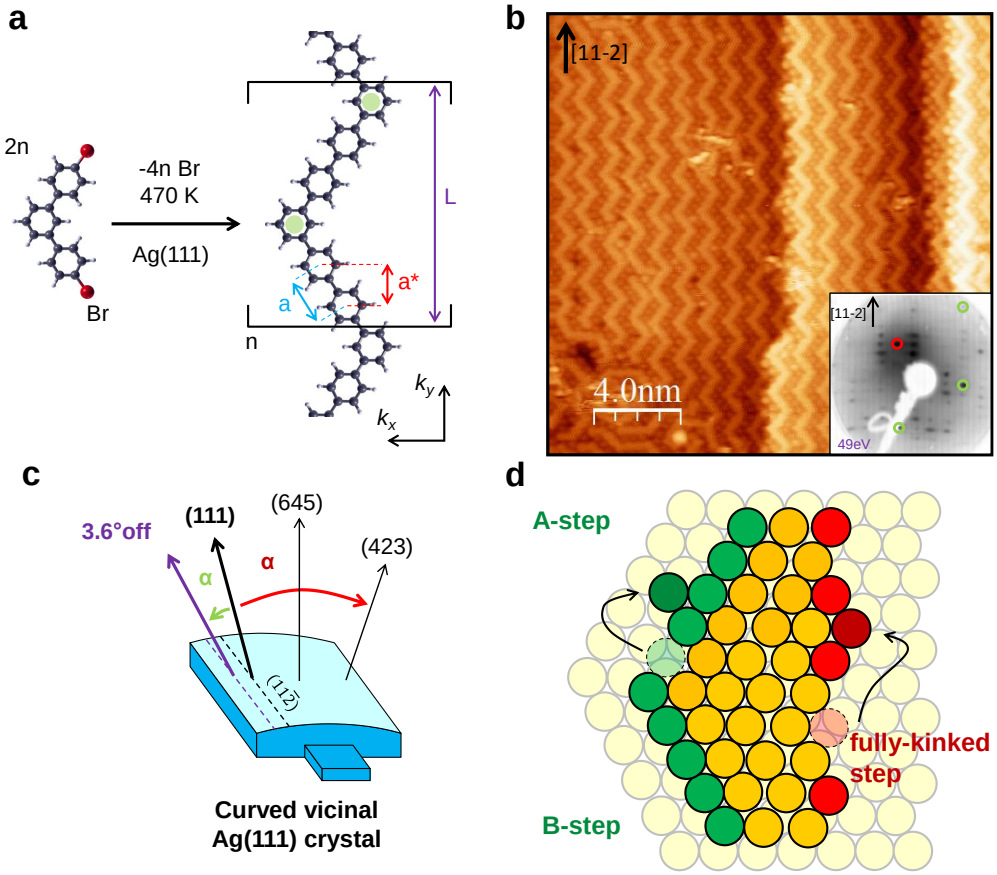

FIGURE 10.1: Structural arrangement of the zigzag chain film grown over a vicinal Ag(111) surface. (a) Schematic representation of the DMTP precursor and the resulting zigzag covalent chain, showing its characteristic lengths: phenyl-phenyl distance (a) and its projection along the chain's average direction (a^*), and polymer superperiodicity (L). (b) High resolution STM image after chain synthesis on a vicinal plane $\sim 3.6^\circ$ off from the (111) crystal position. The zigzag chains are separated by Br atoms and preferentially follow the step parallel direction ([11$\bar{2}$]). (STM parameters $V = -394$ mV, $I = 234$ pA, $T_{sample} = 100$ K). Inset shows the LEED pattern after the chain formation that exhibits single-domain, well-aligned arrangement. The superstructure spots are in registry with the circled main spots (in red the (0,0) and in green the substrate's first order diffractions), implying commensurability to the terrace atoms (LEED parameters: $E_{kin} = 49$ eV, $T_{sample} = 300$ K). (c) Schematic drawing of the curved Ag(111) substrate. (d) Atomic ball model highlighting the three step types present on close-packed vicinal surfaces. In our case, the step termination corresponds to the one ending in the green spheres (100% kinked) that runs along the [11$\bar{2}$] direction.

direction [Figure 10.2 (a)], assuring its molecular origin. This assertion is based on the fact that the real space molecular orbital configuration relates to the k-space positions and intensities of the obtained electronic bands [274]. The faint replicas with $\frac{2\pi}{L}$ periodicity (vertical dashed blue lines), stem from the zigzag chain superperiodicity L [Figure 10.1 (a)], in agreement with the STM dataset.

The 1D nature of these zigzag chains is demonstrated by the lack of dispersion perpendicular to the average chain axis. Figure 10.2 (b) shows a representative cut (E vs k_x) across the center of the 6$^{\text{th}}$ Brillouin zone [green arrow at k_y = 1.39 Å^{-1} in Figure 10.2 (a)], where discrete flat bands are observed. This confirms

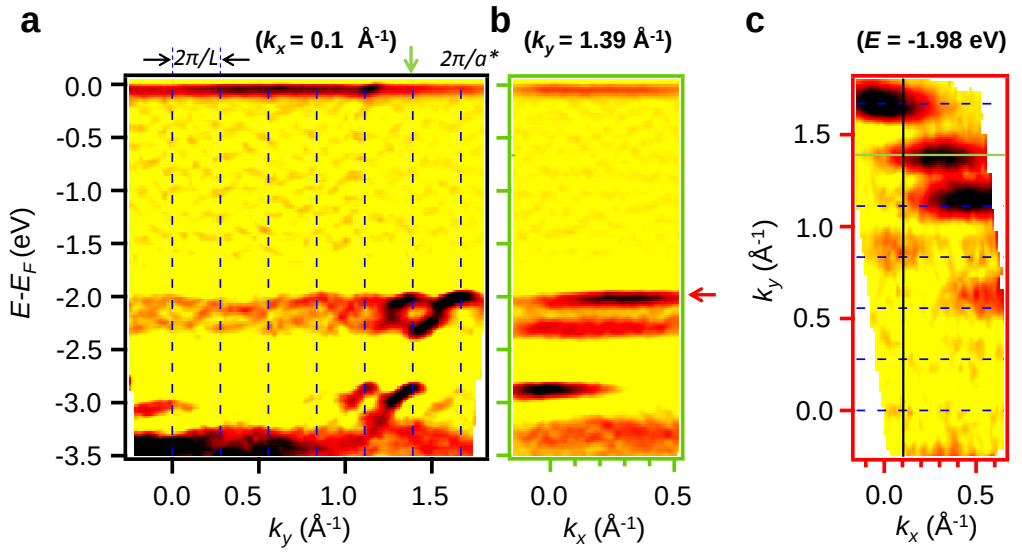

FIGURE 10.2: ARPES electronic band structure of the zigzag chain film grown over a vicinal Ag(111) surface. (a) ARPES experimental band structure of *meta*-junctioned cross-conjugated zigzag chains parallel to the average direction of chains and steps (E vs k_y with $k_x = 0.1$ Å^{-1}). (b) Experimental band structure perpendicular to the chain average axis (E vs k_x, with $k_y = 1.39$ Å^{-1} [green arrow in (a)]. (c) Isoenergetic cut (k_x vs k_y) at the top of the valence molecular band [$E = -1.98$ eV, marked by red arrow in (b)]. The position on the crystal is the same one as in Figure 10.1 (b). The second derivative of the intensity is shown in a linear color scale (highest being black). ARPES parameters: $h\nu = 21.2$ eV, $T_{sample} = 150$ K.

that they stem from different molecular orbitals of the zigzag polymer [275]. The non-dispersive character at the top of the valence band (red arrow at -1.98 eV) can also be traced from the isoenergetic cut (k_x vs k_y) shown in Figure 10.2 (c), where 1D polymer bands replicate at each Brillouin zone center, gaining intensity for the larger k_y values. These photoemission intensity modulations have been simulated with the EPWE method in collaboration with Dr. Zakaria M. Abd El-Fattah from Al-Azhar University (Egypt), which confirms that these features are neither affected by the templating Ag surface nor by the presence of Br atoms intercalated between the chains (see Figure 10.11 in Section 10.4.5).

Indeed, we experimentally find that the presence of Br embedded in between the zigzag chains only causes a rigid shift of the molecular band structure of about 200 $\pm$ 50 meV to higher energy, according to Figure 10.3 and in agreement with previous work [26, 78]. After the Ullmann coupling reaction takes place, zigzag chains condense into islands. The cleaved Br atoms accumulate between the chains (Figure 10.1 and Figure 10.3). These observations have been already reported for zigzag chains grown on Cu(111), hyperbenzene and honeycombene closed rings on Ag(111) and other covalent nanostructures such as PPP chains on Au(111) [78, 269–271]. The Br atoms remain on the Ag(111) up to $\sim$ 600 K and can likely stabilize the long-range ordered zigzag structures observed in the present work. According to Merino-Díez and co-workers [78] the desorption of Br atoms intercalated in between the chains produces a lowering of the workfunction and a shift of the electronic states to higher

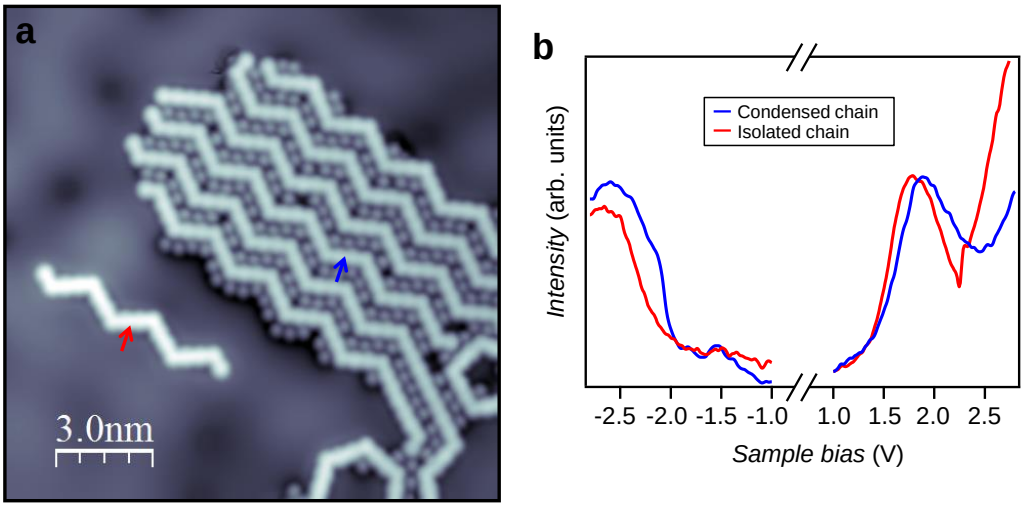

FIGURE 10.3: Effect of Br adatoms on the electronic structure of isolated and condensed chains grown on Ag(111). (a) STM image of a Br stabilized zigzag chain island (condensed chains) and an isolated, Br-free zigzag chain obtained *via* tip manipulation (Imaging parameters: 50 mV, 100 pA; frame: 15 $\times$ 15 nm^2). (b) Corresponding constant-height *dI/dV* spectra for the VB and CB at selected positions. The presence of Br rigidly shifts the VB and CB onsets by 200 ± 50 mV to higher energies (STS parameters: Bias voltage modulation of 10 mV$_{rms}$ at 341 Hz. Close-feedback parameters: -350 mV, 150 pA and 1200 mV, 100 pA for the negative and positive resonances regions, respectively).

binding energies without affecting their effective mass. We obtain similar results when we compare *dI/dV* spectra of tip manipulated isolated chains with island condensed ones [Figure 10.3 (a)]. In particular, the observed rigid shift of the frontier orbitals [cf. Figure 10.3 (b)] implies that the N=4 zigzag chain energy gap is unchanged. This evidences the limited effect of the halogen atoms on the electronic properties of the polymers.

Our ARPES results suggest that the zigzag chains are largely decoupled from the metallic substrate since the observed molecular bands do not show signs of hybridization with the substrate in that energy window [77]. Besides, the chains are semiconducting in nature with a bandgap certainly larger than 2 eV, since no other bands closer to the Fermi energy are observed in the occupied region. The band structure strongly contrasts with that of the poly-(*para*-phenylene) chains, which exhibits a single, highly dispersive molecular band across the entire Brillouin zone [26, 77, 83, 264] [Figure 10.4 (b, e)]. Instead, it closely resembles the one predicted for poly-(*meta*-phenylene) (called PMP hereafter) chains [251], implying that the presence of *meta*-junctions strongly modifies the electronic structure of a polymeric chain [65] (cf. Figure 10.13 in Section 10.4.7).

The weak interaction observed between the zigzag chain film and the substrate is a favorable playground for a systematic theoretical analysis. As a first approximation, we consider the polymers as free-standing and planar. On this basis, we use DFT calculations (performed by Dr. Aran Garcia-Lekue from DIPC) to corroborate the weakly dispersive band structure observed experimentally. The calculated

electronic structure shown in Figure 10.4 (a) exhibits convincing qualitative agreement with the experimental data. In particular, the dispersive character of the first four valence bands (VBs) of the zigzag chain (between -1 eV and -2.5 eV) is consistent with that in Figure 10.2 (a). The energy mismatch can be attributed to the absence of a substrate in the calculations, as well as to the well-known limitation of DFT to accurately predict HOMO-LUMO gaps. Note that the calculated bands span from the $\overline{\Gamma}$ point to the Brillouin zone boundary ($\frac{\pi}{L}$), which in the experiment appears replicated 12 times until $\frac{2\pi}{a^*}$ [see Figure 10.4 (d)]. In this case a k_x integrated band structure is presented in order to capture the replicating bands. For comparison, the calculations are extended to straight PPP chains [Figure 10.4 (b)] which strongly differ in the electronic structure by exhibiting a highly dispersive single VB in this energy window. This is in agreement with the experimental band structure for PPP chains shown in Figure 10.4 (e), where a highly dispersive electronic band is observed peaking at $\frac{2\pi}{a}$. This periodicity corresponds to the phenyl-phenyl distance along the polymer (see Section 10.4.6). Moreover, the zigzag chain exhibits a greater bandgap than its straight counterpart, confirming its enhanced semiconductive character (cf. Figure 10.13).

The experimental value of the frontier orbital bandgap of the zigzag chains can be obtained by low-temperature (4 K) STS. For such measurements (performed in collaboration with the group of Prof. Dimas García de Oteyza from DIPC) we deposit a submonolayer coverage of DMTP molecules on Ag(111). In this way, small zigzag island patches are formed on the surface while still allowing access to the bare substrate for tip calibration and treatment [Figure 10.5]. Figure 10.5 (a) shows the *dI/dV* spectra at the center (red) of a straight arm of a zigzag chain (cf. inset of figure) and the Ag substrate (grey). The VB onset is detected at -2.1 V [coinciding with the ARPES value in Figure 10.2 (b)] while the conduction band (CB) edge is at 1.6 V resulting in an overall bandgap of ~ 3.7 eV. Therefore this value is larger than the 3.2 eV reported for PPP chains grown on Au(111) [29].

DFT calculations can also shed light onto the effect that the periodically spaced *meta*-junctions have on the overall electronic structure by comparing the spatially resolved molecular orbitals at the $\overline{\Gamma}$ point with the π molecular orbitals of benzene [155] [Figure 10.4 (c)]. In the PPP case [Figure 10.4 (b)], VB and CB are constructed by the overlap of Φ_3 and Φ_3^* benzene molecular orbitals, respectively. These orbitals present a large electronic weight on the carbon atoms linking the phenyl rings (*para*-positions), giving rise to highly dispersive valence and conduction bands. Likewise, the less dispersive character of the VB-1 and CB+1 bands can be attributed to the orbital set that exhibits a nodal plane through the *para* carbon atoms (Φ_2 and Φ_2^* orbitals). Contrarily, for the zigzag chains [Figure 10.4 (a)] the VB and CB are a combination of two degenerate orbitals [254]. In particular, the VB is made up of Φ_3 (straight sections) and Φ_2 (elbows) orbitals, which is mirrored in the CB by Φ_3^*

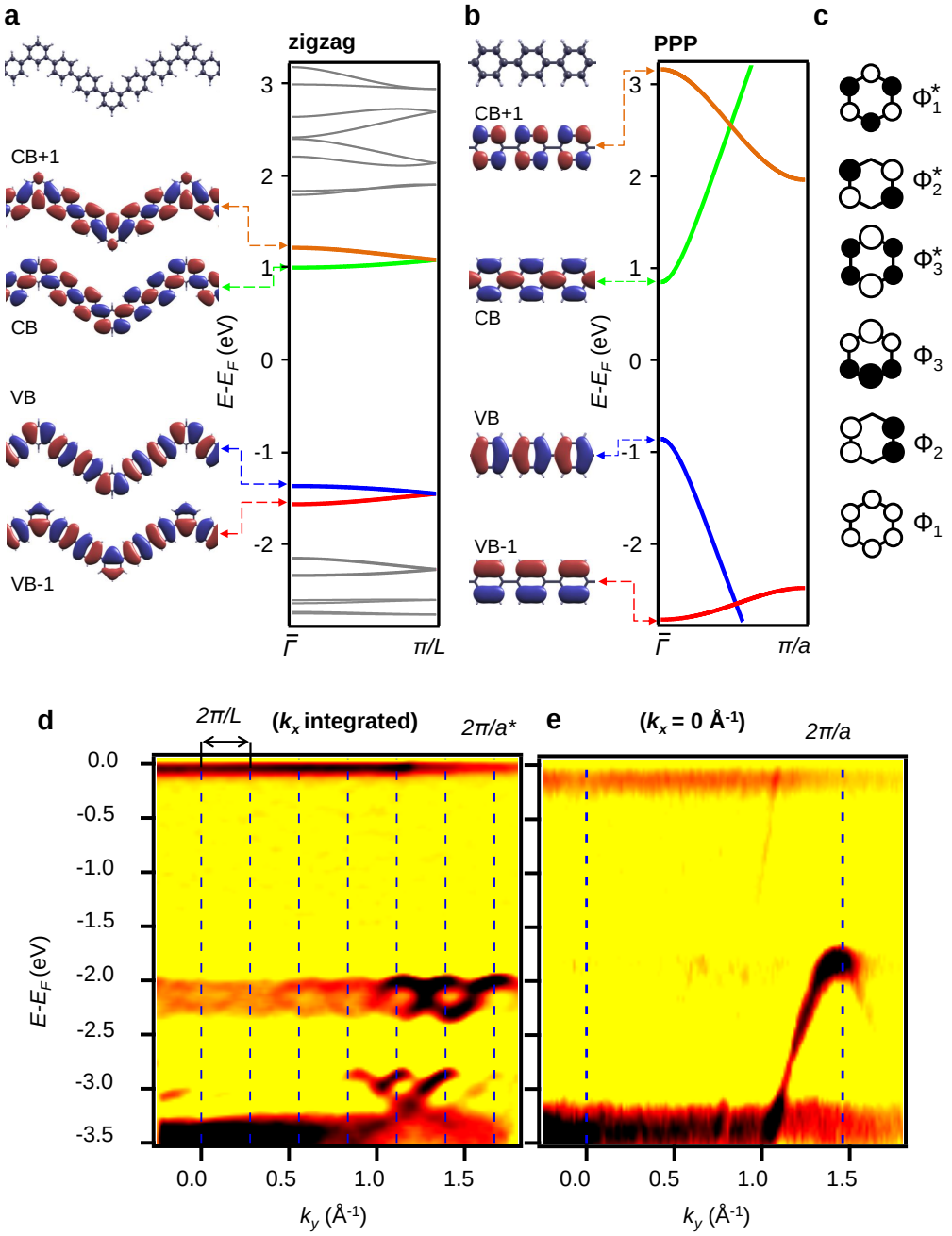

FIGURE 10.4: Comparison of molecular orbital shape and band structure between zigzag chains and straight PPP chains, as obtained from DFT calculations and ARPES. The right plots in (a) and (b) show the calculated electronic band structure, where (a) corresponds to the zigzag polymer and (b) to PPP. The highly dispersive character of the PPP bands contrasts with the practically flat bands of the zigzag chains, accompanied by a notable difference in the frontier orbital bandgap. Left panels in (a) and (b) show the spatially resolved molecular orbitals at $\bar{\Gamma}$ for each band. In a simplistic view, they can be constructed by overlapping different benzene molecular orbitals, which are schematically shown in (c). (d) and (e) show the second derivative of the ARPES spectral intensity (E vs k_y) along the zigzag and PPP chain axis. These plots follow the periodicity of the chain unit cells ($\frac{2\pi}{L}$ and $\frac{\pi}{a}$) marked with vertical dashed blue lines. For the PPP polymer film the substrate used is a Ag(544) vicinal crystal (see Section 10.4.6).

(straight sections) and Φ_2^* (elbows). This orbital mixing, along with the reduced orbital amplitude at the *meta*-positions and expected phase shifts induced by momentum steering at the elbows, results in a diminished orbital interaction (overlap) that leads to a severe weakening of the electron coupling between adjacent straight segments. Indeed, the flat band character is also exhibited by the VB-1 and CB+1, even though they mostly arise from a single type of benzene molecular orbital coupling (Φ_3 and Φ_3^*, respectively). This strong electronic effect governed by the *meta*-junction is generally referred to as cross-conjugation [251, 252] or destructive quantum interference [255–257, 260].

The reduced electronic coupling between neighboring linear segments causes electron localization, an effect that can be adequately addressed with STS. Figure 10.5 (b) presents a color plot representing stacked *dI/dV* point spectra measured along a single straight segment [black dashed line in the inset of Figure 10.5 (a)]. Aside from clearly visualizing an overall bandgap of 3.7 eV (vertical dashed white lines), we observe confinement in the CB within such segments where the spatial modulations of the LDOS are consistent with the first two stationary states of a particle in a box. In particular, their amplitudes die away at the edges of the linear segments (elbow positions of the zigzag chains) but the lower state at 1.9 V features an antinode at the segment's center [the peak in the red spectrum of Fig. 10.5 (a)], whereas the second state at 2.5 V oppositely exhibits a node at that position. Such electron confinement effects have also been observed in related structures, as in the case of finite size PPP chains featuring a single elbow (in *meta*-junction) [65] or in closed-cycle geometries of honeycombenes [271]. In essence, we can conclude that the *meta*-junctions act as scattering barriers for the polymer electrons regardless of the overall geometry, *i.e.* as closed structures [271] or as edged (non-linear) chains [65].

Once we have verified that each straight segment of our zigzag chains acts as a confining unit, reminiscent of a 1D array of weakly interacting QDs [54], it should be possible to tune their electronic properties by modulating the straight segment's length. Varying the 1D QD length should affect the energy levels as well as the corresponding frontier orbital bandgap. To do so, we co-evaporated on Ag(111) linear precursors (DBTP molecules [26]) together with the previously used ones to generate the zigzag chains, as shown in Figure 10.6 (a). The Ullmann coupling reaction is likewise activated by post-annealing to 470 K, resulting in linear segments of phenyl length configurations of $N = 4 + 3n$ (N being the total phenyl number and n the amount of DBTP precursors embedded in the straight segment). Figure 10.6 (b) shows color plots of the *dI/dV* linescan for $N = 7$ (bottom) and $N = 10$ (top) QDs, which evidence the expected squared wavefunction intensity variations in the CBs for the same energy range as Figure 10.5 (b). Most importantly, by comparison to the dashed white lines corresponding to the $N = 4$ segment, we observe that the bandgap shrinks as the size of the segment increases (dashed blue lines). A quantitative analysis of the experimentally determined bandgap is shown in Figure 10.6 (c), revealing a $\frac{1}{N}$ behavior in agreement to previous work for similar chains [65]. Such

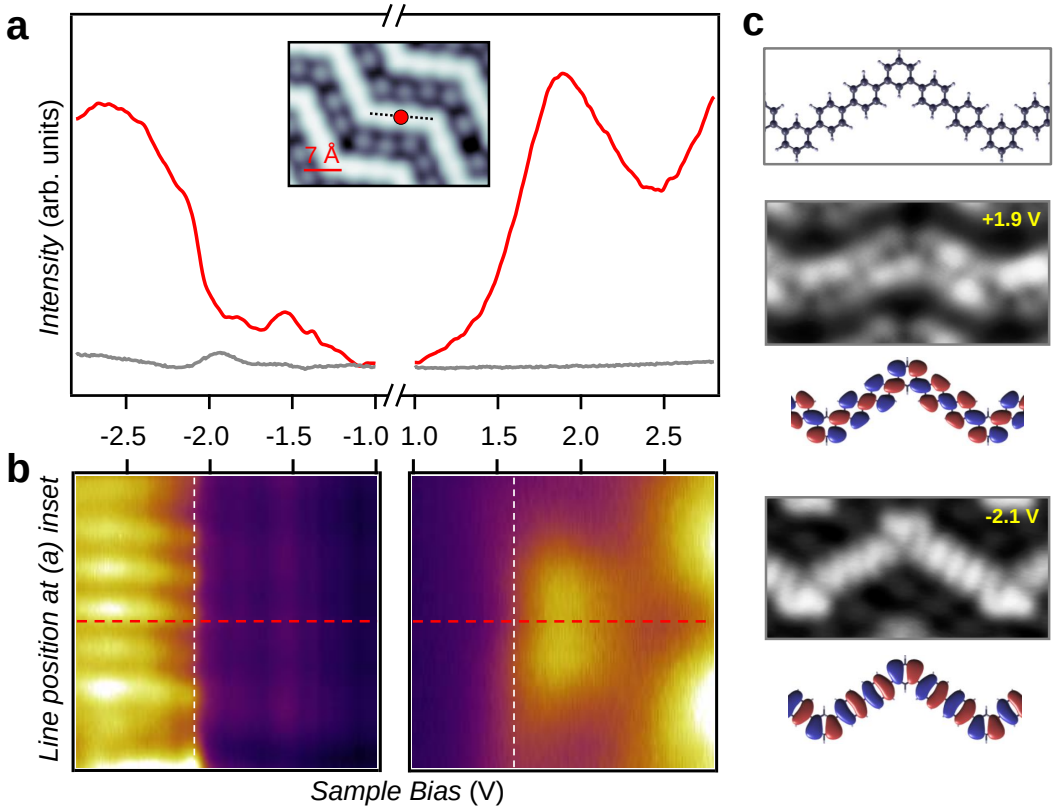

FIGURE 10.5: STS experimental determination of the zigzag chain's frontier orbitals on Ag(111). (a) Constant-height *dI/dV* spectra acquired at the center of a zigzag straight arm (red point in STM image inset) and substrate (grey) (STM imaging parameters: 50 mV, 100 pA; frame: 3.6 × 2.5 nm^2). (b) Constant-height *dI/dV* line-scan spectra along the zigzag arm (indicated by a dotted line in the STM topography inset) for the same bias range of panel (a). The onsets of the VB and CB are clearly defined, yielding a bandgap of $\sim$ 3.7 eV (STS bias voltage modulation for (a) and (b): 10 mV$_{rms}$ at 341 Hz. Close-feedback parameters: -350 mV, 150 pA and 1200 mV, 100 pA for the negative and positive resonances regions, respectively). (c) From top to bottom: ball and stick model of the zigzag chain. High-resolution *dI/dV* maps acquired at constant-height with a CO functionalized STM tip at 1.9 V and -2.1 V, *i.e.* close to the CB and VB onsets (frames: 3.0 × 1.5 nm^2; bias voltage modulation 10 mV$_{rms}$ at 341 Hz). Underneath each map the corresponding DFT gas phase molecular frontier orbitals are shown for comparison.

behavior matches our DFT calculations for planar, free-standing, periodic zigzag chains of different straight segment length, which confirm not only that the bandgap of the cross-conjugated zigzag chains is larger than the one of its linear PPP counterpart, but it is also tunable with a $\frac{1}{N}$ relation (cf. Figures 10.13 and 10.14 in Section 10.4.7).

Finally, we should discuss an additional property of this system that may affect the frontier orbital bandgap: the relative twisting of the phenyl rings (non-planar chain morphology). Figure 10.5 (c) shows high-resolution constant height *dI/dV* maps close to the valence and conduction band onsets, namely at -2.1 eV and 1.9 eV, respectively. Both maps replicate well the molecular orbital simulations of Figure 10.4 (a), which are calculated for planar structures and are depicted below for direct comparison. While the slight discrepancies in nodal positions are attributed to

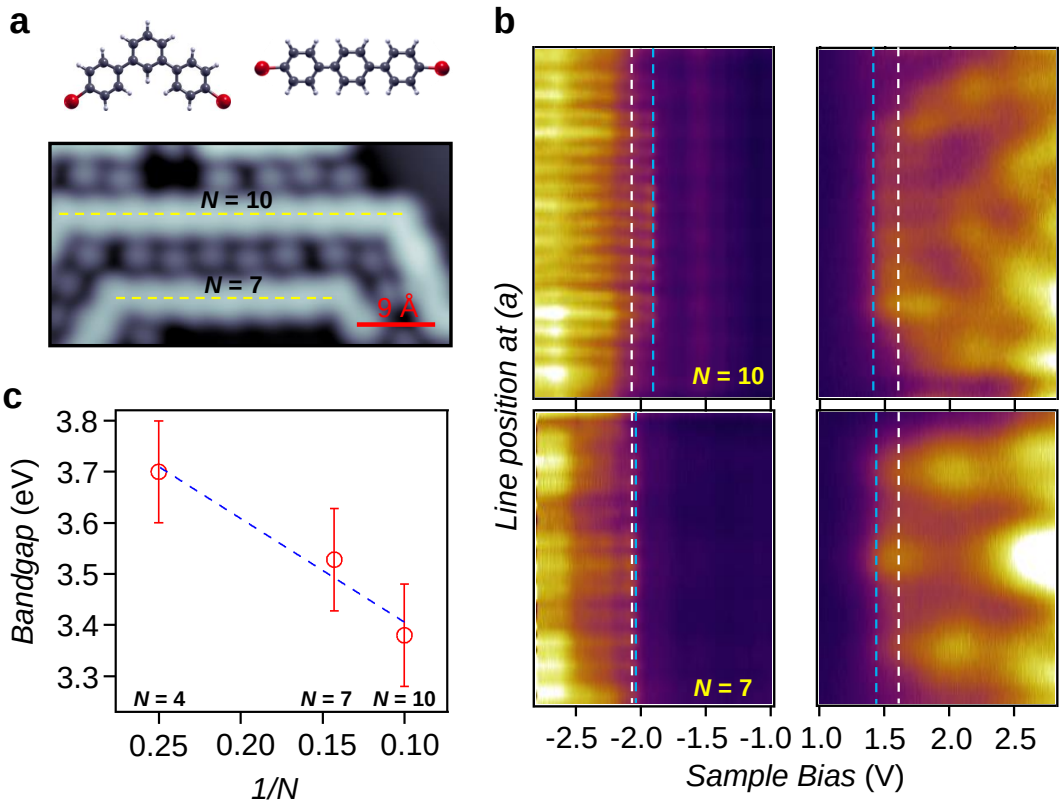

FIGURE 10.6: Tuning the electronic confined states through the linear segment's length (QD size). (a) Schematic representation of the co-evaporated molecular precursors (DMTP and DBTP) that generate longer straight segments between the *meta*-coordinated phenyls. The STM image shows two longer linear segments of 7 and 10 phenyl rings between elbows (Imaging parameters: 50 mV, 100 pA; frame: 4.5×2.3 nm^2). (b) Constant height *dI/dV* line profiles close to the VB and CB onsets along the two segments following the dashed lines in (a). The intensity modulation of the CB confirms the confinement nature of the *meta*-junction termination. Furthermore, the frontier orbital bandgap (vertical dashed blue lines) is reduced compared to the N=4 case, which is indicated by the two vertical dashed white lines. (STS parameters: bias voltage modulation of 10 mV$_{rms}$ at 341 Hz; close-feedback at -350 mV, 150 pA and 1200 mV, 120 pA for the negative and positive resonances regions, respectively). (c) Experimental bandgap extracted for the STS line profiles revealing a linear $\frac{1}{N}$ behavior (see Figure 10.14).

the CO probe functionalization [276], the intensity variations are in turn ascribed to the twisting of the phenyl rings [29]. In order to reveal whether such morphological effects are present, we perform constant height bond resolution imaging with a CO functionalized tip [277]. This is done on condensed zigzag chains (surrounded by Br atoms) that are compared with an isolated chain obtained after tip manipulation [Figure 10.7]. Both types of 1D structures show some very weak intensity variations at the phenyl rings, which suggest that there are slight twists in the configurations. This would agree with the observations for PPP chains where a phenyl twisting of $20 \pm 5°$ was observed with respect to the planar configuration [26]. Indeed, the surrounding morphological conditions are determinant, since the twisting is different when the zigzag chains are condensed into islands (asymmetric arms) or are isolated

(symmetric twisting of consecutive arms). Such subtle variations could be caused by the hindrance of Br or by a different matching to the underlying substrate.

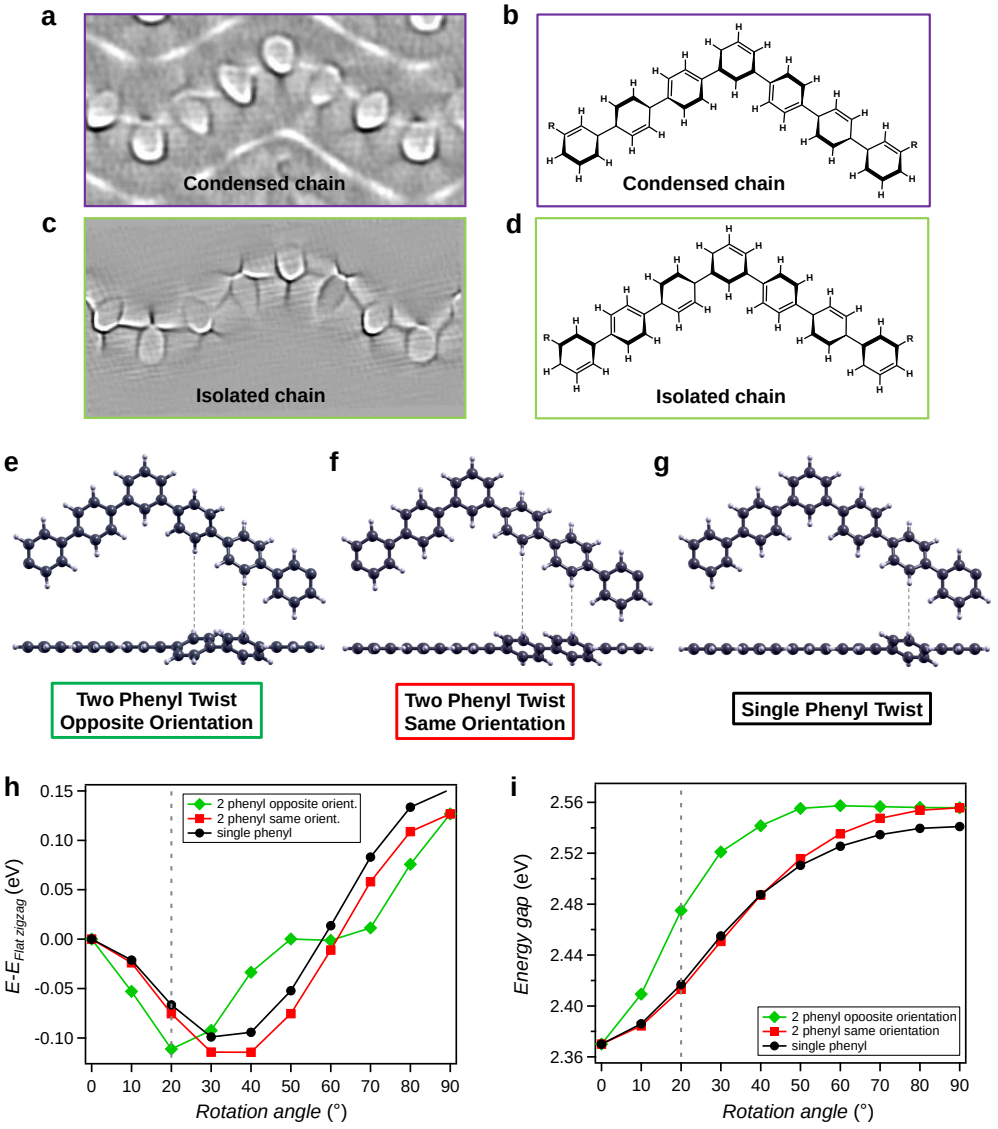

FIGURE 10.7: Influence of phenyl-phenyl twisting on the stability of the zigzag chains and their electronic bandgap. Bond resolution STM images (current signal, post-processed with a Laplace filter) acquired at constant height with a CO-functionalized STM tip (frames: 3.0 × 1.5 nm^2, V_{tip} = 2 mV) of zigzag chains condensed within an island (a) and an isolated chain obtained by tip manipulation (c). These images suggest a slight phenyl twisting, which for the condensed chain is asymmetric with respect to the central *meta*-junction of both straight segments (left ascending and right descending), as shown in (b), whereas it is symmetric with respect to the central *meta*-junciton for both straight arms for the isolated chain, as shown in (d). Influence of phenyl-phenyl twisting on the stability of the zigzag chains and their electronic bandgap. Three different phenyl twisting configurations have been considered: two phenyl twist (opposite orientation) (e), two-phenyl twist (same orientation) (f) and single phenyl twist (g). (h) Energy of the three twisting configurations with respect to the fully planar configuration (zero energy). (i) Evolution of the electronic bandgap with respect to the phenyl rotation angle, for the three different configurations.

To determine the effect of the twisting on the frontier orbital bandgap, we have performed DFT calculations on the N=4 zigzag chain and we consider three phenyl twisting configurations: a single phenyl twisting, twisting of two phenyls with the same orientation and twisting of two phenyls with opposite orientations (see Figure 10.7 (e-g)). As shown in Figure 10.7 (h), in all three cases the energy minimum is found for twisting angles of approximately 20° to 35° with respect to the planar configuration. However, the calculations show that the electronic bandgap is scarcely increased compared to the planar configuration (by about 7%) [Figure 10.7 (i)]. Given that the underlying substrate is known to decrease the phenyl twisting by flattening the chains, we expect this effect to be smaller than $\sim$ 200 meV, validating the use of free-standing, planar configuration geometries in the DFT calculations that support our findings.

10.3 Conclusions

We have been able to synthesize and macroscopically align a saturated film of cross-conjugated oligophenylene zigzag chains on a vicinal Ag(111) surface. We find that these atomically precise chains remain sufficiently decoupled from each other and from the substrate to probe their elusive band structure with ARPES, revealing weakly dispersing one-dimensional electronic bands along the chain direction. DFT band structure calculations and EPWE photoemission intensity simulations satisfactorily reproduce our experimental findings. By means of STS, we find that the zigzag chain has a larger frontier orbital bandgap than its straight counterpart (PPP) and observe electronic confinement in each straight segment of the zigzag chains, reminiscent of 1D arrays of weakly interacting QDs. Such states can be tuned by changing the length of the straight segments, affecting the frontier orbital bandgap, which follows a $\frac{1}{N}$ dependency. Indeed, our molecular orbital simulations confirm that the periodically spaced *meta*-junctions at the elbows of the zigzag chain are the main structural feature responsible for the reduction of electronic coupling between adjacent linear segments. These findings corroborate the important effects that the conductive path topology of a molecular wire has on its frontier orbitals, which are responsible for defining its chemical, optical and electronic properties. Recent advances in transfer techniques ensure that on-surface synthesized and well-aligned organic nanostructures can be collectively transferred onto insulating substrates maintaining their relative arrangement [24, 32, 33], which opens the path to further study the transport and optical properties of these cross-conjugated oligophenylene zigzag chains.

10.4 Supplementary Information for This Chapter

10.4.1 VT-STM and LT-STM/STS Measurements

The STM measurements on the curved Ag(111) crystal were carried out at $\sim$ 100 K using a variable temperature Omicron STM with a Nanonis SPM control system. The bias voltages given in Figure 10.1 (b) and Figure 10.9 (c, f) refer to a grounded tip. STM data were acquired in constant current mode and were processed with the WSxM software [174].

LT-STM/STS measurements were performed by the group of Prof. Dimas García de Oteyza from DIPC with a commercial Scienta-Omicron low temperature system, operating at 4.3 K. For the measurement, the bias voltage was applied to the tip while the sample was electronically grounded. The STM tip was prepared *ex-situ* by clipping a Pt/Ir wire (0.25 mm) and sharpened *in-situ* by repeatedly indenting the tip a few nanometers (1 to 4 nm) into the Ag surface while applying bias voltages from 2 V to 4 V between tip and sample. In order to perform bond-resolved STM imaging, the tip apex was terminated with a CO molecule, directly picked up from the surface, by positioning the sharp metal tip on top of it and applying a 500 ms bias pulse at -2 V. The imaging was performed by measuring at constant height while applying a bias voltage to the tip within the range of 2.0 mV to 3.5 mV. For spectroscopic point spectra and conductance maps, the *dI/dV* signals were measured by a digital lock-in amplifier (Nanonis). STM images were analyzed by using the WSxM software [174].

10.4.2 *Ab-Initio* DFT Calculations

Ab-initio calculations were carried out by Dr. Aran Garcia-Lekue from the DIPC using DFT, as implemented in the SIESTA code [278]. The optB88-vdW functional [279], which accounts for non-local corrections, was adopted for the exchange and correlation potential. For each organic nanostructure, we considered a supercell consisting of a chain infinite along the x axis, with vacuum gaps of 15 Å in y and z directions in order to avoid interactions between chains in adjacent cells. A Monkhorst-Pack k-point grid with 20x1x1 k-points was used for the Brillouin zone sampling and the mesh cut-off for real space integrations was set to 300 Ry. We employed a double- ξ plus polarization (DZP) basis set, and a mesh-cutoff of 300 Ry for the real-space integrations. All structures were fully relaxed until residual forces were less than 0.01 eV/ Å.

10.4.3 The Electron Plane Wave Expansion Method (EPWE)

In collaboration with Dr. Zakaria M. Abd El-Fattah from Al-Azhar University (Egypt), the EPWE method is employed to simulate ARPES data. Within EPWE approach, the photoemission intensity for a given binding energy and photoelectron wave vector is obtained from Fermi's golden rule applied to the in-plane wave function (an initial state) and a normalized plane wave (a final state) for the parallel component of the photoelectron wave function, as detailed in ref. [34]. In this semi-empirical method, zigzag chains are considered free-standing and planar, which implies that the simulated bands in Figure 10.11 are substrate independent and free of Br interactions.

10.4.4 Sample Preparation and Zigzag Alignment on a Ag(111) Curved Vicinal Crystal

A silver crystal surface curved around the (645) direction was used as tunable vicinal substrate for chain formation and alignment [82]. This curved sample exhibits (111) terraces of variable size (position dependent on its curvature) separated by monoatomic steps oriented along the $[11\bar{2}]$ direction. The steps are of fully-kinked type, in which out-protruding atoms have no side neighbors [Figure 10.8 (a, b)]. Notably, periodic roughening of such step-edges bears negligible energy cost, and hence can readily accommodate to the zigzag structure of the chains [82]. The sample was cleaned by repeated cycles of Ar^+ sputtering at energies of 1.0 keV, followed by annealing at 700 K. This produced clean and well-ordered surface step arrays as verified by the splitting of the LEED spots along the surface curvature. The substrate's band structure has the *d*-bands' onset below -3 eV, which provides a large energy window for the zigzag chain bands undisrupted observation [Figure 10.8 (c, d)].

The *meta*-junctioned haloaromatic compound, DMTP, was sublimated from a Knudsen cell at 360 K at a low flux (1 $\frac{ML}{hour}$) while the sample was held at 470 K [263, 280, 281]. Covalently bonded zigzag chains appeared separated by Br adatoms, suggesting some influence from the latter in steering chain growth and alignment. The sample was heated during deposition in order to bypass the organometallic phase and directly form covalent structures. The step flexibility promoted the chain formation while keeping other irregular structures or hyperbenzene macrocycles to a minimum [272]. The structures remained densely packed up to high temperatures ($\sim$ 600 K), beyond which halogen desorption takes place, accompanied by chain misalignment [243, 282].

The saturated zigzag film that presents best order was observed at the vicinal plane $\sim 3.6°$ from the (111) region, corresponding to an average terrace size of 3.8 nm [Figure 10.8 (b)]. The data shown in Figure 10.2 corresponds to this position of the substrate. Here, zigzag chains grow into a long-range ordered polymer film parallel to the steps [Figure 10.9 (c)] and show a (9, 5; 0, 4) matrix superstructure in

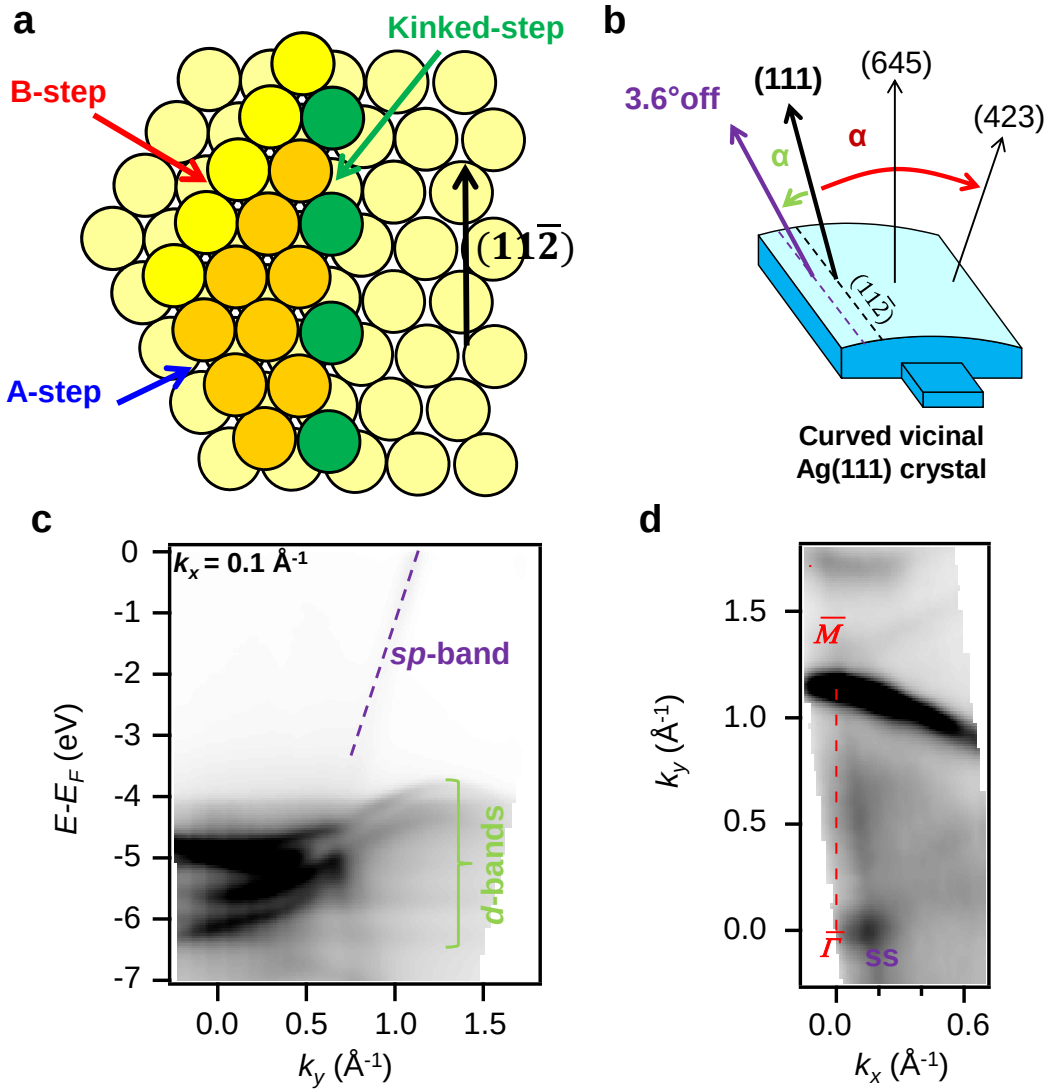

FIGURE 10.8: Atomic and macroscopic geometry of the 100% kinked curved Ag(111) crystal and its electronic structure $\sim 3.6°$ off the (111) plane. (a) Schematic drawing highlighting the three step types present on close-packed vicinal surfaces. In our case, the step termination corresponds to the one ending in the green spheres (100% kinked) that runs along the [11$\bar{2}$] direction. (b) Schematic drawing of the curved Ag(111) substrate. The crystal was polished so that the (111) region is away from the center of the crystal by 9.27°. Zigzag chain films showed best alignment at the position with a local vicinal plane of $\sim 3.6°$ off from the (111) region, where kinked steps are 3.8 nm separated in average from each other. (c) The ARPES band structure (E vs k_y) at k_x = 0.1 Å^{-1} corresponds to the direction parallel to the [11$\bar{2}$]. The characteristic silver *d*-bands exist below -3 eV and the *sp*-band shows a large dispersive character as it raises and crosses the Fermi level (highlighted by a side dashed purple line). (d) Fermi Surface Map (k_x vs k_y at $E = 0$), exhibiting the characteristic Shockley state close to the $\overline{\Gamma}$ point and the dispersive dominant *sp*-bulk bands closer to the $\overline{M}$ point.

LEED [Figure 10.9 (b)]. Contrarily, in the (111) region, zigzag chains condense into multidomains as nicely observed in the STM image [Figure 10.9 (f)] and LEED pattern [Figure 10.9 (e)].

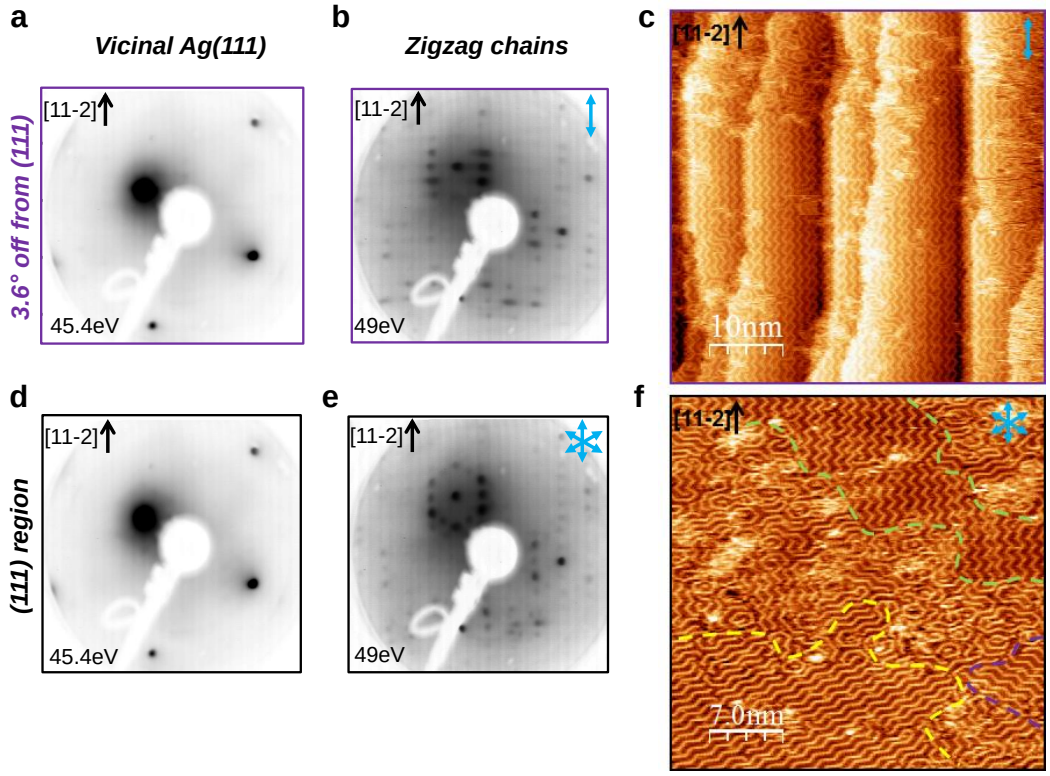

FIGURE 10.9: Uniaxial zigzag chain ordering vs multi-domain structures determined by LEED and STM. Experimental LEED patterns of the silver substrate before (a) and after (b) the formation of the zigzag chain film at the $\sim 3.6^{\circ}$ position off from the (111). This pattern agrees with a (9, 5; 0, 4) matrix, which corresponds to an elbow-elbow distance of 9 atomic spacings of the Ag substrate. (c) Corresponding STM image showing the preferential uniaxial alignment of the zigzag chains parallel to the step direction (STM parameters: size = 50 x 50 nm^2, V = -393.7 mV; I = 234 pA). Panels (d) and (e) show respectively the LEED patterns of the pristine silver substrate before and after forming zigzag chains at the (111) region. At this position, a hexagonal pattern around the (0,0) spot is observed which evidences that the chains primarily follow three main directions. This is accordingly observed in the corresponding STM image in (f), where 120° rotated patches co-exist as highlighted in green, yellow and purple. (STM parameters: size = 35 x 35 nm^2, V = -425.2 mV; I = 254 pA).

10.4.5 ARPES Band Structure and Photoemission Intensity Simulations Using EPWE

The ARPES band structure for the zigzag chains presented in Figure 10.2 corresponds to the second derivative treatement of the photoemission intensity. Such data treatment is used to enhance the weak photoemission features. For completeness, the raw data is included in Figure 10.10.

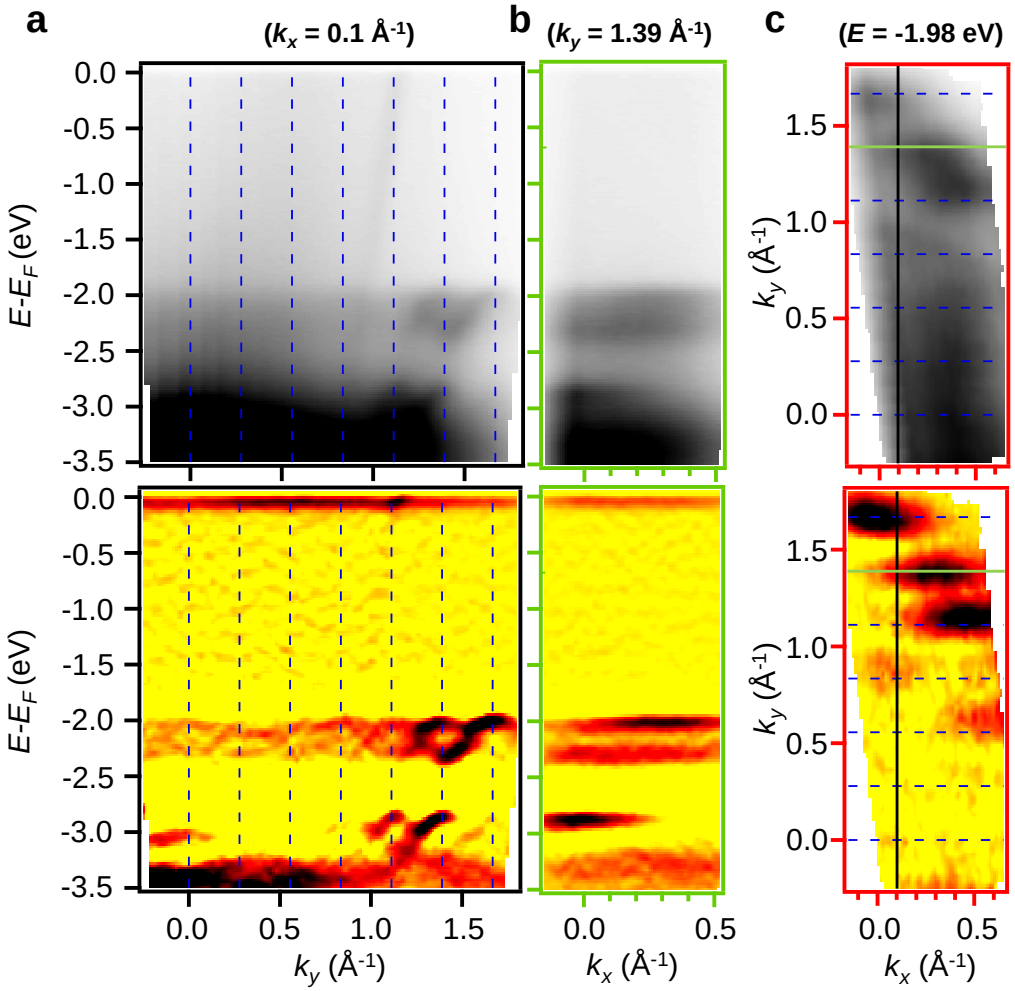

FIGURE 10.10: Raw data comparison to the 2^{nd} derivative treatment for the electronic band structure of zigzag chains at the vicinal plane $\sim 3.6°$ off from the (111) region. The ARPES spectral intensity raw data is shown in the top row and the 2^{nd} derivative in the bottom row. (a) ARPES band maps (E vs k_y for $k_x = 0.1$ Å^{-1}). (b) Band structure perpendicular to the chains average axis (E vs k_x, with $k_y = 1.39$ Å^{-1}). (c) Isoenergetic cut (k_x vs k_y) at the top of the VB ($E = -1.98$ eV). The photoemission intensity presented in (a) has been obtained by following the direction highlighted by the black line. The band structure perpendicular to the main zigzag chain axis shown in (b) is shown as a horizontal green line.

To capture the photoemission intensity modulation observed in ARPES, we perform photoemission intensity simulations using the EPWE method [34, 117]. These simulations (excluding the substrate and Br atoms presence) match the experimental data shown in Figure 10.11 and support the argument of the scarce effects that the underlying Ag substrate and Br atoms have on the electronic properties of the zigzag chains.

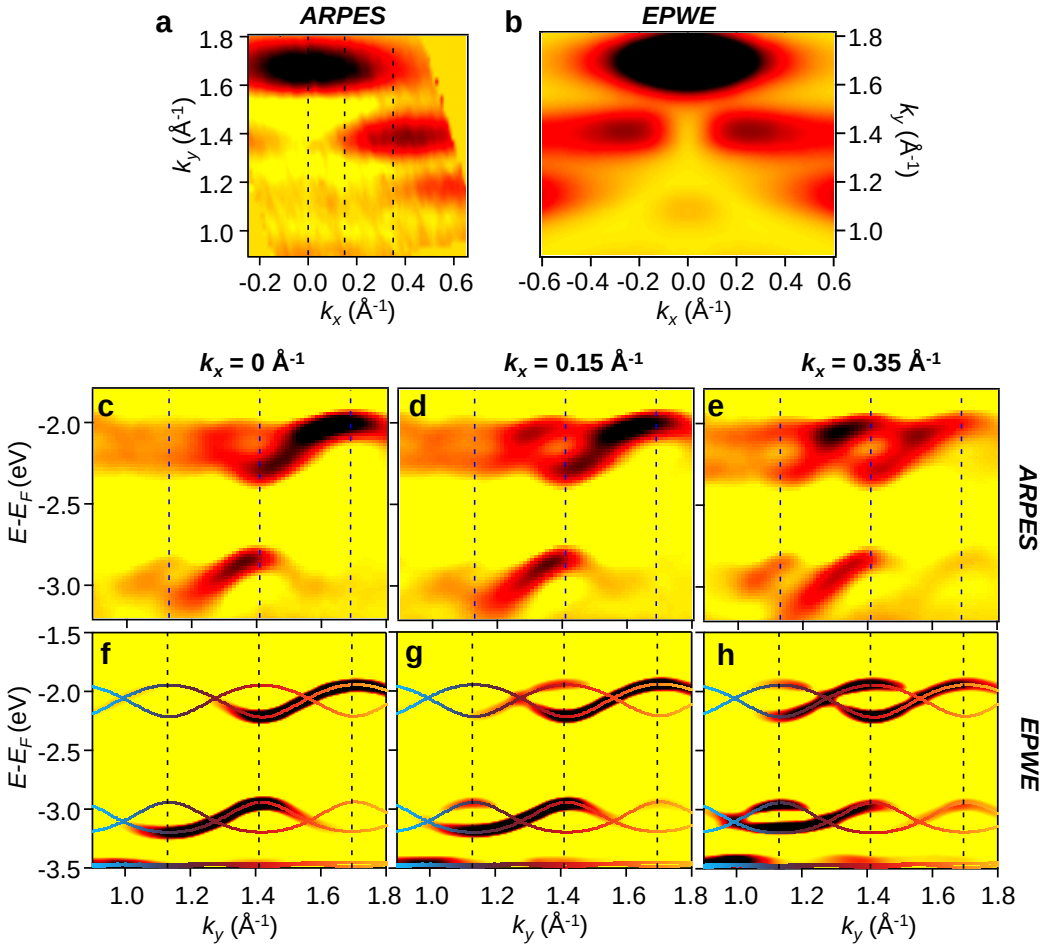

FIGURE 10.11: Experimental ARPES data comparison to EPWE photoemission intensity simulations. The top row (a, b) shows the 2^{nd} derivative of the ARPES and EPWE isoenergetic cuts (k_x vs k_y) performed at the top of the VB (E=-1.98 eV in ARPES). The middle row (c-e) corresponds to the 2^{nd} derivative of the experimental ARPES spectral intensities (E vs k_y) values (indicated as dashed lines in (a)). The bottom row (f-h) shows the equivalent photoemission intensity simulations performed with the EPWE code. Their match is exceptional, supporting the idea of weak electronic interactions between the zigzag chains with the substrate and surrounding Br atoms.

10.4.6 ARPES Band Structure Comparison of Zigzag Chains vs PPP Chains.

The occupied experimental band structure of the zigzag chains is compared with the straight PPP chains in Figure 10.12. The PPP polymer film has likewise been grown using a vicinal Ag substrate with (544) orientation and featuring an average terrace width of 2.4 nm terminated by straight steps rotated 30° from the fully kinked curved Ag(111) [see Figure 10.8 (a)]. Indeed, the step direction of Ag(544) follows the [1$\bar{1}$0] direction and the terraces are slightly smaller than the one used for the zigzag, but can still host in average 3-4 parallel PPP chains. The difference in the electronic nature between both chain types is evident from the dataset and closely follows the DFT calculations reported in Figure 10.4. For the zigzag chains a k_x integrated band structure is presented in order to capture the replicating bands every $\frac{2\pi}{L}$ [Figure 10.12 (b)] where L corresponds to the superperiodicity of the zigzag polymer [Figure 10.12 (a)]. In contrast, PPP chains show a highly dispersive electronic band in the same energy window [Figure 10.12 (d)], peaking at $\frac{2\pi}{a}$ where a corresponds to the phenyl-phenyl distance along the polymer [Figure 10.12 (c)].

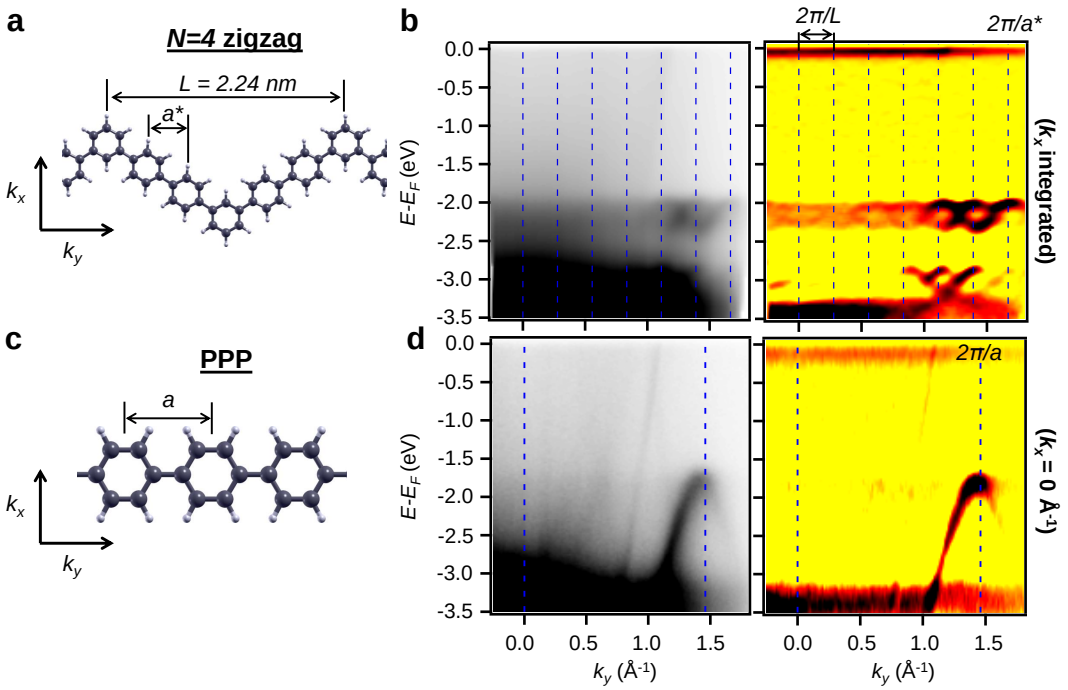

FIGURE 10.12: N=4 zigzag chain ARPES band structure comparison with that of PPP. Schematic representations of the N=4 zigzag chains (a) and the poly-(*para*-phenylene) chains (c). (b) and (d) show their respective raw (left) and second derivative (right) of the ARPES spectral intensity (E vs k_y) along the chain axis. These plots follow the periodicity of the chain unit cells ($\frac{2\pi}{L}$ and $\frac{\pi}{a}$) marked with vertical dashed blue lines. For the PPP polymer film the substrate used is a Ag(544) vicinal crystal.

10.4.7 Band Structure Variations with Straight Segment's Length of the Zigzag Chains from DFT Calculations

To further investigate the evolution of the frontier orbtial bandgap and electronic structure with the straight segment's length, we perform additional DFT calculations. As indicated before and depicted in Figure 10.13, zigzag chains with N=4 bear a closer resemblance to poly-(*meta*-phenylene) rather than to the straight, highly dispersive PPP counterpart. Moreover, a gradual reduction of the electronic bandgap of the frontier orbitals is already observed (PMP > zigzag N=4 > zigzag N=7 > PPP) as the straight segments are enlarged. Such an evolution is clearly shown in Figure 10.14 for a varying number of phenyl rings from 4 up to 11 in a planar, free-standing configuration. In agreement with previous work [65], we find that the band gap shrinks linearly as $\frac{1}{N}$ as the size of the straight segment is increased. This also agrees with our experimental results of Figure 10.6 (c), which are represented on the right axis of the graph. This evidences that while the electronic band dispersion is governed by the periodically spaced *meta*-junctions, the bandgap varies with the size of the straight segments.

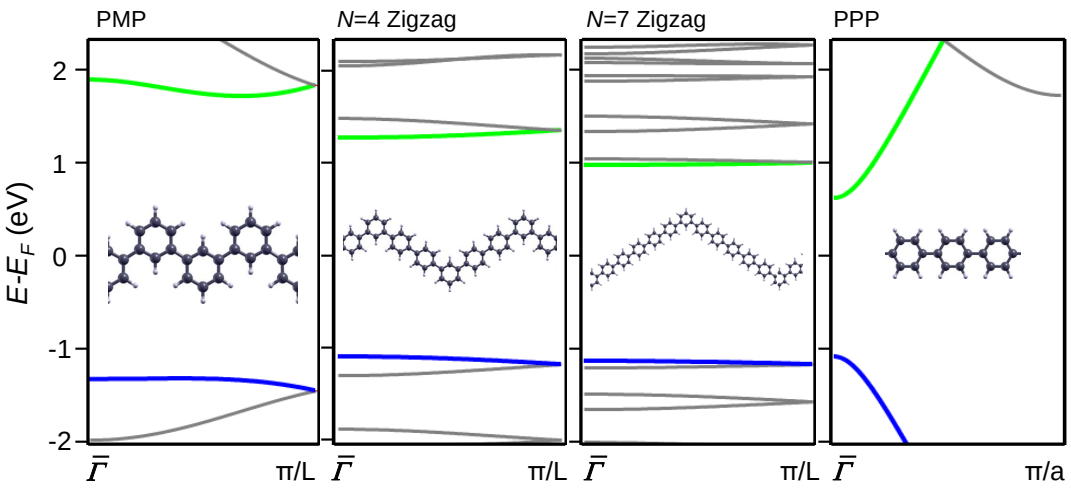

FIGURE 10.13: Band structure comparison between PMP, zigzag and PPP chains, as obtained by DFT calculations. The highly dispersive band structure of PPP chains (on the right) clearly show a different behavior to the other three cases. These plots show a progressive reduction of the electronic bandgap as the *meta*-junctions (elbows) are separated further. We attribute this to the cross-conjugated nature of the polymers hosting periodically spaced *meta*-junctions.

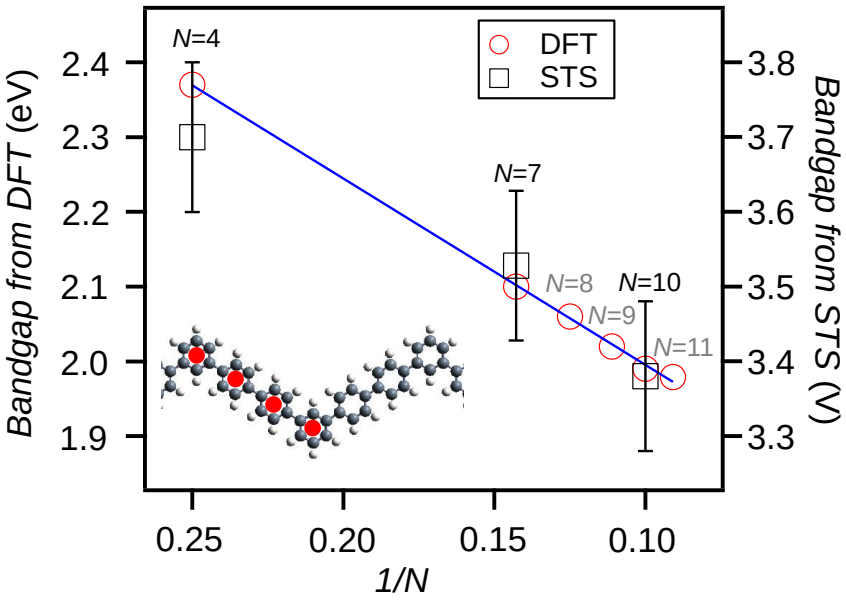

FIGURE 10.14: Evolution of the zigzag chain frontier orbital bandgap with increasing number of phenyl rings at the straight segments. Both DFT (theory) and STS (experimental) show a clear $\frac{1}{N}$ dependency of the bandgap with increasing number of phenyl rings inside the straight segments.

Chapter 11

Conclusions and Outlook

In the following, the ending conclusions from each chapter are collected and merged into a general and global conclusion section for each separate part. As this work does not end at this point, an outlook is included to provide hints of the interesting investigation paths to be performed for these research lines in the future.

11.1 Conclusions to Part II: Nanoporous Networks

In the second part of this thesis we have studied the electronic confinement and QD intercoupling induced by organic and metal-organic nanoporous networks. This has been possible by the experimental characterization of six different self-assembled molecular nanoporous networks grown on Cu(111), Ag(111) and Au(111) substrates as well as on thin Ag films. We have accomplished the generation of long-range ordered nanoporous networks in UHV conditions that fully saturate the surface. This is achieved through performing a careful gradient coverage evaporation process and selecting the proper molecule-molecule interactions in the form of self-healing bonding mechanisms (halogen bonding and metalorganic coordination) as well as picking out the right molecule-substrate interactions and commensuration. These represent essential prerequisites to access their experimental 2DEG electronic band structures with ARPES, as summarized in Figure 11.1. In addition, the LDOS yielding confinement inside each single nanopore have been probed with STM/STS measurements through collaborations with different international groups, which greatly complement the ensemble electronic properties accessed by photoemission.

Simulations by the semi-empirical electron boundary element method in combination with the electron plane wave expansion has been extensively used throughout this thesis. This has allowed us to model and understand the scattering potential landscape of each nanoporous network [Table 11.1] and simulate the LDOS and electronic band structures [Figure 11.1]. In addition, density functional theory and the phase accumulation model have been used to capture subtle overlayer-substrate interactions such as hybridization effects and geometrical variations. All these theoretical methods have been obtained through collaborations. Since EBEM/EPWE is a 2D modelling system, vertical interactions can not be directly captured but are

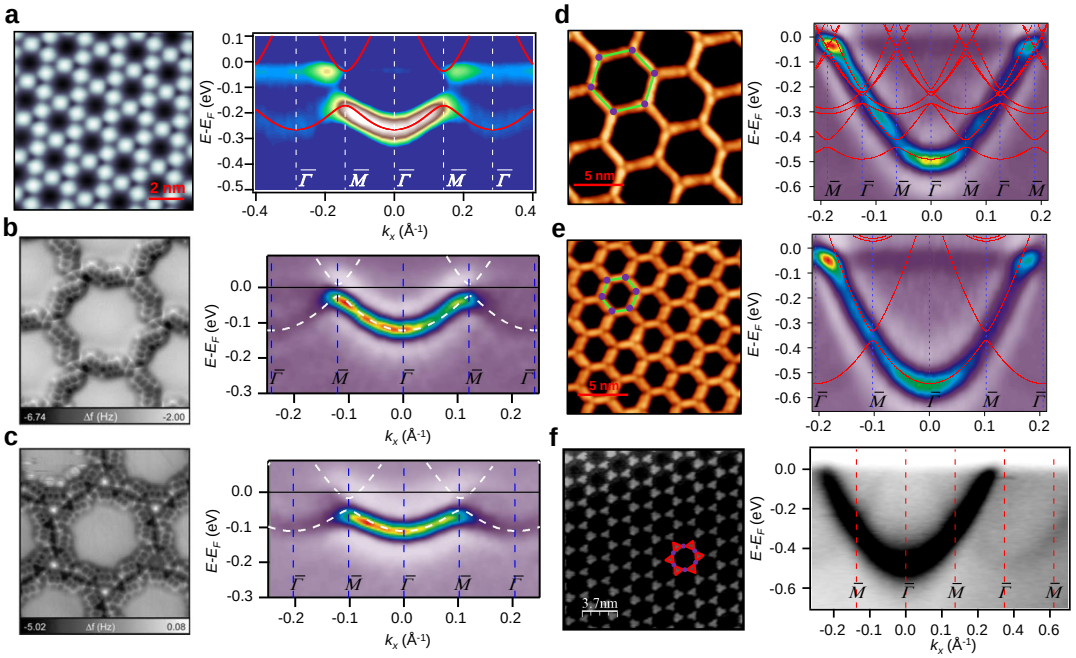

FIGURE 11.1: ARPES electronic band structure of the studied nanoporous networks in a nutshell. (a) 3deh-DPDI metal-organic network on Cu(111). (b, c) Single Wall (SW) and Double Wall (DW) halogen bond stabilized nanoporous networks grown on 3 ML Ag/Au(111) for ARPES and Ag(111) for STS. (d, e) Two homothetic (scalable) Ph6Co and Ph3Co metal-organic nanoporous networks grown on Au(111). (f) Cu-TPyB metal-organic network grown on Cu(111).

accounted for as renormalization of the 2DEG. Our complete experimental and theoretical synergy provides an accurate understanding of the global electronic properties of the studied nanoporous networks and allows us to predict the electronic properties of the broad family of single layer organic nanoporous materials grown on metallic substrates.

The main conclusions from these organometallic nanoporous networks are the following:

1. **Partially localized states in nanoporous networks originate from the Shockley state**.

   In Chapter 4 we validate the origin and nature of the partially localized states that are generated in nanoporous networks. By studying the temperature dependence of the band structure generated by the 3deh-DPDI nanoporous network, we corroborate that the n=1 PLS existing in the pores of the network originates from the pristine Cu(111) Shockley state [Figure 11.1 (a)]. The energies of both states, *i.e.* n=1 PLS and Cu SS, display the same temperature dependence, evidencing their common origin and nature. This experimental demonstration supports that the surface state electrons are affected by the periodic scattering potential landscape exerted by molecular barriers of a nanoporous network, partially localizing them inside each nanocavity.

TABLE 11.1: ARPES fundamental binding energies and extracted effective masses (first two columns). EBEM/EPWE required 2DEG renormalized energy and masses (third and fourth columns) and scattering potential values (last two columns) to match the experimental data.

	$E_B^{\overline{\Gamma}}$ (eV)	m^*/m_0	$E_{EBEM}^{Ref,\overline{\Gamma}}$ (eV)	$m_{EBEM}^{*,Ref}/m_0$	V_{mol} (meV)	V_{met} (meV)
3deh-DPDI/Cu(111)	0.25	0.57	0.40	0.49	390	340/440
SW/ 3ML Ag/Au(111)	0.12	0.47	0.16	0.49	140	–
DW/ 3ML Ag/Au(111)	0.11	0.59	0.16	0.54	140	–
Ph6Co/Au(111)	0.49	0.24	0.52	0.24	250	50
Ph3Co/Au(111)	0.55	0.22	0.59	0.21	250	50
Cu-TPyB/Cu(111)	0.47	0.41	–	–	–	–
Au(111)	0.45	0.255	0.45	0.26	–	–
3ML Ag/Au(111)	0.16	0.38	0.16	0.38	–	–
Cu(111)	0.40	0.42	0.40	0.42	–	–

2. **The scattering potential landscape generated by organic and metal-organic nanoporous networks represents a repulsive scattering potential for surface electrons**.
   The 3deh-DPDI metal-organic nanoporous network is used in Chapter 7 to show that it is possible to unambiguously obtain the scattering potential landscape exerted by a molecular nanoporous overlayer onto a 2DEG and determine the relevant confinement details and interaction effects. We show that the scattering potential must be parametrized as realistically as possible to the network geometry while the flexibility is provided to the 2DEG reference, which requires a slight energy and/or mass renormalization due to the interactions between overlayer and substrate [Table 11.1]. Our simulations unambiguously define that both the molecules and the metal adatoms forming the network exhibit repulsive character to the surface electrons. We also find that slight perturbations in the scattering potential at the metal coordination sites are responsible for the deformation of the confined states spatial shape. We note here that the higher order states are more sensitive than the lower ones to deviations from the correct values used for the scattering potentials.

3. **Electronic states in nanoporous networks can be individually and globally configured with physisorbed Xe adsorbates**.
   We have demonstrated in Chapter 8 that it is possible to engineer the electronic structure of the n=1 PLS by selectively adsorbing Xe guests atoms inside the nanocavities. When globaly adsorbing Xe atoms into all nanocavities, a Pauli repulsion induced ~ 60 meV shift of the n=1 PLS to lower binding energies is detected in STS and corroborated by ARPES band structure measurements. In

addition, we can engineer different interpore coupling configurations by local reposition or removal of 12 Xe atoms with the STM tip. Such configurations yielded distinct localized states, while the electronic features of the surrounding identical QDs remained unaffected. Indeed, residues from the bonding part of the surrounding PLS can still be detected in the single pore LDOS, allowing us to delve into the intricacies of interpore coupling effects.

4. **The quantum dot intercoupling degree can be precisely engineered in nanoporous networks**.
   In Chapter 5, we precisely engineer the QD intercoupling by altering QDs barrier width (from single molecule barrier to a double one) without affecting the QD's size [Figure 11.1 (d, e)]. Halogen-bond stabilized organic nanoporous networks are generated on bulk Ag(111) and 3 ML Ag/Au(111) thin films alike by substitution of a single atom (sulphur vs oxygen) in the precursor molecule. Our findings show that the reduction of the QD intercoupling is associated with a flattening of the band dispersion and an increase of the effective mass that is mirrored by a narrowing of the asymmetric peak widths detected in STS [Figure 11.1 (d, e) and Table 11.1].

5. **The 2DEG can undergo an energy and mass renormalization upon the presence of nanoporous networks**.
   Perhaps one of the most surprising result is found in Chapter 6, where we study the electronic properties of two homothetic (similar) Co-coordinated metal-organic nanoporous networks [Figure 11.1 (d, e)]. Our results evidence a gradual and unusual energy shift of the Au(111) SS to higher binding energies and a lightening of the effective mass concomitant with a charge preservation upon network formation. Notably this downshift is gradual with decreasing pore size and occurs in spite of the demonstrated confining attributes of the nanocavities [Table 11.1].
   Overlayer-substrate interactions must be responsible for this effect on the Au SS reference. DFT calculations and phase accumulation model simulations help us to disentangle possible mechanisms responsible for these downshifts, where Au SS-Co adatom hybridization and Co/molecule vertical displacements appear as the most plausible causes. Similar renormalization effects are also observed on a Cu-coordinated metal-organic nanoporous network [Figure 11.1 (f)], suggesting that this traditionally overlooked effect could be rather general on MOCN with single coordination atoms.

11.2 Conclusions to Part III: Zigzag Chains

In the third part of this thesis, we have used the on-surface Ullmann coupling reaction to synthesize and macroscopically align a saturated film of cross-conjugated zigzag chains with periodically spaced *meta*-junctions on a vicinal Ag(111) surface.

ARPES measurements reveal weakly dispersing 1D electronic bands along the chain direction [Figure 11.2 (a)]. This band structure constrasts with the highly dispersive one of poly-(*para*-phenylene) chains and resembles more the one of poly-(*meta*-phenylene), demonstrating that the electronic band dispersion is governed by the periodically spaced *meta*-junctions.

We find that zigzag chains present a larger frontier orbital bandgap than the straight PPP counterparts (3.7 eV vs 3.2 eV in ref. [29]) and show electron confinement in each straight segment, reminiscent of 1D arrays of weakly interacting QDs [Figure 11.2 (b)]. Such molecular states can be tuned by changing the length of these straight segments, affecting the frontier orbital bandgap, which follows a $\frac{1}{N}$ dependency (where N is the number of phenyl rings per straight section).

These findings corroborate the important effects that the conductive path topology of a molecular wire has on its frontier orbitals, which are responsible for defining its chemical, optical and electronic properties.

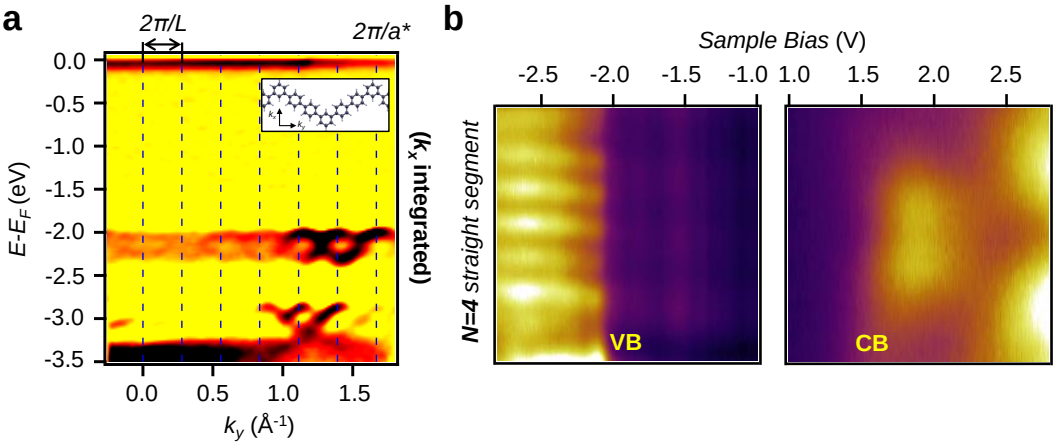

FIGURE 11.2: Zigzag chain electronic structure probed by (a) ARPES and (b) STS. Shallow dispersive bands evidence the loss of electronic coupling between neighboring straight segments, which are concomitant with electron localization effects, reminiscent of QD 1D arrays.

11.3 Outlook

Metal-organic frameworks (MOFs) are an important class of materials that present intriguing opportunities in the fields of sensing, gas storage, catalysis and optoelectronics [283–286]. MOCNs grown on metallic surfaces are also known to show magnetic properties [4, 5], catalytic effects [6, 7], oxidation states [8], exotic tesellation patterns [9–12] and even bear the prospect of exhibiting topological band structures [13, 14]. As an outlook for the near future, the following complementing research lines to this thesis are already initiated:

- **Magnetic Nanoclusters on MOCNs**. Highly ordered and robust MOCNs could be used as extended templates for controlling the ordering and size of magnetic atom nanoclusters and as a consequence, to tune their magnetic properties. The aim would be to induce magnetic atoms to self-assemble within the pores into ordered nanoclusters [287]. We have recently observed that Fe triangular islands grown on Cu(111) translate into well-ordered nanoclusters of controllable size when deposited on top of the Cu-DCA MOCN [Figure 11.3 (a-c)]. The next step is to study the size of these nanoclusters as well as their respective magnetic signal and compare them to the case where there is no MOF presence.

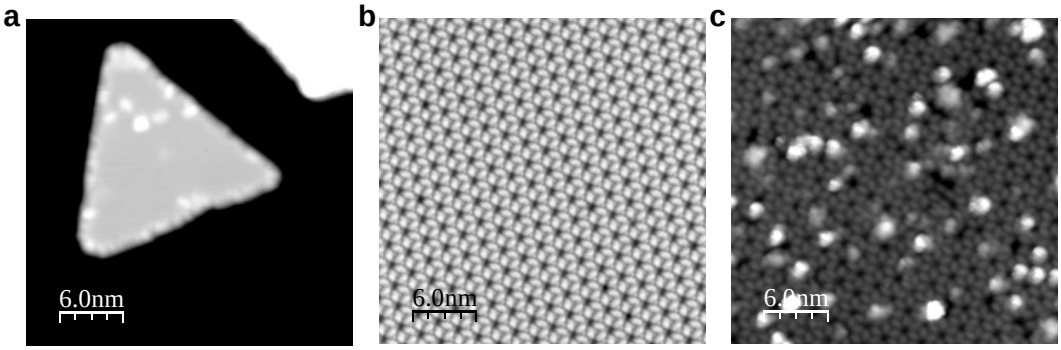

FIGURE 11.3: Fe nanocluster size and assembly control when grown on Cu-DCA MOCN. (a) Fe double atomic height triangular shape islands grown on Cu(111). (b) Long-range ordered Cu-DCA MOCN grown on Cu(111). (c) Fe nanocluster formation and stabilization when grown on top of Cu-DCA MOCN. This project is done in collaboration with Leyre Hernández and Dr. Fernando Bartolomé from ICMA (CSIC-University of Zaragoza).

- **Experimental Validation of Organic Topological Insulators (OTIs)**. Recently, 2D MOCNs have been proposed as a flexible material platform for realizing exotic quantum phases including topological and anomalous quantum Hall insulators [14, 288–292]. For example, it is possible to realize honeycomb and kagome lattices that are expected to give rise to Dirac cones and flat bands. The DCA-Cu MOCN is one of these examples [Figure 11.4 (a)]. If a strong spin-orbit coupling (SOC) is introduced by, for instance, using heavy elements

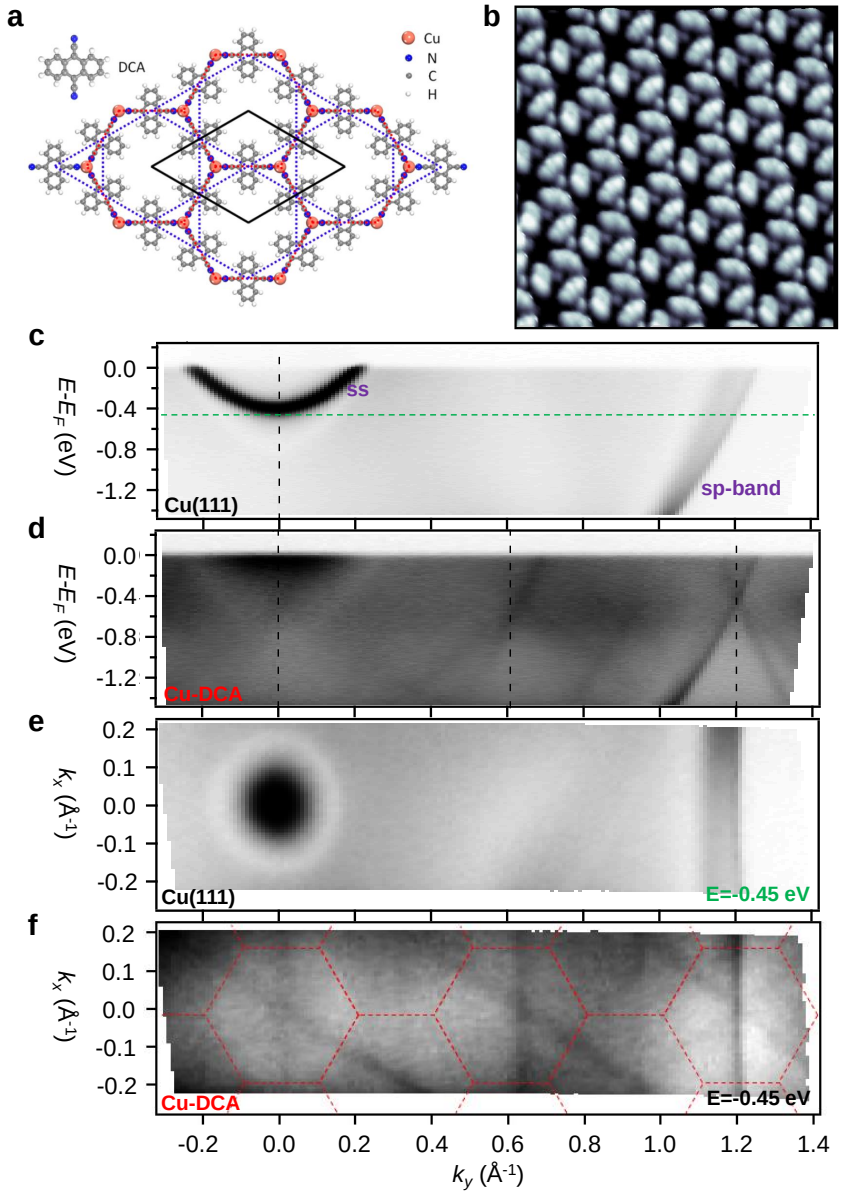

FIGURE 11.4: Metal-organic frameworks as organic topological insulators. (a) Schematic atomic structure of Cu-DCA film. The inset shows the DCA molecule. The red dashed , blue dashed, and black lines outline the honeycomb lattice by the Cu atoms, the Kagome lattice by the DCA molecules, and the unit cell, respectively (adapted from ref. [14]). (b) 10 × 10 nm^2 STM image of the Cu-DCA film grown on Cu(111). Its single domain, long-range order and low defect concentrations are ideal for ARPES band structure measurements. STM parameters: I=300 pA; V=-1 V. (c,d) ARPES raw band structure measurements (E vs k_y) of the pristine Cu(111) surface and Cu-DCA film along the $\overline{\Gamma K}$ high symmetry direction of both substrate and network. (e,f) Isoenergetic cuts (k_x vs k_y) performed at E=-0.45 eV for the pristine Cu(111) and Cu-DCA films respectively. The sp-band appears replicated following the DCA superperiodicity.

as Bi atoms in coordination, this should result in the opening of topologically non-trivial band gaps and the realization of OTIs with topological edge states.

Experimentally, direct synthesis of 2D MOCNs has been essentially confined to metal substrates [9]. For instance, we observe that the DCA-Cu MOCN

forms a single domain, long-range ordered film on Cu(111) [Figure 11.4 (b)]. ARPES band structure measurments on this particular MOCN (E vs k_y) clearly show how the *sp*-band of the Cu(111) surface [Fig. 11.4 (c)] appears replicated following the superperiodicity of the MOCN [vertical dahsed black lines in Fig. 11.4 (d)]. In addition, some intensity is detected at -0.45 eV, reminiscent of non-dispersive bands. However, isonergetic cuts (k_x vs k_y) performed at this energy only highlight the replicating *sp*-bands without any additional feature [cf. Figure 11.4 (e, f)]. This preliminary results suggest that the interaction with the metallic substrate most probably masks the intrinsic electronic properties of the MOCN [293, 294]. Therefore, depositing a 2D-OTIs on a 2D insulating substrate such as hBN or a decoupling layer such as graphene may protect the TI properties from quenching.

Regarding the on-surface synthesis and high-alignment of oligophenylene chains and GNRs on vicinal surfaces, the following research lines are proposed:

- **Image Potential States (IPS) in GNRs and Oligophenylene Chains**. Exotic super atom states have been detected inside graphene nanopores and bay-shape GNR edges [24, 277]. These states are neither related to atomic orbitals nor to the 2DEG confinement from the metallic substrate [295]. Instead, they originate from the free electron–like image potential states (IPS) that are confined at the vacuum side along the GNR edge. They can be regarded as the 2D analog of the super atom states that develop when a graphene sheet bends into a fullerene [296, 297]. In a similar fashion to the multibay-shape GNRs giving rise to rather flat super atom bands [24], zigzag polymers host an ideal geometry with periodic elbows for confining such IPS and coupling them in the long-range. Preliminary DFT calculations on the N=4 zigzag chain band structure [Figure 11.5 (a)] and molecular orbital simulations [Figure 11.5 (b)] at the expected IPS bands [purple and green arrows in Figure 11.5 (a)] evidence confinement of the electron wavefunction. Such localized states observed at the elbow regions may well correlate with the high intensities we observe in the high-resolution *dI/dV* map at 2.3 V [Figure 11.5 (c)], in agreement with previous observations on similar systems [24, 277]. Such IPS could be further tuned and their coupling altered by changing the separation between *meta*-junctions either by synthesizing a pure poly-(*meta*-phenylene) chain or by enlarging the straight segments lengths as well as by functionalizing the DMTP precursors with nitrogen atoms [26].

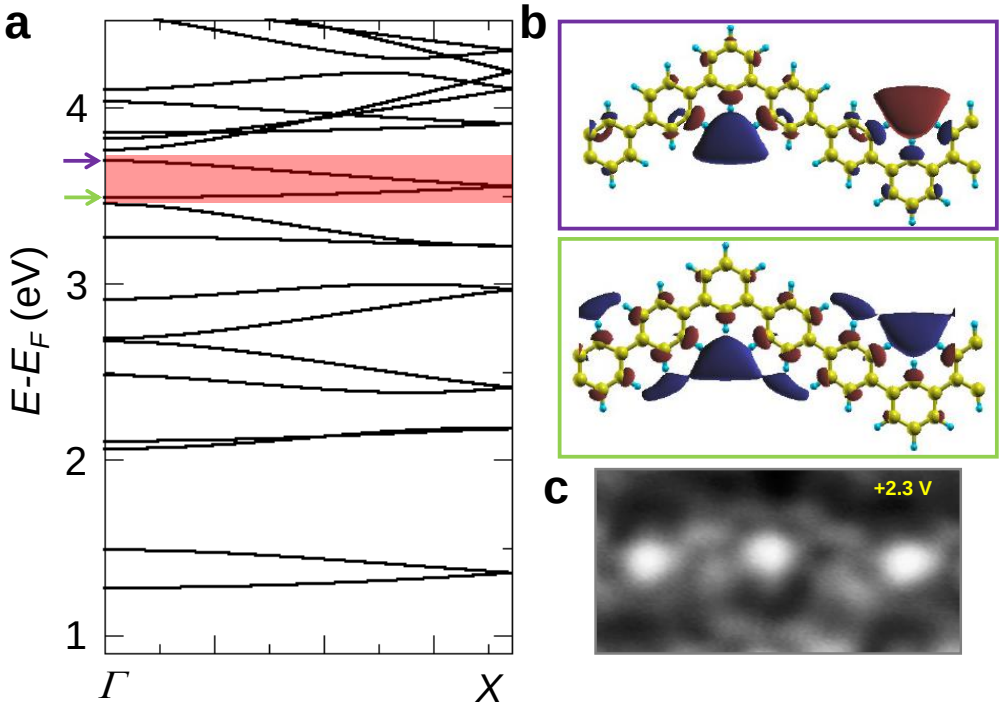

FIGURE 11.5: Image potential states in cross-conjugated oligophenylene zigzag chains. (a) DFT calculated electronic band structure for free-standing zigzag polymers. The possible IPS state coupling induced shallow dispersive bands are highlighted in red. (b) The spatially resolved molecular orbitals at $\overline{\Gamma}$ for both bands [purple and green arrows in (a)] show the electron wavefunction localized in the concave region of each elbow of the zigzag chain. Interestingly, its spatial position spreads outside the carbon backbone. (c) High-resolution constant height *dI/dV* map at 2.3 V shows high intensity collimation at the elbow sites of the zigzag polymer, in resemblance to the predicted IPS.

- **Generation of 1D and 2D ordered structures by the right choice of substrate and precursors**. Recent advances in transfer techniques of on-surface synthesized organic nanostructures onto insulating substrates [24, 32] opens the path towards further studying transport and optical properties of the highly-aligned cross-conjugated oligophenyelene zigzag chains. Most importantly, since the alignment of these polymers or GNRs into films and their directionality may be a necessary prerequisite to conserve during transfer and device fabrication, the use of vicinal surfaces not only would be mandatory for photoemission experiments but also could serve as an alignment tool for GNR and polymer based device fabrication, provided that the nanotemplate is repeatedly conserved [33].

  The development in chemical synthesis has lead to the synthesis of graphene nanoribbons with different edge topologies. By tuning the edge termination from armchair type to zigzag, edge states have been observed [28]. In addition, recently GNRs with non-trivial topology have been grown on metallic substrates, giving rise to exotic topological states [25, 30]. By using the right

vicinal surface, a desirable macroscopic growth and alignment of such GNRs would allow for the experimental observation of their bulk and edge band structure in ARPES, greatly complementing the already available STS information.

The current understading on molecular self-assembly for building nanoporous networks and on-surface synthesis methods for builiding covalent 1D and 2D nanostructures sets the grounds for designing suitable molecular precursors for the formation of long-range ordered COFs. The main current issue is to reduce the defect concentration appearing as tetragonal, pentagonal and heptagonal pores when targeting the formation of a honeycomb COF from three-fold halo-aromatic precursors [63, 75, 298]. Perhaps using four-fold symmetric precursors may give rise to the formation of square-shaped COFs with a lower defect concentration [69, 299].

Appendix A

Resumen de las Conclusiones Principales

A.1 Estructura Electrónica de Redes Orgánicas Nanoporosas Generadas en Superficies de Metales Nobles

En la segunda parte de la tesis se ha estudiado las propiedades de confinamiento electrónico y las bandas electrónicas generadas a partir del acoplamiento entre puntos cuánticos (QDs) existentes en las redes nanoporosas orgánicas y metal-orgánicas generadas sobre superficies metálicas. Esto ha sido posible gracias a la caracterización experimental de hasta seis redes nanoporosas autoensambladas sobre substratos metálicos tales como Cu(111), Ag(111) y Au(111) además de heteroestructuras metálicas compuestas por 3 capas atómicas de Ag en Au(111), todo ello en condiciones controladas de ultra alto vacío (UHV).

Las redes nanoporosas con orden a largo alcance, aquellas que recubren por completo toda la superficie, han sido generadas mediante la selección de interacciones intermoleculares adecuadas a modo de enlaces autocorrectores, tales como enlaces halógenos y metal-orgánicos, junto con una correcta interacción molécula-sustrato y registro con el sustrato. Dichos sistemas se han preparado utilizando gradientes de recubrimiento. Este modo de preparación tan complejo representa un requisito *sine qua non* para observar bandas electrónicas moduladas en medidas de fotoemisión resuelta en ángulo (ARPES). Además, mediante el uso de técnicas espectroscópicas complementarias como la microscopía de efecto túnel (STM/STS), se han estudiado las propiedades de confinamiento electrónico locales, es decir, en cada nanoporo o QD, complementando de manera satisfactoria las bandas electrónicas detectadas en fotoemisión.

El modelo semi empírico denominado método de elementos de frontera del electrón (EBEM) en combinación con la expansión de ondas planas de electrones (EPWE) se ha utilizado de manera recurrente para simular y comprender el complejo sistema de dispersión que cada red nanoporosa ejerce sobre el gas electrónico bi-dimensional (2DEG) presente en las superficies metálicas usadas como substrato. Esto nos ha permitido reconstruir y corroborar tanto las complejas bandas electrónicas como las propiedades locales de confinamiento a nivel de nanoporo mediante las simulación

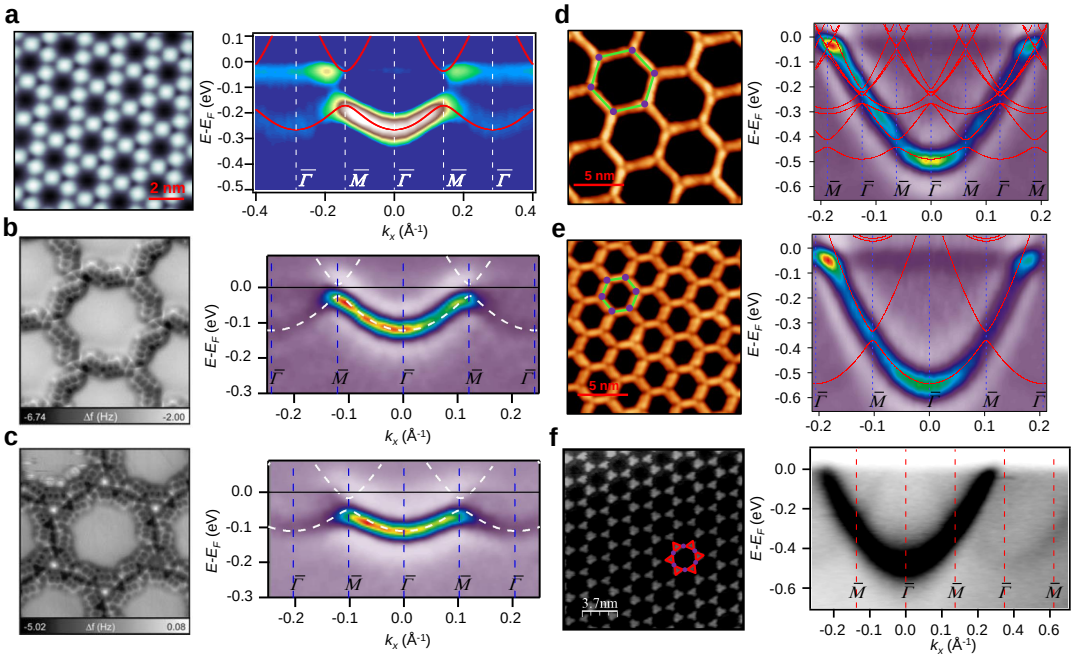

FIGURE A.1: Resumen de la estructura de bandas de las diferentes redes nanoporosas estudiadas con ARPES. (a) Red nanoporosa metal-orgánica 3deh-DPDI en Cu(111). (b, c) Redes nanoporosas estabilizadas con enlaces halógenos con barreras compuestas por moléculas individuales (SW) y dobles (DW) crecidas sobre 3ML Ag/Au(111). (d, e) Redes nanoporosas metal-orgánicas similares compuestas por las moléculas Ph6 y Ph3, respectivamente, en coordinación con átomos de Co y crecidas sobre Au(111). (f) Red nanoporosa metal-orgánica compuesta por la molécula TPyB en coordinación con átomos de Cu y crecida sobre Cu(111).

de las densidades locales de estado (LDOS). Además, los métodos de cálculo de teoría de funcional de densidad (DFT) y modelo de acumulación de fase (PAM) han sido utilizados para abordar en detalle las sutiles interacciones verticales en forma de hibridización y efectos geométricos presentes en la interfase entre la red orgánica nanoporosa y el 2DEG. Esta sinergia entre técnicas experimentales y simulaciones teóricas nos ha aportado una profunda comprensión sobre las propiedades electrónicas derivadas del ensamblaje de cada red nanoporosa en particular.

Los resultados obtenidos sirven para comprender las propiedades electrónicas de las redes nanoporososas orgánicas y metal-orgánicas crecidas sobre superficies metálicas. Los resultados principales se pueden resumir en los siguientes puntos fundamentales:

1. **Los estados parcialmente localizados en las redes nanoporosas se originan o provienen del estado de superficie del sustrato**.
   Mediante el estudio de la dependencia con la temperatura de las bandas electrónicas generadas por la red metal-orgánica nanoporosa 3deh-DPDI (capítulo 4), se corrobora que el primer estado parcialmente localizado (denominado n=1 PLS) existente en los nanoporos, proviene del estado de Shockley de Cu(111). La energía fundamental de ambos estados, es decir, de n=1 PLS y Cu SS, muestra la misma tendencia con la temperatura, lo que evidencia

TABLE A.1: Resumen de las propiedades electrónicas extraídas de las medidas de ARPES, es decir, las energías de ligadura en el punto $\overline{\Gamma}$ y las masas efectivas de las respectivas redes nanoporosas estudiadas. Además se incluyen los potenciales de dispersión, energías de referencia y masas efectivas adoptadas en las simulaciones con EBEM/EPWE.

	$E_B^{\overline{\Gamma}}$ (eV)	m^*/m_0	$E_{EBEM}^{Ref,\overline{\Gamma}}$ (eV)	$m_{EBEM}^{*,Ref}/m_0$	V_{mol} (meV)	V_{met} (meV)
3deh-DPDI/Cu(111)	0.25	0.57	0.40	0.49	390	340/440
SW/ 3ML Ag/Au(111)	0.12	0.47	0.16	0.49	140	–
DW/ 3ML Ag/Au(111)	0.11	0.59	0.16	0.54	140	–
Ph6Co/Au(111)	0.49	0.24	0.52	0.24	250	50
Ph3Co/Au(111)	0.55	0.22	0.59	0.21	250	50
Cu-TPyB/Cu(111)	0.47	0.41	–	–	–	–
Au(111)	0.45	0.255	0.45	0.26	–	–
3ML Ag/Au(111)	0.16	0.38	0.16	0.38	–	–
Cu(111)	0.40	0.42	0.40	0.42	–	–

su naturaleza común. Esta demostración experimental respalda el hecho de que los electrones de superficie son muy sensibles y por ende, se ven drásticamente afectados por los potenciales de dispersión periódicos generados por la red nanoporosa molecular, localizando o atrapando parcialmente dichos electrones en cada nanocavidad o nanoporo.

2. **El mapa de potencial de dispersión producido por las redes nanoporosas tiene un caracter repulsivo sobre el estado de superficie, acompañado de una renormalización de éste tanto en masa como en energía**.
   Mediante el uso de la red nanoporosa metal-orgánica creada por 3deh-DPDI, en el capítulo 7 se demuestra que es posible obtener de forma fehaciente el mapa de potencial de dispersión que representa una red nanoporosa para el 2DEG sobre el cual se ha generado. De esta manera se pueden simular de manera detallada y rigurosa los efectos de confinamiento electrónico e interacciones más relevantes. Demostramos que el mapa de potencial de dispersión se tiene que generar o parametrizar siguiendo detalladamente la geometría de la red nanoporosa, permitiendo un grado de flexibilidad en la referencia del 2DEG. Esto implica que se require de una renormalización en masa y energía causada por interacciones entre el gas electrónico y la red orgánica. Nuestras simulaciones asignan, sin ninguna duda, un carácter repulsivo tanto a moléculas como a los metales de coordinación, sirviendo ambos como barreras repulsivas para los electrones de superficie. Además, los estados confinados en la red 3deh-DPDI, aparecen deformados, adoptando una disposición triangular en algunos casos, en vez de la estructura hexagonal esperada. Estas distorsiones son debidas a pequeñas perturbaciones en el potencial de dispersión de

los metales de coordinación, que debido a su simetría triangular, provocan un cambio espacial en los estados electrónicos.

3. **Los estados electrónicos en redes nanoporosas se pueden configurar tanto individual como globalmente mediante la fisisorción de gases nobles como el Xe**.
   En el capítulo 8 se demuestra que es posible manipular de forma controlada la estructura electrónica del n=1 PLS en la red nanoporosa 3deh-DPDI mediante la absorción global y simultanea de 12 átomos de Xe en cada nanoporo de la red. Además, mediante manipulación individual de átomos de Xe con la punta del STM, es posible obtener diferentes configuraciones de ocupación para alterar los estados localizados de manera individual. En el primero de los casos, mediante medidas de espectroscopía de efecto túnel, observamos que los átomos de Xe generan una interacción denominada repulsión de Pauli, mediante la cual el n=1 PLS presenta un cambio de 60 meV hacia energía de ligadura menores. Estas observaciones locales se corroboran mediante medidas de ARPES, evidenciando un cambio similar en la energía fundamental de la banda electrónica correspondiente a n=1 PLS. En el segundo caso, se procede a alterar las configuraciones a primeros vecinos: un poro vacío rodeado de poros llenos de Xe y viceversa. Estas configuraciones artificialmente construidas muestran que en el poro manipulado residen estados localizados a energías más negativas y de mayor anchura de pico para el primer caso y estados muy localizados a menores energías para el segundo de los casos. Dichos cambios, no afectan al estado electrónico de los poros vecinos pero sí que se observan la cola de los mismos en las posiciones manipuladas. Estos resultados nos aclaran algunos conceptos dentro de la complejidad de las interacciones entre poros existentes en este tipo de redes nanoporosas.

4. **Las redes nanoporosas permiten controlar el acoplamiento electrónico entre QDs con un alto grado de precisión**.
   En el capítulo 5 mostramos que somos capaces de alterar de forma controlada el grado de interacción entre puntos cuánticos (QDs) modificando el grado de comunicación o acoplamiento entre QDs perfectamente ordenados en una red. Esto se ha conseguido mediante la modificación de la anchura de la barrera entre QDs, pasando de una sola molécula en un caso, a dos moléculas en el segundo caso, sin afectar el tamaño del QD [Figuras A.1 (b, c)]. Ambas redes nanoporosas se estabilizan mediante enlaces halógenos y se generan tanto en Ag(111) como en 3 ML Ag/Au(111). La diferencia entre ambos sistemas nanoporosos reside, únicamente, en el uso de un mismo precursor salvo por el canje de un atomo de azufre por uno de oxígeno.
   La combinación de técnicas experimentales de ARPES y STM/STS junto con

simulaciones realizadas con EBEM/EPWE, aportan una visión completa desde el punto de vista fundamental sobre la naturaleza de los procesos de acoplamiento entre QDs. Nuestros hallazgos demuestran de forma fehaciente que la reducción en el acoplamiento entre QDs está diréctamente asociada con una planarización en la dispersión de la banda electrónica generada y un incremento de la masa efectiva del electrón. Estos efectos son respaldados por las observaciones de STS, donde el pico muestra un carácter asimétrico correspondiente a los estados parcialmente localizados en QDs, los cuales sufren un estrechamiento debido a la disminución en el acoplamiento.

5. **Los 2DEG presentes en las superficies metálicas pueden experimentar una renormalización de su energía y masa a causa de las redes nanopororos orgánicas y metal-orgánicas ensambladas encima**.
   Posiblemente el resultado más llamativo se presenta en el capítulo 6, donde hemos estudiado las propiedades electrónicas de dos redes nanoporosas metal-orgánicas similares, ambas coordinadas con átomos de cobalto [Figuras A.1 (d, e)]. Nuestros resultados evidencian un cambio gradual de la energía fundamental hacia mayores energías de ligadura acompañado de un aligeramiento en la masa efectiva del estado de superficie de Au(111) simultáneo a una preservación de la carga total del 2DEG. Notablemente, estos cambios graduales en energía y masa están directamente relacionados con una disminución del tamaño del nanoporo entre ambos sistemas y son compatibles con las observaciones de confinamiento electrónico dentro de cada nanoporo.
   Las interacciones entre las redes nanoporosas y el 2DEG deberían de ser los responsables de los cambios de referencia observados. Los cálculos teóricos realizados con DFT y PAM nos ayudan an entender mejor los posibles mecanismos involucrados en estos efectos electrónicos, siendo la hibridización entre los atómos de Co y el 2DEG, además de posibles desplazamientos verticales de las moléculas, las causas más plausibles. En este sentido, hemos observado similares efectos de renormalización en otra red nanoporosa metal-orgánica, pero esta vez, utilizando átomos de coordinación de cobre [Figura A.1 (f)], lo que sugiere que, estos efectos que tradicionalmente han pasado desapercibidos, podrían ser comunes a redes orgánicas nanoporosas coordinadas con un sólo átomo.

A.2 Estructura Electrónica de Cadenas Orgánicas Covalentes Unidimensionales Sintetizadas en Superficie

En la tercera parte de la presente tesis, hemos hecho uso de la reacción de Ullmann en un cristal vecinal de Ag(111) para sintetizar y alinear una película constituida por cadenas de geometría zigzag compuestas de uniones *meta* periódicamente espaciadas. Las medidas de ARPES revelan bandas electrónicas unidimensiones muy poco dispersivas a lo largo del eje pricipal de las cadenas [Figura A.2 (a)]. Esta estructura de bandas contrasta con la estructura de bandas altamente dispersiva ya conocida para el caso del poly-(*para*-fenileno) (PPP) y se asemeja, en cambio, al poly-(*meta*-fenileno) (PMP), demostrando claramente que la estructura de bandas está gobernada y controlada por las uniones *meta* periódicamente espaciadas.

Mediante mediadas espectroscópicas locales sobre las cadenas zigzag crecidas en Ag(111), observamos que el tamaño de energía prohibida entre los orbitales frontera es de 3.7 eV, sensiblemente mayor que el ya conocido para PPP (3.2 eV [29]) [Figura A.2 (b)]. Además, detectamos indicios claros de confinamiento electrónico en cada segmento recto comprendido entre uniones *meta*, con lo que el polímero en forma zigzag se asemeja a un sistema unidimensional de QDs débilmente acoplados. Estos estados moleculares se pueden modular cambiando la longitud de los segmentos rectos, los cuales están estrictamente definidos por el número de fenilos (N) que la componen, alterando en consecuencia el tamaño de energía prohibida del sistema con una dependencia de $\frac{1}{N}$.

Estos hallazgos corroboran los efectos significativos que el recorrido topológico tiene sobre la conductividad electrónica y los orbitales frontera, los cuales son responsables de definir las propiedades químicas, ópticas y electrónicas de la propia cadena.

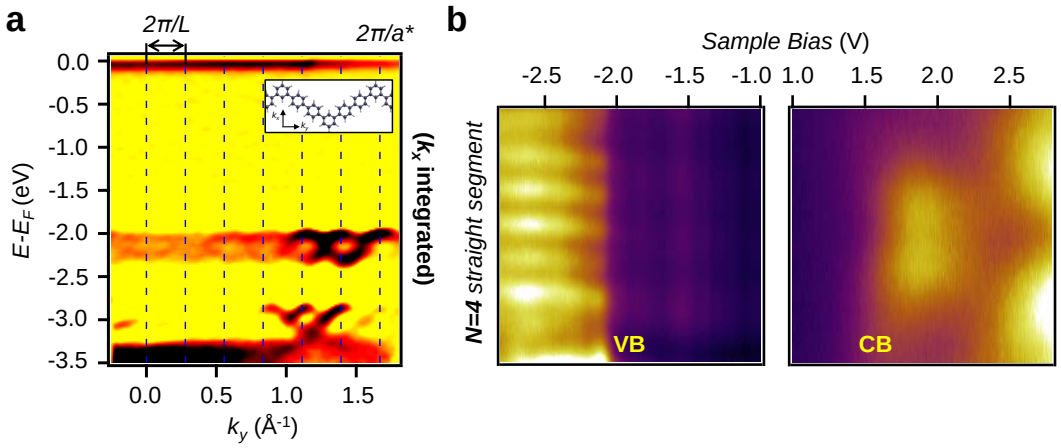

FIGURE A.2: Estructura electrónica de las cadenas zigzag obtenidas mediante (a) ARPES y (b) STS. Las bandas poco dispersivas evidencian una pérdida del acoplamiento electrónico con los segmentos rectos adyacentes, lo cual coincide con efectos de confinamiento que son reminiscentes de redes de QDs unidimensionales.

Appendix B

List of Publications

1. L. A. Miccio, M. Setvin, M. Müller, M. Abadía, I. Piquero-Zulaica, J. Lobo-Checa, F. Schiller, C. Rogero, M. Schmid, D. Sánchez-Portal, U. Diebold, J.E. Ortega. **Interplay between Steps and Oxygen Vacancies on Curved TiO2(110)** *NanoLetters* **16**, pp. 2017-2022 (2016)

2. S. Nowakowska, A. Wäckerlin, I. Piquero-Zulaica, J. Nowakowski, S. Kawai, C. Wäckerlin, M. Matena, T. Nijs, S. Fatayer, O. Popova, A. Ahsan, S. Fatameh Mousavi, T. Ivas, E. Meyer, M. Stöhr, J. E. Ortega, J. Björk, L. H. Gade, J. Lobo-Checa, T. A. Jung. **Configuring Electronic States in an Atomically Precise Breadboard of Quantum Boxes** *Small* **12**, 28, pp. 3759-3763 (2016)

3. Z. M. Abd El-Fattah, P. Lutz, I. Piquero-Zulaica, J. Lobo-Checa, F. Schiller, H. Bentmann, J. E. Ortega, F. Reinert. **Formation of the BiAg2 Surface Alloy on Lattice Mismatched Interfaces** *Physical Review B* **94**, 155447 (2016)

4. J. Brede, J. Slawinska, M. Abadia, C. Rogero, J. E. Ortega, I. Piquero-Zulaica, J. Lobo-Checa, A. Arnau , J. Iribas Cerdá. **Tuning the Graphene on Ir(111) Adsorption Regime by Fe/Ir Surface-Alloying** *2D Materials* **4**, 1 (2016)

5. I. Piquero-Zulaica, S. Nowakowska, J. E. Ortega, M. Stöhr, L. H. Gade, T. A. Jung, J. Lobo-Checa. **Temperature Dependence of the Partially Localized State in a 2D Molecular Nanoporous Network** *Applied Surface Science* **391**, pp. 39-43 (2017)

6. I. Piquero-Zulaica, J. Lobo-Checa, A. Sadeghi, Z. M. Abd El-Fattah, C. Mitsui, T. Okamoto, R. Pawlak, T. Meier, A. Arnau, J. E. Ortega, J. Takeya, S. Goedecker, E. Meyer, S. Kawai. **Precise Engineering of Quantum Dot Array Coupling Through Their Barrier Widths** *Nature Communications* **8**, 787 (2017)

7. M. Abadia, M. Ilyn, I. Piquero-Zulaica, P. Gargiani, C. Rogero, J. E. Ortega and J. Brede. **Polymerization of Well-Aligned Organic Nanowires on a Ferromagnetic Rare-Earth Surface Alloy** *ACS nano* **11**, 12, 12392-12401 (2017)

8. J. E. Ortega, G. Vasseur, I. Piquero-Zulaica, S. Matencio, M. A. Valbuena, J. Rault, F. Schiller, M. Corso, A. Mugarza and J. Lobo-Checa. **Structure and**

Electronic States on Vicinal Ag(111) Surfaces with Densely Kinked Steps *New J. Phys* **20**, 7, 073010 (2018)

9. I. Piquero-Zulaica, A. Garcia-Lekue, L. Colazzo, C. K. Krug, M. S. G. Mohammed, Z. M. Abd El-Fattah, J. M. Gottfried, D. G. de Oteyza, J. E. Ortega, J. Lobo-Checa. **Electronic Structure Tunability by Periodic *meta*-Ligand Spacing in One-Dimensional Organic Semiconductors** *Accepted in ACS nano* (2018) DOI: 10.1021/acsnano.8b06536

10. I. Piquero-Zulaica, Z. M. Abd El-Fattah, J. Li, L. Solianyk, I. Gallardo, A. Arnau, J. E. Ortega, M. Stöhr and J. Lobo-Checa. **Tunable Energy and Mass Renormalization from Homothetic Quantum Dot Arrays** *In preparation*

11. I. Piquero-Zulaica, Z. M. Abd El-Fattah, S. Nowakowska, S. Kawai, O. Popova, M. Matena, M. Enache, M. Stöhr, J. E. Ortega, L. H. Gade, T. A. Jung and J. Lobo-Checa. **Effective Determination of Surface Potential Landscapes from Metal-Organic Nanoporous Overlayers** *In preparation*

12. Z. M. Abd El-Fattah, M. A. Kher-Eldem, I. Piquero-Zulaica, F. J. García de Abajo and J. E. Ortega. **Graphene: Free Electron Scattering Within an Inverted Honeycomb Lattice** *Submitted for publication in 2D Materials*

Bibliography

[1] J. V. Barth, G. Costantini, and K. Kern. "Engineering atomic and molecular nanostructures at surfaces". In: *Nature* 437. 7059 (2005), pp. 671–679.

[2] L. Bartels. "Tailoring molecular layers at metal surfaces". In: *Nature Chemistry* 2. 2 (2010), pp. 87–95.

[3] A. Kumar, K. Banerjee, and P. Liljeroth. "Molecular assembly on two-dimensional materials". In: *Nanotechnology* 28. 8 (2017), p. 082001.

[4] N. Abdurakhmanova et al. "Superexchange-Mediated Ferromagnetic Coupling in Two-Dimensional Ni-TCNQ Networks on Metal Surfaces". In: *Physical Review Letters* 110. 2 (2013), p. 027202.

[5] T. R. Umbach et al. "Ferromagnetic Coupling of Mononuclear Fe Centers in a Self-Assembled Metal-Organic Network on Au(111)". In: *Physical Review Letters* 109. 26 (2012), p. 267207.

[6] R. Gutzler et al. "Mimicking Enzymatic Active Sites on Surfaces for Energy Conversion Chemistry". In: *Accounts of Chemical Research* 48. 7 (2015), pp. 2132–2139.

[7] J. Čechal et al. "CO $_2$ Binding and Induced Structural Collapse of a Surface-Supported Metal–Organic Network". In: *The Journal of Physical Chemistry C* 120. 33 (2016), pp. 18622–18630.

[8] Y. Li et al. "Coordination and Metalation Bifunctionality of Cu with 5,10,15,20-Tetra(4-pyridyl)porphyrin: Toward a Mixed-Valence Two-Dimensional Coordination Network". In: *Journal of the American Chemical Society* 134. 14 (2012), pp. 6401–6408.

[9] L. Dong, Z. Gao, and N. Lin. "Self-assembly of metal–organic coordination structures on surfaces". In: *Progress in Surface Science* 91. 3 (2016), pp. 101–135.

[10] J. I. Urgel et al. "Quasicrystallinity expressed in two-dimensional coordination networks". In: *Nature Chemistry* 8. 7 (2016), pp. 657–662.

[11] L. Yan et al. "Self-assembly of a binodal metal–organic framework exhibiting a demi-regular lattice". In: *Faraday Discussions* 204 (2017), pp. 111–121.

[12] Yi-Qi Zhang et al. "Complex supramolecular interfacial tessellation through convergent multi-step reaction of a dissymmetric simple organic precursor". In: *Nature Chemistry* 10. 3 (2018), pp. 296–304.

[13] X. Zhang and M. Zhao. "Robust half-metallicity and topological aspects in two-dimensional Cu-TPyB". In: *Scientific Reports* 5. 14098 (2015).

[14] L. Z. Zhang et al. "Intrinsic Two-Dimensional Organic Topological Insulators in Metal–Dicyanoanthracene Lattices". In: *Nano Letters* 16. 3 (2016), pp. 2072–2075.

[15] J. Lobo-Checa et al. "Band Formation from Coupled Quantum Dots Formed by a Nanoporous Network on a Copper Surface". In: *Science* 325. 5938 (2009), pp. 300–303.

[16] F. Klappenberger et al. "Dichotomous Array of Chiral Quantum Corrals by a Self-Assembled Nanoporous Kagomé Network". In: *Nano Letters* 9. 10 (2009), pp. 3509–3514.

[17] F. Klappenberger et al. "Tunable Quantum Dot Arrays Formed from Self-Assembled Metal-Organic Networks". In: *Physical Review Letters* 106. 2 (2011), p. 026802.

[18] M. F. Crommie, C. P. Lutz, and D. M. Eigler. "Confinement of Electrons to Quantum Corrals on a Metal Surface". In: *Science* 262. 5131 (1993), pp. 218–220.

[19] M. F. Crommie et al. "Waves on a Metal Surface and Quantum Corrals". In: *Surface Review and Letters* 02. 01 (1995), pp. 127–137.

[20] D. R. Smith. "Metamaterials and Negative Refractive Index". In: *Science* 305. 5685 (2004), pp. 788–792.

[21] K. Nakada et al. "Edge state in graphene ribbons: Nanometer size effect and edge shape dependence". In: *Physical Review B: Condensed Matter and Materials Physics* 54. 24 (1996), pp. 17954–17961.

[22] Ting Cao, Fangzhou Zhao, and Steven G. Louie. "Topological Phases in Graphene Nanoribbons: Junction States, Spin Centers, and Quantum Spin Chains". In: *Physical Review Letters* 119. 7 (2017), p. 076401.

[23] Y.-C. Chen et al. "Molecular bandgap engineering of bottom-up synthesized graphene nanoribbon heterojunctions". In: *Nature Nanotechnology* 10. 2 (2015), pp. 156–160.

[24] C. Moreno et al. "Bottom-up synthesis of multifunctional nanoporous graphene". In: *Science* 360. 6385 (2018), pp. 199–203.

[25] D. J. Rizzo et al. "Topological band engineering of graphene nanoribbons". In: *Nature* 560. 7717 (2018), pp. 204–208.

[26] A. Basagni et al. "Tunable Band Alignment with Unperturbed Carrier Mobility of On-Surface Synthesized Organic Semiconducting Wires". In: *ACS Nano* 10. 2 (2016), pp. 2644–2651.

[27] P. Ruffieux et al. "Electronic Structure of Atomically Precise Graphene Nanoribbons". In: *ACS Nano* 6. 8 (2012), pp. 6930–6935.

[28] P. Ruffieux et al. "On-surface synthesis of graphene nanoribbons with zigzag edge topology". In: *Nature* 531. 7595 (2016), pp. 489–492.

[29] N. Merino-Díez et al. "Width-Dependent Band Gap in Armchair Graphene Nanoribbons Reveals Fermi Level Pinning on Au(111)". In: *ACS Nano* 11. 11 (2017), pp. 11661–11668.

[30] O. Gröning et al. "Engineering of robust topological quantum phases in graphene nanoribbons". In: *Nature* 560. 7717 (2018), pp. 209–213.

[31] A. Celis et al. "Graphene nanoribbons: fabrication, properties and devices". In: *Journal of Physics D: Applied Physics* 49. 14 (2016), p. 143001.

[32] J. P. Llinas et al. "Short-channel field-effect transistors with 9-atom and 13-atom wide graphene nanoribbons". In: *Nature Communications* 8. 633 (2017).

[33] M. Ohtomo et al. "Graphene nanoribbon field-effect transistors fabricated by etchant-free transfer from Au(788)". In: *Applied Physics Letters* 112. 2 (2018), p. 021602.

[34] Z. M. Abd El-Fattah et al. "Graphene: Free electron scattering within an inverted honeycomb lattice". In: *arXiv:1808.06034* (2018).

[35] G. Buchs et al. "Confined electron and hole states in semiconducting carbon nanotube sub-10 nm artificial quantum dots". In: *Carbon* 132 (2018), pp. 304–311.

[36] R. P. Feynman. "There's plenty of room at the bottom: An invitation to enter a new field of physics". In: *Resonance* 16. 9 (2011), pp. 890–905.

[37] N. Taniguchi, ed. *Nanotechnology: integrated processing systems for ultra-precision and ultra-fine products*. Oxford science publications. Oxford [England] ; New York: Oxford University Press, 1996.

[38] V. Balzani. "Nanoscience and nanotechnology: The bottom-up construction of molecular devices and machines". In: *Pure and Applied Chemistry* 80. 8 (2008), pp. 1631–1650.

[39] B. D. Gates et al. "New Approaches to Nanofabrication: Molding, Printing, and Other Techniques". In: *Chemical Reviews* 105. 4 (2005), pp. 1171–1196.

[40] G. Binnig and H. Rohrer. "Scanning tunneling microscopy—from birth to adolescence". In: *Reviews of Modern Physics* 59. 3 (1987), pp. 615–625.

[41] D. M. Eigler et al. "Imaging Xe with a low-temperature scanning tunneling microscope". In: *Physical Review Letters* 66. 9 (1991), pp. 1189–1192.

[42] D. M. Eigler and E. K. Schweizer. "Positioning single atoms with a scanning tunnelling microscope". In: *Nature* 344. 6266 (1990), pp. 524–526.

[43] L. Bartels, G. Meyer, and K.-H. Rieder. "Controlled vertical manipulation of single CO molecules with the scanning tunneling microscope: A route to chemical contrast". In: *Applied Physics Letters* 71. 2 (1997), pp. 213–215.

[44] J.-M. Lehn. "Toward complex matter: Supramolecular chemistry and self-organization". In: *Proceedings of the National Academy of Sciences* 99. 8 (2002), pp. 4763–4768.

[45] G. M. Whitesides. "Self-Assembly at All Scales". In: *Science* 295. 5564 (2002), pp. 2418–2421.

[46] A. Kühnle. "Self-assembly of organic molecules at metal surfaces". In: *Current Opinion in Colloid & Interface Science* 14. 2 (2009), pp. 157–168.

[47] J. V. Barth. "Molecular Architectonic on Metal Surfaces". In: *Annual Review of Physical Chemistry* 58 (2007), pp. 375–407.

[48] E. Goiri et al. "Multi-Component Organic Layers on Metal Substrates". In: *Advanced Materials* 28. 7 (2016), pp. 1340–1368.

[49] S. Conti and M. Cecchini. "Predicting molecular self-assembly at surfaces: a statistical thermodynamics and modeling approach". In: *Physical Chemistry Chemical Physics* 18. 46 (2016), pp. 31480–31493.

[50] G. Pawin et al. "A Homomolecular Porous Network at a Cu(111) Surface". In: *Science* 313. 5789 (2006), pp. 961–962.

[51] U. Schlickum et al. "Metal-Organic Honeycomb Nanomeshes with Tunable Cavity Size". In: *Nano Letters* 7. 12 (2007), pp. 3813–3817.

[52] N. A. A. Zwaneveld et al. "Organized Formation of 2D Extended Covalent Organic Frameworks at Surfaces". In: *Journal of the American Chemical Society* 130. 21 (2008), pp. 6678–6679.

[53] S. Nowakowska et al. "Configuring Electronic States in an Atomically Precise Array of Quantum Boxes". In: *Small* 12. 28 (2016), pp. 3759–3763.

[54] I. Piquero-Zulaica et al. "Precise engineering of quantum dot array coupling through their barrier widths". In: *Nature Communications* 8.787 (2017).

[55] R. Balog et al. "Bandgap opening in graphene induced by patterned hydrogen adsorption". In: *Nature Materials* 9. 4 (2010), pp. 315–319.

[56] M. Ezawa. "Peculiar width dependence of the electronic properties of carbon nanoribbons". In: *Physical Review B: Condensed Matter and Materials Physics* 73. 4 (2006).

[57] R. Lindner and A. Kühnle. "On-Surface Reactions". In: *ChemPhysChem* 16. 8 (2015), pp. 1582–1592.

[58] A. Richter et al. "On-surface synthesis on a bulk insulator surface". In: *Journal of Physics: Condensed Matter* 30. 13 (2018), p. 133001.

[59] A. Gourdon. "On-Surface Covalent Coupling in Ultrahigh Vacuum". In: *Angewandte Chemie International Edition* 47. 37 (2008), pp. 6950–6953.

[60] D. F. Perepichka and F. Rosei. "Chemistry: Extending Polymer Conjugation into the Second Dimension". In: *Science* 323. 5911 (2009), pp. 216–217.

[61] J. A. Lipton-Duffin et al. "Synthesis of Polyphenylene Molecular Wires by Surface-Confined Polymerization". In: *Small* 5. 5 (2009), pp. 592–597.

[62] J. Cai et al. "Atomically precise bottom-up fabrication of graphene nanoribbons". In: *Nature* 466. 7305 (2010), pp. 470–473.

[63] M. Lackinger. "Surface-assisted Ullmann coupling". In: *Chemical Communications* 53. 56 (2017), pp. 7872–7885.

[64] E. Carbonell-Sanromà et al. "Quantum Dots Embedded in Graphene Nanoribbons by Chemical Substitution". In: *Nano Letters* 17. 1 (2017), pp. 50–56.

[65] S. Wang, W. Wang, and N. Lin. "Resolving Band-Structure Evolution and Defect-Induced States of Single Conjugated Oligomers by Scanning Tunneling Microscopy and Tight-Binding Calculations". In: *Physical Review Letters* 106. 20 (2011), p. 206803.

[66] J. Eichhorn et al. "On-surface Ullmann polymerization *via* intermediate organometallic networks on Ag(111)". In: *Chemical Communications* 50. 57 (2014), pp. 7680–7682.

[67] S.-W. Hla et al. "Inducing All Steps of a Chemical Reaction with the Scanning Tunneling Microscope Tip: Towards Single Molecule Engineering". In: *Physical Review Letters* 85. 13 (2000), pp. 2777–2780.

[68] F. Ullmann. "Ueber symmetrische Biphenylderivate". In: *Justus Liebig's Annalen der Chemie* 332. 1-2 (1904), pp. 38–81.

[69] L. Grill et al. "Nano-architectures by covalent assembly of molecular building blocks". In: *Nature Nanotechnology* 2. 11 (2007), pp. 687–691.

[70] R. Gutzler. "Band-structure engineering in conjugated 2D polymers". In: *Physical Chemistry Chemical Physics* 18. 42 (2016), pp. 29092–29100.

[71] O. Ourdjini et al. "Substrate-mediated ordering and defect analysis of a surface covalent organic framework". In: *Physical Review B: Condensed Matter and Materials Physics* 84. 12 (2011), p. 125421.

[72] Y.-Q. Zhang et al. "Homo-coupling of terminal alkynes on a noble metal surface". In: *Nature Communications* 3. 1286 (2012).

[73] S. Clair, M. Abel, and L. Porte. "Growth of boronic acid based two-dimensional covalent networks on a metal surface under ultrahigh vacuum". In: *Chemical Communications* 50. 68 (2014), pp. 9627–9635.

[74] A. Rastgoo-Lahrood et al. "Reversible intercalation of iodine monolayers between on-surface synthesised covalent polyphenylene networks and Au(111)". In: *Nanoscale* 9. 15 (2017), pp. 4995–5001.

[75] S. Whitelam et al. "Common Physical Framework Explains Phase Behavior and Dynamics of Atomic, Molecular, and Polymeric Network Formers". In: *Physical Review X* 4. 1 (2014), p. 011044.

[76] S. Linden et al. “Electronic Structure of Spatially Aligned Graphene Nanoribbons on Au(788)”. In: *Physical Review Letters* 108. 21 (2012), p. 216801.

[77] G. Vasseur et al. “Quasi one-dimensional band dispersion and surface metallization in long-range ordered polymeric wires”. In: *Nature Communications* 7. 10235 (2016).

[78] N. Merino-Díez et al. “Switching from Reactant to Substrate Engineering in the Selective Synthesis of Graphene Nanoribbons”. In: *The Journal of Physical Chemistry Letters* 9. 10 (2018), pp. 2510–2517.

[79] B. V. Senkovskiy et al. “Finding the hidden valence band of N = 7 armchair graphene nanoribbons with angle-resolved photoemission spectroscopy”. In: *2D Materials* 5. 3 (2018), p. 035007.

[80] A. Mugarza and J. E. Ortega. “Electronic states at vicinal surfaces”. In: *Journal of Physics: Condensed Matter* 15. 47 (2003), S3281.

[81] M. Corso et al. “Electronic states in faceted Au(111) studied with curved crystal surfaces”. In: *Journal of Physics: Condensed Matter* 21. 35 (2009), p. 353001.

[82] J. E. Ortega et al. “Structure and electronic states of vicinal Ag(111) surfaces with densely kinked steps”. In: *New Journal of Physics* 20. 7 (2018), p. 073010.

[83] G. Vasseur et al. “II Band Dispersion along Conjugated Organic Nanowires Synthesized on a Metal Oxide Semiconductor”. In: *Journal of the American Chemical Society* 138. 17 (2016), pp. 5685–5692.

[84] K. Oura, ed. *Surface science: an introduction*. Advanced texts in physics. Berlin ; New York: Springer, 2003.

[85] F. Reinert and S. Hüfner. “Photoemission spectroscopy—from early days to recent applications”. In: *New Journal of Physics* 7 (2005), p. 97.

[86] F. J. Himpsel. “Angle-resolved measurements of the photoemission of electrons in the study of solids”. In: *Advances in Physics* 32. 1 (1983), pp. 1–51.

[87] K. E. Smith and S. D. Kevan. “The electronic structure of solids studied using angle resolved photoemission spectroscopy”. In: *Progress in Solid State Chemistry* 21. 2 (1991), pp. 49–131.

[88] A. Damascelli, Z. Hussain, and Z.-X. Shen. “Angle-resolved photoemission studies of the cuprate superconductors”. In: *Reviews of Modern Physics* 75. 2 (2003), pp. 473–541.

[89] A. Damascelli. “Probing the Electronic Structure of Complex Systems by ARPES”. In: *Physica Scripta* T109 (2004), p. 61.

[90] H. Hertz. “Ueber einen Einfluss des ultravioletten Lichtes auf die electrische Entladung”. In: *Annalen der Physik und Chemie* 267. 8 (1887), pp. 983–1000.

[91] A. Einstein. “Über einen die Erzeugung und Verwandlung des Lichtes betreffenden heuristischen Gesichtspunkt”. In: *Annalen der Physik* 322. 6 (1905), pp. 132–148.

[92] H. Ishii et al. "Energy Level Alignment and Interfacial Electronic Structures at Organic/Metal and Organic/Organic Interfaces". In: *Advanced Materials* 11. 8 (1999), pp. 605–625.

[93] Ph. Hofmann et al. "Unexpected surface sensitivity at high energies in angle-resolved photoemission". In: *Physical Review B: Condensed Matter and Materials Physics* 66. 24 (2002), p. 245422.

[94] A. Tamai et al. "Spin-orbit splitting of the Shockley surface state on Cu(111)". In: *Physical Review B: Condensed Matter and Materials Physics* 87. 7 (2013), p. 075113.

[95] H. Oka et al. "Spin-polarized quantum confinement in nanostructures: Scanning tunneling microscopy". In: *Reviews of Modern Physics* 86. 4 (2014), pp. 1127–1168.

[96] Y. Hasegawa and Ph. Avouris. "Direct observation of standing wave formation at surface steps using scanning tunneling spectroscopy". In: *Physical Review Letters* 71. 7 (1993), pp. 1071–1074.

[97] P. Avouris and I.-W. Lyo. "Observation of Quantum-Size Effects at Room Temperature on Metal Surfaces With STM". In: *Science* 264. 5161 (1994), pp. 942–945.

[98] J. Li et al. "Electron Confinement to Nanoscale Ag Islands on Ag(111): A Quantitative Study". In: *Physical Review Letters* 80. 15 (1998), pp. 3332–3335.

[99] P. Han and P. S. Weiss. "Electronic substrate-mediated interactions". In: *Surface Science Reports* 67. 2 (2012), pp. 19–81.

[100] F. Reinert et al. "Direct measurements of the L -gap surface states on the (111) face of noble metals by photoelectron spectroscopy". In: *Physical Review B: Condensed Matter and Materials Physics* 63. 11 (2001), p. 115415.

[101] S. LaShell, B. A. McDougall, and E. Jensen. "Spin Splitting of an Au(111) Surface State Band Observed with Angle Resolved Photoelectron Spectroscopy". In: *Physical Review Letters* 77. 16 (1996), pp. 3419–3422.

[102] M. Ilyn et al. "Step-doubling at Vicinal Ni(111) Surfaces Investigated with a Curved Crystal". In: *The Journal of Physical Chemistry C* 121. 7 (2017), pp. 3880–3886.

[103] A. Mugarza et al. "Modelling nanostructures with vicinal surfaces". In: *Journal of Physics: Condensed Matter* 18. 13 (2006), S27.

[104] J. Zhang et al. "Probing the spatial and momentum distribution of confined surface states in a metal coordination network". In: *Chemical Communications* 50. 82 (2014), pp. 12289–12292.

[105] C. J. Chen. *Introduction to Scanning Tunneling Microscopy*. Oxford University Press, 2007.

[106] M. K. Muntwiler. "Nanostructured magnetic interfaces: case studies and new experiment control software". PhD thesis. University of Zürich, 2004.

[107] J.-Y. Park et al. "Modification of surface-state dispersion upon Xe adsorption: A scanning tunneling microscope study". In: *Physical Review B: Condensed Matter and Materials Physics* 62. 24 (2000), R16341–R16344.

[108] M. F. Crommie, C. P. Lutz, and D. M. Eigler. "Imaging standing waves in a two-dimensional electron gas". In: *Nature* 363. 6429 (1993), pp. 524–527.

[109] R. Paniago et al. "Temperature dependence of Shockley-type surface energy bands on Cu(111), Ag(111) and Au(111)". In: *Surface Science* 336. 1-2 (1995), pp. 113–122.

[110] F. J. Giessibl. "Atomic Resolution of the Silicon (111)-(7x7) Surface by Atomic Force Microscopy". In: *Science* 267. 5194 (1995), pp. 68–71.

[111] R. Pawlak et al. "Atomic-Scale Mechanical Properties of Orientated C_{60} Molecules Revealed by Noncontact Atomic Force Microscopy". In: *ACS Nano* 5. 8 (2011), pp. 6349–6354.

[112] P. Jelínek. "High resolution SPM imaging of organic molecules with functionalized tips". In: *Journal of Physics: Condensed Matter* 29. 34 (2017), p. 343002.

[113] S. Kawai. "Revealing mechanical and structural properties of molecules on surface by high-resolution atomic force microscopy". In: *Polymer Journal* 49 (2017), pp. 3–11.

[114] L. Gross et al. "The Chemical Structure of a Molecule Resolved by Atomic Force Microscopy". In: *Science* 325. 5944 (2009), pp. 1110–1114.

[115] A. Mugarza et al. "Electron Confinement in Surface States on a Stepped Gold Surface Revealed by Angle-Resolved Photoemission". In: *Physical Review Letters* 87. 10 (2001), p. 107601.

[116] F. J. García de Abajo et al. "Lateral engineering of surface states – towards surface-state nanoelectronics". In: *Nanoscale* 2. 5 (2010), pp. 717–721.

[117] A. Mugarza et al. "Measurement of electron wave functions and confining potentials via photoemission". In: *Physical Review B: Condensed Matter and Materials Physics* 67. 8 (2003), p. 081404.

[118] P. Hohenberg and W. Kohn. "Inhomogeneous Electron Gas". In: *Physical Review* 136. 3B (1964), B864–B871.

[119] W. Kohn and L. J. Sham. "Self-Consistent Equations Including Exchange and Correlation Effects". In: *Physical Review* 140. 4A (1965), A1133–A1138.

[120] J. C. Cuevas et al. "Theoretical description of the electrical conduction in atomic and molecular junctions". In: *Nanotechnology* 14. 8 (2003), R29–R38.

[121] B. Gunter Kretz. "Electronic and transport properties of 2D Dirac materials: graphene and topological insulators". PhD thesis. Universidad del País Vasco UPV-EHU, 2018.

[122] P. M. Echenique and J. B. Pendry. "The existence and detection of Rydberg states at surfaces". In: *Journal of Physics C: Solid State Physics* 11. 10 (1978), pp. 2065–2075.

[123] Z. M. Abd El-Fattah et al. "Modifying the Cu(111) Shockley surface state by Au alloying". In: *Physical Review B: Condensed Matter and Materials Physics* 86. 24 (2012), p. 245418.

[124] Z. M. Abd El-Fattah. "Surface states manipulation via surface/interface defects and adsorbates". PhD thesis. Universidad del País Vasco (UPV-EHU), 2012.

[125] P. Harrison. *Quantum Wells, Wires and Dots: Theoretical and Computational Physics of Semiconductor Nanostructures*. Chichester, UK: John Wiley & Sons, Ltd, 2005.

[126] F. Forster et al. "Systematic studies on surface modifications by ARUPS on Shockley-type surface states". In: *Surface Science* 600. 18 (2006), pp. 3870–3874.

[127] M. C. Cottin et al. "Anisotropic scattering of surface state electrons at a point defect on Bi(111)". In: *Applied Physics Letters* 98. 2 (2011), p. 022108.

[128] K. Müller et al. "Multimorphism in molecular monolayers: Pentacene on Cu(110)". In: *Physical Review B: Condensed Matter and Materials Physics* 79. 24 (2009), p. 245421.

[129] N. Kepčija et al. "Quantum confinement in self-assembled two-dimensional nanoporous honeycomb networks at close-packed metal surfaces". In: *The Journal of Chemical Physics* 142. 10 (2015), p. 101931.

[130] F. Baumberger et al. "Tailoring Confining Barriers for Surface States by Step Decoration: CO / Vicinal Cu(111)". In: *Physical Review Letters* 88. 23 (2002), p. 237601.

[131] J. Lobo-Checa et al. "Tuning the Surface State Dimensionality of Cu Nanostripes". In: *Physical Review Letters* 93. 13 (2004), p. 137602.

[132] Y. Pennec et al. "Supramolecular gratings for tuneable confinement of electrons on metal surfaces". In: *Nature Nanotechnology* 2. 2 (2007), pp. 99–103.

[133] J. Li et al. "Tunnelling spectroscopy of surface state scattering and confinement". In: *Surface Science* 422. 1-3 (1999), pp. 95–106.

[134] G. Rodary et al. "Quantization of the electron wave vector in nanostructures: Counting k -states". In: *Physical Review B: Condensed Matter and Materials Physics* 75. 23 (2007), p. 233412.

[135] E. J. Heller et al. "Scattering and absorption of surface electron waves in quantum corrals". In: *Nature* 369. 6480 (1994), pp. 464–466.

[136] G. A. Fiete and E. J. Heller. "*Colloquium* : Theory of quantum corrals and quantum mirages". In: *Reviews of Modern Physics* 75. 3 (2003), pp. 933–948.

[137] H. K. Harbury and W. Porod. "Elastic scattering theory for electronic waves in quantum corrals". In: *Physical Review B: Condensed Matter and Materials Physics* 53. 23 (1996), pp. 15455–15458.

[138] A. I. Rahachou and I. V. Zozoulenko. "Elastic scattering of surface electron waves in quantum corrals: Importance of the shape of the adatom potential". In: *Physical Review B: Condensed Matter and Materials Physics* 70. 23 (2004), p. 233409.

[139] N. N. Negulyaev et al. "Direct Evidence for the Effect of Quantum Confinement of Surface-State Electrons on Atomic Diffusion". In: *Physical Review Letters* 101. 22 (2008), p. 226601.

[140] J. Fernández et al. "Manipulation of the surface density of states of Ag(111) by means of resonators: Experiment and theory". In: *Physical Review B: Condensed Matter and Materials Physics* 94. 7 (2016), p. 075408.

[141] H. Jensen et al. "Electron dynamics in vacancy islands: Scanning tunneling spectroscopy on Ag(111)". In: *Physical Review B: Condensed Matter and Materials Physics* 71. 15 (2005), p. 155417.

[142] J. E. Ortega et al. "Scattering of surface electrons by isolated steps versus periodic step arrays". In: *Physical Review B: Condensed Matter and Materials Physics* 87. 11 (2013), p. 115425.

[143] L. Gross et al. "Scattering of Surface State Electrons at Large Organic Molecules". In: *Physical Review Letters* 93. 5 (2004), p. 056103.

[144] Ph. Avouris. "Real space imaging of electron scattering phenomena at metal surfaces". In: *Journal of Vacuum Science & Technology B: Microelectronics and Nanometer Structures* 12. 3 (1994), p. 1447.

[145] K. Schouteden and C. Van Haesendonck. "Lateral Quantization of Two-Dimensional Electron States by Embedded Ag Nanocrystals". In: *Physical Review Letters* 108. 7 (2012), p. 076806.

[146] L. Niebergall et al. "Electron confinement in hexagonal vacancy islands: Theory and experiment". In: *Physical Review B: Condensed Matter and Materials Physics* 74. 19 (2006), p. 195436.

[147] J. E. Ortega et al. "One-dimensional versus two-dimensional surface states on stepped Au (111)". In: *Physical Review B: Condensed Matter and Materials Physics* 65. 16 (2002), p. 165413.

[148] L. Bürgi et al. "Confinement of Surface State Electrons in Fabry-Pérot Resonators". In: *Physical Review Letters* 81. 24 (1998), pp. 5370–5373.

[149] J. E. Ortega et al. "Interplay between structure and electronic states in step arrays explored with curved surfaces". In: *Physical Review B: Condensed Matter and Materials Physics* 83. 8 (2011), p. 085411.

[150] J.-M. Lehn. *Supramolecular Chemistry: Concepts and Perspectives*. Weinheim, FRG: Wiley-VCH Verlag GmbH & Co. KGaA, 1995.

[151] S. Stepanow et al. "Surface-Assisted Assembly of 2D Metal–Organic Networks That Exhibit Unusual Threefold Coordination Symmetry". In: *Angewandte Chemie International Edition* 46. 5 (2007), pp. 710–713.

[152] K. Müller, M. Enache, and M. Stöhr. "Confinement properties of 2D porous molecular networks on metal surfaces". In: *Journal of Physics: Condensed Matter* 28. 15 (2016), p. 153003.

[153] J. Wyrick et al. "Do Two-Dimensional Noble Gas Atoms Produce Molecular Honeycombs at a Metal Surface?" In: *Nano Letters* 11. 7 (2011), pp. 2944–2948.

[154] S. Wang et al. "Tuning two-dimensional band structure of Cu(111) surface-state electrons that interplay with artificial supramolecular architectures". In: *Physical Review B: Condensed Matter and Materials Physics* 88. 24 (2013), p. 245430.

[155] R. Hoffmann. "A chemical and theoretical way to look at bonding on surfaces". In: *Reviews of Modern Physics* 60. 3 (1988), pp. 601–628.

[156] P. Liljeroth et al. "Variable Orbital Coupling in a Two-Dimensional Quantum-Dot Solid Probed on a Local Scale". In: *Physical Review Letters* 97. 9 (2006), p. 096803.

[157] D. Malterre et al. "ARPES and STS investigation of Shockley states in thin metallic films and periodic nanostructures". In: *New Journal of Physics* 9. 10 (2007), pp. 391–391.

[158] I. Piquero-Zulaica et al. "Temperature dependence of the partially localized state in a 2D molecular nanoporous network". In: *Applied Surface Science* 391 (2017), pp. 39–43.

[159] A. Shchyrba et al. "Covalent assembly of a two-dimensional molecular "sponge" on a Cu(111) surface: confined electronic surface states in open and closed pores". In: *Chemical Communications* 50. 57 (2014), pp. 7628–7631.

[160] K. Seufert et al. "Controlled Interaction of Surface Quantum-Well Electronic States". In: *Nano Letters* 13. 12 (2013), pp. 6130–6135.

[161] M. Stöhr et al. "Lateral Manipulation for the Positioning of Molecular Guests within the Confinements of a Highly Stable Self-Assembled Organic Surface Network". In: *Small* 3. 8 (2007), pp. 1336–1340.

[162] D. Kuhne et al. "Rotational and constitutional dynamics of caged supramolecules". In: *Proceedings of the National Academy of Sciences* 107. 50 (2010), pp. 21332–21336.

[163] Z. Cheng et al. "Adsorbates in a Box: Titration of Substrate Electronic States". In: *Physical Review Letters* 105. 6 (2010), p. 066104.

[164] S. Nowakowska et al. "Interplay of weak interactions in the atom-by-atom condensation of xenon within quantum boxes". In: *Nature Communications* 6. 6071 (2015).

[165] R. Zhang et al. "Two-Dimensional Superlattices of Bi Nanoclusters Formed on a Au(111) Surface Using Porous Supramolecular Templates". In: *ACS Nano* 9. 8 (2015), pp. 8547–8553.

[166] M. Pivetta et al. "Formation of Fe Cluster Superlattice in a Metal-Organic Quantum-Box Network". In: *Physical Review Letters* 110. 8 (2013), p. 086102.

[167] M. Matena et al. "On-surface synthesis of a two-dimensional porous coordination network: Unraveling adsorbate interactions". In: *Physical Review B: Condensed Matter and Materials Physics* 90. 12 (2014), p. 125408.

[168] M. Stöhr et al. "Controlling Molecular Assembly in Two Dimensions: The Concentration Dependence of Thermally Induced 2D Aggregation of Molecules on a Metal Surface". In: *Angewandte Chemie International Edition* 44. 45 (2005), pp. 7394–7398.

[169] A. Shchyrba et al. "Controlling the Dimensionality of On-Surface Coordination Polymers via Endo- or Exoligation". In: *Journal of the American Chemical Society* 136. 26 (2014), pp. 9355–9363.

[170] R. Paniago et al. "High-resolution photoemission study of the surface states near $\overline{\Gamma}$ on Cu(111) and Ag(111)". In: *Surface Science* 331-333 (1995), pp. 1233–1237.

[171] J. A. Knapp et al. "Temperature dependence of bulk and surface energy bands in copper using angle-resolved photoemission". In: *Physical Review B: Condensed Matter and Materials Physics* 19. 6 (1979), pp. 2844–2849.

[172] E. Knoesel, A. Hotzel, and M. Wolf. "Temperature dependence of surface state lifetimes, dephasing rates and binding energies on Cu(111) studied with time-resolved photoemission". In: *Journal of Electron Spectroscopy and Related Phenomena* 88-91 (1998), pp. 577–584.

[173] H. Yamane and N. Kosugi. "Site-Specific Organic/Metal Interaction Revealed from Shockley-Type Interface State". In: *The Journal of Physical Chemistry C* 120. 42 (2016), pp. 24307–24313.

[174] I. Horcas et al. "WSXM: A software for scanning probe microscopy and a tool for nanotechnology". In: *Review of Scientific Instruments* 78. 1 (2007), p. 013705.

[175] W. Wang et al. "Single-Molecule Resolution of an Organometallic Intermediate in a Surface-Supported Ullmann Coupling Reaction". In: *Journal of the American Chemical Society* 133. 34 (2011), pp. 13264–13267.

[176] S. Kawai et al. "Extended Halogen Bonding between Fully Fluorinated Aromatic Molecules". In: *ACS Nano* 9. 3 (2015), pp. 2574–2583.

[177] T. Okamoto et al. "V-Shaped Organic Semiconductors With Solution Processability, High Mobility, and High Thermal Durability". In: *Advanced Materials* 25. 44 (2013), pp. 6392–6397.

[178] T. Clark et al. "Halogen bonding: the σ-hole: Proceedings of "Modeling interactions in biomolecules II", Prague, September 5th–9th, 2005". In: *Journal of Molecular Modeling* 13. 2 (2007), pp. 291–296.

[179] G. R. Desiraju et al. "Definition of the halogen bond (IUPAC Recommendations 2013)". In: *Pure and Applied Chemistry* 85. 8 (2013), pp. 1711–1713.

[180] S. Kawai et al. "Organometallic Bonding in an Ullmann-Type On-Surface Chemical Reaction Studied by High-Resolution Atomic Force Microscopy". In: *Small* 12. 38 (2016), pp. 5303–5311.

[181] J. Shang et al. "Assembling molecular Sierpiński triangle fractals". In: *Nature Chemistry* 7. 5 (2015), pp. 389–393.

[182] W. Wang et al. "Cooperative Modulation of Electronic Structures of Aromatic Molecules Coupled to Multiple Metal Contacts". In: *Physical Review Letters* 110. 4 (2013), p. 046802.

[183] A. A. Kordyuk. "ARPES experiment in fermiology of quasi-2D metals (Review Article)". In: *Low Temperature Physics* 40. 4 (2014), pp. 286–296.

[184] D. Lu et al. "Angle-Resolved Photoemission Studies of Quantum Materials". In: *Annual Review of Condensed Matter Physics* 3 (2012), pp. 129–167.

[185] H. Cercellier et al. "Interplay between structural, chemical, and spectroscopic properties of Ag / Au (111) epitaxial ultrathin films: A way to tune the Rashba coupling". In: *Physical Review B: Condensed Matter and Materials Physics* 73. 19 (2006), p. 195413.

[186] F. J. Giessibl. "High-speed force sensor for force microscopy and profilometry utilizing a quartz tuning fork". In: *Applied Physics Letters* 73. 26 (1998), pp. 3956–3958.

[187] S. Kawai et al. "Atomically controlled substitutional boron-doping of graphene nanoribbons". In: *Nature Communications* 6. 8098 (2015).

[188] G. D. Nguyen et al. "Atomically precise graphene nanoribbon heterojunctions from a single molecular precursor". In: *Nature Nanotechnology* 12. 11 (2017), pp. 1077–1082.

[189] R. A. Durr et al. "Orbitally Matched Edge-Doping in Graphene Nanoribbons". In: *Journal of the American Chemical Society* 140. 2 (2018), pp. 807–813.

[190] G. Reecht et al. "Oligothiophene Nanorings as Electron Resonators for Whispering Gallery Modes". In: *Physical Review Letters* 110. 5 (2013), p. 056802.

[191] L. Genovese et al. "Daubechies wavelets as a basis set for density functional pseudopotential calculations". In: *The Journal of Chemical Physics* 129. 1 (2008), p. 014109.

[192] C. Hartwigsen, S. Goedecker, and J. Hutter. "Relativistic separable dual-space Gaussian pseudopotentials from H to Rn". In: *Physical Review B: Condensed Matter and Materials Physics* 58. 7 (1998), pp. 3641–3662.

[193] L. Genovese et al. "Efficient solution of Poisson's equation with free boundary conditions". In: *The Journal of Chemical Physics* 125. 7 (2006), p. 074105.

[194] Thai Thanh Thu Bui et al. "The Nature of Halogen ··· Halogen Interactions: A Model Derived from Experimental Charge-Density Analysis". In: *Angewandte Chemie International Edition* 48. 21 (2009), pp. 3838–3841.

[195] M. Ruiz-Osés et al. "Non-Covalent Interactions in Supramolecular Assemblies Investigated with Electron Spectroscopies". In: *ChemPhysChem* 10. 6 (2009), pp. 896–900.

[196] F. Forster, S. Hüfner, and F. Reinert. "Rare Gases on Noble-Metal Surfaces: An Angle-Resolved Photoemission Study with High Energy Resolution †". In: *The Journal of Physical Chemistry B* 108. 38 (2004), pp. 14692–14698.

[197] E. Bertel and N. Memmel. "Promotors, poisons and surfactants: Electronic effects of surface doping on metals". In: *Applied Physics A Materials Science and Processing* 63. 6 (1996), pp. 523–531.

[198] C. Liu et al. "Interaction between Adatom-Induced Localized States and a Quasi-Two-Dimensional Electron Gas". In: *Physical Review Letters* 96. 3 (2006), p. 036803.

[199] C. Didiot et al. "Interacting quantum box superlattice by self-organized Co nanodots on Au(788)". In: *Physical Review B: Condensed Matter and Materials Physics* 76. 8 (2007), p. 081404.

[200] P. Mishra et al. "Spatially Resolved Magnetic Anisotropy of Cobalt Nanostructures on the Au(111) Surface". In: *Nano Letters* 17. 9 (2017), pp. 5843–5847.

[201] N. Armbrust et al. "Model potential for the description of metal/organic interface states". In: *Scientific Reports* 7. 46561 (2017).

[202] Q. Sun et al. "Dehalogenative Homocoupling of Terminal Alkynyl Bromides on Au(111): Incorporation of Acetylenic Scaffolding into Surface Nanostructures". In: *ACS Nano* 10. 7 (2016), pp. 7023–7030.

[203] Y.-L. Zhao et al. "Donor/Acceptor Properties of Aromatic Molecules in Complex Metal–Molecule Interfaces". In: *Langmuir* 33. 2 (2017), pp. 451–458.

[204] K. K. Gomes et al. "Designer Dirac fermions and topological phases in molecular graphene". In: *Nature* 483. 7389 (2012), pp. 306–310.

[205] N. V. Smith. "Phase analysis of image states and surface states associated with nearly-free-electron band gaps". In: *Physical Review B: Condensed Matter and Materials Physics* 32. 6 (1985), pp. 3549–3555.

[206] F. Schiller et al. "Electronic structure of Mg : From monolayers to bulk". In: *Physical Review B: Condensed Matter and Materials Physics* 70. 12 (2004), p. 125106.

[207] J. E. Ortega and F. J. Himpsel. "Quantum well states as mediators of magnetic coupling in superlattices". In: *Physical Review Letters* 69. 5 (1992), pp. 844–847.

[208] Y. Hasegawa, T. Suzuki, and T. Sakurai. "Modification of electron density in surface states: standing wave observation on Pd overlayers by STM". In: *Surface Science* 514. 1-3 (2002), pp. 84–88.

[209] M. A. Mueller et al. "Probing interfacial properties with Bloch electrons: Ag on Cu(111)". In: *Physical Review B: Condensed Matter and Materials Physics* 40. 8 (1989), pp. 5845–5848.

[210] G. Kresse and J. Hafner. "Ab initio molecular dynamics for liquid metals". In: *Physical Review B: Condensed Matter and Materials Physics* 47. 1 (1993), pp. 558–561.

[211] G. Kresse and J. Furthmüller. "Efficient iterative schemes for *ab initio* total-energy calculations using a plane-wave basis set". In: *Physical Review B: Condensed Matter and Materials Physics* 54. 16 (1996), pp. 11169–11186.

[212] G. Kresse and J. Furthmüller. "Efficiency of ab-initio total energy calculations for metals and semiconductors using a plane-wave basis set". In: *Computational Materials Science* 6. 1 (1996), pp. 15–50.

[213] J. P. Perdew, K. Burke, and M. Ernzerhof. "Generalized Gradient Approximation Made Simple [Phys. Rev. Lett. 77, 3865 (1996)]". In: *Physical Review Letters* 78. 7 (1997), pp. 1396–1396.

[214] N. Gonzalez-Lakunza et al. "Formation of Dispersive Hybrid Bands at an Organic-Metal Interface". In: *Physical Review Letters* 100. 15 (2008), p. 156805.

[215] Z. M. Abd El-Fattah et al. "Lifshitz Transition across the $\mathrm{Ag/Cu(111)}$ Superlattice Band Gap Tuned by Interface Doping". In: *Physical Review Letters* 107. 6 (2011), p. 066803.

[216] S. Kawai et al. "Van der Waals interactions and the limits of isolated atom models at interfaces". In: *Nature Communications* 7. 11559 (2016).

[217] C. Hückstädt et al. "Work function studies of rare-gas/noble metal adsorption systems using a Kelvin probe". In: *Physical Review B: Condensed Matter and Materials Physics* 73. 7 (2006), p. 075409.

[218] A. Sadeghi et al. "Multiscale approach for simulations of Kelvin probe force microscopy with atomic resolution". In: *Physical Review B: Condensed Matter and Materials Physics* 86. 7 (2012), p. 075407.

[219] L. Bürgi, H. Brune, and K. Kern. "Imaging of Electron Potential Landscapes on Au(111)". In: *Physical Review Letters* 89. 17 (2002), p. 176801.

[220] J. Ziroff et al. "Adsorption energy and geometry of physisorbed organic molecules on Au(111) probed by surface-state photoemission". In: *Surface Science* 603. 2 (2009), pp. 354–358.

[221] F. Forster et al. "Surface and interface states on adsorbate covered noble metal surfaces". In: *Surface Science* 532-535 (2003), pp. 160–165.

[222] H. González-Herrero et al. "Graphene Tunable Transparency to Tunneling Electrons: A Direct Tool To Measure the Local Coupling". In: *ACS Nano* 10. 5 (2016), pp. 5131–5144.

[223] J. Tesch et al. "Structural and electronic properties of graphene nanoflakes on Au(111) and Ag(111)". In: *Scientific Reports* 6. 23439 (2016).

[224] S. Joshi et al. "Boron Nitride on Cu(111): An Electronically Corrugated Monolayer". In: *Nano Letters* 12. 11 (2012), pp. 5821–5828.

[225] D. Malterre et al. "Symmetry breaking and gap opening in two-dimensional hexagonal lattices". In: *New Journal of Physics* 13. 013026 (2011).

[226] H. Dil et al. "Surface Trapping of Atoms and Molecules with Dipole Rings". In: *Science* 319. 5871 (2008), pp. 1824–1826.

[227] W. Krenner et al. "Assessment of Scanning Tunneling Spectroscopy Modes Inspecting Electron Confinement in Surface-Confined Supramolecular Networks". In: *Scientific Reports* 3.1454 (2013).

[228] J. Teyssandier, S. De Feyter, and K. S. Mali. "Host–guest chemistry in two-dimensional supramolecular networks". In: *Chemical Communications* 52. 77 (2016), pp. 11465–11487.

[229] M. A. Chesters, M. Hussain, and J. Pritchard. "Xenon monolayer structures on copper and silver". In: *Surface Science* 35 (1973), pp. 161–171.

[230] Th. Seyller et al. "Observation of top-site adsorption for Xe on Cu(111)". In: *Chemical Physics Letters* 291. 5-6 (1998), pp. 567–572.

[231] D. M. Eigler, C. P. Lutz, and W. E. Rudge. "An atomic switch realized with the scanning tunnelling microscope". In: *Nature* 352. 6336 (1991), pp. 600–603.

[232] A. Yazdani, D. M. Eigler, and N. D. Lang. "Off-Resonance Conduction Through Atomic Wires". In: *Science* 272. 5270 (1996), pp. 1921–1924.

[233] G. Kichin et al. "Single Molecule and Single Atom Sensors for Atomic Resolution Imaging of Chemically Complex Surfaces". In: *Journal of the American Chemical Society* 133. 42 (2011), pp. 16847–16851.

[234] L. Limot et al. "Surface-State Localization at Adatoms". In: *Physical Review Letters* 94. 3 (2005), p. 036805.

[235] F. E. Olsson et al. "Localization of the Cu(111) Surface State by Single Cu Adatoms". In: *Physical Review Letters* 93. 20 (2004), p. 206803.

[236] J.-Y. Park et al. "Adsorption and growth of Xe adlayers on the Cu(111) surface". In: *Physical Review B: Condensed Matter and Materials Physics* 60. 24 (1999), pp. 16934–16940.

[237] H. C. Manoharan, C. P. Lutz, and D. M. Eigler. "Quantum mirages formed by coherent projection of electronic structure". In: *Nature* 403. 6769 (2000), pp. 512–515.

[238] K. S. Novoselov et al. "Electric Field Effect in Atomically Thin Carbon Films". In: *Science* 306. 5696 (2004), pp. 666–669.

[239] A. H. Castro Neto et al. "The electronic properties of graphene". In: *Reviews of Modern Physics* 81. 1 (2009), pp. 109–162.

[240] Y.-W. Son, M. L. Cohen, and S. G. Louie. "Energy Gaps in Graphene Nanoribbons". In: *Physical Review Letters* 97. 21 (2006), p. 216803.

[241] A. Narita et al. "New advances in nanographene chemistry". In: *Chemical Society Reviews* 44. 18 (2015), pp. 6616–6643.

[242] Q. Shen, H.-Y. Gao, and H. Fuchs. "Frontiers of on-surface synthesis: From principles to applications". In: *Nano Today* 13 (2017), pp. 77–96.

[243] D. G. de Oteyza et al. "Substrate-Independent Growth of Atomically Precise Chiral Graphene Nanoribbons". In: *ACS Nano* 10. 9 (2016), pp. 9000–9008.

[244] P. H. Jacobse et al. "Electronic components embedded in a single graphene nanoribbon". In: *Nature Communications* 8. 119 (2017).

[245] P. B. Bennett et al. "Bottom-up graphene nanoribbon field-effect transistors". In: *Applied Physics Letters* 103. 25 (2013), p. 253114.

[246] V. Passi et al. "Field-Effect Transistors Based on Networks of Highly Aligned, Chemically Synthesized $N = 7$ Armchair Graphene Nanoribbons". In: *ACS Applied Materials & Interfaces* 10. 12 (2018), pp. 9900–9903.

[247] S. Günes, H. Neugebauer, and N. S. Sariciftci. "Conjugated Polymer-Based Organic Solar Cells". In: *Chemical Reviews* 107. 4 (2007), pp. 1324–1338.

[248] G. Li, W.-H. Chang, and Y. Yang. "Low-bandgap conjugated polymers enabling solution-processable tandem solar cells". In: *Nature Reviews Materials* 2. 8 (2017), p. 17043.

[249] H. Masai and J. Terao. "Stimuli-responsive functionalized insulated conjugated polymers". In: *Polymer Journal* 49 (2017), pp. 805–814.

[250] P. Guiglion and M. A. Zwijnenburg. "Contrasting the optical properties of the different isomers of oligophenylene". In: *Physical Chemistry Chemical Physics* 17. 27 (2015), pp. 17854–17863.

[251] S. Y. Hong et al. "Origin of the Broken Conjugation in m-Phenylene Linked Conjugated Polymers". In: *Macromolecules* 34. 18 (2001), pp. 6474–6481.

[252] M. H. van der Veen et al. "Molecules with Linear pi-Conjugated Pathways between All Substituents Omniconjugation". In: *Advanced Functional Materials* 14. 3 (2004), pp. 215–223.

[253] C. García-Fernández et al. "Exploring the Relation Between Intramolecular Conjugation and Band Dispersion in One-Dimensional Polymers". In: *The Journal of Physical Chemistry C* 121. 48 (2017), pp. 27118–27125.

[254] A. A. Kocherzhenko, F. C. Grozema, and L. D. A. Siebbeles. "Single molecule charge transport: from a quantum mechanical to a classical description". In: *Physical Chemistry Chemical Physics* 13. 6 (2011), pp. 2096–2110.

[255] D. Z. Manrique et al. "A quantum circuit rule for interference effects in single-molecule electrical junctions". In: *Nature Communications* 6. 6389 (2015).

[256] C. M. Guédon et al. "Observation of quantum interference in molecular charge transport". In: *Nature Nanotechnology* 7. 5 (2012), pp. 305–309.

[257] T. Markussen, R. Stadler, and K. S. Thygesen. "The Relation between Structure and Quantum Interference in Single Molecule Junctions". In: *Nano Letters* 10. 10 (2010), pp. 4260–4265.

[258] P. A. Limacher and H. P. Lüthi. "Cross-conjugation". In: *Wiley Interdisciplinary Reviews: Computational Molecular Science* 1. 4 (2011), pp. 477–486.

[259] A. L. Thompson et al. "Using Meta Conjugation To Enhance Charge Separation versus Charge Recombination in Phenylacetylene Donor-Bridge-Acceptor Complexes". In: *Journal of the American Chemistry Society* 127. 47 (2005), pp. 16348–16349.

[260] T. Tada and K. Yoshizawa. "Molecular design of electron transport with orbital rule: toward conductance-decay free molecular junctions". In: *Physical Chemistry Chemical Physics* 17. 48 (2015), pp. 32099–32110.

[261] J. Terao et al. "Design principle for increasing charge mobility of π-conjugated polymers using regularly localized molecular orbitals". In: *Nature Communications* 4.1691 (2013).

[262] L. Talirz, P. Ruffieux, and R. Fasel. "On-Surface Synthesis of Atomically Precise Graphene Nanoribbons". In: *Advanced Materials* 28. 29 (2016), pp. 6222–6231.

[263] Q. Fan et al. "Surface-Assisted Organic Synthesis of Hyperbenzene Nanotroughs". In: *Angewandte Chemie International Edition* 52. 17 (2013), pp. 4668–4672.

[264] M. Abadía et al. "Polymerization of Well-Aligned Organic Nanowires on a Ferromagnetic Rare-Earth Surface Alloy". In: *ACS Nano* 11. 12 (2017), pp. 12392–12401.

[265] L. Cai et al. "Direct Formation of C–C Double-Bonded Structural Motifs by On-Surface Dehalogenative Homocoupling of *gem* -Dibromomethyl Molecules". In: *ACS Nano* 12. 8 (2018), pp. 7959–7966.

[266] I. Piquero-Zulaica et al. "Electronic Structure Tunability by Periodic *meta*-Ligand Spacing in One-Dimensional Organic Semiconductors". In: *ACS Nano* (2018).

[267] C. J. Judd et al. "Ullmann Coupling Reactions on Ag(111) and Ag(110); Substrate Influence on the Formation of Covalently Coupled Products and Intermediate Metal-Organic Structures". In: *Scientific Reports* 7.14541 (2017).

[268] M. Di Giovannantonio et al. "Insight into Organometallic Intermediate and Its Evolution to Covalent Bonding in Surface-Confined Ullmann Polymerization". In: *ACS Nano* 7. 9 (2013), pp. 8190–8198.

[269] Q. Fan et al. "Surface-Assisted Formation, Assembly, and Dynamics of Planar Organometallic Macrocycles and Zigzag Shaped Polymer Chains with C–Cu–C Bonds". In: *ACS Nano* 8. 1 (2014), pp. 709–718.

[270] M. Koch et al. "Substrate-controlled linking of molecular building blocks: Au(111) vs. Cu(111)". In: *Surface Science* 627 (2014), pp. 70–74.

[271] M. Chen et al. "On-Surface Synthesis and Characterization of Honeycombene Oligophenylene Macrocycles". In: *ACS Nano* 11. 1 (2017), pp. 134–143.

[272] Q. Fan et al. "On-Surface Pseudo-High-Dilution Synthesis of Macrocycles: Principle and Mechanism". In: *ACS Nano* 11. 5 (2017), pp. 5070–5079.

[273] M. Di Giovannantonio et al. "On-Surface Growth Dynamics of Graphene Nanoribbons: The Role of Halogen Functionalization". In: *ACS Nano* 12. 1 (2018), pp. 74–81.

[274] H. Offenbacher et al. "Orbital tomography: Molecular band maps, momentum maps and the imaging of real space orbitals of adsorbed molecules". In: *Journal of Electron Spectroscopy and Related Phenomena* 204 (2015), pp. 92–101.

[275] G. Koller et al. "Intra- and Intermolecular Band Dispersion in an Organic Crystal". In: *Science* 317. 5836 (2007), pp. 351–355.

[276] L. Gross et al. "High-Resolution Molecular Orbital Imaging Using a p -Wave STM Tip". In: *Physical Review Letters* 107. 8 (2011), p. 086101.

[277] J. Hieulle et al. "On-Surface Route for Producing Planar Nanographenes with Azulene Moieties". In: *Nano Letters* 18. 1 (2018), pp. 418–423.

[278] J. M. Soler et al. "The SIESTA method for *ab initio* order- *N* materials simulation". In: *Journal of Physics: Condensed Matter* 14. 11 (2002), pp. 2745–2779.

[279] J. Klimeš, David R Bowler, and Angelos Michaelides. "Chemical accuracy for the van der Waals density functional". In: *Journal of Physics: Condensed Matter* 22. 2 (2010), p. 022201.

[280] Q. Fan, J. M. Gottfried, and J. Zhu. "Surface-Catalyzed C-C Covalent Coupling Strategies toward the Synthesis of Low-Dimensional Carbon-Based Nanostructures". In: *Accounts of Chemical Research* 48. 8 (2015), pp. 2484–2494.

[281] Q. Fan et al. "Confined Synthesis of Organometallic Chains and Macrocycles by Cu-O Surface Templating". In: *ACS Nano* 10. 3 (2016), pp. 3747–3754.

[282] P. J. Goddard, K. Schwaha, and R. M. Lambert. "Adsorption-desorption properties and surface structural chemistry of bromine on clean and sodium-dosed Ag(111)". In: *Surface Science* 71. 2 (1978), pp. 351–363.

[283] C. H. Hendon et al. "Grand Challenges and Future Opportunities for Metal–Organic Frameworks". In: *ACS Central Science* 3. 6 (2017), pp. 554–563.

[284] L. E. Kreno et al. "Metal–Organic Framework Materials as Chemical Sensors". In: *Chemical Reviews* 112. 2 (2012), pp. 1105–1125.

[285] L. Zhu et al. "Metal–Organic Frameworks for Heterogeneous Basic Catalysis". In: *Chemical Reviews* 117. 12 (2017), pp. 8129–8176.

[286] V. Stavila, A. A. Talin, and M. D. Allendorf. "MOF-based electronic and opto-electronic devices". In: *Chemical Society Reviews* 43. 16 (2014), pp. 5994–6010.

[287] R. Baltic et al. "Magnetic properties of single rare-earth atoms on graphene/Ir(111)". In: *Physical Review B: Condensed Matter and Materials Physics* 98. 2 (2018), p. 024412.

[288] Z. F. Wang, N. Su, and F. Liu. "Prediction of a Two-Dimensional Organic Topological Insulator". In: *Nano Letters* 13. 6 (2013), pp. 2842–2845.

[289] Z. F. Wang, Z. Liu, and F. Liu. "Organic topological insulators in organometallic lattices". In: *Nature Communications* 4. 1471 (2013).

[290] L. Dong et al. "Two-Dimensional π-Conjugated Covalent-Organic Frameworks as Quantum Anomalous Hall Topological Insulators". In: *Physical Review Letters* 116. 9 (2016), p. 096601.

[291] Ya-ping Wang et al. "Discovery of intrinsic quantum anomalous Hall effect in organic Mn-DCA lattice". In: *Applied Physics Letters* 110. 23 (2017), p. 233107.

[292] X. Zhang et al. "Theoretical Discovery of a Superconducting Two-Dimensional Metal–Organic Framework". In: *Nano Letters* 17. 10 (2017), pp. 6166–6170.

[293] Z. Yang et al. "Two-dimensional delocalized states in organometallic bisacetylide networks on Ag(111)". In: *Nanoscale* 10. 8 (2018), pp. 3769–3776.

[294] H. Sun et al. "Deconstruction of the Electronic Properties of a Topological Insulator with a Two-Dimensional Noble Metal–Organic Honeycomb–Kagome Band Structure". In: *The Journal of Physical Chemistry C* 122. 32 (2018), pp. 18659–18668.

[295] Y.-Q. Zhang et al. "Intermolecular Hybridization Creating Nanopore Orbital in a Supramolecular Hydrocarbon Sheet". In: *Nano Letters* 16. 7 (2016), pp. 4274–4281.

[296] M. Feng, J. Zhao, and H. Petek. "Atomlike, Hollow-Core-Bound Molecular Orbitals of C60". In: *Science* 320. 5874 (2008), pp. 359–362.

[297] J. Zhao et al. "The Superatom States of Fullerenes and Their Hybridization into the Nearly Free Electron Bands of Fullerites". In: *ACS Nano* 3. 4 (2009), pp. 853–864.

[298] M. Fritton et al. "The influence of *ortho* -methyl substitution in organometallic self-assembly – a comparative study on Cu(111) *vs.* Ag(111)". In: *Chemical Communications* 54. 70 (2018), pp. 9745–9748.

[299] T. Lin et al. "Steering On-Surface Polymerization with Metal-Directed Template". In: *Journal of the American Chemical Society* 135. 9 (2013), pp. 3576–3582.

Universidad del País Vasco

Euskal Herriko Unibertsitatea